How do Microbes Eat Rocks?
Modelling Biogeochemical Reactions at the Rock/Water Interface in Fractured Limestone Aquifers

Dissertation

der Mathematisch-Naturwissenschaftlichen Fakultät

der Eberhard Karls Universität Tübingen

zur Erlangung des Grades eines

Doktors der Naturwissenschaften

(Dr. rer. nat.)

vorgelegt von

Elena Petrova

aus Shkotovo, Russland

Tübingen

2022

Gedruckt mit Genehmigung der Mathematisch-Naturwissenschaftlichen Fakultät der Eberhard Karls Universität Tübingen.

Tag der mündlichen Qualifikation:	22.05.2023
Dekan:	Prof. Dr. Thilo Stehle
1. Berichterstatter/-in:	Prof. Dr. Peter Grathwohl
2. Berichterstatter/-in:	Prof. Dr. Christiane Zarfl

To my son

*

“Learn what is to be taken seriously and laugh at the rest.”

(H.Hesse)

*

Сыплют волны, с колесами споря,

Серебристые брызги вокруг.

Ни смущения в сердце, ни горя, —

Будь счастливым, мой маленький друг!

(М. Цветаева)

Abstract

Groundwater contamination of the fractured aquifers by agricultural pollutants has been happening worldwide since more than a century, boosting the scientific research to develop new modelling approaches for reactive transport simulation in aquifers. Spatially implicit methods like travel time approaches have been gaining interest, attracting by their lower computational demand and flexibility. At the same time, detailed mechanistic models of reactive transport in the fractured systems allow percipient understanding of underlying geochemical processes and provide veritable quantification of the latter. In this work, we connect a spatially explicit model of denitrification and isotope transport, and analytical solutions of atrazine transport in the fractured system, with a spatially implicit travel time approach. The work aims to study reactive behaviour of agriculturally produced contaminants on the catchment scale and quantify the fractured system parameters of the Muschelkalk aquifer. Reactive transport modelling was employed for this purpose with MIN3P and analytical solutions for a single fracture. Reactive transport models included advective flow in the fracture as well as possible (multicomponent) diffusive exchange with the rock matrix and redox processes taking place along the flow path. Determination of the travel times and transport parameters is done by direct modelling of tritium, helium, radiogenic helium, and argon-39 isotopes and accounting for multicomponent diffusion and radioactive decay within the streamline. Stochastic simulations of the atrazine transport under parametric uncertainty were employed for predictive quantification of travel time-dependent groundwater vulnerability. Conceptual model selection of denitrification and investigation of the redox evolution on the catchment scale was done with the MIN3P code. Results were verified with observations made across the Ammer catchment. The gained knowledge highlights the significance of comprehensive process-based hydrogeochemical modelling along with an uncertainty assessment on the catchment scale. It also demonstrates the relevance of reactive transport modelling for correct calibration as a prerequisite for prediction of the long-term evolution and transport of solutes in groundwater.

Zusammenfassung

Grundwasserverschmutzungen von Kluftgrundwasserleitern durch landwirtschaftliche Schadstoffe finden weltweit seit mehr als hundert Jahre statt, was die wissenschaftliche Forschung zur Entwicklung neuer Modellierungsansätze für die reaktive Transportsimulation in Grundwasserleitern befördert. Räumlich implizite Methoden haben durch ihren geringeren rechnerischeren Bedarf und ihre Flexibilität an Interesse gewonnen. Gleichzeitig erlauben detaillierte mechanistische Modelle des reaktiven Transports in geklüfteten Systemen ein anschauliches Verständnis der zugrunde liegenden geochemischen Prozesse und eine veritable Quantifizierung der letzteren. In dieser Arbeit verbinden wir ein räumlich explizites Modell der Denitrifikation und des Isotopentransports und analytische Lösungen des Atrazintransports in einem Kluft-Aquifer, mit einem räumlich impliziten Verweilzeitansatz. Die Arbeit zielt darauf ab, das reaktive Verhalten landwirtschaftlich produzierter Schadstoffe auf der Einzugsgebietsskala zu untersuchen und die Kluft-Systemparameter des geklüfteten Muschelkalk-Aquifers zu quantifizieren. Zu diesem Zweck wurden reaktive Transportmodelle in MIN3P und analytische Lösungen für eine einzelne Kluft verwendet. Die Modelle reaktiven Transports beinhalteten advektive Strömung in der Kluft sowie diffusiven Austausch mit der Gesteinsmatrix und Redoxprozesse entlang der Stromlinie. Die Bestimmung der Verweilzeiten und Transportparameter erfolgt durch eine direkte Modellierung von Tritium, ^{3}Helium, ^{4}Helium und ^{39}Argon -Isotopen unter Berücksichtigung der Mehrkomponentendiffusion und des radioaktiven Zerfalls innerhalb der Stromlinie. Stochastische Simulationen des Atrazintransports unter parametrischer Unsicherheit wurden zur vorhersagenden Quantifizierung der verweilzeitabhängigen Grundwasservulnerabilität eingesetzt. Die konzeptionelle Modellauswahl der Denitrifikation und die Untersuchung der Redoxentwicklung auf der Einzugsgebietsskala erfolgten mithilfe des MIN3P-Codes. Die Ergebnisse wurden mithilfe von Beobachtungen im gesamten Ammereinzugsgebiet verifiziert. Die gewonnenen Erkenntnisse unterstreichen die Bedeutung einer umfassenden prozessbasierten hydrogeochemischen Modellierung zusammen mit einer Unsicherheitsbewertung auf der Einzugsgebietsskala. Es zeigt auch die Relevanz der reaktiven Transportmodellierung für die korrekte Kalibrierung als Voraussetzung für die Vorhersage der langfristigen Entwicklung und des Transports von gelösten Stoffen im Grundwasser.

.

Acknowledgements

The journey of doing the PhD was exciting and adventurous, and would not be possible without the great assistance and company. I would like to express my sincere gratitude to all of those, who made my PhD time an unforgettable experience, continuously supported me, challenged me, and just were there when it was needed.

First of all; I would like to heartfully thank Prof. Dr. Peter Grathwohl for deciding to give me a chance to pursue a PhD under his supervision and giving me so much of trust with this step. His careful guidance, sparkling inspiration, positive thinking and continuous commitment to his students and team were always an example for me. It has been a privilege to be supervised and to have a chance to work together with him.

I also would like to express my deepest gratitude to Dr. Michael Finkel who was involved in every part of my dissertation and was always there for the fruitful (and sometimes spontaneous) discussion, advice, and encouragement. I would also like to thank Michael for keeping the team spirit by organising ski weekends which I enjoyed a lot.

My third supervisor, Prof. Dr. Uli Mayer deserves particular recognition for being available from overseas for an impactful discussion and continuous support with the MIN3P code.

My deep gratefulness goes to Prof. Dr. Olaf Cirpka who has given his heart and precious time to the (I)RTG program, and made the best of it. I feel deeply honoured to take a part in this program. Additional appreciations go to Olaf for all the (non)scientific discussions and talks we had.

I owe very special thanks to Dr. Evgenii (Jenia) Kortunov who was still there when I started my PhD and took his time and energy to introduce me to the MIN3P modelling. I also deeply appreciate continuous discussions and talks throughout my journey and feel thankful for meeting him.

I would like to thank Dr. Karsten Osenbrück for the helpful discussions and sharing the ideas, especially in the isotope study. My warm thanks go to Dr. Jana Meierdierks who helped me with sorption experiments and who also was always there for help, discussion, sharing a piece of a cake or an idea.

There have been many events and meetings which made an impact on me besides direct scientific collaborations.

Thanks to the administration and technical teams - Dr. Wolfgang Bott, Elisabetha Kraft, Marion Schäffling, Willi Kappler, Dr. Peter Merkel and particularly, to Monika Jekelius for their tireless efforts and careful guidance through the jungle of administrative, bureaucratic, visa, and cultural aspects. I owe many thanks for this help.

Furthermore, I would like to thank Prof. Dr. Andreas Kappler, Dr. Herman Rügner, Dr Marc Schwientek, Dr. Fernando Mazo D'Affonseca, Dr. Eva Blendinger, Dr. Natalia Jakus, who supported me in various ways during the research.

My deepest gratitude goes to my scientific supervisor from MS studies Prof. Dr. Alexey Lekhov who created the solid base for my PhD and who has always been an example for me.

I had a chance to enjoy the company of wonderful colleagues and outstanding scientists, and I would like to thank them for insightful discussions. My gratitudes to the IRTG and CAMPOS teams, and particularly to Jenia, Jeremy, Marvin, Matthias, Reynold, Carolin, Veronika, Stefan, Simon, Sergey, Jonas, Philipp, Julia, Michelle, Ran, Ana Gonzales-Nicolas, Hemanti, Christine, Jorge, I want to thank Tübingen for giving me a gift of meeting you!

I thank my friends who were supporting me in the hardest times of the sinusoid, and were sharing my happiness in the time of a rise. Warm hugs to Petya, Anna, Anna, Anna, Pasha, Vova, Viktoria, Santa-Vanta, Max, Max, Aurelie&Trevor, Olesya, Alyona, Lena, Olivier, die Ärzte, Jana, Gaelle, Ivo, Mina, Ilya, and Lai-lai, Ira, and Philipp, even if you don't like the sentiments ;P.

I want to thank all those who fight against the war in the world. I thank the literature, poetry and music for supporting me in the hard times.

Last but not least, I want to thank my family, my father and his passed wife who unintentionally raised me to think independently and to rebel against the system.

And mainly, my son Ярослав which literally went through the entire PhD journey with me, and who teached me an absolute love, and this is more than anything in this world.

Content

1. INTRODUCTION

Fractured aquifers supply at least 25 % of the global population with drinking water (Hartmann et al., 2014; Chen et al., 2017). Being a part of the global water circle, fractured aquifers are influenced by various contaminants. Since the last century, agricultural practice and industrial development deteriorated groundwater quality, and boosted scientific developments in hydrogeochemical modeling.

Requests on the prediction of spatio-temporal behaviour of pollutants resulted in a sequence of conceptual models for solving these issues within the fractured system (Berre et al., 2019). Even though any model describes only a simplified version of reality, and not reality itself (Box, 1976), it should still be good enough for practical applicability. Model quality is defined by its ability to imitate real-world behaviour, and is limited by uncertainty and the number of parameters needed to describe the model (Höge, 2019). That is why the demand for appropriate concepts of the reactive transport modelling in the fractured systems of different complexity levels has been growing over the last 50 years leading to single or multiple continuum porous medium models, discrete fracture network models, and travel time-based models (Deng and Spycher, 2019).

Eulerian models of reactive transport (e.g. Refsgaard et al., 2014) are useful for quantifying fluxes and the turnover of solutes and making deterministic predictions. However, the application of such models is limited due to typically high computational costs, heterogeneity, and data scarcity. With the idea of travel time-based models about 30 years ago (Dagan and Nguyen, 1989) this complication could partially be resolved. In travel time-based models, in contrast to the spatially explicit Eulerian models, the travel time replaces spatial coordinates as independent variables (Cvetkovic et al., 1994) reducing the dimensionality of the problem, and therefore providing a short-cut for solving reactive transport problems in porous or fractured media (Cvetkovic and Dagan, 1994; Dagan and Cvetkovic, 1996; Finkel et al., 2016; Loschko et al., 2016; Luo and Cirpka, 2008; Molin and Cvetkovic, 2010; Rubin et al., 1994; Seeboonruang and Ginn, 2006; Sanz-Prat et al., 2015, 2016).

Within the travel time concept, fractured systems can be seen as a network of fractures (advective component) with matrix diffusion-limited mass transfer (Neretnieks, 1980; Sidborn and Neretnieks, 2007). Parameterization of a travel time model comprises reactive tracer transport (i.e., including rock-water interactions, redox processes, etc.), and spatial-temporal characteristics of flow by accounting for probability density functions (PDFs) of travel times. The concentration of any component at a sampling location is the result of the convolution of its reactive function, defined for a specific parameter set, and the distribution of the travel times.

The probability density function of the travel time is typically described by some non-negative transfer function whose shape is assumed a priori and described by a parametric function with just a few shape-scale parameters. The most common ones are log-normal, gamma (Kirchner et al., 2000), or inverse Gaussian distribution (Leray et al., 2016). More sophisticated descriptions such as multi-modal, non-parametric travel time distribution (Liao et al., 2011) or storage selection functions (Rodriguez et al., 2020) are created for well-described systems to account for unconventional features of the PDF.

1.1. TRAVEL TIME ESTIMATION

Albeit being an extremely helpful parameter for reactive transport, travel time can't be measured directly. Traditionally, travel time is determined by tracer tests (eg. Abbott et al., 2016) or by solving the inverse problem for various environmental tracers bearing a time signal (Anderson, 2005; Cirpka et al., 2007; Gudkov et al., 2014; Opazo et al., 2016). Among the latter, isotopes are widely used for travel time estimation via the "piston flow" model (Maloszewski and Zuber, 1996). Under the assumption of purely advective flow, analytical solutions are applied for computing groundwater ages (Schlosser et al., 1988). However, as shown before (Goode, 1996; Neumann et al., 2008), the assumption of the purely advective solute transport is questionable in fractured systems, due to extensive diffusive exchange with the rock matrix which depends on porosity. In this case, direct estimation of groundwater age should involve isotope tracers as suggested by Goode (1996). That means any measurement of the solute in the fractured system represents the inverse of the convolution integral (Cirpka and

Kitanidis, 2000) between the reactive breakthrough of the tracer and the mixing function of travel time.

Travel time, as well as the shape parameter of PDF, and the transport parameters of the reactive curve, are obtained from the measurement by calibrating the measured and modelled isotope concentrations. Thus, calibration quality is limited by the parametric uncertainty of the tracer breakthrough and PDF. Full description of the isotopes commonly used in groundwater dating like $^{3}H/^{3}He$, ^{39}Ar, or ^{4}He demands four parameters: fracture aperture, porosity, mean travel time, and a shape parameter for the parametric travel time PDF (Tang et al., 1981; Trinchero et al., 2019).

Calibration of the observed concentration to a modelled one requires optimization of the abovementioned four parameters. Since every parameter is uncertain, there may be many parameter combinations leading to a good match between observed and modelled concentrations, which correspond to equifinality issue caused by parametric uncertainty. Solving this optimization provides the base for defining the age coordinates of more sophisticated transport of agriculture-related compounds.

1.2. NITRATE AND ATRAZINE

Transport of agriculturally produced solutes is one of the most acknowledged groundwater contamination problems worldwide (Chen et al., 2019; Kortunov, 2018; Nasseri et al., 2009; Puckett et al.2011; Silva et al., 2012; Sundermann et al., 2020). Extensive use of fertilizers and manure in the second half of the 20^{th} century (Puckett et al., 2011) resulted in diffuse contamination of aquifers e.g. by nitrate and atrazine.

Mechanistic models of denitrification in the fractured aquifers, including analytical solutions and mass-balance considerations (Grisak and Pickens, 1981; Neretnieks, 1980; Osenbrück et al., 2021; Tang et al., 1981), spatially explicit models (Howden et al., 2011; Refsgaard et al., 2014), and travel-time based models (Loschko et al., 2016; Kortunov, 2018), improved the understanding of the nitrogen turnover on different scales. Studies on the determination of the key mechanisms of bacterial denitrification (Jakus et al., 2021), model complexity (Störiko et al., 2021), sources of nitrate and behaviour within the unsaturated zone (Visser et al., 2021) provided helpful insights on denitrification controls.

Focusing on the reactive species in sedimentary rocks, pyrite is known as an important electron donor-providing mineral in redox processes leading to oxygen reduction and denitrification. The importance of the abiotic oxidation of iron bearing minerals for redox evolution in fractured crystalline rocks was elucidated e.g. by Sidborn (2007). Frequent iron bearing minerals comprise siderite, ankerite, or Fe^{2+}- containing saddle dolomites and thus often mixtures of Fe^{2+} - bearing minerals have to be considered. The solubility of siderite e.g., is pH-dependent and since the oxidation of pyrite (by O_2) and subsequent precipitation of ferrihydrite, as well as denitrification, lowers pH will thus enhance the release of Fe^{2+} from iron containing carbonates (saddle dolomite, siderite, etc.) in the rock matrix. By testing different scenarios of denitrification and electron donor sources, Kortunov (2018) identified the most plausible geochemical set-ups. He showed that denitrification is significant even if nitrate is depleted solely in the fracture. When nitrate is depleted also in the rock matrix, the concentration of nitrate in the fracture is decreasing dramatically within the first years of travel time.

Wide agricultural application of atrazine since the last century led to groundwater pollution exceeding threshold values in many countries worldwide. Atrazine was (and in many countries still is) used extensively as a non-selective herbicide, as a weed control component in concentrations (~1 kg ha^{-1}), and as a total herbicide in concentrations up to 9 kg ha^{-1} (Tappe et al., 2002). In Europe atrazine was used until the early 1990s when it was banned or severely restricted in most European countries due to its potentially harmful properties and widespread appearance in groundwater. In Europe, the legal threshold for all pesticides in source waters is 0.1 µg/L for single substances and 0.5 µg/L for the sum of pesticides plus metabolites (European Drinking Water Directive, 98/83/EEC). After it was banned, many studies reported ongoing atrazine contamination of groundwater (Vonberg et al., 2014; Chen et al., 2019). Controls on atrazine persistence in the soil and groundwater are still not clear (Chavez Rodriguez et al., 2021). The main challenge is the correct parameterization of the model and massive uncertainty of catchment scale parameters and data scarcity.

1.3. ADDRESSING PARAMETRIC UNCERTAINTY

Facing uncertainty is unavoidable in groundwater models. Depending on the model type and the research purpose, one may still use deterministic approaches or use a model ensemble of very limited size (for example for a computationally demanding model), or come up with a qualitative prediction. Stochastic modelling acknowledges the parametric uncertainty (Fiori et al., 2016) trying to account for parametric uncertainty.

Research in the field of uncertainty reduction by stochastic methods a gained great pace in recent years. Monte Carlo methods (Sobol, 1973) are numerical methods of solving mathematical tasks by means of random variables and statistical evaluation of their characteristics. Although the base for Monte Carlo methods was known for a long time, until 1940 the application was restricted literally by manual computations. After extensive computer development, they got more feasible and further developed. Particular interest received variance-based methods (Bianchi et al., 2015; Troldborg et al., 2012;), artificial intelligence and so-called surrogate models (Gan et al., 2018).

Surrogate models boosted within the last years as a useful tool for pre-evaluation of computationally heavy models. The term “surrogate model” includes the whole family of mechanistic model approximations (Asher et al., 2015; Lukaczyk, 2015). In this relatively short period of time, there have been remarkable breakthroughs through the understanding complex multiparametric models and response relationships to parameter change. Mono- or multiobjective, surrogate models have been serving for accessing the multidimensional parametric space with the goal of sensitivity analysis (Erdal and Cirpka, 2019; Erdal et al., 2020), stochastic model calibration (Chen *et al.*, 2013; Scheurer *et al.*, 2021), or choosing the computational techniques (Razavi et al., 2012; Scheurer et al., 2021).

1.4. SCOPE OF THE STUDY

This study aimed to address the abovementioned aspects of solute transport in fractured systems with regard to specific reactive agricultural compounds such as nitrate and atrazine, as well as groundwater age isotopes. Throughout the thesis, the idea of improvement of model predictions by using

multiple compounds was addressed in various ways. Major research questions can be summarized as follows:

- How to effectively estimate groundwater age from the isotope measurements? Does it help to use multiple tracers, and/or multiple measurements for uncertainty reduction? Which aquifer characteristics except groundwater age could be deduced from multi tracer isotope modelling? Can the Muschelkalk aquifer be described by a pair of effective fracture aperture and porosity, relevant for all locations?
- Can biotic denitrification in a fractured limestone aquifer function effectively considering limited access of microbes to small pores of the rock matrix? Which parameters are important for quantifying denitrification? Is it possible to calibrate the denitrification model using limited nitrate measurements?
- What is the analytical relationship of the transport parameters to the travel time of the maximum atrazine concentration? How to design groundwater management considering the parameter uncertainty in atrazine transport?

.

Structure of the thesis

The thesis aims to answer the abovementioned questions on the example of the Muschelkalk fractured aquifer and consists of the following sections:

In section 2, nitrate catchment-scale transport was studied by a mechanistic model (MIN3P), accounting for a complete geochemical system of reactions possible on such a scale. The changes in typical denitrification redox zones and their evolution were tested by different combinations of iron- bearing minerals. The sensitivity of parameter changes on denitrification was tested by local sensitivity analysis.

Section 3 illustrates the issue of parametric uncertainty even for a relatively low-demanding system from the reactive viewpoint. Reactive transport of groundwater age tracers $^{3}H/^{3}He$, ^{4}He, and ^{39}Ar were studied based on the travel time-based single fracture model using MIN3P and analytical solutions. With the assistance of the direct mechanistic modelling of the tracer propagation in the fracture, four parameters (fracture aperture, porosity, mean travel time, and the shape parameter of the travel time distribution) defining the model output were

identified. Partial uncertainty reduction and estimation of the groundwater ages within the catchment were done by stochastic multiobjective optimization.

In section 4 atrazine transport and related groundwater management problems were addressed by stochastic predictions under parametric uncertainty. To address the atrazine transport problem in deterministic way, an analytical approximation of the peak travel time was derived. A binary model based on sorption experiments performed on the rock samples from three different facies types and ranges of other transport parameters, was applied for deriving the probabilistic forecast and characterisation of atrazine transport in the Upper Muschelkalk aquifer.

References

Abbott, B. W., Baranov, V., Mendoza-Lera, C., Nikolakopoulou, M., Harjung, A., Kolbe, T., Balasubramanian, M. N., Vaessen, T. N., Ciocca, F., Campeau, A., Wallin, M. B., Romeijn, P., Antonelli, M., Gonçalves, J., Datry, T., Laverman, A. M., de Dreuzy, J. R., Hannah, D. M., Krause, S., Oldham, C. and Pinay, G. (2016) 'Using multi-tracer inference to move beyond single-catchment ecohydrology', Earth-Science Reviews, 160, pp. 19–42. doi: 10.1016/j.earscirev.2016.06.014.

Anderson, M. P. (2005) 'Heat as a ground water tracer', Ground Water, 43(6), pp. 951–968. doi: 10.1111/j.1745-6584.2005.00052.x.

Asher, M ., Croke, B. F. W., Jakeman, A. J. and Peeters, L. J. M. (2015) 'A review of surrogate models and their application to groundwater modeling', Water Resources Research, 51(46), pp. 5957–5973. doi: 10.1002/2015WR016967.

Berre, I., Doster, F. and Keilegavlen, E. (2019) 'Flow in fractured porous media: a review of conceptual models and discretization approaches', Transport in Porous Media, 130(1), pp. 215–236. doi: 10.1007/s11242-018-1171-6.

Bianchi, M., Kearsey, T. and Kingdon, A. (2015) 'Integrating deterministic lithostratigraphic models in stochastic realizations of subsurface heterogeneity. Impact on predictions of lithology, hydraulic heads and groundwater fluxes', Journal of Hydrology, 531, pp. 557–573. doi: 10.1016/j.jhydrol.2015.10.072.

Box, G. E. P. (1976) 'Science and Statistics', Journal ofthe American Statistical Association, 71, pp. 791–799. doi: 10.1641/B570910.

Chavez Rodriguez, L., Ingalls, B., Meierdierks, J., Kundu, K., Streck, T. and Pagel, H. (2021) 'Modeling bioavailability limitations of atrazine degradation in soils', Frontiers in Environmental Science, 9, pp. 1–13. doi: 10.3389/fenvs.2021.706457.

Chen, M., Sun, Y., Fu, P., Carrigan, C. R. and Lu, Z. (2013) 'Surrogate-based optimization of hydraulic fracturing in pre-existing fracture networks Computers & Geosciences Surrogate-based optimization of hydraulic fracturing in pre-existing fracture networks', Computers and Geosciences, 58(August), pp. 69–79. doi: 10.1016/j.cageo.2013.05.006.

Chen, N., Valdes, D., Marlin, C., Blanchoud, H., Guerin, R., Rouelle, M. and Ribstein, P. (2019) 'Water, nitrate and atrazine transfer through the unsaturated zone of the Chalk aquifer in northern France', Science of the Total Environment, 652, pp. 927–938. doi: 10.1016/j.scitotenv.2018.10.286.

Chen, Z., Auler, A. S., Bakalowicz, M., Drew, D., Griger, F., Hartmann, J., Jiang, G., Moosdorf, N., Richts, A., Stevanovic, Z., Veni, G. and Goldscheider, N. (2017) 'The World Karst Aquifer Mapping project: concept, mapping procedure and map of Europe', Hydrogeology Journal, 25(3), pp. 771–785. doi: 10.1007/s10040-016-1519-3.

Cirpka, O. A., Fienen, M. N., Hofer, M., Hoehn, E., Tessarini, A., Kipfer, R. and Kitanidis, P. K. (2007) 'Analyzing bank filtration by deconvoluting time series of electric conductivity', Ground Water, 45(3), pp. 318–328. doi: 10.1111/j.1745-6584.2006.00293.x.

Cirpka, O. A. and Kitanidis, P. K. (2000) 'An advective-dispersive stream tube approach for the transfer of conservative-tracer data to reactive

transport', Water Resources Research, 36(5), pp. 1209–1220. doi: 10.1029/1999WR900355
Cvetkovic, V. and Dagan, G. (1994) 'Transport of kinetically sorbing solute by steady random velocity in heterogeneous porous formations', J. Fluid Mech, pp. 189–215. doi: 10.1017/S0022112094000807.
D. H. Tang, Sudicky, E. a. and Frind, E. O. (1981) 'Contaminant Transport in Fractured Porous Media: Analytical Solution for a Single Fracture', Water Resources Research, 20(7), p. 1021. doi: 10.1029/WR020i007p01021.
Dagan, G. and Cvetkovic, V. (1996) 'Reactive transport and immiscible flowin geological media', Proc. R. Soc. London, pp. 285–301. doi: 10.1098/rspa.1996.0016.
Dagan, G., V. Nguyen, V. (1989) 'A comparison of travel time and concentration approaches to modeling transport by groundwater', Journal of Contaminant Hydrology, 4 (1), pp. 79-91. doi: 10.1016/0169-7722(89)90027-2.
Deng, H. and Spycher, N. (2019) 'Modeling reactive transport processes in fractures', Reviews in Mineralogy and Geochemistry, 85(1), pp. 49–74. doi: 10.2138/rmg.2019.85.3.
Erdal, D. and Cirpka, O. A. (2019) 'Global sensitivity analysis and adaptive stochastic sampling of a subsurface-flow model using active subspaces', Hydrology and Earth System Sciences, 23(9), pp. 3787–3805. doi: 10.5194/hess-23-3787-2019.
Erdal, D., Xiao, S., Nowak, W. and Cirpka, O. A. (2020) 'Sampling behavioral model parameters for ensemble-based sensitivity analysis using Gaussian process emulation and active subspaces', Stochastic Environmental Research and Risk Assessment, 34(11), pp. 1813–1830. doi: 10.1007/s00477-020-01867-0.
Finkel, M., Grathwohl, P. and Cirpka, O. A. (2016) 'A travel time-based approach to model kinetic sorption in highly heterogeneous porous media via reactive hydrofacies', Water Resources Research, 52(12), pp. 9390–9411. doi: 10.1002/2016WR019147.
Fiori, A., Cvetkovic, V., Dagan, G., Attinger, S., Bellin, A., Dietrich, P., Zech, A. and Teutsch, G. (2016) 'Debates—Stochastic subsurface hydrology from theory to practice: The relevance of stochastic subsurface hydrology to practical problems of contaminant transport and remediation. What is characterization and stochastic theory good for?', Water Resources Research, 52(12), pp. 9228–9234. doi: 10.1002/2015WR017525.
Gan, Y., Liang, X. Z., Duan, Q., Ye, A., Di, Z., Hong, Y. and Li, J. (2018) 'A systematic assessment and reduction of parametric uncertainties for a distributed hydrological model', Journal of Hydrology, 564(July), pp. 697–711. doi: 10.1016/j.jhydrol.2018.07.055.
Goode, D. J. (1996) 'Direct simulation of groundwater age', Water Resources Research, 32(2), pp. 289–296. doi: 10.1029/95WR03401.
Grisak, G. E. and Pickens, J. F. (1981) 'An analytical solution for solute transport through fractured media with matrix diffusion', Journal of Hydrology, 52(1–2), pp. 47–57. doi: 10.1016/0022-1694(81)90095-0.
Gudkov, A. V., Kamensky, I. L., Melikhova, G. S., Skiba, V. I., Tokarev, I. V. and Tolstikhin, I. N. (2014) 'The tritium-helium-3 method and its application to groundwater dating by the example of the Kirovsk mine region,

Murmansk oblast', Geochemistry International, 52(7), pp. 587–594. doi: 10.1134/S001670291405005X.
Hartmann, A., Goldscheider, N., Wagener, T., Lange, J. and Weiler, M. (2014) 'Karst water resources in a changing world: Review of hydrological modeling approaches', Reviews of Geophysics, (37), pp. 849–849. doi: 10.1002/2013RG000443.
Höge, M. (2019) 'Bayesian multi-model frameworks properly addressing conceptual uncertainty in applied modelling'. University of Tübingen, PhD Dissertation. doi: 10.15496/publikation-29155
Howden, N. J. K., Burt, T. P., Worrall, F., Mathias, S. and Whelan, M. J. (2011) 'Nitrate pollution in intensively farmed regions: What are the prospects for sustaining high-quality groundwater?', Water Resources Research, 47, p. W00L02. doi: 10.1029/2011WR010843.
Jakus, N., Mellage, A., Höschen, C., Maisch, M., Byrne, J. M., Mueller, C. W., Grathwohl, P. and Kappler, A. (2021) 'Anaerobic Neutrophilic Pyrite Oxidation by a Chemolithoautotrophic Nitrate-Reducing Iron(II)-Oxidizing Culture Enriched from a Fractured Aquifer', Environmental Science and Technology, 55(14), pp. 9876–9884. doi: 10.1021/acs.est.1c02049.
Kirchner JW, Feng X, Neal C. (2000) 'Fractal stream chemistry and its implications for contaminant transport in catchments'. Nature. 2 3;403(6769):524-7. doi: 10.1038/35000537
Kortunov E, (2018). 'Reactive transport and long-term redox evolution at the catchment scale'. PhD Thesis, Univ. Tübingen, Germany. doi: 10.15496/publikation-25162.
Leray, S., Engdahl, N. B., Massoudieh, A., Bresciani, E. and McCallum, J. (2016) 'Residence time distributions for hydrologic systems: Mechanistic foundations and steady-state analytical solutions', Journal of Hydrology, 543, pp. 67–87. doi: 10.1016/j.jhydrol.2016.01.068.
Liao, Z. and Cirpka, O. A. (2011) 'Shape-free inference of hyporheic travel time distributions from synthetic conservative and "smart" tracer tests in streams', Water Resources Research, 47(7), pp. 1–14. doi: 10.1029/2010WR009927.
Loschko, M., Wöhling, T., Rudolph, D. L. and Cirpka, O. A. (2016) 'Cumulative relative reactivity: A concept for modeling aquifer-scale reactive transport', Water Resources Research, 52(10), pp. 8117–8137. doi: 10.1002/2016WR019080.
Lukaczyk, T. W. (2015) 'Surrogate modeling and active subspaces for efficient optimization of supersonic aircraft', PhD Thesis, University of Stanford, USA, 6.
Luo, J. and Cirpka, O. A. (2008) 'Travel time-based descriptions of transport and mixing in heterogeneous domains', Water Resources Research, 44(May), pp. 1–16. doi: 10.1029/2007WR006035.
Maloszewski, P. and Zuber, A. (1996) 'Lumped parameter models for the interpretation of environmental tracer data', International Atomic Energy Agency, (Ed.), Manual on mathematical models in isotope hydrogeology, TECDOC-910: Vienna, Austria, International Atomic Energy Agency Publishing Section, pp. 9–58.
Molin, S. and Cvetkovic, V. (2010) 'Microbial risk assessment in heterogeneous aquifers: 1. Pathogen transport', Water Resources Research, 46(5), pp. 1–16. doi: 10.1029/2009wr008036.

Neretnieks, I. (1980) ‘Diffusion in the rock matrix: An important factor in radionuclide retardation?’, Journal of Geophysical Research: Solid Earth, 85(B8), pp. 4379–4397. doi: 10.1029/JB085iB08p04379.
Neumann, R. B., Labolle, E. M. and Harvey, C. F. (2008) ‘The effects of dual-domain mass transfer on the tritium-helium-3 dating method’, Environmental Science and Technology, 42(13), pp. 4837–4843. doi: 10.1021/es7025246.
Opazo, T., Aravena, R. and Parker, B. (2016) ‘Nitrate distribution and potential attenuation mechanisms of a municipal water supply bedrock aquifer’, Applied Geochemistry, 73, pp. 157–168. doi: 10.1016/j.apgeochem.2016.08.010.
Puckett, L. J., Tesoriero, A. J. and Dubrovsky, N. M. (2011) ‘Nitrogen contamination of surficial aquifers--a growing legacy’, Environmental science & technology, 45(3), pp. 839–844. doi: 10.1021/es1038358.
Razavi, S., Tolson, B. A. and Burn, D. H. (2012) ‘Review of surrogate modeling in water resources’, Water Resources Research, 48(7). doi: 10.1029/2011WR011527.
Refsgaard, J. C., Auken, E., Bamberg, C. a., Christensen, B. S. B., Clausen, T., Dalgaard, E., Effersø, F., Ernstsen, V., Gertz, F., Hansen, A. L., He, X., Jacobsen, B. H., Jensen, K. H., Jørgensen, F., Jørgensen, L. F., Koch, J., Nilsson, B., Petersen, C., De Schepper, G., Schamper, C., Sørensen, K. I., Therrien, R., Thirup, C. and Viezzoli, A. (2014) ‘Nitrate reduction in geologically heterogeneous catchments - A framework for assessing the scale of predictive capability of hydrological models’, Science of the Total Environment, 468–469, pp. 1278–1288. doi: 10.1016/j.scitotenv.2013.07.042.
Rodriguez, N. B., Benettin, P. and Klaus, J. (2020) ‘Multimodal water age distributions and the challenge of complex hydrological landscapes’, Hydrological Processes, 34(12), pp. 2707–2724. doi: 10.1002/hyp.13770.
Rubin, Y., Cushey, M. A. and Bellin, A. (1994) ‘Modeling of transport in groundwater for environmental risk assessment’, Stochastic Hydrology and Hydraulics, 8(1), pp. 57–77. doi: 10.1007/BF01581390.
Sanz-Prat, A., Lu, C., Finkel, M. and Cirpka, O. A. (2015) ‘On the validity of travel-time based nonlinear bioreactive transport models in steady-state flow’, Journal of Contaminant Hydrology, 175–176, pp. 26–43. doi: 10.1016/j.jconhyd.2015.02.003.
Sanz-Prat, A., Lu, C., Finkel, M. and Cirpka, O. A. (2016) ‘Using travel times to simulate multi-dimensional bioreactive transport in time-periodic flows’, Journal of Contaminant Hydrology, 187, pp. 1–17. doi: 10.1016/j.jconhyd.2016.01.005.
Scheurer, S., Schäfer Rodrigues Silva, A., Mohammadi, F., Hommel, J., Oladyshkin, S., Flemisch, B. and Nowak, W. (2021) ‘Surrogate-based Bayesian comparison of computationally expensive models: application to microbially induced calcite precipitation’, Computational Geosciences, 25(6), pp. 1899–1917. doi: 10.1007/s10596-021-10076-9.
Schlosser, P., Stute, M., Dörr, H., Sonntag, C. and Münnich, K. O. (1988) ‘Tritium/3He dating of shallow groundwater’, Earth and Planetary Science Letters, 89(3–4), pp. 353–362. doi: 10.1016/0012-821X(88)90122-7.
Seeboonruang, U. and Ginn, T. R. (2006) ‘Upscaling heterogeneity in aquifer reactivity via exposure-time concept: Forward model’, Journal of

Contaminant Hydrology, 84(3–4), pp. 127–154. doi: 10.1016/j.jconhyd.2005.12.011.
Sidborn, M. (2007) 'Modelling long-term redox processes and oxygen scavenging in fractured crystalline rocks' PhD Thesis, KTH, Sweden.
Sidborn, M. and Neretnieks, I. (2007) 'Long term redox evolution in granitic rocks: Modelling the redox front propagation in the rock matrix', Applied Geochemistry, 22(11), pp. 2381–2396. doi: 10.1016/j.apgeochem.2007.05.007.
Sobol, I. M. (1973) Numerical Monte Carlo Methods. Moscow: Nauka.
Störiko, A., Pagel, H., Mellage, A. and Cirpka, O. A. (2021) 'Does it pay off to explicitly link functional gene expression to denitrification rates in reaction models?', Frontiers in Microbiology, 12(6), pp. 1–13. doi: 10.3389/fmicb.2021.684146.
Sundermann, G., Wägner, N., Cullmann, A. and von Hirschhausen, Christian R.; Kemfert, C. (2020) 'Nitrate pollution of groundwater long exceeding trigger value: Fertilization practices require more transparency and oversight', DIW Weekly Report, ISSN 2568-7697, Deutsches Institut für Wirtschaftsforschung (DIW), Vol. 10(8/9), pp. 61–72. doi: 10.18723/diw_dwr:2020-8-1.
Tang, D. H., Frind, E. O. and Sudicky, E. A. (1981) 'Contaminant transport in fractured porous media: Analytical solution for a single fracture', Water Resources Research, 17(3), pp. 555–564. doi: 10.1029/WR017i003p00555.
Tappe, W., Groeneweg, J. and Jantsch, B. (2002) 'Diffuse atrazine pollution in German aquifers', Biodegradation, 13(1), pp. 3–10. doi: 10.1023/A:1016325527709.
Trinchero, P., Sidborn, M., Puigdomenech, I., Iraola, A., Bosbach, D. and Deissmann, G. (2019) 'Groundwater age dating in fractured rock using 4He data', Journal of Hydrology X, 4, p. 100036. doi: 10.1016/j.hydroa.2019.100036.
Troldborg, M., Nowak, W., Lange, I. V., Santos, M. C., Binning, P. J. and Bjerg, P. L. (2012) 'Application of Bayesian geostatistics for evaluation of mass discharge uncertainty at contaminated sites', Water Resources Research, 48(9), pp. 1–19. doi: 10.1029/2011WR011785.
Visser, A. N., Lehmann, M. F., Rügner, H., D'Affonseca, F. M., Grathwohl, P., Blackwell, N., Kappler, A. and Osenbrück, K. (2021) 'Fate of nitrate during groundwater recharge in a fractured karst aquifer in Southwest Germany', Hydrogeology Journal, 29(3), pp. 1153–1171. doi: 10.1007/s10040-021-02314-2.
Vonberg, D., Vanderborght, J., Cremer, N., Pütz, T., Herbst, M. and Vereecken, H. (2014) '20 years of long-term atrazine monitoring in a shallow aquifer in western Germany', Water Research, 50. doi: 10.1016/j.watres.2013.10.032.

2. TRAVEL TIME-BASED MODELLING OF NITRATE REDUCTION IN A FRACTURED LIMESTONE AQUIFER BY PYRITE AND IRON CARBONATES UNDER PORE SIZE LIMITATION*

Abstract. We investigate denitrification in a ferric iron-containing fractured micritic limestone aquifer (Triassic Upper Muschelkalk) in south-west Germany by numerical simulations. Low porosity values (average value of 1%), partly small pore sizes of the rock matrix (~ 0.1 µm), and thus potential absence of microbial activity in the rock matrix suggest that denitrification is taking place solely in the fracture. A key question is whether the nitrate reduction derived from groundwater observations in the study area at 25 locations can be explained by a model that restricts microbial denitrification to the fractures. A travel time-based reactive transport model is developed to efficiently simulate long-term nitrate reduction on the catchment scale. The model employs a 2-D numerical reaction model describing the fracture-rock matrix system and parametric travel time distributions. The role of (i) biotic and abiotic iron oxidation, (ii) the type and amount of iron bearing minerals, and (iii) mass transfer between matrix and fracture are investigated. The simulations show that pyrite and siderite (used as surrogate for iron carbonates) together as a source of electron donors provide enough reduction potential to decrease the nitrate concentrations as observed in the field. This confirms the hypothesis that diffusion-controlled mass transfer of electron donors from the matrix to the fracture is sufficient to establish considerable denitrification in the fracture. Uncertainty in modelled concentrations is demonstrated as a result of both the geochemical aquifer properties and the unknown shape of travel time distributions.

* Reproduced from: Petrova, E., Kortunov, E., Mayer, K. U., Grathwohl, P. and Finkel, M. (2022) Travel time-based modelling of nitrate reduction in a fractured limestone aquifer by pyrite and iron carbonates under pore size limitation, *Journal of Contaminant Hydrology*, 248. doi: 10.1016/j.jconhyd.2022.103983.

2.1. INTRODUCTION

About 25% of the global population depends on groundwater supply from fractured carbonate aquifers. In some countries such aquifers provide 50% of the drinking water (Chen et al., 2017). Carbonate rocks occupy about 12% of the surface worldwide and 35% in Europe (Bakalowicz, 2005; Vías et al., 2006). The substantial increase of fertilizer use and manure produced in agriculture, which started about 100 years ago (Puckett et al., 2011; Strebel et al., 1989), has led to vast and diffuse inputs of nitrate into fractured aquifers worldwide – with significant impact on groundwater quality (e.g., Hernández-del Amo et al., 2018; Howden et al., 2011; Opazo et al., 2016; Paradis, et al., 2018; Pauwels et al., 2010; Refsgaard et al., 2014).

Several studies investigated the factors controlling the fate of nitrate using field data and numerical simulations in fractured systems (e.g., Howden et al., 2011; Refsgaard et al., 2014). Nitrate reduction includes redox reactions and is strongly affected by fracture-matrix interactions (Rivett et al., 2008). Nitrate and other solutes diffuse from the fractures into the rock matrix and vice versa (e.g., Neretnieks, 1980; Neuman, 2005). If the size of the pores in the rock matrix does not permit microbial growth, as suggested for some Jurassic and Carboniferous Limestones and Cretaceous Chalk deposits (Johnson et al., 1998; Whitelaw and Edwards, 1980), redox reactions are limited to the rock surface of the fractures. In this case, nitrate reduction is controlled by diffusive flux of the electron donor towards the fracture. Pyrite and other Fe (II) bearing minerals are known to be important electron-donors in redox processes leading to oxygen reduction and denitrification. The importance of the abiotic oxidation of iron bearing minerals for redox evolution in fractured crystalline rocks was elucidated by Sidborn and Neretnieks (2007). However, abiotic oxidation of such minerals by NO_3^- alone is considered insufficient (Appelo and Postma, 2005). Other iron bearing minerals can also act as an electron donor source such as siderite, ankerite or Fe^{2+} containing saddle dolomites and thus often mixtures of Fe^{2+} bearing minerals must be considered.

Reactive transport of pollutants through the fractured media has been studied by help of models since the 1980s when analytical solutions were developed to

quantify the effect of the matrix diffusion during advective transport of radionuclides in single fractures for potential nuclear waste repositories (Grisak and Pickens, 1981; Neretnieks, 1980; Tang et al., 1981). Later such solutions were expanded to include systems of fractures and first-order decay (Sudicky and Frind, 1982, 1984). Sidborn and Neretnieks (2004, 2007, 2008) simulated oxygen transport and redox evolution in granites using various numerical models and developed simplified analytical solutions. A variety of further analytical and semi-analytical models were developed that focus on different specific features: stagnant flow zones and layered systems (Mahmoudzadeh et al., 2013), multiple radioactive decay products (Mahmoudzadeh et al., 2016; Shahkarami et al., 2015) and chemical reactions (Andersen and Evje, 2016) including different reaction rates in fractures and in the matrix (Zhu et al., 2016), source decay and sorption (West et al., 2004). A series of semi-analytical solutions for transport in fractured shales was derived by Huang and Goltz (2015).

Numerical models allow to account for complex multi-component reaction systems, spatial or temporal changes in parameters and boundary conditions, and multiple reactions pathways taking place instantaneously. Three major concepts have been developed for the description of fractured systems in numerical models (Deng and Spycher, 2019): single or multiple continuum porous medium models, discrete fracture network models, and travel time-based models.

Equivalent single continuum models replace the fractured system with a porous one which has properties corrected for the effect of fractures (Berkowitz et al., 1988; Liu et al., 2016). Dual continuum models (Warren and Root; 1963; Lichtner, 2000) differentiate between fractures and matrix that are coupled to allow interaction. Various concepts of the fracture-matrix interactions and interconnection have been proposed (Lichtner, 2000; Tecklenburg et al., 2016). Triple and multiple continuum approaches (e.g., Wu et al., 2004) were considered to account for different scales of fracture density.

Discrete fracture networks were successfully applied for transport simulations in crystalline (Abdelghani et al., 2015) and sedimentary rocks (Molson et al., 2012). Trinchero et al. (2017, 2019) used a deterministic 3-D discrete fracture network

model based on extensive field and laboratory studies. Discrete fracture network models may also account for fracture properties (Frampton et al., 2019), fracture-matrix mass transfer and heterogeneity of hydraulic properties (Cvetkovic et al., 2016). Different algorithms were applied (e.g., Lavoine et al., 2020) in order to overcome the uncertainty in topology, connectivity and other statistical parameters of fractures. A review on the discrete fracture networks was presented in Lei et al. (2017).

Multi-dimensional spatially distributed models, though offering intuitively an explicit idea of the modelled area, face several limitations, which are mainly caused by tremendous computational cost and difficulties in parameter identification, in particular at larger scales, which often prevent a reliable description of spatial heterogeneity of aquifer properties due to the lack of available data. There are only a few studies in which such models are used to predict the water quality in a fractured aquifer at catchment scale (Blessent et al., 2011; Orban et al., 2010; Refsgaard et al., 2014). Blessent et al. (2011) pointed out the uncertainty associated to the fracture network connectivity and geometry. Stochastic modelling may consider this uncertainty but requires very long computing time (days if not weeks) on multiple processors (Refsgaard, Auken, C. A. Bamberg, et al., 2014).

Travel time-based models were proposed to overcome these limitations. In these models, in contrast to the spatially explicit Eulerian models, the travel time replaces spatial coordinates as independent variables. Conceptually, this leads to quasi one-dimensional solute transport under the assumption that reaction fronts coincide with groundwater isochrones (i.e., lines of equal travel time). Reactive transport is solved as a function of travel time, which is defined as the time that a water particle resides in the domain of interest, from the entry point at the domain inlet to the point of observation. The effect of geochemical reactions on the solutes of interest is quantified in the travel-time domain using an appropriate analytical or numerical model to provide a reaction function. This is done apart from the modelling of the hydraulic system, which is represented by the distribution of travel time in the model domain. This distribution is interpreted as the result of many non-interacting stream tubes being mixed upon the observation rather than within the domain. Reactive-species concentrations in

groundwater are then quantified through convolution of reaction function and travel time distribution. Travel time-based solute transport models reduce the required computational effort dramatically and have been frequently applied in the past (e.g. Assteerawatt, 2008; Bellin et al., 1993; Cirpka and Kitanidis, 2000; Cvetkovic and Frampton, 2010; Cvetkovic and Dagan, 1994; Dagan and Nguyen, 1989; Dagan and Cvetkovic, 1996; Finkel et al. 2016; Loschko et al., 2016; Luo et al., 2008a and 2008b; Maher, 2010; Malmström et al., 2008; Molin and Cvetkovic, 2010; Robinson and Chu, 2013; Seeboonruang and Ginn, 2006; Vu et al., 2019; Zhao et al., 2011). Owing to the efficiency of the travel time approach, investigating alternative reaction models and the sensitivity of the model parameters in a stochastic manner are possible (Malmström et al., 2008; Sanz-Prat et al., 2015 and 2016).

In this study, we develop a travel time-based transport to simulate nitrate transport in fractured aquifers. Relevant geochemical reactions both within fracture and rock matrix as well as mass-transfer processes are described by means of a 2-D numerical model. The geochemical modelling results are used to provide the reaction function that quantifies the change in nitrate concentration within the fracture as a function of travel time. By convolution with parametric probability density functions of groundwater travel time, nitrate concentrations in groundwater are calculated. The travel time-based model is applied to quantify denitrification in a carbonate aquifer (Upper Muschelkalk) in the catchment of the river Ammer close to the city of Tübingen, Germany (Grathwohl et al., 2013). Thanks to the intense use of the aquifer for water supply, the monitoring of quarrying activities, and intense research activities, a comprehensive field data set is available for the catchment. The data shows considerable nitrate reduction in groundwater by means of an inverse correlation between measured nitrate concentration and derived groundwater age for a variety of measurement locations in the catchment. A key question is whether these observations can be explained by microbial denitrification being restricted to the fractures. Given the low porosity and small pore sizes of the Upper Muschelkalk rock matrix, it can be expected that a relevant microbial population may not develop in the matrix pore space, and microbial activity is restricted to the fracture. In this case, nitrate reduction is controlled by the diffusive transfer of electron donors, which are

released within the rock matrix due to pyrite oxidation and siderite dissolution, to the fracture. Although the available field data and knowledge from previous work may be rated as exceptional, and some idea of the carbonate aquifer's geometry, structure and heterogeneity could be developed, the aquifer properties can be determined only approximately. We first consider a reference scenario that reflects the current knowledge of the conditions in the case study area by a set of best-guess effective values for the input parameters of the geochemical model. The model simulation includes a preconditioning phase to take into account the redox evolution during about 10000 years of oxic recharge since the end of glaciation followed by a 100-years period of nitrate input. The role of individual parameters is studied in a sensitivity analysis. Parameter uncertainty is also taken into account in the comparison of modelled and measured nitrate concentrations versus travel time. Finally, the model is applied to predict the further propagation of the nitrate front in the long-term.

2.2. CASE STUDY AREA

The study area is located in the catchment of the Ammer river close to the city of Tübingen, Germany (Fig. 3.1). We consider the Upper Muschelkalk aquifer, which has a total thickness of up to 80 m (see D'Affonseca et al. (2020) for a 3-D high-resolution geological model of the study area). The Upper Muschelkalk consists of numerous meter-scale cyclic limestone layers (Aigner and Bachmann,1992; Koehrer et al., 2010; Warnecke and Aigner, 2019). Cycles consist of alternating limestone and thin clay-marlstone horizons (Koehrer et al., 2010). The main fracture network is connected to the bedding planes between limestones and clay layers. In this study we focus on the micritic limestone facies, which covers up to 90% of the thickness of Upper Muschelkalk in the Ammer catchment. Visual observations have been performed in the quarries across the catchment and in the core samples to obtain fracture characteristics in the Upper Muschelkalk. Fractures vary by origin, orientation and spacing. The typical spacing that has been detected ranges between a few decimeters to several meters.

The porosity of micritic limestone is low and varies in the range between about 0.1 and 2% (Adams and Diamond, 2017; Palermo et al., 2010), with pore sizes less than 0.1 μm (Rügner et al., 1999). The limestones are comprised of calcite,

dolomite, siderite, pyrite and some minor contents of clay minerals and other iron carbonates (saddle dolomite). Pyrite is commonly present in the rocks, its concentration is ranging between 0.5 and 2 Vol. % (Adams and Diamond, 2017; Aigner and Bachmann, 1992; Koehrer et al., 2010; Warnecke and Aigner, 2019). Scanning electron microscopy indicates the presence of siderite and saddle dolomites with contents of up to 1 Vol. % (Kortunov, 2018) comparable to the findings for limestones in other sedimentary basins (Ellwood et al., 1988). The mutual presence of siderite and pyrite has been observed previously in various limestones (Ellwood et al., 1988; Haese et al., 1997; Koehrer et al., 2010). While pyrite is formed during different stages of diagenesis, siderite tends to form during the second phase of diagenesis as a result of pyrite oxidation and re-precipitation.

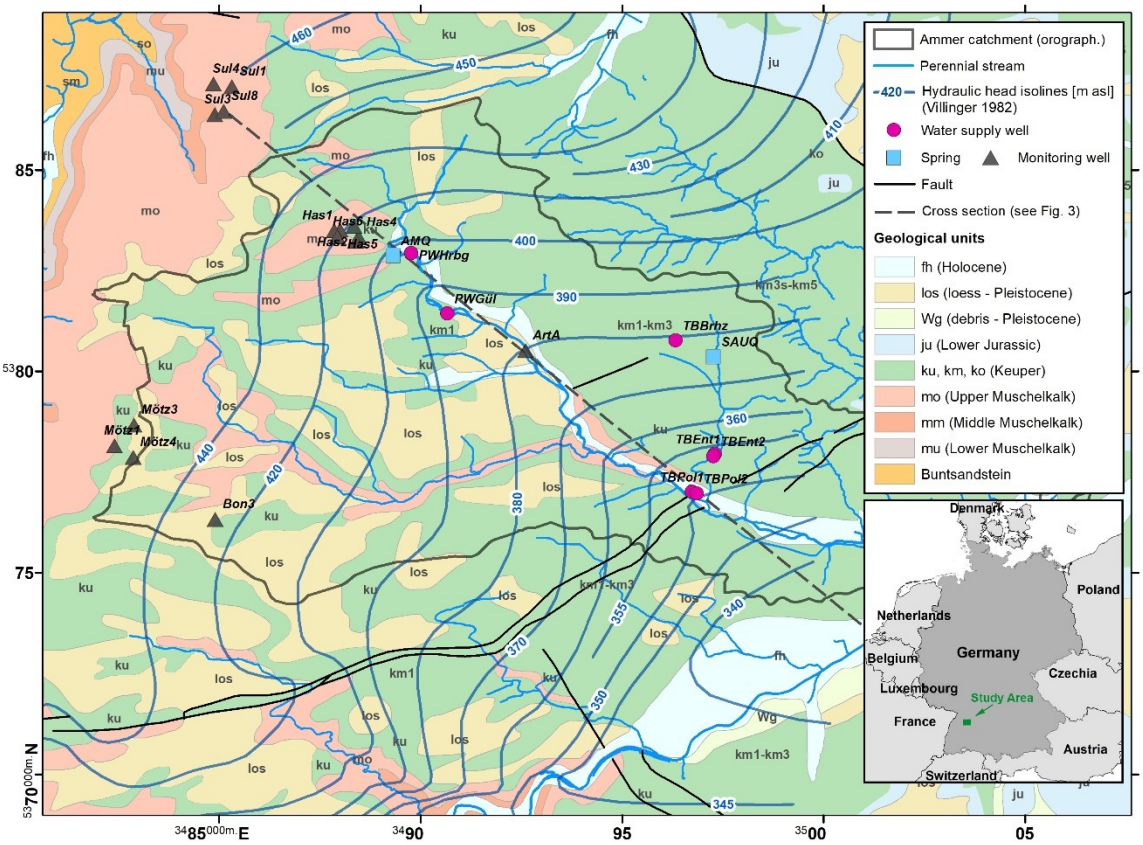

Figure 2.1. Geologic map of the Ammer catchment area with location of sampled spots (water supply wells, springs, and monitoring wells.

The typical redox sequence (Appelo and Postma, 2005) is formed both in fracture and matrix. Provided that microbial denitrification is occuring in the rock matrix,

nitrate does not migrate much further than dissolved oxygen. Relatively high NO_3^- concentrations observed in the limestone aquifer in the anoxic zone (Table 3.1) indicate that denitrification in the study area is rather slow. The source of nitrate in the study area is the fertilizer applied to the agricultural areas (Visser et al., 2021), which cover large parts of the catchment (Liu et al., 2018). By stochastic modeling of nitrate leaching through a series of soil columns representing the variety of soil forms in the study area, Weber (2020) estimated an effective average nitrate concentration in groundwater recharge of 31 mg/L (0.5 mmol/L) within the catchment of the Ammer river.

Routine sampling campaigns in the Ammer catchment conducted in 2011, 2014 and 2018 give an overview on groundwater chemistry. A detailed description of sampling strategy, measurement methodology and data analysis is given in Visser et al. (2021). The results of these campaigns include nitrate concentrations as well as estimates of the apparent groundwater age derived from tritium/helium ratios (equating the terms ‘apparent groundwater age’ and ‘apparent tracer age’, see Suckow (2014) for a detailed discussion) at 25 groundwater wells and springs in the catchment (Table 3.1 and Fig. 3.2, locations are shown in Fig. 3.1).

Measured nitrate concentrations in groundwater range from very low values below the detection limit (e.g., at the production well “TBBrhz”) to a maximum of 0.79 mmol/L (at the monitoring well “Has5”). The pattern of measured data largely depends on the type of measurement location (Fig. 3.2): While the data from monitoring wells show an irregular pattern, the data measured at springs and production wells reveal the expected trend of decreasing nitrate concentrations with increasing apparent groundwater age, which we denote below as mean travel time $\bar{\tau}$. Most likely, this is due to differences in the size of associated capture zones and the variation in relevant characteristics. Samples taken at monitoring wells have originated from small capture zones where nitrate input and subsurface properties are supposed to vary considerably from capture zone to capture zone. Samples from production wells or springs stem from rather large capture zones with – to a certain extent – averaged characteristics, which, therefore, are expected to be described much better by the model than the samples from the monitoring wells.

Table 2.1. Values of apparent groundwater age and nitrate concentrations measured at wells and springs in the study area and characteristical information.

Location	Apparent GW age [years]	NO3 [mmol/l]	Type[1)]	Altitude [m asl]	Depth [m asl]	Intake depth [m bgs]	Flow rate[2)] [L/s]	screen interval [m asl]	
Sul3	0.6	0.15	1	510.9	474.4	33	0.01	489.9	479.9
Mötz1	1	0.09	1	519.2	449.2	57	0.10	464.2	449.2
Sul4	1.3	0.58	1	547.1	504.6	38	0.05	515.1	505.1
Sul8	2.1	0.09	1	528.4	489.4	34	0.02	501.4	494.4
PWGül	4.1	0.55	2	386.0	359.8	ca. 20	11	386.0	386.0
AMQ	4.2	0.49	3	403.0	402.5				
Sul1	5	0.21	1	576.0	484	84	0.05	508.0	488.0
Has2	5.3	0.36	1	474.2	405.7	64	0.01	414.0	406.0
PWHrbg	5.8	0.48	2	401.0	393.3				
Has1	8.4	0.53	1	499.1	412.9	82	0.02	423.6	413.6
Has6	11.6	0.74	1	496.2	408.6	85	0.01	416.2	409.2
Has5	12.9	0.79	1	490.7	403	83	0.03	408.7	403.7
TBPol1	13.1	0.29	2	352.0	260	33	35	342.0	314.0
TBEnt1	13.4	-[3)]	2	364.2	318.6	33	50	339.2	326.2
Mötz4	13.9	0.4	1	545.7	446.7	94	0.20	463.7	446.7
SAUQ	15.2	0.46	3	390.0	389.5				
TBEnt2	15.4	0.04	2	365.0	321.7	34	35	340.0	327.0
TBPol2	16.3	0.24	2	350.0	304.4	32	50	339.4	311.4
Has4	22.3	0.41	1	469.3	389.3	72	0.10	399.3	389.3
TBAlt3	24.4	0.17	4	377.0	316.5	54	60	351.5	318.5
Mötz3	25.5	0.24	1	553.5	442.5	92	0.16	461.5	451.5
Has3a	25.9	0.36	1	447.4	389.4	53	0.10	397.4	389.4
Bon3	30.7	0.11	2	488.2	376.2	105	0.1	388.2	378.2
ArtA	31.1	0.02	5	378.5	320.7	29	1.0	359.5	320.7
TBBrhz	37.7	-[3)]	1	395.7	330.7	54	26	354.7	333.5

[1)] Sampling point types: 1 - monitoring well, 2 - production well, 3 – spring (natural outflow), 4 - former production well, 5 - exploration well

[2)] Flow rate: sampling rate with submersible pump or average well production rate

[3)] Below detection limit

Assuming a spatially rather constant nitrate input from agricultural land, measured nitrate concentration can be directly attributed to different total

denitrification stage. The degree of nitrate reduction correlates with corresponding values of mean travel time $\bar{\tau}$.

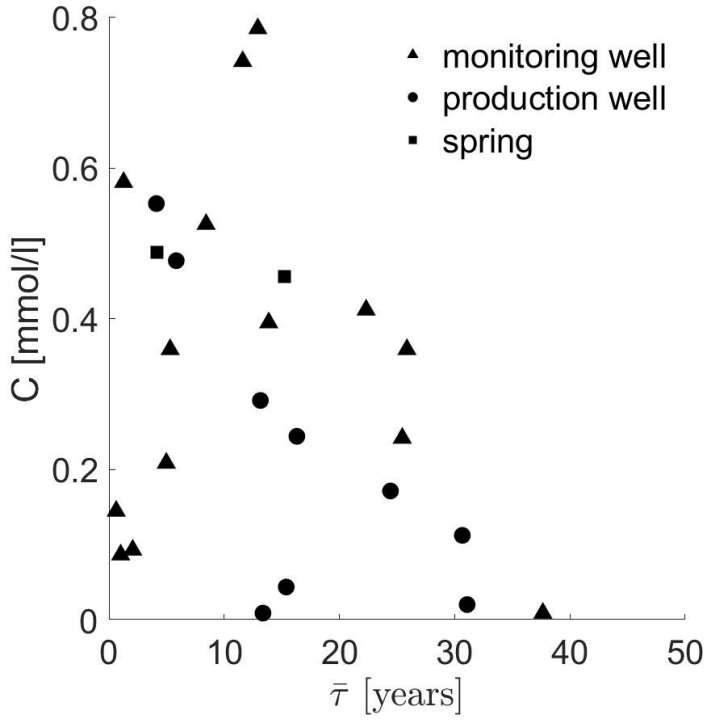

Figure 2.2. Measured nitrate concentration vs. apparent groundwater age derived from tritium/helium ratios.

2.3. MODELLING APPROACH

2.3.1. TRAVEL TIME-BASED MODEL CONCEPT

We consider the fractured aquifer to consist of two domains, fractures and rock matrix. Due to the small permeability of the micritic limestone, water flow in the matrix is assumed to be very low and is therefore neglected. The flow is assumed to pass through the connected system of fractures providing continuous exposure of water parcels to the surface of the limestone rock matrix.

The geochemical properties of both domains are assumed to be spatially constant within the model domain. Under this assumption of a geochemically homogeneous system, the travel-time based model approach consists of two tasks that can be conducted separately: the evaluation of the distribution of travel times of groundwater through the model domain towards the well or spring of

interest (in terms of a probability density function – pdf), and a single simulation of reactive transport to provide the reaction function.

The reaction model represents any of the flow paths of the water parcels through the fractured aquifer in terms of travel time. Groundwater flow is assumed to be at steady state under fully water saturated conditions. The spatial extent of the reactive transport model, the initial conditions within the model domain as well as the chemistry of the water that enters the model at the upgradient boundary are set according to the specific conditions given at the site. Mineral composition and other model parameters are considered as effective values representing the properties of the rock formation in the model domain ‘in average’. As there is no spatial differentiation with respect to geochemical properties, it is not relevant in which area of the catchment and in which particular fracture the solute propagates through the subsurface.

The groundwater captured by an individual well, spring or other measurement location is a mixture of different water fractions that travelled to the location along individual flow paths with different residence or travel time through the aquifer domain of interest (see Fig. 3.2 for an exemplary illustration). The distribution of travel time characterizes the ensemble of heterogeneous pathways in the domain. Differences in travel time result from and describe heterogeneity on all scales including density, connectivity, orientation and width of fractures, channeling within fractures (e.g., Guiheneuf et al., 2017) as well as travel distance.

Being associated with a particular sub domain, i.e. capture zone, each sampling location is characterized by its specific pdf of travel time. The shape of these travel time distributions is not known in natural aquifer systems and can be estimated only with considerable uncertainty. For the estimation, numerical multi-dimensional flow models together with particle-tracking routines may be used or parametric distributions that meet certain statistical characteristics. The validity of either form of estimation largely depends on the level of knowledge about the aquifer system. In this work we use a gamma distribution as probability distribution, which has been applied previously for fractured systems (Kirchner et al., 2000; Hrachowitz et al., 2010):

$$f_i(\tau, \alpha_i, \beta_i) = \frac{\tau^{\alpha_i - 1}}{\beta_i^{\alpha_i} \Gamma(\alpha_i)} e^{\frac{-\tau}{\beta_i}} \quad (2.1)$$

where $\Gamma(\alpha_i)$ is the gamma function

$$\Gamma(\alpha_i) = \int_0^\infty e^{-\tau} \tau^{\alpha_i - 1} d\tau. \quad (2.2)$$

The unknown shape parameter α_i and the scale parameter β_i of the gamma distribution are related to each other via the distribution's mean value $\bar{f}_i = \bar{\tau}_i = \alpha_i \beta_i$. If we assume to know the mean travel time $\bar{\tau}_i$ at the considered location, i, to be equal to the apparent groundwater age estimated using tritium/helium measurements, the scale parameter can be substituted: $\beta_i = \bar{\tau}_i / \alpha_i$. This leads to a formulation for the location-specific pdf of travel time, $f_i(\tau, \bar{\tau}_i, \alpha_i)$, having only one unknown parameter, the shape parameter α_i:

$$f_i(\tau, \bar{\tau}_i, \alpha_i) = \frac{\tau^{(\alpha_i - 1)}}{\left(\frac{\bar{\tau}_i}{\alpha_i}\right)^{\alpha_i} \Gamma(\alpha_i)} e^{\frac{-\tau \alpha_i}{\bar{\tau}_i}} \quad (2.3)$$

This shape parameter is determined by calibration – as will be explained further below. Given the results of the reactive transport simulation in terms of the nitrate concentration as a function of real time t and travel time τ, $C_r(t, \tau)$, the nitrate concentration in groundwater, $C_{GW,i}(t)$, at some sampling location i is calculated by convolution (e.g., Cirpka & Kitanidis, 2000):

$$C_{GW,i}(t) = C_{GW}(t, \bar{\tau}_i, \alpha) = \int_0^\infty C_r(t, \tau)\, f(\tau, \alpha, \bar{\tau}_i) d\tau, \quad (2.4)$$

where $f(\tau, \alpha, \bar{\tau}_i)$ is the pdf of travel time at the measurement location i, described by a gamma distribution for a given mean travel time $\bar{\tau}_i$ and shape parameter α. The model calibration consists of two steps: (i) the appropriate parameterization of the reactive model and (ii) the measurement-point-wise fitting of the gamma distribution's shape parameter (see section 2.4.3 for further details).

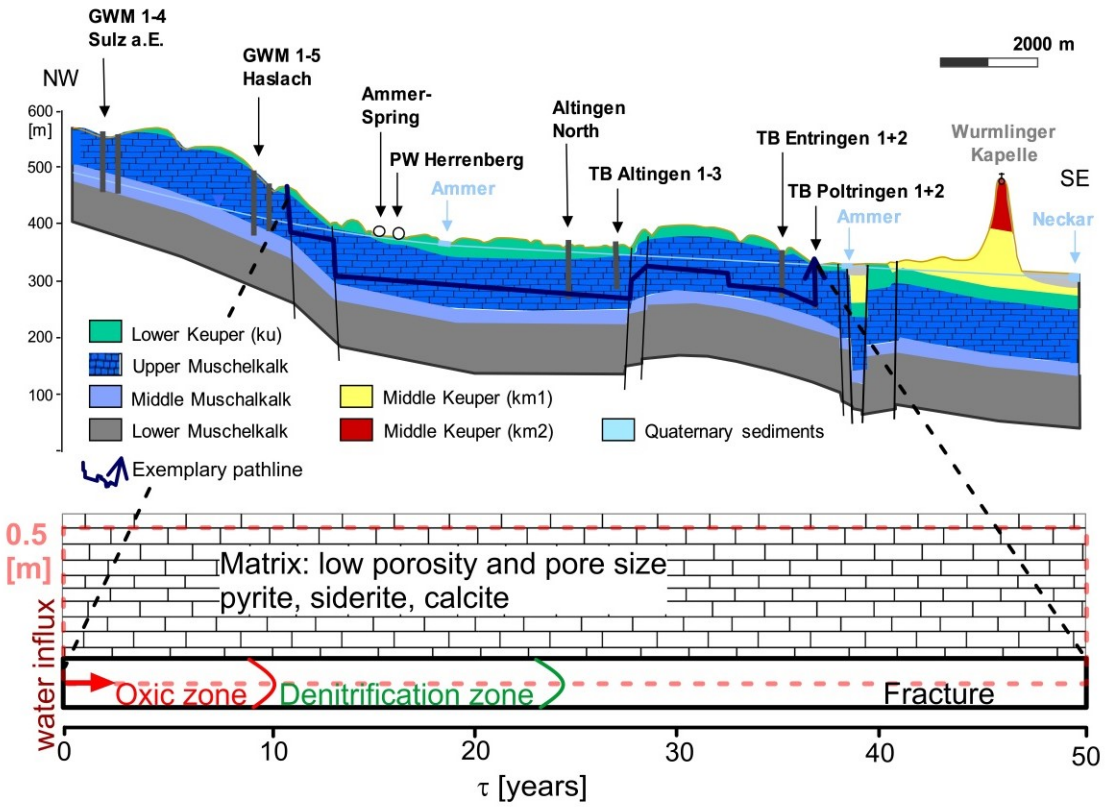

Figure 2.3. Schematic representation of a potential solute transport pathline through the Muschelkalk formation along a NW-SE cross-section adapted from Villinger (1982) (Top), and the domain of the model used for catchment scale transport simulation (travel time ≤ 50 years) with redox zonation scheme (Bottom).

2.3.2. Reaction model

The reaction model describes a single fracture and the adjacent part of the rock matrix. Transport of solutes in the fracture is convective, transport in the matrix is purely diffusive. Due to the symmetry, it is sufficient to model only one half of the fracture-matrix system (Fig. 2.4). For the simulations, we chose the multi-component reactive transport code MIN3P_THCm (Mayer et al., 2002; Su et al., 2021). In flow direction, the model is discretized into 100 columns of uniform length (Δx = 0.1 m). Following the travel time-based approach, any location x in the model is interpreted in terms of travel time τ with $\tau = x/v$ where v is the average flow velocity in the fracture (0.2 m/year). A specified flux (Neumann) boundary condition is applied to the upgradient boundary (x = 0) of the fracture

such that the length of the model in terms of travel time is 50 years, which is well above the largest value of measured apparent groundwater age (38 years, see Table 2.1). Downgradient, at the fracture outlet, ($x = L_x = 10$ m), a Dirichlet boundary is employed with a fixed hydraulic head to maintain free drainage. Perpendicular to the fracture, the matrix is discretized using a variable grid size, with Δz ranging from 0.1 mm (near the fracture) to 40 mm comprising a total number of 67 layers resulting in a total model thickness of $L_z = 0.5$ m (Fig. 2.4). The conductivity of the matrix compartment was set to a very low value (10^{-14} m/s) leading to negligible flow in the matrix. The diffusion coefficient in water, D_{aq}, is set to 1.5×10^{-9} m^2/s for all aqueous species. Initial water chemistry in the fracture and the matrix is assumed to be in equilibrium with the rock minerals. The model is preconditioned to simulate the evolution of redox conditions in the aquifer due to oxic recharge (with O_2 pressure of 0.209 atm.) since the last ice age (following Spiessl et al. (2008) for biotite oxidation in granites). Subsequently, nitrate input is considered for a period of 100 years.

Model parameter settings have been defined in relation to a reference scenario, hereafter also denoted as the base case. For this base case, nitrate input concentration is assumed to 31 mg/L (0.5 mmol/L), pyrite and siderite contents in the rock matrix are set to 0.25 Vol. % each (corresponding to 0.44 and 0.35 mass %), calcite content is 99.5 % (99.21 %), the oxidation preconditioning period is 10000 years, fracture aperture is 0.2 mm, and matrix porosity is set to 1 %.

2.3.3. GEOCHEMICAL SYSTEM

Following the assumption that the limited pore-size of the rock matrix does not allow for the development of any relevant microbial mass in the matrix pore space, microbial activity in terms of microbial denitrification in the fracture and the release of the required electron donor (Fe^{2+}) in the matrix are spatially separated in the model. Furthermore, we do not consider any filling of the fracture that may otherwise contribute in terms of a direct provision of electron donors. Therefore, diffusive mass-transfer between matrix and fracture strongly controls denitrification.

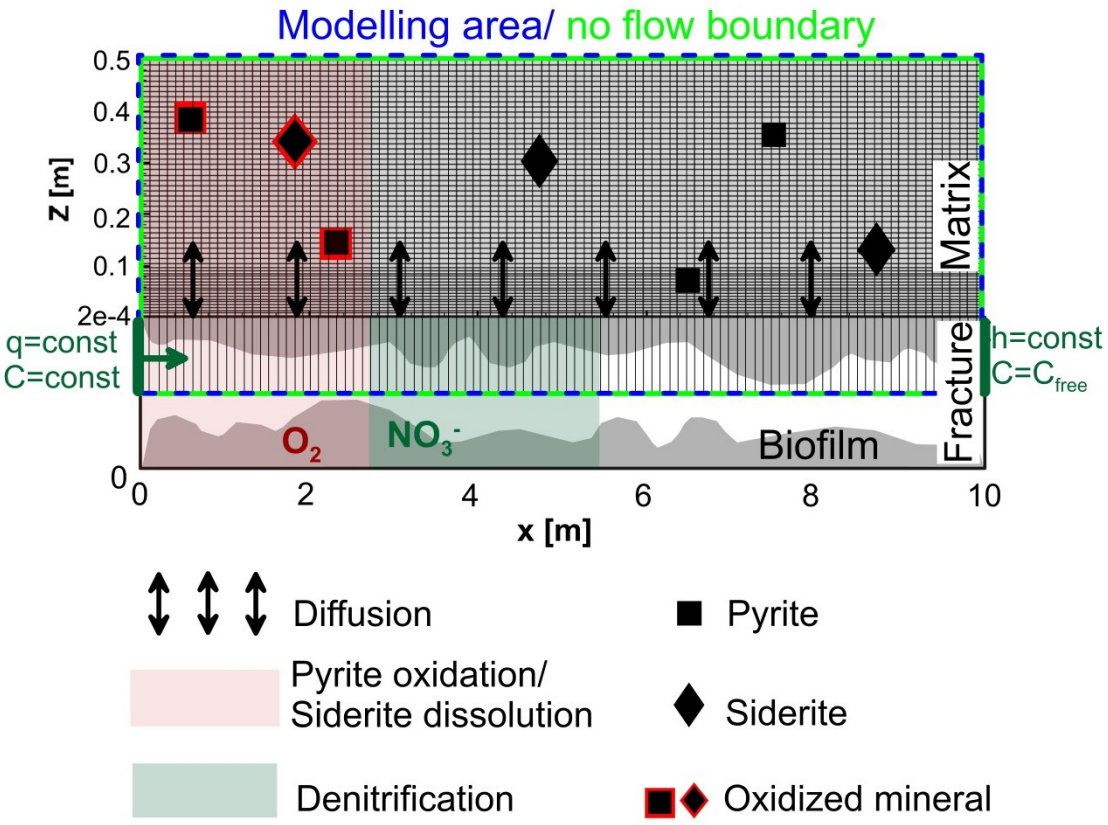

Figure 2.4. Schematic representation of the reaction model: available minerals, processes, redox zones, model domain, discretization and boundary conditions. Symbols illustrate Fe(II) bearing minerals that are initially homogeneously distributes in the rock matrix and are subject to oxidation and dissolution.

The hydrogeochemical model considers redox-sensitive species most relevant for denitrification in the aquifer, such as dissolved oxygen of atmospheric origin, agriculturally-produced nitrate (Visser et al., 2021), sulphate, and ferrous iron. Fe^{2+} is produced by siderite dissolution and pyrite oxidation. Rock matrix composition is defined by primary (carbonate/calcite) and secondary (siderite, pyrite) minerals of the sedimentary basin. The main geochemical components and reactions considered in the model are described in Table 3.2 and Appendix 2.1. Figure 2.4 shows a conceptual scheme of the redox zonation within the fracture-matrix system and considered exchange processes such as diffusion, mineral dissolution and microbial denitrification. The latter has been proofed by cultivation experiments with groundwater samples (Jakus, 2021a,b). For

dissolution/precipitation of calcite, siderite, ferrihydrite, and goethite, constant reaction rates were assumed. Equilibrium constants for these components are based on previously published values (Ball and Nordstrom, 1991). To improve convergence, Fe^{2+} oxidation to Fe^{3+} is combined with iron hydroxide precipitation and therefore Fe^{3+} is not present in aqueous phase. Ferrihydrite and goethite are produced by oxygen reduction and denitrification respectively. In order to distinguish between oxidation and nitrate biotic reduction of Fe^{2+}, these processes are implemented in the reaction model as goethite and ferrihydrite precipitation. Other sources of goethite and ferrihydrite formation are not considered. For the oxidation of pyrite the shrinking core model was used for sulphur with the same parameters as were published in previous studies (Langman et al., 2014; Bao et al., 2017), followed by iron reduction by nitrate or oxygen (Table 3.2). Denitrification takes place exclusively in anoxic conditions (Appelo and Postma, 2005), which is controlled in the model by an inhibition term. Note that pyrite is depleted only abiotically via oxygen reduction and does not directly contribute to the nitrate reduction because biotic reactions do not take place in the matrix but are limited to the fracture. As mineral forms and concentrations are not known exactly, we consider siderite as the iron carbonate phase which can dissolve and provide additional Fe^{2+} to the system. Siderite serves as representative for other minerals such as ankerite or saddle dolomites ($Ca_x(Fe,Mg,Mn)_{(1-x)}(CO_3)_2$), which might also occur as potential sources of Fe^{2+}. The reaction model also accounts for porosity changes due to precipitation of the secondary minerals and dissolution of carbonates and pyrite.

2.4.RESULTS AND DISCUSSION

2.4.1 REACTIVE TRANSPORT MODELLING – BASE CASE

The water chemistry in the fracture as modelled for the base case at the end of the simulation period is shown in Fig. 2.5. Oxygen vanishes due to pyrite oxidation within a travel time of about 2 year (after 10,000 years of preconditioning as described in section 2.2). As long as oxygen is present, nitrate does not react; the slight decrease in the concentration is caused by diffusion into the rock matrix. When the oxygen is gone, nitrate reduction starts.

Table 2.2. Main components and geochemical reactions considered, equilibrium constants, rates and parameters used in the fracture-matrix reactive transport model

Components		
O_2 (aq), $CaCO_3$, pH, Ca^{2+}, Fe^{2+}, SO_4^{2-}, NO_3^-, N_2 (aq), Cons. tracer		
Minerals: Calcite, Pyrite, Siderite, Ferrihydrite, Goethite		
Reactions	**Equilibrium constants, rates and parameters**	
	log K_{eq} [-]	k_{eff} [mol/l·bulk·s]
Carbonate species		
$H_2CO_3 \rightleftarrows H^+ + HCO_3^-$	-6.36	
$HCO_3^- \rightleftarrows H^+ + CO_3^{2-}$	-10.33	
Gases (in equilibrium with aqueous phase)		
O_2 (g) $\rightleftarrows O_2$ (aq)	-2.89	
CO_2 (g)+ $H_2O \rightleftarrows H_2CO_3$	-18.20	
N_2 (g) $\rightleftarrows N_2$ (aq)	-3.18	
Carbonate dissolution		
$CaCO_3$ (s) $\rightleftarrows Ca^{2+} + CO_3^{2-}$	-8.48	1×10^{-6}
$FeCO_3$ (s) $\rightleftarrows Fe^{2+} + CO_3^{2-}$	-10.45	1×10^{-9}
Oxygen reduction by Fe^{2+} - ferrihydrite precipitation		
$4Fe^{2+} + O_2$ (aq)+ $10H_2O \rightleftarrows 4Fe(OH)_3$ (s) + $8H^+$	-15.90	
Nitrate biotic reduction by Fe^{2+} – goethite precipitation*		
$10Fe^{2+} + 2NO_3^-$+ $14H_2O \rightleftarrows 10FeOOH$ (s) + N_2 (aq) + $18H^+$	-70.30	1×10^{-6}
Oxygen reduction by pyrite	**Shrinking core parameters**	
FeS_2 (s) + 3.5O_2 (aq)+ $H_2O \rightleftarrows Fe^{2+}$+ $2SO_4^{2-}$ + $2H^+$	$S_{py} = 1\times10^{-6}$ mol l^{-1} s^{-1} $r_{py}^p = 50\mu m$, $r_{py}^r = 49\ \mu m$ $D_{py,O2} = 2.41\times10^{-9}$ m^2 s^{-1}	

* Inhibited in the presence of oxygen (Appelo and Postma, 2005), in the model for concentrations of O_2 (aq) > 10^{-10} mol/l.

At this stage, Fe^{2+} is present in the fracture and nitrate decreases rapidly. Denitrification is followed by goethite and ferrihydrite precipitation; this and pyrite oxidation produces H^+ in the fracture (Tab. 3.1), which lowers pH from 9.1 in

equilibrium with carbonate rocks to 6.9-7.1 (neutral values). As the pH decreases, more siderite dissolves and more Fe^{2+} is released (Fig. 2.5). Downstream of the nitrate reduction front in the fracture, the pH is slightly increasing again. Concentrations of goethite in the fracture are comparable to ferrihydrite. Goethite as a product of denitrification precipitates conjointly with the nitrate decrease.

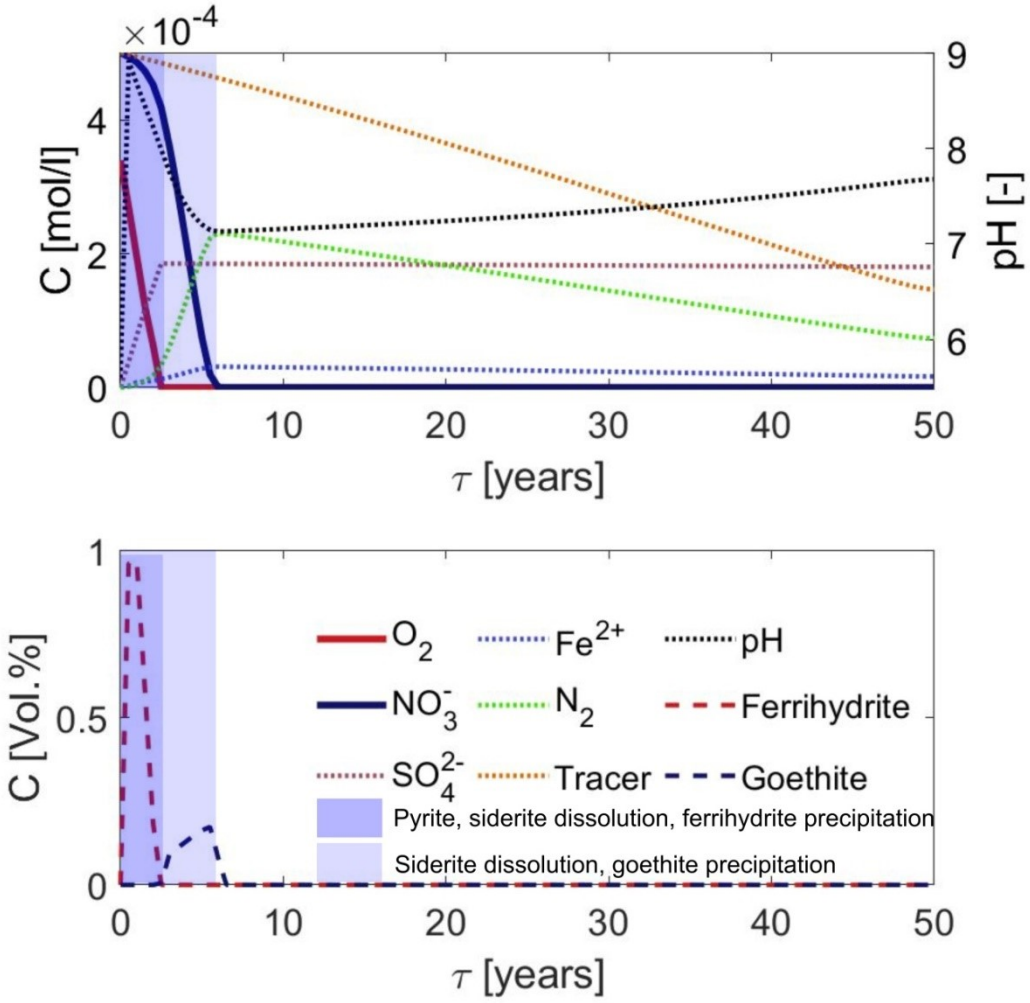

Figure 2.5. Modelled concentration profiles of the main species in the fracture water at the end of the simulation period (t = 10100 years; 10000 years O_2 + 100 years NO_3^-) for the reference scenario (pyrite and siderite content = 0.25 Vol. % each, porosity of rock matrix ε = 1.0 %, D_{aq} = 1.5×10^{-9} m^2/s). The low pH value at the fracture inlet refers to the injected water.

After a travel time of about another 4.5 years in the anoxic zone the groundwater is free of nitrate. An increasing amount of N_2 appears in the fracture as a product

of denitrification. Further downstream of the reaction front of nitrate, N_2 behaves as a conservative tracer diffusing into the rock matrix. Sulphate concentration in the fracture equilibrated with the matrix during the 10000 years long preconditioning period and is not significantly affected during anthropogenic nitrate input within the last 100 years. Correspondingly, the concentration of SO_4^{2-} stays almost at a constant level downstream of the oxygen front.

Figure 2.6 shows the distribution of the main reaction species in the rock matrix. Pyrite oxidation takes place in the closest vicinity to the fracture inlet and limits the diffusive propagation of oxygen further into the rock matrix. The concentration profile of nitrate equals the profile of the tracer close to the fracture inlet and starts to deviate from it as soon as the oxygen in the fracture is vanished. The end of denitrification correlates with the residual Fe^{2+}.

During the first 10000 years oxygen is spreading in the first 2 mm of the rock matrix dissolving 0.54 mol of pyrite. The subsequent 100 years of nitrate input result in consumption of additional 0.19 mol of siderite (Fig. 2.6). Secondary siderite precipitates in the rock matrix as a result of diffusive redistribution of Fe^{2+} (see SM 1). Fe^{2+} oxidation leads to ferrihydrite and goethite precipitation in amounts of 0.45 and 0.21 mol accordingly, which means that 32% of produced Fe^{2+} is consumed in denitrification.

2.4.2. SENSITIVITY ANALYSIS

To understand the model behaviour in relation and response to parameter changes, a series of model simulations with different parameter settings were performed. These settings were generated by a systematic variation of individual parameters (one-at-a-time method) of the base case model. We considered a number of fractured aquifer properties, namely fracture aperture, rock matrix porosity, and total mineral concentration, which all are expected to vary across the catchment. Further, we investigate the role of nitrate input concentration and the relevance of the duration of the preconditioning period.

The parameter ranges were set in accordance to the field observations and the literature research about Muschelkalk properties.

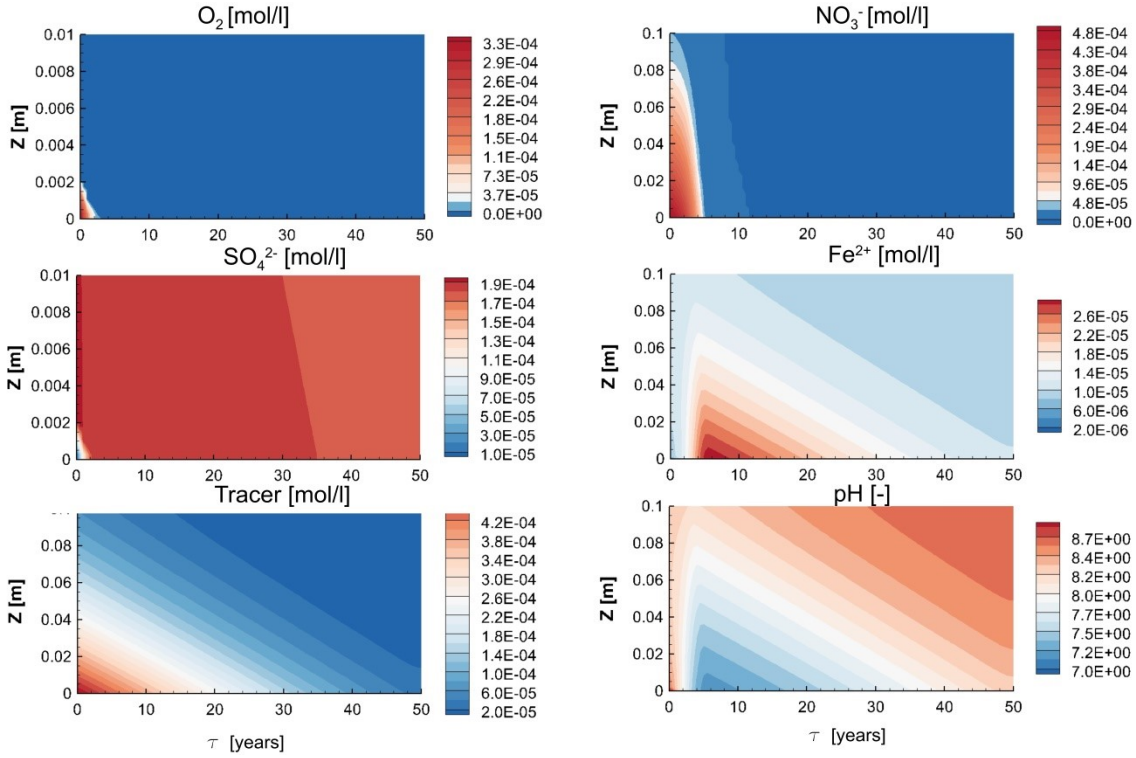

Figure 2.6. Water chemistry simulated for the rock matrix after 10 000 years of oxic recharge followed by 100 years of nitrate input (t = 10100 years) in the model domain close to the fracture (0 < z < 0.1 m).

Minimum and maximum values of the parameters considered in this sensitivity analysis are summed up in Table 3.3 in comparison to the base case settings. Relative parameter change is defined as $\Delta p = P_i/P_0$, where P_0 and P_i denote the reference (base case) value of the parameter and its variation, respectively. Model sensitivity in response to individual parameter changes is evaluated by means of the difference in travel time required to reduce the nitrate input concentration that enters the fracture across the upgradient model boundary by 60 %, which is hereafter denoted as $\tau_{60\%}$. The results of this sensitivity analysis are compiled in Fig. 2.7. Note that nitrate degradation in the fracture starts only after oxygen is completely depleted. Thus, the location of the oxygen front (in terms of travel time) represents a lower limit for $\tau_{60\%}$. For the base case, the oxygen-free zone in the fracture starts at approx. $\tau = 2$ years. Nitrate reduction by 60% is achieved within approx. 4.5 years, and complete denitrification within 5.5 years (see Fig.2.5).

Table 2.3. Parameter ranges and reference values used in the sensitivity analysis.

Parameter	Unit	Base case	Minimum value	Maximum value
Fracture aperture	[mm]	0.2	0.02	1.0
Input nitrate concentration	[mmol/l]	0.5	0.05	5
Matrix porosity	[-]	0.01	0.002	0.08
Total content of Fe(II) bearing minerals (with 1:1 ratio of pyrite and siderite)	[Vol. %]	0.5	0.05	5
Duration of oxygen input	[years]	10000	3000	30000

Changes of the oxygen input duration cause only a slight variation of $\tau_{60\%}$ values. Obviously, the preconditioning of the redox system in the model domain is nearly completed after 3000 years such that any longer oxygen input does not remarkably change the initial conditions relevant for the nitrate transport through the system. The decrease of the nitrate input load, either due to a lower input concentration or a lower fracture aperture, obviously, leads to a faster nitrate reduction (Fig. 2.7). Vice versa, $\tau_{60\%}$ increases with nitrate input concentration and fracture aperture. Decrease of the fracture aperture is raising the surface area to volume ratio of the fracture-matrix system prompting quasi-parabolic dependency similar to existing analytical solutions for the fractured systems (e.g., Rahman, et al. 2004; Sidborn and Neretnieks, 2007).

A change in mineral content has only a minor effect on the value of $\tau_{60\%}$ as long as there is a sufficient amount of minerals available (approx. 30% of the base case content, i.e. 0.15 Vol. %) As soon as the mineral concentration is decreasing, it follows the same degree of dependency as the fracture aperture increase (Rahman, et al. 2004; Sidborn, and Neretnieks, 2007). Matrix porosity controls the diffusive mass transfer between matrix and fracture. With larger porosity, values of $\tau_{60\%}$ are reduced considerably. This is due to a faster reduction of both oxygen and nitrate. Please note that, in all modelled scenarios,

porosity changes due to precipitation and diagenesis of the rock matrix are insignificant.

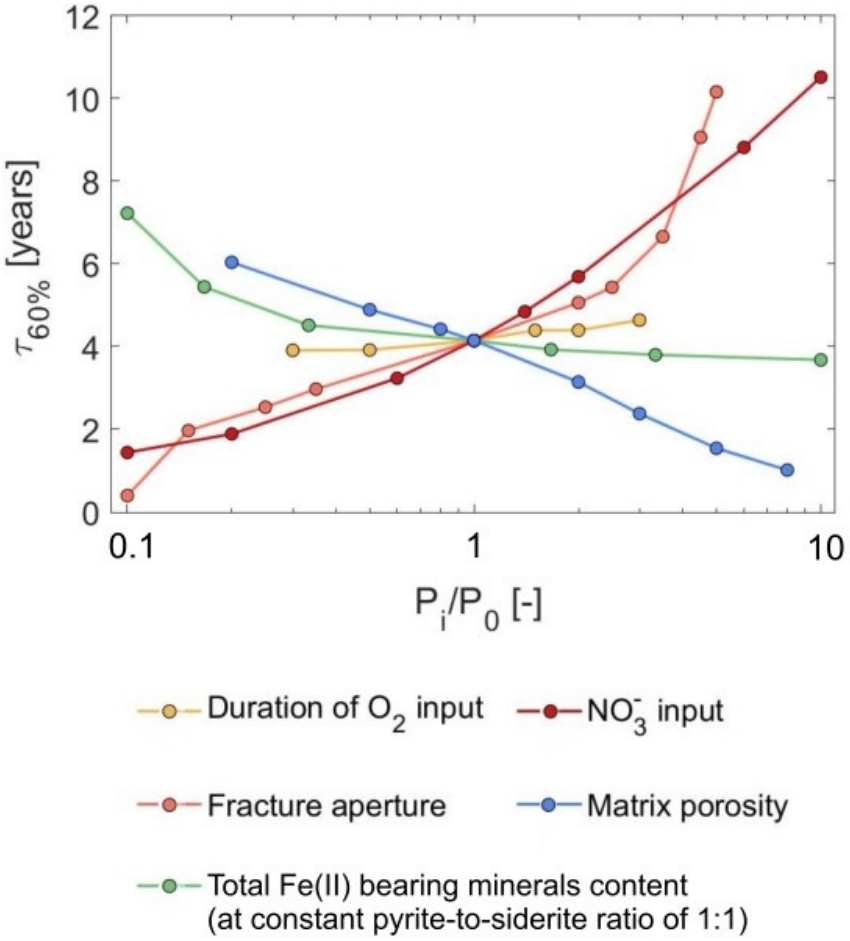

Figure 2.7. Model sensitivity in terms of the travel time $\tau_{60\%}$ required for a 60 % reduction of NO_3^- to changes in model input parameter.

The denitrification potential has been found to be at maximum if pyrite and an iron carbonate (here: siderite) are present in the rock matrix in comparable concentrations (reference scenario). The dominance of one mineral fraction leads to significantly lower denitrification (please see SM 2 for the scenario where only pyrite is present, and SM 3 where only siderite is present).

2.4.3. CALIBRATION OF TRAVEL TIME DISTRIBUTION'S SHAPE TO CALCULATE NITRATE CONCENTRATION IN GROUNDWATER

The modelled nitrate concentration in groundwater, $C_{GW,i}(t^*)$, at some particular location i for a given time t^* depends on the outcome of the reactive transport

simulation (reaction function) and on the specific pdf of travel time (see Eqns. (3.1-4)) at the considered location. With this approach, the modelled concentration of nitrate in groundwater depends on the parameter setting of the geochemical model and the shape parameter α_i in $f_i(\tau, \bar{\tau}_i, \alpha_i)$. For a given reaction curve, representing the result of the geochemical model (with a particular parameter setting) for the time of interest (here: t^* = 100 a), the concentration value $C_{GW,i}(t^*, \bar{\tau}_i, \alpha_i)$ is a function of the shape parameter α_i of the pdf of travel time. By comparison with the measured concentration, the 'optimal' α_i value providing the best model fit can be determined. However, uncertainty in geochemical model parameters leads to a non-uniqueness of the model calibration. Consequently, any pair of measured values of nitrate concentration in groundwater and mean travel time may be explained through the model by different parameter combinations. This is illustrated for the example of a single concentration measurement at location 'TBBrhz' ($C_{GW,TBBrhz}$ = 9.68 10^{-3} mmol/l, $\bar{\tau}_{Sul1}$ = 37.7 years), against which the model (namely the travel time distribution's shape parameter α_{BBrhz}) has been fitted (Fig. 2.8). For clarification, the fitting is shown for two different parameter settings of the geochemical model (here: different total mineral concentration, 0.05 Vol. % and 0.5 Vol. %, respectively).

2.4.2. COMPARISON WITH FIELD DATA

In order to prove the feasibility of the model approach, we compare modelled nitrate concentration with the data $(\bar{\tau}, C_{GW})_i$ measured in monitoring and production wells as well as springs (Table 3.1). In order to reflect in an exemplary way the uncertainty demonstrated in the sensitivity analysis, two different parameter settings are considered here: (i) the reference scenario (base case) as has been discussed above, and (ii) a scenario with limited availability of minerals (total mineral content MC = 0.05 Vol. %).

Modelling with these two settings provide the reaction curves that correspond to the bounds of this parameter range (recall that model results are insensitive to an increase in mineral content compared to the base case, as depicted in Fig. 2.7). In the context of this exemplary analysis, we may claim: these two reaction

curves are forming the envelope of plausible reactive model results (see Fig. 2.8a and purple shaded areas in right column of Fig. 2.9).

By convolution with the pdf of travel time $f(\tau, \bar{\tau}, \alpha)$, we obtain a 'plausibility area' in which the model can explain the measured data pairs $(\bar{\tau}, C/C_0)_i$. The shape of this area varies with the shape parameter α (see blue shaded areas in right column of Fig. 2.9).

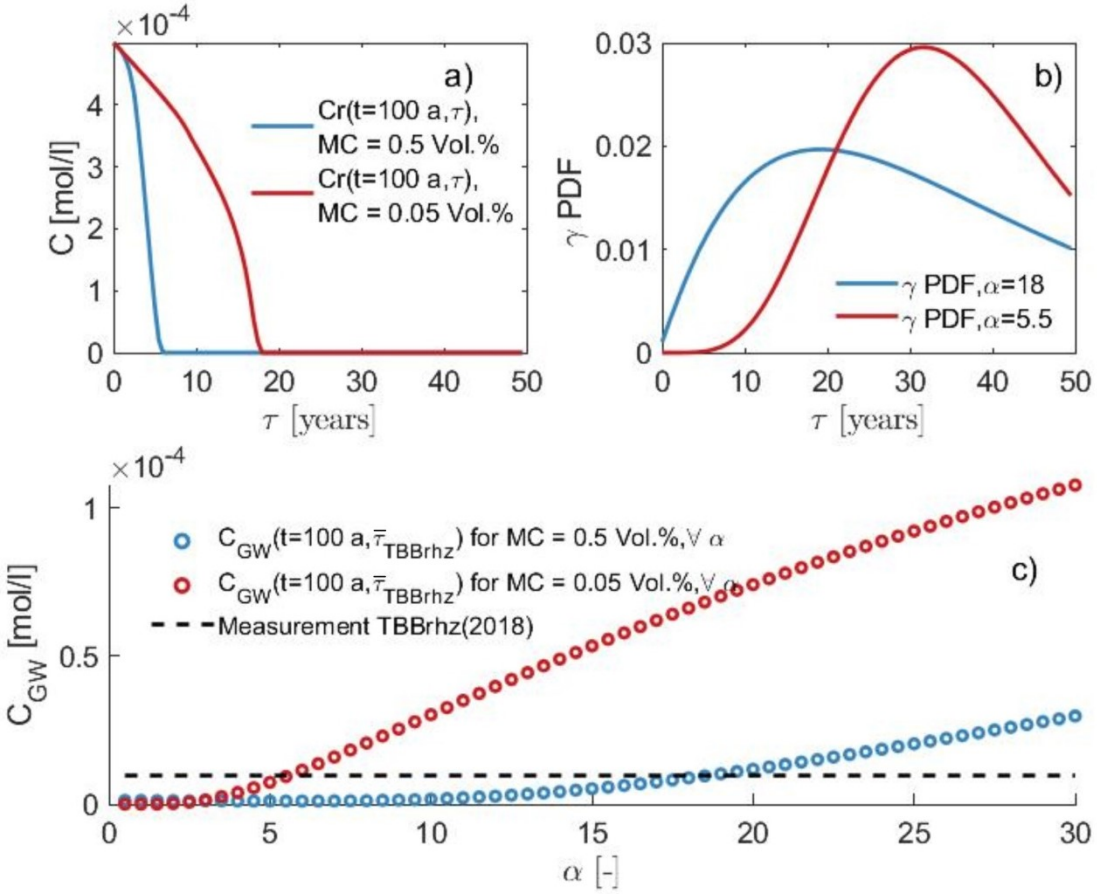

Figure 2.8. Illustration of the calculation of nitrate concentrations in groundwater combining geochemical model results with specific travel time distributions. (a) reaction curves $C_r(t = 100\ a, \bar{\tau}_{TBBrhz} = 37.7\ a)$ for two different model settings with respect to total mineral content (MC); (b) pdf of travel time for given $\bar{\tau}_{TBBrhz} = 37.7\ a$ and calibrated shape parameters (values of α_{TBBrhz} for which the model reproduces the measured value as depicted in part (c)); (c) modelled $C_{GW,TBBrhz}(t^*, \bar{\tau}_{TBBrhz}, \alpha_{TBBrhz})$ values for given reaction curves (see part (a)) as a function of shape parameter α_{TBBrhz} of the pdf of travel time.

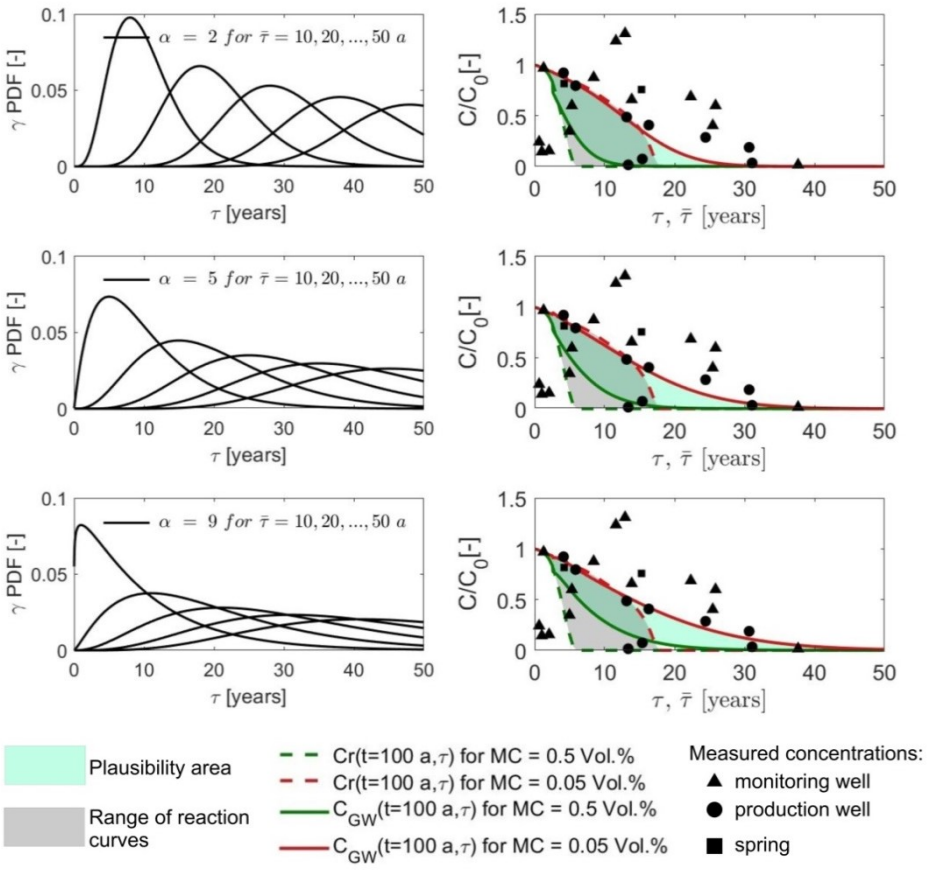

Figure 2.9. Comparison of model results with nitrate concentrations measured in groundwater (plotted as relative values C/C_0 with C_0 = 31 mg/L = 0.5 mmol/L). Left: pdf of travel time for three selected shape parameter values α (2, 5, and 10) and mean travel time values $\bar{\tau}$ from 10 to 50 years. Right: reaction curves, C_r, for the reference as well as a limited-mineral-availability scenario, and corresponding modelled groundwater concentrations, C_{GW}, for a travel time distribution with a shape as illustrated in the left column; blue area marks concentrations which may be calibrated with reasonable values of α.

For all data pairs located within this plausibility area, it is possible to exactly fit the model by different model parameter settings. Model fits can be achieved for all production wells and springs and most of the monitoring wells. All data points above the plausibility area indicate either a mismatch with the assumed initial nitrate concentration (this is obviously the case where measured nitrate concentration is above the average concentration used as model input concentration) or less favourable conditions for denitrification (as could be

represented in the model deviating other parameters' values from the base case setting). Except for a few monitoring wells where rather low nitrate concentrations have been measured at very young apparent groundwater age (see Table 2.1 and Fig. 2.2), the model sufficiently explains the field observations. The simulations indicate that observed nitrate concentrations can be explained by microbial denitrification in the fracture alone.

2.4.3. LONG-TERM PREDICTION OF NITRATE FRONT PROPAGATION

Due to ongoing agricultural practices in the study area, we expect a continuous input of nitrate also in the future. Consequently, the nitrate reduction front will propagate further downgradient. Figure 2.10 shows how the reaction curve for denitrification will develop during the next centuries according to the reference scenario model (Fig.2.10 - left). The nitrate reduction front is retarded but does not move linear with time. This is in accordance with analytical solutions for specific (simplified) cases describing a similar setting, which show that the retardation factor increases with the square root of time. A current reduction of fertilization would considerably slow down the front propagation (see Fig. 2.10 - right for the example of a 50% reduction).

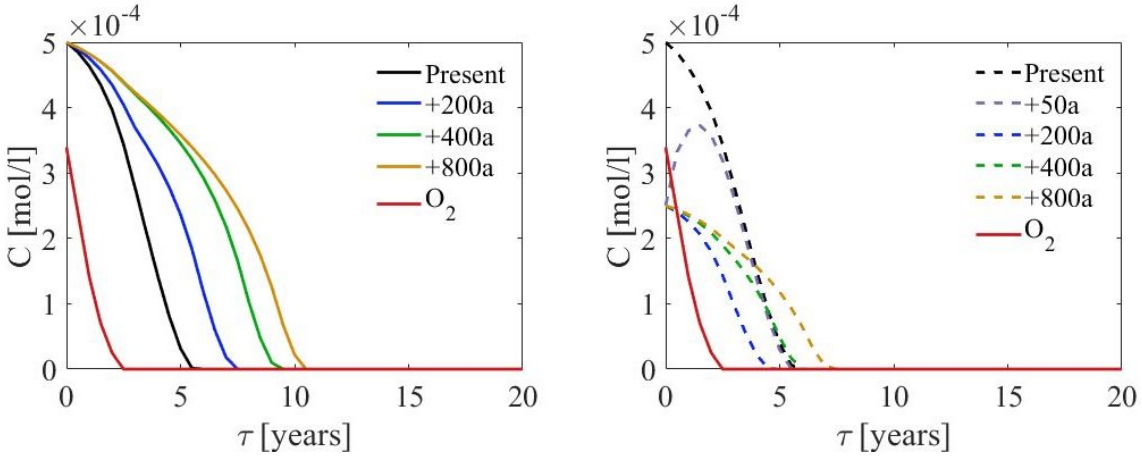

Figure 2.10. Prediction of the nitrate front propagation in the next 800 years from today. Left: development of the reaction curve in the fracture assuming the concentration of NO_3^- application will not change. Right: development of the reaction curve in the fracture for a 50% reduction of nitrate input from today onwards.

2.5. CONCLUSION AND OUTLOOK

The travel time-based hydrogeochemical model developed in the study is a comparably simple but computationally efficient tool to simulate solute transport in a fractured aquifer on the catchment scale. Simulation results for the Muschelkalk aquifer in the catchment of the river Ammer show that the model is able to realistically describe measured nitrate concentrations in groundwater for the special properties of the aquifer considered in this work, namely for low porosity and small size of the pores of the rock matrix, which restricts bacterial activity to the fracture. Though being diffusion-limited, mass transfer of electron donors from the matrix to the fracture obviously is sufficient to establish nitrate reduction in the fracture large enough to achieve the nitrate decrease over the travel time observed in the catchment. Denitrification is driven by redox reactions involving pyrite and iron carbonate together, and causes a decrease in pH which further enhances release of Fe^{2+} from siderite dissolving in the rock matrix which may be considered as a self-enhancing process. If pyrite and siderite are present simultaneously, then an optimum in NO_3^- degradation is observed. Diffusive flux of the electron donor from the rock matrix to the fracture and the location of the oxygen front are the major factors controlling the nitrate reduction. The model response on parameter variations has shown that fracture aperture, input concentration and porosity are of a high importance for the location and propagation of the nitrate reduction front, whereas the duration of system preconditioning (assumed time since the last glaciation) is of minor importance. All physical and geochemical parameters required to describe nitrate transport in fractured aquifers vary in space and can be evaluated in nature only with considerable uncertainty. The unknown shape of the location-specific travel time distributions adds even more uncertainty. With the simplified model approach proposed in this work, this uncertainty can be addressed by stochastic simulations. These will extend the findings on the role of individual geochemical parameters presented herein. Further work will include also the additional consideration of solutes that are subject to other processes, such as sorption and radioactive decay.

Acknowledgements

Financial support for this research was provided by the DFG (German Research Foundation) through the Research Training Group ‘Integrated Hydrosystem Modelling’ (GRK 1829/1) and through the Collaborative Research Center CAMPOS (SFB 1253) under the grant 281741268. The authors would like to thank Dr. Chuanche Lu and Prof. Dr. Richard Amos for helpful discussions.

References

Abdelghani, F.B., Aubertin, M., Simon, R., Therrien, R., 2015. Numerical simulations of water flow and contaminants transport near mining wastes disposed in a fractured rock mass. International Journal of Mining Science and Technology 25(1), 37–45. doi: 10.1016/J.IJMST.2014.11.003

Adams, A., Diamond, L.W., 2017. Early diagenesis driven by widespread meteoric infiltration of a Central European carbonate ramp: A reinterpretation of the Upper Muschelkalk. Sedimentary Geology 362, 37–52. doi: 10.1016/j.sedgeo.2017.10.002

Aigner, T., Bachmann, G.H., 1992. Sequence-stratigraphic framework of the German Triassic. Sedimentary Geology 80(1–2), 115–135. doi: 10.1016/0037-0738(92)90035-P

Andersen, P.Ø., Evje, S., 2016. A model for reactive flow in fractured porous media. Chemical Engineering Science 145, 196–213. doi: 10.1016/j.ces.2016.02.008

Appelo, C.A.J., Postma, D., 2005. Geochemistry, Groundwater and Pollution, Second Edition. A. A. Balkema Publishers, Leiden, The Netherlands. 649 pages

Assteerawatt, A., 2008. Flow and Transport Modelling of Fractured Aquifers based on a Geostatistical Approach. PhD Thesis, Univ. Stuttgart, Germany. http://dx.doi.org/10.18419/opus-289

Bakalowicz, M., 2005. Karst groundwater: a challenge for new resources. Hydrogeology Journal, 13(1), 148–160. doi: 10.1007/s10040-004-0402-9

Ball, J.W., Nordstrom, D.K., 1991. User's Manual for WATEQ4F, with Revised Thermodynamic Data Base and Test Cases for Calculating Speciation of Major, Trace, and Redox Elements in Natural Waters. U.S. Geological Survey, Open-File Report 91-183, Washington DC, 189 p.

Bao, Z., Haberer, C. M., Maier, U., Amos, R. T., Blowes, D. W. Grathwohl, P., 2017. Modeling controls on the chemical weathering of marine mudrocks from the Middle Jurassic in Southern Germany. Chemical Geology, 459, 1–12. doi: 10.1016/J.CHEMGEO.2017.03.021

Bellin, A., Rinaldo, A., Bosma, W. J. P., van der Zee, S. E. A. T. M., Rubin, Y., 1993. Linear equilibrium adsorbing solute transport in physically and chemically heterogeneous porous formations: 1. Analytical solutions, Water Resour. Res., 29(12), 4019– 4030, doi: 10.1029/93WR02303.

Berkowitz, B., Bear, J., Braester, C., 1988. Continuum models for contaminant transport in fractured porous formations, Water Resources Research, 24(8), 1225 – 1236, doi: 10.1029/WR024i008p01225.

Blessent, D., Therrien, R., Gable, C.W., 2011. Large-scale numerical simulation of groundwater flow and solute transport in discretely-fractured crystalline bedrock. Adv. Water Resour. 34, 1539–1552. doi: 10.1016/j.advwatres.2011.09.008

Chen, Z., Auler, A. S., Bakalowicz, M., Drew, D., Griger, F., Hartmann, J., Jiang, G., Moosdorf, N., Richts, A., Stevanovic, Z., Veni, G., Goldscheider, N., 2017.

The World Karst Aquifer Mapping project: concept, mapping procedure and map of Europe. Hydrogeology Journal, 25 (3), 771–785. doi: 10.1007/s10040-016-1519-3

Cirpka, O. A., Kitanidis, P. K., 2000. An advective-dispersive stream tube approach for the transfer of conservative-tracer data to reactive transport. 36(5), Water Resources Research, 1209–1220. doi: 10.1029/1999WR900355

Cvetkovic, V., Dagan, G., 1994. Transport of kinetically sorbing solute by steady random velocity in heterogeneous porous formations. J. Fluid Mech, 189–215. doi: 10.1017/S0022112094000807

Cvetkovic, V., Fiori, A., Dagan, G. , 2016. Tracer travel and residence time distributions in highly heterogeneous aquifers: Coupled effect of flow variability and mass transfer. Journal of Hydrology, 543, 101–108. doi: 10.1016/j.jhydrol.2016.04.072

Cvetkovic, V., Frampton, A., 2010. Transport and retention from single to multiple fractures in crystalline rock at Äspö (Sweden): 2. Fracture network simulations and generic retention model. Water Resources Research, 46(5), 1–17. doi: 10.1029/2009WR008030

D'Affonseca, F. M., Finkel, M., Cirpka, O. A., 2020. Combining implicit geological modeling, field surveys, and hydrogeological modeling to describe groundwater flow in a karst aquifer. Hydrogeology Journal. doi: 10.1007/s10040-020-02220-z

Dagan, G., Cvetkovic, V., 1996. Reactive transport and immiscible flow in geological media. I. General Theory. Proc.R.Soc.Lond. A. 452:285-301. doi: 10.1098/rspa.1996.0016

Dagan, G., Nguyen, V., 1989. A comparison of travel time and concentration approaches to modeling transport by groundwater. Journal of Contaminant Hydrology, 4(1), 79-91. doi: 10.1016/0169-7722(89)90027-2.

Deng, H., Spycher, N., 2019. Modeling reactive transport processes in fractures. Rev. Mineral. Geochemistry 85, 49–74. doi: 10.2138/rmg.2019.85.3

Ellwood, B. B., Chrzanowski, T. H., Hrouda, F., Long, G. J., Buhl, M. L., 1988. Siderite formation in anoxic deep-sea sediments: A synergetic bacteria controlled process with improtant implications in paleomagnetism.Geology, 16(11), 980. doi: 10.1130/00917613(1988)016<0980:SFIADS>2.3.CO;2

Finkel, M., Grathwohl, P., Cirpka, O.A., 2016. A travel time-based approach to model kinetic sorption in highly heterogeneous porous media via reactive hydrofacies. Water Resour. Res. 52, 9390–9411. doi: 10.1002/2016WR019147

Frampton, A., Hyman, J. D., Zou, L., 2019. Advective Transport in Discrete Fracture Networks With Connected and Disconnected Textures Representing Internal Aperture Variability. Water Resources Research, 55(7), 5487–5501. doi: 10.1029/2018WR024322

Grathwohl, P., 1998. Diffusion in natural porous media: contaminant transport, sorption/desorption and dissolution kinetics (Vol. 1). Springer US. doi: 10.1007/978-1-4615-5683-1

Grathwohl P., Rügner H., Wöhling T., Osenbrück K., Schwientek M., Gayler S., Wollschläger U., Selle B., Pause M., Delfs J.-O., Grzeschik M., Weller U., Ivanov M., Cirpka O. A., Maier U., Kuch B., Nowak W., Wulfmeyer V., Warrach-Sagi K., Streck T., Attinger S., Bilke L., Dietrich P., Fleckenstein J.H., Kalbacher T., Kolditz O., Rink K., Samaniego L., Vogel H.-J., Werban U., Teutsch G., 2013. Catchments as reactors: a comprehensive approach for water fluxes and solute turnover. Environ Earth Sci 69, 317–333. doi: 10.1007/s12665-013-

Grisak, G. E., and Pickens, J. F., 1981. An analytical solution for solute transport through fractured media with matrix diffusion. Journal of Hydrology, 52(1–2), 47–57. doi: 10.1016/0022-1694(81)90095-0

Guiheneuf, N., et al., 2017. Insights about transport mechanisms and fracture flow channeling from multi-scale observations of tracer dispersion in shallow fractured crystalline rock. Journal of Contaminant Hydrology, 206, 18-33. doi: 10.1016/j.jconhyd.2017.09.003

Haese, R.R., Wallmann, K., Dahmke, A., Kretzmann, U., Müller, P.J., Schulz, H.D., 1997. Iron species determination to investigate early diagenetic reactivity in marine sediments. Geochim. Cosmochim. Acta 61, 63–72. doi: 10.1016/S0016-7037(96)00312-2

Hernández-del Amo, E., Menció A., Gich F., Mas-Pla J., Bañeras L., 2018. Isotope and microbiome data provide complementary information to identify natural nitrate attenuation processes in groundwater. Science of The Total Environment, (613–614). doi: 10.1016/j.scitotenv.2017.09.018.

Howden, N. J. K., Burt, T. P., Worrall, F., Mathias, S., and Whelan, M. J. , 2011. Nitrate pollution in intensively farmed regions: What are the prospects for sustaining high-quality groundwater? Water Resources Research, 47, W00L02. doi: 10.1029/2011WR010843

Hrachowitz, M., Soulsby, C., Tetzlaff, D., Malcolm, I. A., Schoups, G., 2010. Gamma distribution models for transit time estimation in catchments: Physical interpretation of parameters and implications for time-variant transit time assessment, Water Resour. Res., 46, W10536. doi: 10.1029/2010WR009148

Huang, J., and Goltz, M. N., 2015. Semianalytical solutions for transport in aquifer and fractured clay matrix system. Water Resources Research, 51(9), 7218–7237. doi: 10.1002/2014WR016073

Jakus, N., Blackwell, N., Osenbrück, K., Straub, D., Byrne James, M., Wang, Z., Glöckler, D., Elsner, M., Lueders, T., Grathwohl, P., Kleindienst, S., Kappler, A. and Stams Alfons J, M. (2021) ‘Nitrate removal by a novel lithoautotrophic nitrate-reducing, iron(II)-oxidizing culture enriched from a pyrite-rich

limestone aquifer', Applied and Environmental Microbiology, 87(16), pp. e00460-21. doi: 10.1128/AEM.00460-21.

Jakus, N., Mellage, A., Höschen, C., Maisch, M., Byrne, J. M., Mueller, C. W., Grathwohl, P. and Kappler, A. (2021) 'Anaerobic neutrophilic pyrite oxidation by a chemolithoautotrophic nitrate-reducing iron(II)-oxidizing culture enriched from a fractured aquifer', Environmental Science and Technology, 55(14), pp. 9876–9884. doi: 10.1021/acs.est.1c02049.

Johnson, A. C., Hughes, C. D., Williams, R. J., Chilton, P. J. (1998). Potential for aerobic isoproturon biodegradation and sorption in the unsaturated and saturated zones of a chalk aquifer. Journal of Contaminant Hydrology, 30(3–4), 281–297. doi: 10.1016/S0169-7722(9700048-X

Kirchner JW, Feng X, Neal C., 2000. Fractal stream chemistry and its implications for contaminant transport in catchments. Nature. Feb 3;403(6769):524-7. doi: 10.1038/35000537

Koehrer, B. S., Heymann, C., Prousa, F., Aigner, T., 2010. Multiple-scale facies and reservoir quality variations within a dolomite body - Outcrop analog study from the Middle Triassic, SW German Basin. Marine and Petroleum Geology, 27, 2, 386–411. doi: 10.1016/j.marpetgeo.2009.09.009

Kortunov E, 2018. Reactive transport and long-term redox evolution at the catchment scale. PhD Thesis, Univ. Tübingen, Germany. doi: 10.15496/publikation-25162.

Langman, J., Moore, M., Ptacek, C., Smith, L., Sego, D., Blowes, D., 2014. Diavik Waste Rock Project: evolution of mineral weathering, element release, and acid generation and neutralization during a five-year humidity cell experiment. Minerals, 4, 2, 257–278. doi: 10.3390/min4020257

Lavoine, E., Davy, P., Darcel, C., Munier, R., 2020. A Discrete Fracture Network model with stress-driven nucleation: impact on clustering, connectivity, and topology. Frontiers in Physics, 8(January), 1–10. doi: 10.3389/fphy.2020.00009

Lei, Q., Latham, J.-P., Tsang, C.-F., 2017. The use of discrete fracture networks for modelling coupled geomechanical and hydrological behaviour of fractured rocks. Computers and Geotechnics, 85, 151–176. doi: 10.1016/J.COMPGEO.2016.12.024

Lichtner, P. C., 2000. Critique of dual continuum formulations of multicomponent reactive transport in fractured porous media. Geophysical Monograph Series, 122, 281–298. doi: 10.1029/GM122p0281

Liu, R., Li, B., Jiang, Y., Huang, N., 2016. Review: Mathematical expressions for estimating equivalent permeability of rock fracture networks. Hydrogeology Journal, 24(7), 1623–1649. doi: 10.1007/s10040-016-1441-8

Liu, Y., Zarfl, C., Basu, N. B., Schwientek, M., Cirpka, O. A., 2018. Contributions of catchment and in-stream processes to suspended sediment transport in a dominantly groundwater-fed catchment. Hydrology and Earth System Sciences, 22(7), 3903–3921. doi: 10.5194/hess-22-3903-2018

Loschko, M., Wöhling, T., Rudolph, D.L., Cirpka, O.A., 2016. Cumulative relative reactivity: A concept for modeling aquifer-scale reactive transport. Water Resour. Res. 52, 8117–8137. doi: 10.1002/2016WR019080

Luo, J., Cirpka, O. A., Dentz, M., Carrera, J., 2008b. Temporal moments for transport with mass transfer described by an arbitrary memory function in heterogeneous media, Water Resour. Res., 44, W01502, doi: 10.1029/2007WR006262.

Luo, J., Wu, W.-M., Carley, J., Fienen, M., Cheng, H., Watson, D., Criddle, C., Jardine, P., and Kitanidis, P., 2008a. Estimating first-order reaction rate coefficient for transport with nonequilibrium linear mass transfer in heterogeneous media, J. Contam. Hydrol., 98(1–2), pp. 50–60. doi: 10.1016/j.jconhyd.2008.03.002.

Maher, K., 2010. The dependence of chemical weathering rates on fl uid residence time. Earth and Planetary Science Letters, 294(1–2), 101–110. doi: 10.1016/j.epsl.2010.03.010

Mahmoudzadeh, B., Liu, L., Moreno, L., Neretnieks, I., 2016. Solute transport through fractured rock: Radial diffusion into the rock matrix with several geological layers for an arbitrary length decay chain. J. Hydrol. 536, 133–146. doi: 10.1016/j.jhydrol.2016.02.046

Mahmoudzadeh, B., Liu, L., Moreno, L., Neretnieks, I., 2013. Solute transport in fractured rocks with stagnant water zone and rock matrix composed of different geological layers-Model development and simulations. Water Resources Research, 49(3), 1709–1727. doi: 10.1002/wrcr.20132

Malmström, M. E., Berglund, S., Jarsjö, J., 2008. Combined effects of spatially variable flow and mineralogy on the attenuation of acid mine drainage in groundwater. Applied Geochemistry, 23(6), 1419–1436. doi: 10.1016/j.apgeochem.2007.12.029

Mayer, K. U., Frind, E. O., Blowes, D. W., 2002. Multicomponent reactive transport modeling in variably saturated porous media using a generalized formulation for kinetically controlled reactions. Water Resources Research, 38(9), 13–21. doi: 10.1029/2001WR000862

Molin, S., Cvetkovic, V., 2010. Microbial risk assessment in heterogeneous aquifers: 1. Pathogen transport, Water Resour. Res., 46, W05518, doi: 10.1029/2009WR008036.

Molson, J., Aubertin, M., Bussière, B., 2012. Reactive transport modelling of acid mine drainage within discretely fractured porous media: Plume evolution from a surface source zone. Environmental Modelling and Software, 38, 259–270. doi: 10.1016/j.envsoft.2012.06.010

Neretnieks, I., 1980. Diffusion in the rock matrix: An important factor in radionuclide retardation? Journal of Geophysical Research: Solid Earth, 85(B8), 4379–4397. doi: 10.1029/JB085iB08p04379

Neuman, S. P., 2005. Trends, prospects and challenges in quantifying flow and transport through fractured rocks. Hydrogeology Journal, 13(1), 124–147. doi: 10.1007/s10040-004-0397-2

Opazo, T., Aravena, R., Parker, B., 2016. Nitrate distribution and potential attenuation mechanisms of a municipal water supply bedrock aquifer. Applied Geochemistry, 73, 157–168. doi: 10.1016/j.apgeochem.2016.08.010

Orban, P., Brouyère, S., Batlle-Aguilar, J., Couturier, J., Goderniaux, P., Leroy, M., Maloszewski, P., Dassargues, A., 2010. Regional transport modelling for nitrate trend assessment and forecasting in a chalk aquifer. J. Contam. Hydrol. 118, 79–93. doi: 10.1016/j.jconhyd.2010.08.008

Osenbrück, K., Blendinger, E., Leven, C., Rügner, H., Finkel, M., Jakus, N., Schulz, H. and Grathwohl, P. (2021a) 'Nitrate reduction potential of a fractured Middle Triassic carbonate 1 aquifer in southwest Germany', Hydrogeol J 30, 163–180 (2022). doi:10.1007/s10040-021-02418-9

Palermo, D., Aigner, T., Nardon, S., Blendinger, W., 2010. Three-dimensional facies modeling of carbonate sand bodies: Outcrop analog study in an epicontinental basin (Triassic, southwest Germany). AAPG Bulletin, 94(4), 475–512. doi: 10.1306/08180908168

Paradis, D., Ballard, J.-M., Lefebvre, R., Savard, M.M., 2018. Multi-scale nitrate transport in a sandstone aquifer system under intensive agriculture. Hydrogeol. J. 26, 511–531. doi: 10.1007/s10040-017-1668-z

Pauwels, H., Ayraud-Vergnaud, V., Aquilina, L., Molénat, J. , 2010. The fate of nitrogen and sulfur in hard-rock aquifers as shown by sulfate-isotope tracing. Applied Geochemistry, 25(1), 105–115. doi: 10.1016/J.APGEOCHEM.2009.11.001

Puckett, L. J., Tesoriero, A. J., Dubrovsky, N. M., 2011. Nitrogen contamination of surficial aquifers--a growing legacy. Environmental Science and Technology, 45(3), 839–844. doi: 10.1021/es1038358

Rahman, M.M., Liedl, R., Grathwohl, P., 2004. Sorption kinetics during macropore transport of organic contaminants in soils: Laboratory experiments and analytical modeling. Water Resour. Res. 40. doi: 10.1029/2002WR001946

Refsgaard, J. C., Auken, E., Bamberg, C. A., Christensen, B. S. B., Clausen, T., Dalgaard, E., Effersø, F., Ernstsen, V., Gertz, F., Hansen, A. L., He, X., Jacobsen, B. H., Jensen, K. H., Jørgensen, F., Jørgensen, L. F., Koch, J., Nilsson, B., Petersen, C., De Schepper, G., Schamper, C., Sørensen, K. I., Therrien, R., Thirup, C., Viezzoli, A. , 2014. Nitrate reduction in geologically heterogeneous catchments - A framework for assessing the scale of predictive capability of hydrological models. Science of the Total Environment, 468–469, 1278–1288. doi: 10.1016/j.scitotenv.2013.07.042

Rivett, M. O., Buss, S. R., Morgan, P., Smith, J. W. N., Bemment, C. D., 2008. Nitrate attenuation in groundwater: A review of biogeochemical controlling processes. doi: 10.1016/j.watres.2008.07.020

Robinson, B. A., Chu, S., 2013. A residence-time-based transport approach for the groundwater pathway in performance assessment models. Computers and Geosciences, 52, 155–163. doi: 10.1016/j.cageo.2012.09.001

Rügner, H., Kleineidam, S., Grathwohl, P., 1999. Long term sorption kinetics of phenanthrene in aquifer materials. Environ. Sci. Technol. 33, 1645–1651. doi: 10.1021/es980664x

Sanz-Prat, A., Lu, C., Finkel, M., Cirpka, O. A., 2015. On the validity of travel-time based nonlinear bioreactive transport models in steady-state flow, J. Contam. Hydrol., 175–176, pp. 26–43. doi:10.1016/j.jconhyd.2015.02.003.

Sanz-Prat, A., Lu,C., Finkel, M., Cirpka, O. A., 2016. Using travel times to simulate multi-dimensional bioreactive transport in timeperiodic flows, J. Contam. Hydrol., 187, pp. 1–17. doi:10.1016/j.jconhyd.2016.01.005.

Seeboonruang, U., Ginn T. R., 2006. Upscaling heterogeneity in aquifer reactivity via exposure-time concept: Forward model, J. Contam. Hydrol., 84(3–4), pp. 127–154. doi: 10.1016/j.jconhyd.2005.12.011

Shahkarami, P., Liu, L., Moreno, L., Neretnieks, I., 2015. Radionuclide migration through fractured rock for arbitrary-length decay chain: Analytical solution and global sensitivity analysis. Journal of Hydrology, 520, 448–460. doi: 10.1016/j.jhydrol.2014.10.060

Sidborn, M, Neretnieks, I., 2008. Long-term oxygen depletion from infiltrating groundwaters: Model development and application to intra-glaciation and glaciation conditions. Journal of Contaminant Hydrology, 100(1–2), 72–89. doi: 10.1016/j.jconhyd.2008.05.010

Sidborn, M., Neretnieks, I., 2007. Long term redox evolution in granitic rocks: Modelling the redox front propagation in the rock matrix. Applied Geochemistry, 22(11), 2381–2396. doi: 10.1016/j.apgeochem.2007.05.007

Sidborn, M., Neretnieks, I., 2004. Modelling biochemical processes in rocks: Analysis and exploratory simulations of competition of different processes important for ferrous mineral oxidation and oxygen depletion. Mater. Res. Soc. Symp. Proc. 807, 829–834. doi: 10.1557/proc-807-829

Spiessl, S. M., MacQuarrie, K. T. B., Mayer, K. U., 2008. Identification of key parameters controlling dissolved oxygen migration and attenuation in fractured crystalline rocks. Journal of Contaminant Hydrology, 95(3–4), 141–153. doi: 10.1016/j.jconhyd.2007.09.002

Strebel O., Duynisveld W.H.M., Böttcher J., 1989. Nitrate pollution of groundwater in western Europe, Agriculture, Ecosystems & Environment, 26(3–4), 189-214, doi: 10.1016/0167-8809(89)90013-3.

Su, D., Mayer, K.U., MacQuarrie, K.T.B., 2021. MIN3P-HPC: A High-Performance Unstructured Grid Code for Subsurface Flow and Reactive Transport Simulation. Math Geosci 53, 517–550. doi: 10.1007/s11004-020-09898-7

Suckow, A., 2014. The age of groundwater - Definitions, models and why we do not need this term. Appl. Geochemistry 50, 222–230. doi: 10.1016/j.apgeochem.2014.04.016

Sudicky, E. A., Frind, E. O., 1982. Contaminant transport in fractured porous media: Analytical solutions for a system of parallel fractures. Water Resources Research, 18(6), 1634–1642. doi: 10.1029/WR018i006p01634

Sudicky, E. A., Frind, E. O., 1984. Contaminant Transport in Fractured Porous Media: Analytical Solution for a Two-Member Decay Chain in a Single Fracture. Water Resources Research, 20(7), 1021–1029. doi: 10.1029/WR020i007p01021

Tang, D. H., Frind, E. O., Sudicky, E. A., 1981. Contaminant transport in fractured porous media: Analytical solution for a single fracture. Water Resources Research, 17(3), 555–564. doi: 10.1029/WR017i003p00555

Tecklenburg, J., Neuweiler, I., Carrera, J., Dentz, M., 2016. Multi-rate mass transfer modeling of two-phase flow in highly heterogeneous fractured and porous media. Advances in Water Resources, 91, 63–77. doi: 10.1016/j.advwatres.2016.02.010

Trinchero, P., Puigdomenech, I., Molinero, J., Ebrahimi, H., Gylling, B., Svensson, U., Bosbach, D., Deissmann, G., 2017. Continuum-based DFN-consistent numerical framework for the simulation of oxygen infiltration into fractured crystalline rocks. Journal of Contaminant Hydrology, 200, 60–69. doi: 10.1016//j.jconhyd.2017.04.001

Trinchero, P., Sidborn, M., Puigdomenech, I., Svensson, U., Ebrahimi, H., Molinero, J., Gylling, B., Bosbach, D., Deissmann, G., 2019. Transport of oxygen into granitic rocks : Role of physical and mineralogical heterogeneity. Journal of Contaminant Hydrology, 220, 108–118. doi: 10.1016/j.jconhyd.2018.12.001

Vías, J. M., Andreo, B., Perles, M. J., Carrasco, F., Vadillo, I., and Jiménez, P., 2006. Proposed method for groundwater vulnerability mapping in carbonate (karstic aquifers: the COP method. Hydrogeology Journal, 14(6), 912–925. doi: 10.1007/s10040-006-0023-6

Villinger, E., 1982. Grundwasserbilanzen im Karstaquifer des Oberen Muschelkalks im Oberen Gäu. Geologisches Jahrbuch. Schweizerbart Science Publishers,Stuttgart, Germany.

Visser, A.N., Lehmann, M.F., Rügner, H., D'Affonseca, F.M., Grathwohl, P., Blackwell, N., Kappler, A., Osenbrück, K., 2021. Fate of nitrate during groundwater recharge in a fractured karst aquifer in Southwest Germany. Hydrogeol. J. 1153–1171. doi: 10.1007/s10040-021-02314-2

Vu, Phuong T., Ni, Chuen-Fa, Li, Wei-Ci, Lee, I-Hsien, Lin, Chi-Ping., 2019. Particle-Based Workflow for Modeling Uncertainty of Reactive Transport in 3D Discrete Fracture Networks. Water 11, 12: 2502. doi: 10.3390/w11122502

Warnecke, M., Aigner, T., 2019. Influence of subtle paleo-tectonics on facies and reservoir distribution in epeiric carbonates: Integrating stratigraphic analysis and modelling (U. Muschelkalk, SW Germany). Sedimentary Geology, 383, 82–100. doi: 10.1016/j.sedgeo.2019.01.015

Warren, J. E., Root, P. J., 1963. The Behavior of Naturally Fractured Reservoirs. Society of Petroleum Engineers Journal, 3(03), 245–255. doi: 10.2118/426-pa

West, M. R., Kueper, B. H., Novakowski, K. S., 2004. Semi-analytical solutions for solute transport in fractured porous media using a strip source of finite width. doi: 10.1016/j.advwatres.2004.08.011

Whitelaw, K., Edwards, R. A., 1980. Carbohydrates in the unsaturated zone of the Chalk, England. Chemical Geology. 29(1–4), 281–291. doi: 10.1016/0009-2541(8090025-X

Wu, Y. S., Liu, H. H., Bodvarsson, G. S., 2004. A triple-continuum approach for modeling flow and transport processes in fractured rock. Journal of Contaminant Hydrology, 73(1–4), 145–179. doi: 10.1016/j.jconhyd.2004.01.002

Zhao, Z., Jing, L., Neretnieks, I., Moreno, L., 2011. Numerical modeling of stress effects on solute transport in fractured rocks. Computers and Geotechnics, 38, 2, 113–126. doi: 10.1016/j.compgeo.2010.10.001

Zhu, Y., Zhan, H., Jin, M., 2016. Analytical solutions of solute transport in a fracture–matrix system with different reaction rates for fracture and matrix. Journal of Hydrology, 539, 447–456. doi: 10.1016/j.jhydrol.2016.05.056

APPENDIX 2. 1. NUMERICAL FLOW AND TRANSPORT MODEL

The governing equation for flow in the saturated system is:

$$S_s \frac{\partial h}{\partial t} - \nabla \cdot (k_{ra} K \nabla h) - Q_a = 0, \quad \text{(A1)}$$

where S_s is the specific storage coefficient (m^{-1}), h the hydraulic potential (m), ϕ the porosity (–), t time (s), K the tensor of hydraulic conductivity (m s^{-1}), k_{ra} the relative permeability (–) and Q_a a source/sink-term (s^{-1}).

The governing equation for the advective- dispersive transport in the fracture and diffusive-reactive transport within the rock matrix is:

$$\frac{\partial}{\partial t}\left(S_{aq} \phi C_j^c\right) + \nabla \cdot \left(\boldsymbol{q} C_j^c\right) - \nabla \cdot \left(\boldsymbol{D}\, \nabla C_j^c\right) - Q = 0, \quad \text{(A2)}$$

where C_j^c denotes the solute concentration of the jth component in solution(mol l^{-1}), **q** the Darcy flux-vector (m s^{-1}), Q the source/sink term from geochemical reactions (kg m^{-3} s^{-1}). **D** is the hydrodynamic dispersion tensor (m^2 s^{-1}) which for the case of pure diffusion reduces to:

$$\theta_{aq}\, \boldsymbol{D} = D_e \quad \text{(A3)}$$

The effective matrix diffusion coefficient D_e is defined as:

$$D_e = \frac{D_{aq}\, \varepsilon}{\tau_f} \quad \text{(A4)}$$

where D_{aq} is the diffusion coefficient in water (m^2 s^{-1}) and τ_f is the tortuosity factor (-), expressed based on an empirical function of the matrix porosity (Grathwohl, 1998b):

$$\tau_f = \varepsilon^{-1.2} \quad \text{(A5)}$$

Thus, the effective diffusion coefficient D_e becomes:

$$D_e = D_{aq}\, \varepsilon^{2.2} \quad \text{(A6)}$$

Changes of mineral quantities are described by a set of mass conservation equations:

$$\frac{d\varphi_i}{dt} = V_i^m R_i^m \; i = 1, N_m \quad \text{(A7)}$$

where φ_i is the volume fraction of the mineral (m^3 mineral m^{-3} porous medium), V_i^m is the molar volume of the mineral i (m^3 mineral mol^{-1}), and R_i^m is the overall dissolution rate for the mineral i (mol m^{-3} porous medium s^{-1}).

The reaction-driven source/sink term Q for component i is computed from the sum of contributions of reaction rates R_j (kg m^{-3} s^{-1}) in the aqueous phase solution and mineral dissolution/precipitation:

$$Q_i = \theta_{aq} \sum_{i \in N} R_j \nu_{i.j} \;\; N \in \mathbb{N} \tag{A8}$$

where $\nu_{i,j}$ is the stoichiometric coefficient of component i in reaction j.

The overall reaction rate, R_j of surface-controlled mineral dissolution/precipitation used for dissolution/precipitation of calcite, gypsum, siderite, ferrihydrite and goethite is:

$$R_j = -k_{eff,j}\left(1 - \frac{IAP}{K_{eq,j}}\right) \tag{A9}$$

where $k_{eff,j}$ and $K_{eq,j}$ refer to the effective rate constant (mol m^{-3} s^{-1}) and the equilibrium constant for reactive species j, and IAP is the ion activity product.

The shrinking core model is applied for pyrite oxidation by O_2 in the rock matrix. The model assumes that dissolution is controlled by the diffusive flux through a non-reactive coating (Mayer et al., 2015). The radius of the dissolving crystals is getting smaller during the process while the non-reactive coating gets thicker. Specific effective reactions rates for pyrite oxidation by O_2 are computed as follows:

$$R_{py-O_2(aq)} = -10^3 \cdot S_{py} \cdot D_{py,O_2(aq)} \cdot \frac{r_{py}^p}{(r_{py}^p - r_{py}^r) r_{py}^r} \cdot \frac{C_{O_2}}{\nu_{py-O_2(aq),O_2(aq)}} \tag{A10}$$

where r_{py}^p (m) and r_{py}^r (m) are the initial and unreacted particle radii. S_{py} (m^2 m^{-3}) refers to the reactive surface area scaling factor. $D_{py,O_2(aq)}$ (m^2 s^{-1}) denotes the intra-particle diffusion coefficient of solute in water, and $\nu_{py-O_2(aq),O_2(aq)}$ denotes the stoichiometric coefficient of pyrite oxidation by O_2.

Due to various mineral precipitation and dissolution reactions, the porosity of the rock matrix might be altered. In MIN3P, the porosity is updated after each time step based on the mineral mass balance:

$$\phi^{t+\Delta t} = \phi^{t} - \sum_{i=1}^{N_m} (\varphi_i^{t+\Delta t} - \varphi_i^{t}) \qquad \text{(A11)}$$

where $\phi^{t+\Delta t}$ (–) and ϕ^{t} (–) are the porosities at times t+Δt and t. In accordance, $\varphi_i^{t+\Delta t}$ (–) and φ_i^{t} (–) refer to the volume fractions of reactive mineral i at times t+Δt and t. N_m (–) denotes the total number of reactive minerals.

3. ENHANCING RELIABILITY OF ESTIMATED TRAVEL TIME DISTRIBUTIONS USING MULTI-ISOTOPE MODELS OPTIMISATION

Abstract

Quantification of the travel time distribution in fractured aquifers is typically non-unique and exhibits high parametric uncertainty. Knowledge of the travel time distribution, however, is crucial for predicting reactive contaminant transport in the fracture system. In this work we aim to reduce the uncertainty in estimation of mean travel time, and the shape parameter of the travel time distribution by means of multiobjective optimization. We treat fracture aperture, matrix porosity and solute specific diffusion coefficients as unknown parameters, and concentration measurement at each location as objective function. For pre-selection of potentially plausible model runs Gaussian Processes Emulation was applied within the four-parametric space. Transport parameters are estimated stochastically by combining direct modelling of the groundwater ages with the multitracer approach. We confirm the hypothesis that using tritium and helium, and for older groundwater ^{39}Ar isotopes together with radiogenic helium measurements, allows reducing the uncertainty in the travel time distribution, fracture aperture and porosity estimates. In the work, we show that including additional tracers in calibration strategy helps to exclude the bimodality of the mean groundwater age estimates in fractured rocks with matrix diffusion.

***** Reproduced from: Elena Petrova, Karsten Osenbrück, Werner Aeschbach, Jürgen Sültenfuß, Uli Mayer, Peter Grathwohl, Michael Finkel. Enhancing Reliability of Estimated travel time distributions using multi-isotope model optimisation (2023). Paper in preparation.

3.1. INTRODUCTION

Groundwater travel time distribution is a crucial prerequisite for quantitative characterisation of the reactive transport in aquifers. It defines the fate of solutes originating from different sources. Knowing the travel time distributions thus allows quantifying and predicting the solute evolution in the aquifer. Travel time is defined as the time a particle needs to travel from the inlet boundary to the observation point (Sanz-Prat et al., 2016). Any observation point that is reached by more than one flow paths is capturing the distribution of travel times resulting in the probability density function (PDF) (Cirpka and Kitanidis, 2000; Dagan and Cvetkovic, 1996). Reactive transport processes contributing to the distribution of travel times such as local dispersion, mass transfer between mobile and immobile phases, sorption and hydrodynamic instability (Luo and Cirpka, 2008) are described individually within each streamtube.

The travel time concept is widely used in conservative and reactive transport problems for porous (Dagan and Nguyen, 1989; Atchley et al., 2013; Finkel et al., 2016; Sanz-Prat et al., 2015) and fractured aquifers (Cvetkovic et al., 1999). A travel time-based model requires conceptualization and quantification of solute's reactive behaviour within a flow path, and the estimation of the travel time distribution at a given location. While reactive transport may be described based on conceptual models and tracer-specific reactive performance, travel time distribution can't be measured directly even when a parametric PDF is considered (Cirpka and Kitanidis, 2000; McGuire and McDonnell, 2006). That is why the travel time distribution is typically inferred by solving the inverse of the convolution integral (Cirpka and Kitanidis, 2000) from measurements of natural tracers (e.g. Gardner et al., 2016), solute- and heat tracer tests (e.g. Cox et al., 2007), and/or electrical conductivity (Cirpka et al., 2007). One of the most commonly used tracers for analytical travel time estimates are isotopes and biogeochemical tracers (Castro et al., 2000; Schlosser et al., 1988; Sterte et al., 2020; Trinchero et al., 2019). Solving this inverse problem is directly related to the quality and quantity of available concentration measurements, the underlying assumptions about the reactive behaviour, model complexity, and quality of the measured model parameters.

In fractured rock systems, the estimation of travel time includes additional processes such as component-specific mass exchange between fractures and the rock matrix

(LaBolle, et al., 2006; Neumann, et al., 2008). Mass exchange between these two media is described with dual porosity or multiple interacting continua models (Molins et al., 2019). To account for these processes, Goode (1996) suggested using direct modelling of the groundwater age tracers which includes diffusion-reaction processes and travel time distribution. The approach proposed by Goode involves considering measured concentration as convolution of the solute's concentration profile with travel time distribution.

Conceptualisation of the fractured system is done according to the available and often incomplete hydrogeological information and creates parametric and conceptual uncertainty (Cvetkovic and Frampton, 2010; Cvetkovic et al., 2016). On a Darcy scale, reactive transport in the fractured rocks is often conceptualised by combination of fast advective flow in fractures and slow diffusive exchange with the rock matrix (MacQuarrie et al., 2010). Dominant transport features are fracture aperture, matrix porosity, solute diffusion coefficients and sorption (Meng et al., 2018; Tang et al., 1981; Sidborn and Neretnieks, 2007). Parameterization of reactive transport in fractured rocks may be done by combining field observations with laboratory experiments and geological data.

On the catchment scale the key issue is availability and reliability of the data. A reactive transport model generally involves parametric and measurement uncertainty, and is limited to spatio-temporal variability of parameters on the studied scale. Measurement uncertainty originates from the analytical precision and sampling conditions (Visser et al., 2014), and is basically included in any measured parameter value. Therefore, calibration as a task to fit observed concentrations with the parametric model often results in non-uniqueness of a solution: measured data may be explained by a series of likely parameter combinations equally well fitting to the observed value.

A favourable way to characterise reactive transport and to account for the parametric uncertainty is to perform stochastic model realisations (e.g. see debates: Cirpka and Valocchi, 2016). Stochastic optimisation methods like gradient descent or Marcov Chain Monte Carlo typically confront the bottleneck of computationally demanding reactive transport models (Atchley et al., 2013; Loschko et al., 2016). For this reason surrogate models were developed as an attractive and comparably easy to implement tool which allows extensive access to preliminary model predictions

(Owen et al., 2017; Rajabi and Ketabchi, 2017). Gaussian processes emulation (GPE) as a subclass of surrogate models have been profitably serving in initial evaluation of computationally demanding models (Asher et al., 2015; Laloy and Jacques, 2019; Erdal et al., 2020). Under condition of a high computational cost of a single reactive transport model run and potentially big amount of ineffective model runs, GPE has been employed for the pre-selection of the suitable parameter combinations (Erdal and Cirpka, 2019; Rajabi and Ketabchi, 2017) which would lead to a low discrepancy between the model outcome and the measurement. Multiple tracers approach has been employed widely to further reduce the uncertainty of the posterior parameter distribution (e.g., Abbott et al., 2016; Gardner et al., 2016; Wersin et al., 2008; Widory et al., 2004). The optimal results are reached when no additional uncertainty is introduced when considering new components: for example, when all models describing the tracers' behaviour are based on the same parameter set.

The overarching goal of this work was to quantify groundwater travel time distribution and the main transport parameters of the fractured limestone aquifer Muschelkalk in SW Germany. The aim was to reduce parametric uncertainty by applying stochastic multiobjective optimization to different solute measurements which reactive functions are described through the same parameter set. For this purpose four isotope measurements (^{3}H, ^{3}He, ^{4}He and Ar^{39}) were used for stochastic calibration in each of the sampling locations across the catchment. In order to compare the results, stochastic calibration was performed based on measurements of a single solute (mono-objective optimization), as well as based on measurements of all solutes together (multi-objective optimization). We used the process-based modelling of the isotope transport to account for the effect of the diffusive mass transfer between rock matrix and fracture (Neumann et al., 2008). The direct model of ^{3}H and ^{3}He reactive transport in the single fracture was set up numerically using MIN3P code (Su et al., 2017). For the ^{4}He and Ar^{39} measurements, analytical solutions (Tang, Frind and Sudicky, 1981; Trinchero *et al.*, 2019a) were applied to obtain concentration profile along the fracture.

Concentration profiles were then used for the convolution with a two-parametric γ-shaped travel time distribution to obtain a concentration at the given location. Following this procedure, four parameters: fracture aperture, matrix porosity, mean

travel time, and the shape parameter of travel time PDF, were optimized stochastically by matching with the concentration measurements. Resulting ensembles of location-specific posterior parameter distributions were compared for single- and multiobjective optimisation in all locations in the fractured limestone aquifer with the focus on uncertainty reduction, facies-specific characterisation of the groundwater capturing zones, and precise evaluation of the mean travel time under parametric uncertainty.

3.2. MATERIALS AND METHODS

3.2.1. STUDY SITE

The Upper Muschelkalk is a fractured carbonate locally karstified aquifer that comprises an important drinking water reservoir of SW Germany. It consists of limestone and dolomites which comprise shoal, tempestite, and basinal rock facies (Palermo et al., 2010; Schauer et al., 1997) with porosity of 0.15-0.3, 0.005-0.1, and 0.005-0.05 correspondingly (Osenbrück et al., 2021). The sedimentary system in the Upper Muschelkalk was affected by extensive fracturing during the rifting of the Atlantic in the Jurassic-Early Cretaceous and the subsidence of the Upper Rhine Graben rift in late Eocene-Quaternary (Ring and Bolhar 2020). Additionally, a series of horizontal and lateral displacements exist in the area (D'Affonseca et al., 2020), producing a series of fractures with the range of apertures derived from the cubic law $1\ 10^{-4}$ – $1\ 10^{-3}$ m (Petrova et al., 2022). The catchment of the Ammer River originates in the Ammer Springs areas, takes a south-east direction till the city of Tübingen and has a total length of around 22.5 km.

3.2.2. GROUNDWATER SAMPLING

Groundwater samples for the analysis of tritium, and helium and neon isotopes (^{3}He, ^{4}He, ^{20}Ne, ^{22}Ne) were taken in several sampling campaigns (2011/2012 at production wells and karstic springs; 2014 at monitoring wells; and 2017/2018 at all available groundwater sites)**. Sampling locations were selected to be broadly distributed across the Ammer catchment (Appendix 3.3).

Submersible pumps were used for sampling the monitoring wells (diameters of 10.2 and 12.7 cm) with pumping rates between 0.01 and 0.20 L/s. Samples were taken after exchanging the water volume inside the well at least 1.5 times. At the drinking water wells, water samples were collected from a tap at the borehole head during

** All samples described hereafter were taken and analyzed within CAMPOS project under supervision of Dr. Karsten Osenbrück and were provided for this piece of research solely for modelling purpose.

water extraction with 10 to 50 L/s as provided by the installed production pumps. Groundwater samples from the artesian well were either taken from the artesian outflow or by using a submersible pump when the pressure head dropped below the well top during the summer season. Water samples from the karstic Ammer springs were collected as grab samples for tritium or using passive diffusion samplers (Gardner and Solomon, 2009) placed into the natural spring for He and Ne isotopes. Prior to each sampling, dissolved oxygen, pH, water temperature, and specific electrical conductivity were measured in the field using handheld probes (WTW GmbH) inserted into a flow-through cell, which was directly connected to the pump or borehole head.

Water samples for tritium analysis were collected in 500 mL plastic bottles. Groundwater samples for noble gas analysis were taken in duplicate in copper tubes (about 40 ml volume) sealed by stainless steel clamps to provide reliable and durable isolation from the atmosphere. During sampling, any contamination due to contact with the atmosphere was prevented by ensuring a gas-tight connection by flexible tubing between the wells and the sample containers. The entire setup was well-flushed and inspected to remove any gas bubbles. Due to the relatively low pumping rates, the build-up of gas bubbles due to degassing could not be prevented at some of the monitoring wells. Duplicate groundwater samples for the analysis of ^{39}Ar were collected at the drinking water well TBBrhz in February 2020 in pre-evacuated, gas-tight, 5 L stainless steel containers, which were directly connected to the borehole head.

3.2.2.1. TRITIUM AND HELIUM ISOTOPE ANALYSES

Helium and neon isotopes were measured at the Bremen Mass Spectrometric Facility following the methods described by Sültenfuß et al. (2004). After extraction of the dissolved gases in the laboratory, the Ne and He isotopes were purified in a two-level cryosystem at 25 and 14 K. ^{4}He, ^{20}Ne, and ^{22}Ne were measured with a quadrupole mass spectrometer (Balzer QMG112A). After separation from Ne, ^{3}He, and ^{4}He were analyzed with a high-resolution sector field mass spectrometer (MAP 215-50). Typical precision for He and Ne concentration is better than 1%, for ^{3}He/^{4}He ratios better than 0.5%.

Tritium was analyzed with the ^{3}He-ingrowth method (Sültenfuß et al., 2004). The water samples were degassed and stored for ^{3}He accumulation in dedicated He-free

glass bulbs. After a storage period of 2–6 months, tritiogenic ^{3}He was analyzed with the mass spectrometric system with a detection limit of 0.01 TU (tritium unit). The uncertainty is typically less than 3% for samples of >1 TU and 0.01 TU for very low concentrations.

3.2.2.2. ARGON-39 ANALYSES

A single measurement of ^{39}Ar was done in the location Breitenholz with the potentially oldest water (D'Affonseca et al., 2020). After gas extraction of the water samples in the laboratory, ^{39}Ar was measured using the atom trap trace analysis facility (ArTTA) at the University of Heidelberg (Ritterbusch et al. 2014; Feng et al. 2019). For argon purification, the extracted gas was transferred to a 900 °C titanium sponge getter. A second titanium sponge getter at room temperature was used to adsorb hydrogen, and the remaining gas fraction, consisting of >99% argon, was captured on a charcoal trap and transported to the ArTTA setup (Feng et al. 2019). In the ultrahigh vacuum of the ArTTA, the purified Ar gas is converted to metastable argon (Ar*) in an RF-discharge source for laser cooling. Liquid nitrogen cooling is applied to reduce the initial velocity of the atoms. The flux into the small detection region is provided by two transversal laser cooling stages, which collect the divergent atoms from the effusive source and collimate them into a compressed beam. Subsequently, the longitudinal velocity is reduced from thermal velocities to a few meters per second by a Zeeman slower. Single ^{39}Ar atoms are finally captured and detected in a magnetooptical trap, guaranteeing perfect selectivity by millions of resonant photon scattering processes in a spatially confined region. The gas collected from several turbomolecular pumps maintaining the ultrahigh vacuum is cleaned with a non-evaporative getter and restored to enable full recycling of the sample. With this procedure, the required sample size is as low as 0.5 mL STP. Each sample is framed by at least two reference measurements using an artificial sample with 10 times enriched ^{39}Ar compared with modern concentration. To infer the sample concentration from the number of atoms detected, long-term memory effects are determined by background measurements with ^{39}Ar-free samples. A Bayesian analysis is used to obtain the probability density function for the sample concentration. Concentrations of $^{39}Ar/Ar$ are reported as pmAr (%-modern argon) representing the ratio of the counting rates (atoms/h) of the sample and the atmosphere.

3.2.2.3. SEPARATION OF HELIUM COMPONENTS

The ^{3}He dissolved in groundwater is usually composed of different sources that must be separated to determine tritiogenic helium ($^{3}He_{tri}$) (Schlosser et al. 1988; Solomon and Cook, 2000). The concentration of ^{3}He and ^{4}He measured in groundwater is the sum of atmospheric helium, helium from excess air, and radiogenic helium. Atmospheric He isotopes have been calculated using Henry's law for the temperature (10.5 ± 1.0°C) at the water table and the altitude (500 ± 50 m) of recharge area (salinity can be neglected) and the $^{3}He/^{4}He$ ratio of atmospheric air of $1.384\ 10^{-6}$. Excess air, which is introduced into groundwater during recharge (Heaton and Vogel, 1981; Aeschbach-Hertig et al., 1999) was estimated from the difference of measured and expected ^{20}Ne concentrations assuming a closed equilibrium with atmospheric air (CE model; Aeschbach-Hertig et al., 2000) and a fractionation factor F of 0.4 ± 0.2, which is close to the median value reported by Aeschbach-Hertig et al. (2002) for different aquifers. Radiogenic helium from the decay of U and Th series elements in the subsurface was determined assuming a $^{3}He/^{4}He$ ratio of $2 \pm 1\ 10^{-8}$, which is consistent with average $^{3}He/^{4}He$ ratios in deep groundwater of similar Triassic rock formations (Osenbrück et al., 1998). Although measured Ne concentrations were usually higher than expected atmospheric Ne concentrations, the component separation resulted in negative values of radiogenic He for some of the monitoring wells, which was attributed to slight degassing during sampling. For these samples, an equilibrium degassing model (Visser et al., 2007; Aeschbach-Hertig et al., 2008) was applied to correct the tritiogenic helium concentrations until all calculated He components became positive. The radiogenic ^{4}He concentrations of these samples were not used for the travel-time optimizations.

3.2.2.4. TRITIUM INPUT FUNCTION

The input function of tritium was constructed by calculating annual weighted means from the long-term tritium measured in rainfall at the precipitation monitoring station in Stuttgart (Schmidt et al. 2020), which is part of the GNIP network (Global Network of Isotopes in Precipitation) of the International Atomic Energy Agency (IAEA). For the period from 1953-1960 and 1968-1970 (no data in Stuttgart) yearly tritium concentrations were determined from the correlation between tritium in precipitation in GNIP stations Stuttgart and Ottawa (Canada). Monthly tritium concentrations were converted to yearly averages using the fraction of precipitation contributing to

groundwater recharge. The fraction contributing to groundwater recharge was calculated using the alpha value introduced by Grabczak et al. (1984), where alpha is the contributing fraction of precipitation during the summer season divided by that of the winter season. An alpha value of 0.53 was derived from stable isotopes of water in precipitation of the station Stuttgart (Stumpp et al. 2014) and measured time series data from the karstic Ammer spring. The resulting input function of the tritium (Fig.3.1) was applied on a yearly-step basis in the MIN3P model of the tritium and helium transport in the fracture (Appendix 3.2).

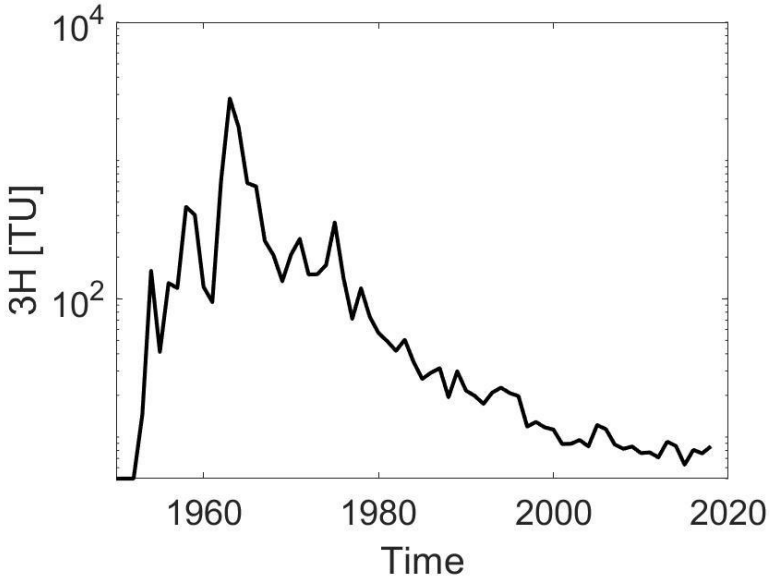

Figure 3.1. Input function of tritium in the Muschelkalk aquifer, Stuttgart meteostation (Fuenfgeld, 2020)

3.3. MODELLING APPROACH

3.3.1. CONCEPTUAL CONSIDERATIONS

Concentration of a tracer at any sampling location C_{GW} in the fractured aquifer is a result of convolution of (i) the concentration in the fracture C_r at a certain time t and travel distance τ defined for a specific parameter set par, and (ii) the probability density function of the travel times PDF (Cirpka and Kitanidis, 2000). For a parametric *PDF* described by a γ-distribution for a given mean travel time $\bar{\tau}$ and a shape parameter α:

$$C_{GW}(t,\bar{\tau}) = \int_0^{\infty} C_r(t,\tau,par)\, PDF(\tau,\alpha,\bar{\tau})d\tau \qquad (3.1)$$

A 2D illustration of the concept is shown on fig. 3.2. Flow paths (fractures) with different travel times mix in a given sampling location which results in averaging of individual travel times and corresponding concentrations.

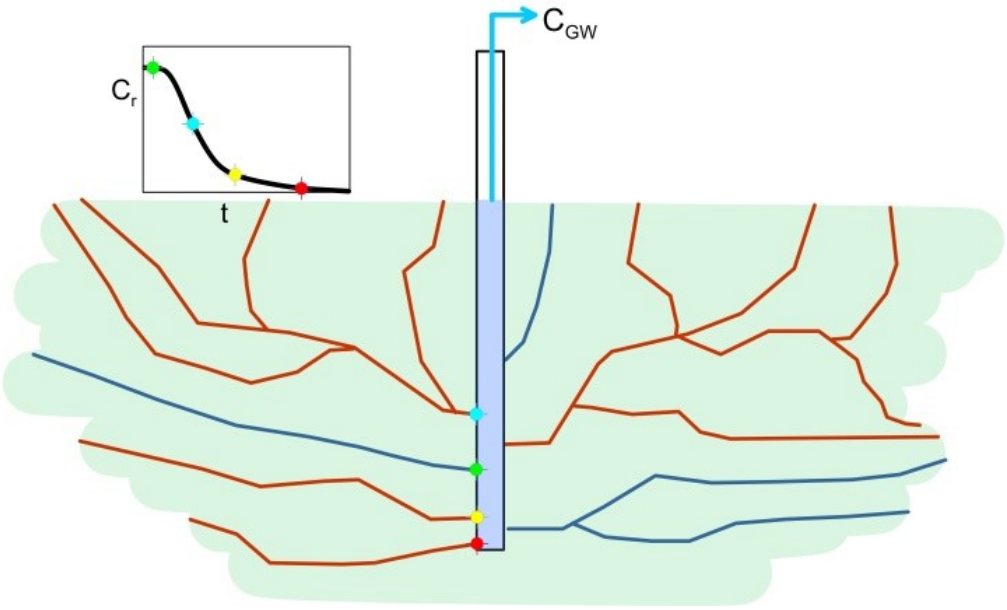

Figure 3.2 Schematic representation of the modelling concept: blue and red lines denote streamlines with faster and slower water, respectively; colored dots represent the stage of the breakthrough curve at the sampled streamline. Concentration in the sampling location C_{GW} is thus a result of the flow paths mixing.

This implies that any measured concentration of a solute represents the abovementioned convolution integral. To match the concentration via the reactive transport model, a set of corresponding parameters in eq.3.1 has to be calibrated to provide a corresponding modelled concentration. For an arbitrary reactive behaviour, this calibration leads to minimizing the error between measured and observed concentration of the component through varying reactive function parameters, mean travel time, and the shape parameter of the travel time distribution. Noticeably, the calibration task depends on more than one parameter and will likely result in the ensemble of parameter combinations satisfying the minimum error. To account for the measurement uncertainty we introduce a safety margin which corresponds to the confidence interval for every measurement, and minimize the normalized deviation between the model and observation:

$$E_i = \frac{|C_{obs} - C_{mod}|}{3\sigma_i} \quad (3.2)$$

where σ denotes the 99% confidence interval of the measurement error. For a set of observations, the total error to minimize is defined through the maximum of the errors within a location (Hawkins, 1945):

$$E_t = max(E_i) < 1 \quad (3.3)$$

3.3.2. STOCHASTIC MODEL FORMULATION

Minimization (eq. 3.3) was done in a stochastic way with the help of surrogate modelling following the GPE "on-the-fly" approach (Erdal et al., 2020) by sampling the model within possible ranges of calibration parameters. Every parameter may vary within ranges of magnitudes. The mathematical formulation of the GPE "on-the-fly" is described in detail in Erdal et al. (2020). Briefly, a surrogate model provides an initial idea of the output within the parameter space using only a few model evaluations and helps to improve the sampling scheme. Then, only favourable unique parameter combinations are sampled to obtain an ensemble of a defined size. In our case, we use the GPE for selecting an ensemble of parameter combinations that have the potential to satisfy the acceptance criteria (eq. 1).

The following sampling scheme was applied for each sampling location:

1) Sample a uniform prior of the Latin Hypercube to draw *n* parameter sets. For a single model case, *n* = 500, for a multiobjective optimization *n* = 900.

2) Train the GPE based on E_i or E_t for the response of a single model or multiple models accordingly.

3) Based on the GPE results, compute the probability of satisfying the condition (eq.3.3) in 10000 random locations in the parametric space. Select points with the highest probability. The probability threshold criteria changed during the calibration depending on the initial and posterior quality of the GPE from 0.2 to 0.9.

4) For the selected points, run the full model, and add to the ensemble those model outcomes that satisfy (eq.3.3).

Steps 2 – 4 are repeated until the ensemble is filled with the successful model runs. Parameter distributions for every location were compared for the case of a single model calibration and calibration of all the models together (multi-objective). To account for the measurement uncertainty, each member of the posterior parameter

distribution is considered to be equally good (Fig.3.3), meaning no ranking within the parameter distributions satisfying eq.3.3 was done. Calibration was completed for each sampling location individually.

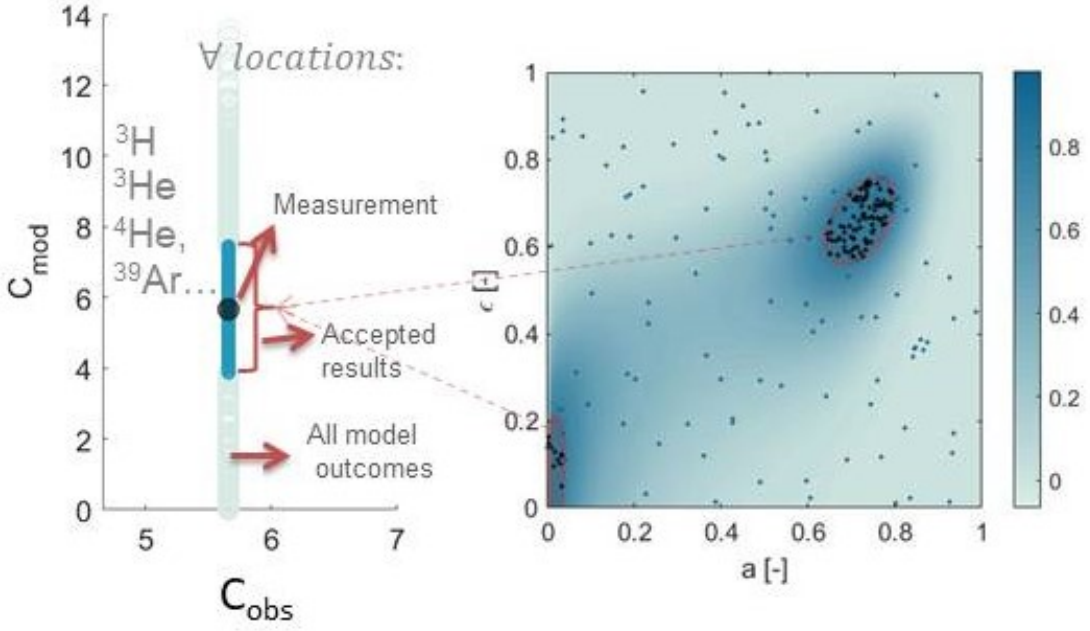

Fig.3.3. Schematic representation of the GPE-based sampling in a two-dimensional parameter space.

Firstly, posterior parameter ensembles were obtained for the ^{3}H and ^{3}He model, and ^{4}He and ^{39}Ar models separately. An average burn-in phase was defined as the number of model runs needed to obtain a stable GPE predicting varied between 300 and 4000 model evaluations. Tritium and helium measurements were available in 30 locations, while additional radiogenic helium measurements were available in 13 of them (Appendix 3.3). For the ^{3}H and He measurements, all available measurements within one location were considered together within the *minimax* algorithm (eq. 3.3). To explore the effect of including multiple components, optimization was performed using all available measurements of all models within one location.

3.3.3. Models and Tracers

For every reaction function, we consider a single fracture model with constant effective fracture aperture and matrix porosity along the streamline with solely advective flow in the fracture and diffusive exchange with the rock matrix.

Tritium and helium. Tritium ^{3}H is a radioactive isotope of hydrogen with a half-life of 12.43 years which was massively released in the atmosphere by the nuclear tests in 160-170s (UNSCEAR, 2016). The low background tritium emission of 0.15-0.2 a^{-1} in comparison to the loads of during the nuclear tests 650 kg a^{-1} makes is attractive groundwater age tracer. Helium as a product of tritium decay is commonly measured and used together with tritium concentration to obtain the groundwater age. Specifics of the tritium and helium groundwater dating in fractured media are discussed and in Appendix 3.2.

Radiogenic helium. Radiogenic helium is one of the naturally occurring stable isotopes commonly used for groundwater dating (Osenbrück et al., 1998; Castro et al., 2000). It evolves in the rock matrix by alpha decay of uranium and thorium (Solomon, 2000) and diffuses to the fracture. The production rate of helium under standard temperature and pressure conditions is (Castro et al., 2000):

$$G(4He) = \frac{(1-\varepsilon)\rho}{\varepsilon}(1.207 \cdot 10^{-13}[U] + 2.867 \cdot 10^{-14}[Th])\ [\text{cm}^3\ \text{STP}\,\text{g}^{-1}_{\text{rock}}\,\text{yr}^{-1}] \qquad (3.4)$$

where ε and ρ denote the porosity and the bulk density of the rock and $[U]$ and $[Th]$ are concentrations of uranium and thorium in the rock, respectively. Concentrations of uranium and thorium in limestones are *[U]* = 2.2 ppm *[Th]* = 4.3 ppm (Grigoriev, 2009). Trinchero et al. (2019) provide an analytical solution for the steady-state ^{4}He transport in the fracture:

$$c_f = \frac{t_w(L)G\,\varepsilon}{a}\left(\frac{x}{L} + \frac{\left(exp\,(-v\,L)\ - exp\,\left(v\,L\left(\frac{x}{L}-1\right)\right)\right)}{v\,L}\right) \qquad (3.5)$$

where *x, L, a, ε, t_w*, and *G* denote distance along the fracture, total fracture length, fracture half aperture, matrix porosity, groundwater age at the fracture outlet, and ^{4}He bulk production rate in matrix. As follows from the solution (eq.3.5) provides ^{4}He concentration is monotonically increasing along the streamline (Fig. 3.4). Reactive curve C_r of ^{4}He was used to obtain the concentration in a location as a result of the convolution integral (eq. 3.1).

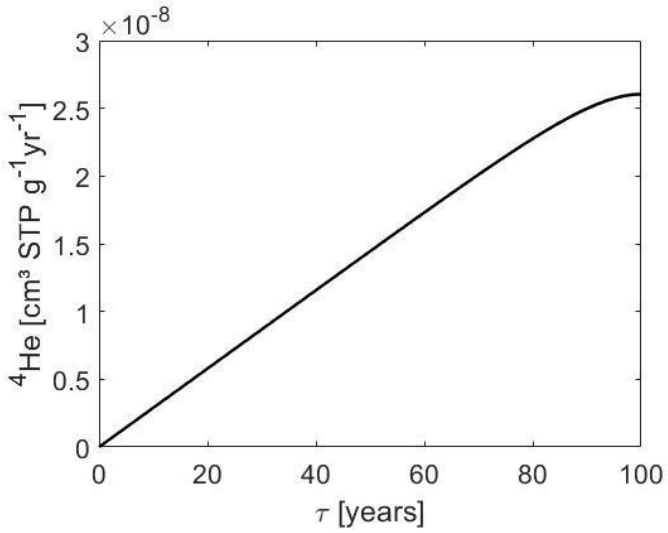

Figure 3.4. Example of the radiogenic helium concentration profile in the fracture (from the eq. 3.5).

Argon-39. Ar-39 is produced by interaction of cosmic rays with the atmosphere. The current atmospheric ratio of Ar-39/Ar equals 100 %-modern Argon (or 100 pmAr) = 180 Bq/L. Ar-39 has a half-life of 296 years. Reactive ^{39}Ar transport in the fracture is described by the analytical solution of Tang et al. (1981):

$$\frac{C}{C_0} = 0.5\, exp\left(-\frac{\lambda \cdot z}{v}\right) \cdot [exp\left(-\frac{z \cdot \lambda^{\frac{1}{2}}}{v \cdot A}\right) erfc\left(\frac{z}{2 \cdot v \cdot A \cdot T'} - \lambda^{\frac{1}{2}} T'\right) + exp\left(\frac{z \cdot \lambda^{\frac{1}{2}}}{v \cdot A}\right) erfc\left(\frac{z}{2 \cdot v \cdot A \cdot T'} + \lambda^{\frac{1}{2}} T'\right)] \quad (3.6)$$

$$\lambda = ln\,(2)\,/296 \text{ years} \quad (3.7)$$

$$T' = (t - \frac{z}{v})^{1/2} \quad (3.8)$$

$$A = \frac{a}{\varepsilon\,(D')^{1/2}} \quad (3.9)$$

$$D' = \tau\, D^* \quad (3.10)$$

where v [L T^{-1}], a [L], D' [L^2 T^{-1}], ε [-],τ [-] , D^* [L^2 T^{-1}] denote the groundwater velocity in the fracture, half-aperture of the fracture, effective diffusion coefficient, matrix porosity, tortuosity of the matrix pores, and molecular diffusion coefficient in water accordingly.

3.4. RESULTS AND DISCUSSION

The resulting location-specific modal values of the mean travel time are depicted in figures 3.5-3.6. The mean travel time values of the Muschelkalk aquifer are filling the interval of 0-62 years. Most of the locations reflect the travel time of 10-30 years with only a few outliers to younger and older values. The youngest travel time is captured by karstic Ammer spring Amq, Arteser Altingen (exploration well), and TB Altingen 3 (production well). The oldest travel times are captured by monitoring wells in Breitenholz and Golfplatz Bondorf. These travel times estimates are consistent with the data analysis results from the previous study (Osenbrück et al., 2021, Visser et al., 2021) and the overall idea of the aquifer functioning (D'Affonseca et al., 2020).

Confirming theoretical considerations and the previous work of Neumann et al (2008), mean travel times derived from the stochastic modelling results deviate from analytically estimated (Fig. 3.5). In most of the cases, the mean travel time estimated from the modelling is exceeding the analytically estimated value. The least deviating are mean travel time values of around 20 years, and the oldest (up to 60 years) and youngest (0-10 years) travel times are most different from the analytical estimates. At the same time, the difference between analytically computed value and the one derived from the model is irregular; meaning no clear trend or pattern could be seen.

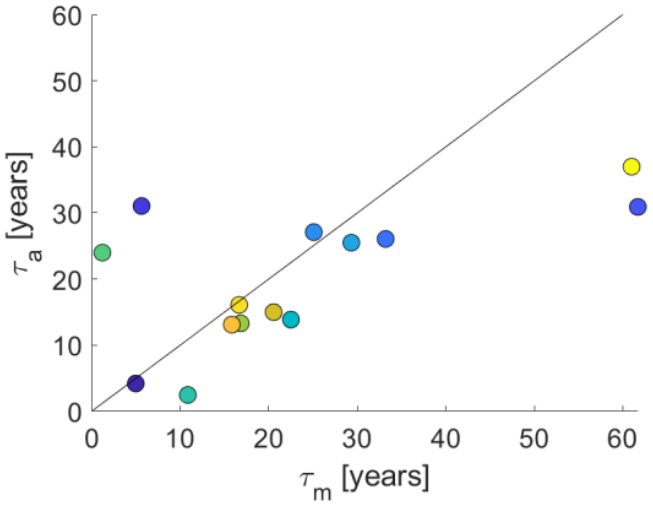

Figure 3.5. Mean travel times estimated through the modelling of the groundwater age tracers τ_m vs. analytical travel time estimates τ_a; black line corresponds to 1:1 ratio.

Posterior distributions of the location-specific mean travel time, shape parameter of the gamma PDF, fracture apertures, and porosity are provided in the S.M.6. Travel times of 1-40 years (figure 3.6, left) are in good agreement with the general understanding of the aquifer structure (D'Affonseca et al. 2020). Posterior mean travel times within the multiobjective optimization are typically close to those obtained through ^{3}H/He modelling with two outliers in locations ArtA and TbAlt3. At the same time, accounting for ^{4}He as an additional tracer allowed to decrease the standard deviation of the mean travel time by up to 2-5 times (Fig.3.6 right).

While estimates of the ^{4}He always provide wide ranges of the mean travel times and other transport parameters, the tritium-helium dating often results in narrower ranges of the mean travel times. This may have to do with the fact that the tritium-helium model includes in fact two semi-independent measurements – tritium and helium, the reactive behaviour of both should match to calibrate the model. Secondly, for this model often more than a single measurement was available, resulting in quasi time-series (Appendix 3.3). The resulting mean travel time obtained via calibration of only tritium and helium is different from the case when an additional model of ^{4}He production and transport is considered (Fig.3.6 left, S.M.5). Although the posterior distribution of parameters obtained within ^{4}He model is quite wide, common combination of aperture, porosity, mean travel time and the shape parameter of the γ-PDF does help to tighten the posterior the mean travel time in most of the locations (Fig. 3.6).

The results of multiobjective optimization and the width of parameter ranges vary at every location (S.M.3-6). In 10 out of 13 locations optimization ends with quite a narrow range of possible mean travel time with a confidence interval of less than 5 years. In two locations, however, TBAlt3 and Möz3, mean travel time can only be estimated with a confidence interval of 15 years. Whereas in Möz3 only a single measurement was available, the TBAlt3 location was sampled three times in 2004, 2011, and 2018.

Therefore, the assumption that more measurements would improve the calibration results cannot be directly confirmed from this experiment. To improve the mean travel time estimates, additional information about aquifer properties would be beneficial. For example, more narrow ranges of other parameters (aperture, porosity, shape

parameter of the travel time distribution) or even better, reduction of the problem dimensionality would lead to a precise calibration.

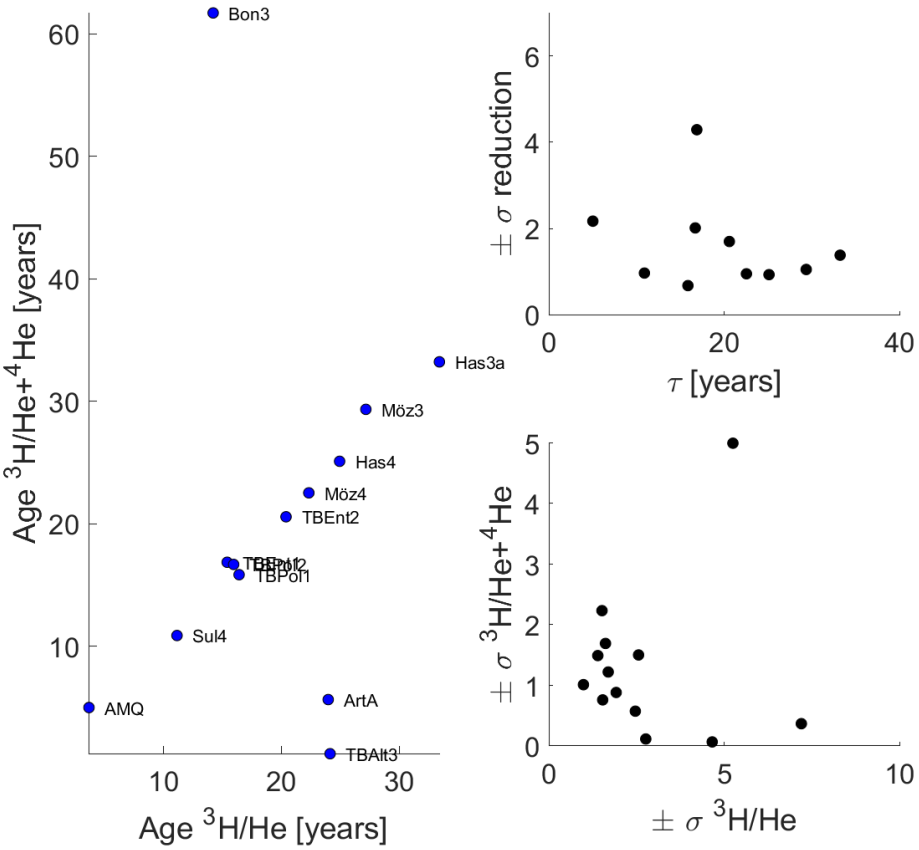

Figure 3.6. Effect of the multiobjective optimisation. Left: comparison between mean τ obtained through the single model the ^{3}He/He and two models together ^{3}H/He +^{4}He. Right: Comparison of standart deviations for the single model the ^{3}He/He and two models together ^{3}H/He +^{4}He.

The uncertainty reduction potential is more pronounced with the higher concentration of the measured ^{4}He. No significant uncertainty reduction was gained in locations with the lowest concentrations (Möz3-4, Sul 4, Has 3A-4) due to higher relative confidence intervals and a broad range of possibly fitting parameters. The reaction curve of radiogenic helium is to a large extent linear (Fig. 3.4) with the upper concentration limit of 1 10^{-6}(cm³STPg^{-1}yr^{-1}) defined by parameter ranges. That means lower concentrations are generally more likely to appear.

Breitenholz location is worth mentioning separately, as a very special measurement of ^{39}Ar was available there. Preliminary geological and hydrogeological studies

suggested that the Breitenholz well was capturing the oldest water among all locations. The modelling results of the tritium-helium model show a three-peaked travel time histogram with the possible travel time values of 0-60 years meaning that more data are necessary to estimate the mean travel time successfully. At the same time, low tritium and high helium concentrations in the groundwater allow for narrowing down the estimation of aperture and porosity: apertures are less than 1 mm and porosity is less than 10 %. The concentration profile of the additional tracer ^{39}Ar in the fracture is different from the tritium and helium. As could be seen from Fig. 3.7, matching its concentration to the measurement in addition to the calibration of tritium and helium models is leading to a much narrower possible mean travel time interval of 60±3 years.

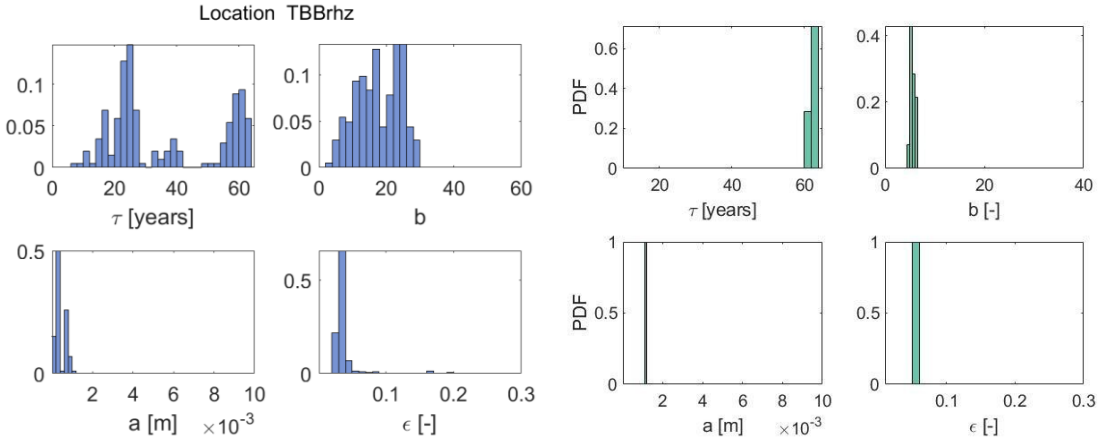

Figure 3.7. Left: Posterior parameter distributions after tritium and helium model. Right: Posterior parameter distributions after including ^{4}He and ^{39}Ar data.

The acquired location-specific ranges of parameters exhibit substantial variability across all locations (S.M.4). Majority of locations except Poltringen and Bondorf demonstrate lower porosity values, typically less than 5%, indicative of a micritic limestone. Calibration results in Sul. 3 and 4 were insensitive to the porosity changes reflecting unchanged posterior distribution. In most locations except AmQ, Möz3, and ArtA effective apertures are anticipated to be on a millimeter scale. The fracture aperture is a parameter which varies within three orders of magnitude and at the same time is highly important for reactive transport (for details please see Chapter 4). Therefore, narrowing down the range of possible aperture values would enhance the calibration quality.

In addressing the challenge of uncertain spatial parameter variations, a key inquiry is how to reduce the model complexity. Considering the variability of the aperture and porosity within one location as well as within the catchment, would it be possible to describe the aquifer with a single value of effective aperture and porosity? Posterior distributions of aperture and porosity were analysed to assess the hypothesis that all locations within the catchment could be described within the catchment-scale effective values.

The ranges of aperture and porosity were split into 10 intervals each. For each combination of aperture a_i and porosity ε_j intervals, a probability P that at least one combination of aperture and porosity for every location is falling in this interval was computed:

$$P_{i,j} = \frac{\sum any(a \in a_i \; and \; \varepsilon \in \varepsilon_j)}{n} \tag{3.11}$$

Where $n, ai = [ai_{min}, ai_{max}]$, $\varepsilon_j = [\varepsilon_{jmin}, \varepsilon_{jmax}], a, \varepsilon$ denote to the amount of locations, intervals, and ensembles of parameter combinations.

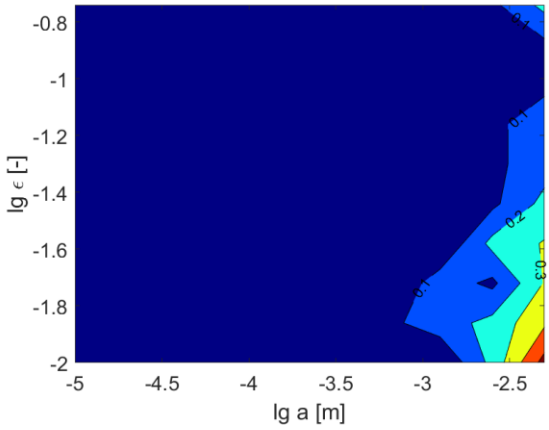

Figure 3.8. Probability that a parameter combination of aperture and porosity covers all sampled locations and can be used as an effective value; please mind the logarithmic scale of the axes.

The probability values computed this way are depicted in Fig. 3.8. No single parameter combination covers all measurements. There is a general trend of increasing probability towards larger apertures and lower porosities referring to the low reaction capacity. The apertures less than 1 mm are leading to a good fit only in single locations, whereas for larger apertures, almost every porosity value can provide a good fit at least in one location. This highlights the significance of the

aperture and underscores the potential for improvement by investigating possible fracture aperture distributions across the catchment.

3.5. CONCLUSIONS

In this modelling study, Gaussian Processes Emulation was applied in a four-dimensional parametric space for stochastic multiobjective optimization of the isotope data in the fractured limestone aquifer. Single fracture models of ^{3}H, ^{3}He, ^{4}He, and ^{39}Ar were used together with the γ-*PDF* of the travel time to stochastically estimate transport parameters (aperture, porosity, mean travel time, and the shape parameter of the γ-*PDF*) at every sampled location. The objective was to evaluate the mean travel time in each location and to examine the hypothesis that an analytical estimate based on the tritium/helium ratio would deviate from the advective travel time. To achieve this, a single fracture reactive transport model was used to calibrate the advective travel time in each sampled location based on the available measurements. Considering that the problem is four-dimensional meaning that four parameters are unknown, the calibration was done in a stochastic way.

Most of the locations in the Ammer catchment reflect the travel time of 10-30 years with only a few outliers to younger and older mean travel times. $^{3}H/He$ model alone often (but not always) provides a good guess about the transport and mixing parameters. Considering the second and third tracer helps to reduce the uncertainty in the mean travel time by 2-5 times and to get rid of double peaks (to reach unimodality of the posterior histogram). The measurement of ^{39}Ar helped to improve the calibration in the Breitenholz location.

In the majority of the locations, groundwater is captured from the micritic limestone with the porosity less than 5%. Although posterior parameter distributions highlight quite wide ranges of possible apertures and porosities within a location, the effective combination of a porosity and aperture which would fit all the observations in the catchment, was not found.

Additional measurements such as time series of tritium or helium concentrations, although often lead to a better result, do not always guarantee a significant improvement in calibration. To improve the calibration results, the optimal solution seems to be decreasing problem dimensionality, meaning, fixing some parameters or

narrowing down parameter ranges. For example, fracture aperture has also high variability within three orders of magnitude. This suggests aperture measurements to be promising fieldwork to perform in order to improve the calibration quality.

Acknowledgments

Financial support for this research was provided by the DFG (German Research Foundation) through the Research Training Group ‘Integrated Hydrosystem Modelling’ (GRK 1829/2) and through the Collaborative Research Center CAMPOS (SFB 1253/1).

REFERENCES

Abbott, B. W., Baranov, V., Mendoza-Lera, C., Nikolakopoulou, M., Harjung, A., Kolbe, T., Balasubramanian, M. N., Vaessen, T. N., Ciocca, F., Campeau, A., Wallin, M. B., Romeijn, P., Antonelli, M., Gonçalves, J., Datry, T., Laverman, A. M., de Dreuzy, J. R., Hannah, D. M., Krause, S., Oldham, C. and Pinay, G. (2016) 'Using multi-tracer inference to move beyond single-catchment ecohydrology', *Earth-Science Reviews*, 160, pp. 19-42. doi: 10.1016/j.earscirev.2016.06.014.

Aeschbach-Hertig W, Peeters F, Beyerle U, and Kipfer R (1999) Interpretation of dissolved atmospheric noble gases in natural waters. *Water Resour. Res*. 35(9), 2779-2792.

Aeschbach-Hertig W, Peeters F, Beyerle U, and Kipfer R (2000) Palaeotemperature reconstruction from noble gases in ground water taking into account equilibration with entrapped air. *Nature* 405, 1040-1044.

Aeschbach-Hertig W., Beyerle U, Holocher J, Peeters F, and Kipfer R (2002) Excess air in groundwater as a potential indicator. In International Conference on Study of environmental change using isotope techniques (IAEA-CN-80/29), pages 174-183.

Aeschbach-Hertig W, El-Gamal H, Wieser M, and Palcsu L (2008) Modeling excess air and degassing in groundwater by equilibrium partitioning with a gas phase. *Water Resour. Res*. 44, W08449. doi:10.1029/2007WR006454

Asher, M ., Croke, B. F. W., Jakeman, A. J. and Peeters, L. J. M. (2015) 'A review of surrogate models and their application to groundwater modeling', *Water Resources Research*, 51(46), pp. 5957–5973. doi: 10.1002/2015WR016967.

Atchley, A. L., Maxwell, R. M. and Navarre-Sitchler, A. K. (2013) 'Using streamlines to simulate stochastic reactive transport in heterogeneous aquifers: Kinetic metal release and transport in CO2 impacted drinking water aquifers', *Advances in Water Resources*, 52, pp. 93–106. doi: 10.1016/j.advwatres.2012.09.005.

Castro, M. C., Stute, M. and Schlosser, P. (2000) 'Comparison of 4He ages and 14C ages in simple aquifer systems: Implications for groundwater flow and chronologies', *Applied Geochemistry*, 15(8), pp. 1137–1167. doi: 10.1016/S0883-2927(99)00113-4.

Cirpka, O. A., Fienen, M. N., Hofer, M., Hoehn, E., Tessarini, A., Kipfer, R. and Kitanidis, P. K. (2007) 'Analyzing bank filtration by deconvoluting time series of electric conductivity', *Ground Water*, 45(3), pp. 318–328. doi: 10.1111/j.1745-6584.2006.00293.x.

Cirpka, O. A. and Kitanidis, P. K. (2000) 'An advective-dispersive stream tube approach for the transfer of conservative-tracer data to reactive transport', *Water Resources Research*, 36(5), pp. 1209–1220. doi: 10.1029/1999WR900355.

Cirpka, O. A. and Valocchi, A. J. (2016) 'Debates—Stochastic subsurface hydrology from theory topractice: Does stochastic subsurface hydrology help solvingpractical problems of contaminant hydrogeology?', *Journal of the American Water Resources Association*, 5(3), pp. 2–2. doi: 10.1111/j.1752-1688.1969.tb04897.x.

Cox, M. H., Su, G. W. and Constantz, J. (2007) 'Heat, chloride, and specific

conductance as ground water tracers near streams', *Ground Water*, 45(2), pp. 187–195. doi: 10.1111/j.1745-6584.2006.00276.x.
Cvetkovic, V., Fiori, A. and Dagan, G. (2016) 'Tracer travel and residence time distributions in highly heterogeneous aquifers: Coupled effect of flow variability and mass transfer', *Journal of Hydrology*, 543, pp. 101–108. doi: 10.1016/j.jhydrol.2016.04.072.
Cvetkovic, V. and Frampton, A. (2010) 'Transport and retention from single to multiple fractures in crystalline rock at Äspö (Sweden): 2. Fracture network simulations and generic retention model', *Water Resources Research*, 46(5), pp. 1–17. doi: 10.1029/2009WR008030.
Cvetkovic, V., Selroos, J. O. and Cheng, H. (1999) 'Transport of reactive tracers in rock fractures', 378, pp. 335–356.
D'Affonseca, F. M., Finkel, M. and Cirpka, O. A. (2020) 'Combining implicit geological modeling, field surveys, and hydrogeological modeling to describe groundwater flow in a karst aquifer', *Hydrogeology Journal*. doi: 10.1007/s10040-020-02220-z.
Dagan, G. and Cvetkovic, V. (1996) 'Reactive transport and immiscible flow in geological media', *Proc. R. Soc. London*, pp. 285–301. doi: 10.1098/rspa.1996.0016.
Dagan, G. and Nguyen, V. (1989) 'A comparison of travel time and concentration approaches to modeling transport by groundwater', *Journal of Contaminant Hydrology*, 4, pp. 79–91.
Ebser SC (2018) Dating of ice and ocean samples with Atom Trap Trace Analysis of ^{39}Ar. PhD thesis (Heidelberg University, Heidelberg, Germany).
Erdal, D. and Cirpka, O. A. (2019) 'Global sensitivity analysis and adaptive stochastic sampling of a subsurface-flow model using active subspaces', *Hydrology and Earth System Sciences*, 23(9), pp. 3787–3805. doi: 10.5194/hess-23-3787-2019.
Erdal, D., Xiao, S., Nowak, W. and Cirpka, O. A. (2020) 'Sampling behavioral model parameters for ensemble-based sensitivity analysis using Gaussian process emulation and active subspaces', *Stochastic Environmental Research and Risk Assessment*, 34(11), pp. 1813–1830. doi: 10.1007/s00477-020-01867-0.
Feng Z, Bohleber P, Ebser S., Ringen L, Schmidt M, Kersting A, Hopkins P, Hoffmann H, Fischer A, Aeschbach W, and Oberthaler MK (2019) Dating glacier ice of the last millennium by quantum technology. PNAS 116(18), 8781-8786.
Fuenfgeld, F. (2020) Tritium-Helium Dating of Groundwater in the Fractured and Karstified Muschelkalk Aquifer of the Ammer Catchment.
Gardner, W. P., Hokr, M., Shao, H., Balvin, A., Kunz, H. and Wang, Y. (2016) 'Investigating the age distribution of fracture discharge using multiple environmental tracers, Bedrichov Tunnel, Czech Republic', *Environmental Earth Sciences*, 75(20), pp. 1–16. doi: 10.1007/s12665-016-6160-x.
Gardner P, and Solomon DK (2009) An advanced passive diffusion sampler for the determination of dissolved gas concentrations. *Water Resour Res* 45(6), W06423. doi: 10.1029/2008WR007399
Goode, D. J. (1996) 'Direct simulation of groundwater age', *Water Resources Research*, 32(2), pp. 289–296. doi: 10.1029/95WR03401.
Grabczak J, Rózański K, Maloszewski P,and Zuber A (1984) Estimation of the tritium input function with the aid of stable isotopes. Catena 11, 105-114.

Grigoriev N.A. Chemical element distribution in the upper continental crust. Ekaterinburg: UB RAS, 2009.
Hawkins D. Theory of Games and Economic Behavior. Philosophy of Science. 1945;12(3):221-227. doi:10.1086/286866
Heaton THE, and Vogel JC (1981) “Excess air” in groundwater. *J. Hydrol* 50, 201-216.
Hrachowitz, M., Soulsby, C., Tetzlaff, D., Malcolm, I. A. and Schoups, G. (2010) ‘Gamma distribution models for transit time estimation in catchments : Physical interpretation of parameters and implications for time - variant transit time assessment’, 46. doi: 10.1029/2010WR009148.
Jutebring Sterte, E., Lidman, F., Lindborg, E., Sjöberg, Y. and Laudon, H. (2020) ‘Linking groundwater travel times to stream chemistry, isotopic composition and catchment characteristics’, *Hydrology and Earth System Sciences Discussions*, (April), pp. 1–23. doi: 10.5194/hess-2020-121.
LaBolle, E. M., Fogg, G. E. and Eweis, J. B. (2006) ‘Diffusive fractionation of 3H and 3He in groundwater and its impact on groundwater age estimates’, *Water Resources Research*, 42(7), pp. 1–11. doi: 10.1029/2005WR004756.
Laloy, E. and Jacques, D. (2019) ‘Emulation of CPU-demanding reactive transport models: a comparison of Gaussian processes, polynomial chaos expansion, and deep neural networks’, *Computational Geosciences*, 23(5), pp. 1193–1215. doi: 10.1007/s10596-019-09875-y.
Loschko, M., Wöhling, T., Rudolph, D. L. and Cirpka, O. A. (2016) ‘Cumulative relative reactivity: A concept for modeling aquifer-scale reactive transport’, *Water Resources Research*, 52(10), pp. 8117–8137. doi: 10.1002/2016WR019080.
Luo, J. and Cirpka, O. A. (2008) ‘Travel time-based descriptions of transport and mixing in heterogeneous domains’, *Water Recourses Research,* 44(May), pp. 1–16. doi: 10.1029/2007WR006035.
MacQuarrie, K. T. B., Mayer, K. U., Jin, B. and Spiessl, S. M. (2010) ‘The importance of conceptual models in the reactive transport simulation of oxygen ingress in sparsely fractured crystalline rock’, *Journal of Contaminant Hydrology*, 112(1), pp. 64–76. doi: 10.1016/j.jconhyd.2009.10.007.
Mcguire, K. J. and Mcdonnell, J. J. (2006) ‘A review and evaluation of catchment transit time modeling’, pp. 543–563. doi: 10.1016/j.jhydrol.2006.04.020.
Meng, S., Liu, L., Mahmoudzadeh, B., Neretnieks, I. and Moreno, L. (2018) ‘Solute transport along a single fracture with a finite extent of matrix: A new simple solution and temporal moment analysis’, *Journal of Hydrology*, 562(May), pp. 290–304. doi: 10.1016/j.jhydrol.2018.05.016.
Molins, S., Trebotich, D., Arora, B., Steefel, C. I. and Deng, H. (2019) ‘Multi-scale Model of Reactive Transport in Fractured Media: Diffusion Limitations on Rates’, *Transport in Porous Media*, 128(2), pp. 701–721. doi: 10.1007/s11242-019-01266-2.
Neumann, R. B., Labolle, E. M. and Harvey, C. F. (2008) ‘The effects of dual-domain mass transfer on the tritium-helium-3 dating method’, *Environmental Science and Technology*, 42(13), pp. 4837–4843. doi: 10.1021/es7025246.
Osenbrück, K., Blendinger, E., Leven, C., Rügner, H., Finkel, M., Jakus, N., Schulz, H. and Grathwohl, P. (2021) ‘Nitrate reduction potential of a fractured Middle Triassic carbonate 1 aquifer in southwest Germany’, (0123456789).
Osenbrück, K., Lippmann, J. and Sonntag, C. (1998) ‘Dating very old pore waters in

impermeable rocks by noble gas isotopes', *Geochimica et Cosmochimica Acta*, 62(18), pp. 3041–3045. doi: 10.1016/S0016-7037(98)00198-7.
Owen, N. E., Challenor, P., Menon, P. P. and Bennani, S. (2017) 'Comparison of Surrogate-Based Uncertainty Quantification Methods for Computationally Expensive Simulators', *SIAM/ASA Journal on Uncertainty Quantification*, 5(1), pp. 403–435. doi: 10.1137/15m1046812.
Palermo, D., Aigner, T., Nardon, S. and Blendinger, W. (2010) 'Three-dimensional facies modeling of carbonate sand bodies: Outcrop analog study in an epicontinental basin (Triassic, southwest Germany)', *AAPG Bulletin*, 94(4), pp. 475–512. doi: 10.1306/08180908168.
Rajabi, M. M. and Ketabchi, H. (2017) 'Uncertainty-based simulation-optimization using Gaussian process emulation: Application to coastal groundwater management', *Journal of Hydrology*, 555(April 2018), pp. 518–534. doi: 10.1016/j.jhydrol.2017.10.041.
Ring U, Bolhar R (2020) Tilting, uplift, volcanism and disintegration of the South German block. *Tectonophysics* 795:228611. doi: 10.1016/j.tecto.2020.228611
Ritterbusch F, Ebser S., Welte J., Reichel T, Kersting A, Purtschert R, Aeschbach-Hertig W, and Oberthaler MK (2014) Groundwater dating with Atom Trap Trace Analysis of ^{39}Ar. Geophys Res Lett 41, 6758-6764.
Sanz-Prat, A., Lu, C., Amos, R. T., Finkel, M., Blowes, D. W. and Cirpka, O. A. (2016) 'Exposure-time based modeling of nonlinear reactive transport in porous media subject to physical and geochemical heterogeneity', *Journal of Contaminant Hydrology*, 192, pp. 35–49. doi: 10.1016/j.jconhyd.2016.06.002.
Sanz-Prat, A., Lu, C., Finkel, M. and Cirpka, O. A. (2015) 'On the validity of travel-time based nonlinear bioreactive transport models in steady-state flow', *Journal of Contaminant Hydrology*, 175–176, pp. 26–43. doi: 10.1016/j.jconhyd.2015.02.003.
Schauer, M. and Aigner, T. (1997) 'Cycle stacking pattern, diagenesis and reservoir geology of peritidal dolostones, Trigonodus-Dolomite, Upper Muschelkalk (Middle Triassic, SW-Germany)', *Facies*, 37(1), pp. 99–113. doi: 10.1007/BF02537373.
Schlosser, P., Stute, M., Dörr, H., Sonntag, C. and Münnich, K. O. (1988) 'Tritium/3He dating of shallow groundwater', *Earth and Planetary Science Letters*, 89(3–4), pp. 353–362. doi: 10.1016/0012-821X(88)90122-7.
Schmidt A, Frank G, Stichler W, Duester L, Steinkopff T, and Stumpp C (2020) Overview of tritium records from precipitation and surface waters in Germany. *Hydrol Proc* 34(6), 1489-1493.
Sidborn, M. and Neretnieks, I. (2007) 'Long term redox evolution in granitic rocks: Modelling the redox front propagation in the rock matrix', *Applied Geochemistry*, 22(11), pp. 2381–2396. doi: 10.1016/j.apgeochem.2007.05.007.
Solomon, D. K. (2000) '4He in Groundwater', in Cook, P. G. and Herczeg, A. L. (eds) *Environmental Tracers in Subsurface Hydrology*. Boston, MA: Springer US, pp. 425–439. doi: 10.1007/978-1-4615-4557-6_14.
Solomon DK, and Cook PG (2000) ^{3}H and ^{3}He. In: Environmental Tracers in Subsurface Hydrology, Cook PG, Herczeg AL (eds). Kluwer Academic Publishers, Boston, 397-424.

Stumpp C, Klaus J, and Stichler W (2014) Analysis of long-term stable isotopic composition in German precipitation. *J Hydrol* 517, 351-361.

Sültenfuß J., Roether W, and Rhein M (2004) The Bremen mass spectrometric facility for the measurement of helium isotopes, neon, and tritium in water. In: International Symposium on Quality Assurance for Analytical Methods in Isotope Hydrology, International Atomic Energy Agency, Vienna.

Su, D., Xie, M., Mayer, K. U. and Kerry, T. B. (2017) 'MIN3P-THCm User Manual for Parallel Configuration – Draft'.

Tang, D. H., Frind, E. O. and Sudicky, E. A. (1981) 'Contaminant transport in fractured porous media: Analytical solution for a single fracture', *Water Resources Research*, 17(3), pp. 555–564. doi: 10.1029/WR017i003p00555.

Trinchero, P., Delos, A., Molinero, J., Dentz, M. and Pitkänen, P. (2014) 'Understanding and modelling dissolved gas transport in the bedrock of three Fennoscandian sites', *Journal of Hydrology*, 512, pp. 506–517. doi: 10.1016/j.jhydrol.2014.03.011.

Trinchero, P., Sidborn, M., Puigdomenech, I., Iraola, A., Bosbach, D. and Deissmann, G. (2019a) 'Groundwater age dating in fractured rock using 4He data', *Journal of Hydrology X*, 4(April), p. 100036. doi: 10.1016/j.hydroa.2019.100036.

Trinchero, P., Sidborn, M., Puigdomenech, I., Iraola, A., Bosbach, D. and Deissmann, G. (2019b) 'Groundwater age dating in fractured rock using 4He data', *Journal of Hydrology X*, 4(July), p. 100036. doi: 10.1016/j.hydroa.2019.100036.

Visser, A., Broers, H. P., Purtschert, R., Sültenfuß, J. and De Jonge, M. (2013) 'Groundwater age distributions at a public drinking water supply well field derived from multiple age tracers (85Kr, 3H/ 3He, and 39Ar)', *Water Resources Research*, 49(11), pp. 7778–7796. doi: 10.1002/2013WR014012.

Visser, A., Fourré, E., Barbecot, F., Aquilina, L., Labasque, T., Vergnaud, V. and Esser, B. K. (2014) 'Intercomparison of tritium and noble gases analyses, 3H/3He ages and derived parameters excess air and recharge temperature', *Applied Geochemistry*, 50, pp. 130–141. doi: 10.1016/j.apgeochem.2014.03.005.

Visser A, Broers HP, and Bierkens MFP (2007) Dating degassed groundwater with $^{3}H/^{3}He$, Water Resour. Res. 43, WR10434. doi:10.1029/2006WR005847

Wersin, P., Soler, J. M., Van Loon, L., Eikenberg, J., Baeyens, B., Grolimund, D., Gimmi, T. and Dewonck, S. (2008) 'Diffusion of HTO, Br-, I-, Cs+, 85Sr2+ and 60Co2+ in a clay formation: Results and modelling from an in situ experiment in Opalinus Clay', *Applied Geochemistry*, 23(4), pp. 678–691. doi: 10.1016/j.apgeochem.2007.11.004.

Widory, D., Kloppmann, W., Chery, L., Bonnin, J., Rochdi, H. and Guinamant, J. L. (2004) 'Nitrate in groundwater: An isotopic multi-tracer approach', *Journal of Contaminant Hydrology*, 72(1–4), pp. 165–188. doi: 10.1016/j.jconhyd.2003.10.010.

APPENDIX 3.1. CONSIDERATIONS ABOUT THE ANALYTICAL TRAVEL TIME DISTRIBUTION

The travel time function to be defined by Gamma distribution (Hrachowitz et al., 2010):

$$f_i(,\alpha,b) = \frac{^{b-1}}{\alpha^b \Gamma(b)} e^{\frac{-\tau}{\alpha}} \quad \text{(A1)}$$

where $\underline{\tau_i}$ and b refer to the mean travel time at the location i, and the shape parameter of the gamma function $\Gamma(b)$:

$$\Gamma(b) = \int_0^\infty \quad e^{-\tau} \quad ^{b-1} d\tau. \quad \text{(A2)}$$

The unknown shape parameter b and the scale parameter α of the gamma distribution are related to each other via the distribution's mean value $\underline{f_i} = \underline{\tau_i} = \alpha_i\, b_i$. That means that travel time distribution in a location *i* is defined through two parameters: mean travel time and shape parameter:

$$f_i\left(,\underline{\tau_i}, b\right) = \frac{^{(b-1)}}{\left(\frac{\tau_i}{b}\right)^b \Gamma(b)} e^{\frac{-\tau b}{\underline{\tau_i}}}, \quad \text{(A3)}$$

Since the gamma distribution looks only realistic when the shape parameter $b_i < \underline{\tau_i}$, we use additional conditioning to account for this.

APPENDIX 3.2. VERIFICATION OF THE TRITIUM-HELIUM MODEL

Tritium/helium measurement is one of the most commonly used methods for groundwater age estimates (Visser et al., 2013). Following the idea of purely advective transport in the flow path, the groundwater age is typically derived from concentrations of tritium and produced by its decay helium (Schlosser et al., 1988).

$$\tau = \frac{1}{\lambda} ln \left(1 + \frac{^3He}{^3H}\right) \quad \text{(A4)}$$

where λ denotes the radioactive decay constant for tritium and is calculated from its half-life of 12.43 years as $\lambda = \ln(2)/T_{1/2}$, corresponding concentrations of tritium and helium are given in TU.

In aquifers with considerable diffusive exchange, in fact, analytically computed groundwater ages are known to deviate from the advective groundwater age in fractures (Neumann et al., 2008). To confirm this effect of diffusive exchange in fractured aquifer on the GW age estimation reported, e.g., by LaBolle et al. (2006)

and Neumann et al. (2008), a reference travel time-based model was set up using the MIN3P numerical model (Su et al., 2017). Verification of ^{3}H and ^{3}He transport was based on the analytical solution of Tang et al. (1981) (Appendix 2). Typical parameters of the fractured aquifer (a = 0.2 mm, ε = 1%) and diffusion coefficients of ^{3}H and ^{3}He according to LaBolle et al. (2006) were used (D_{3H} = 2.2e^{-9} m^2/s, D_{He} = 8.2e^{-9} m^2/s). The transient input concentration of ^{3}H was implemented in MIN3P as a transient boundary condition with 68 annual values (Fig. A.2.1).

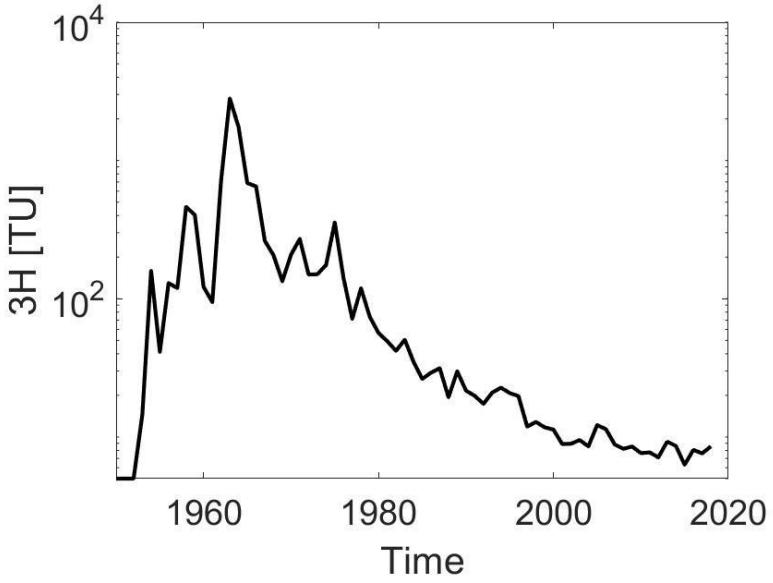

Figure A.3.2.1. Input function of tritium in the Muschelkalk aquifer, Stuttgart meteostation (Fuenfgeld, 2020)

Four single fracture tritium-helium models of increasing complexity were implemented in MIN3P (table 1): (i) advection only, (ii) matrix diffusion and constant input of tritium, (iii) different diffusion coefficients of tritium and helium, and (iv) the real function of tritium (Fig.A.2.1). Figure A.2.2 shows analytically computed ages (eq. 4) vs. the "true" advective groundwater travel times in the fracture for every model.

Setting up the model

Batch reaction – Validation with analytical solution

The radioactive decay of tritium was implemented in the MIN3P database. Results were verified with analytical solution.

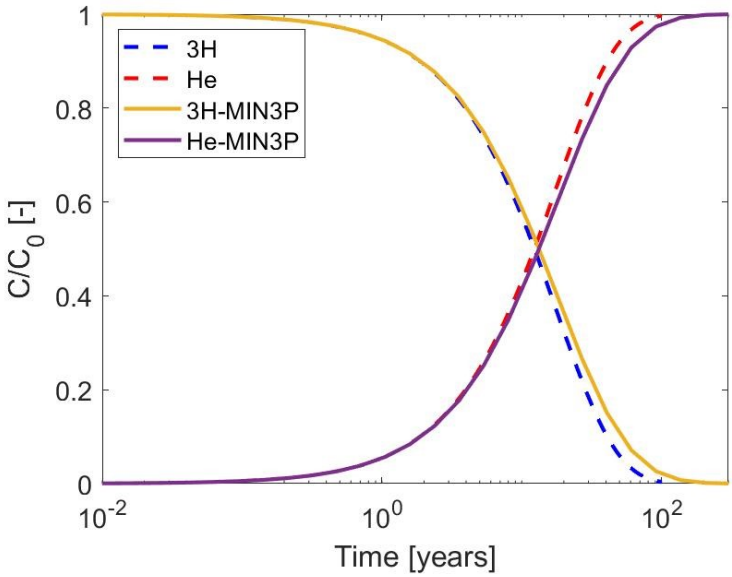

Figure A.3.2.2. Validation of the MIN3p to the analytical solution of the ^{3}H radioactive decay.

2D transport with constant diffusion coefficient, equal for all the species in the model – validation with the analytical solution (Tang et al., 1981).

On this stage, advective-diffusive transport of the decaying ^{3}H was implemented. Assuming no sorption and unlimited matrix, the equation for the fracture:

$$\frac{\partial c}{\partial t} + v\frac{\partial c}{\partial z} - D\frac{\partial^2 c}{\partial z^2} + \lambda c + \frac{q}{b} = 0 \quad \text{(A5)}$$

Initial condition:

$C(z,0) = 0$

Boundary conditions:

$C(0,t) = c_0$

$C(\infty,t) = 0$

The analytical solution (Tang et al., 1981) for ^{3}H (as a solute not undergoing sorption) if longitudinal dispersion in the fracture is neglected – is:

$$\frac{C}{C_0} = 0.5\exp\left(-\frac{\lambda \cdot z}{v}\right)\cdot\left[\exp\left(-\frac{z\cdot\lambda^{\frac{1}{2}}}{v\cdot A}\right)erfc\left(\frac{z}{2\cdot v\cdot A\cdot T'} - \lambda^{\frac{1}{2}}T'\right)\right.$$

$$\left. + \exp\left(\frac{z\cdot\lambda^{\frac{1}{2}}}{v\cdot A}\right)erfc\left(\frac{z}{2\cdot v\cdot A\cdot T'} + \lambda^{\frac{1}{2}}T'\right)\right] \quad \text{(A6)}$$

where

$$\lambda = \ln(2)/12.3 = 0.0564\ \text{a}^{-1} \quad \text{(A7)}$$

$$T' = (t - \frac{z}{v})^{1/2} \quad \text{(A8)}$$

$$A = \frac{b}{\varepsilon\,(D\prime)^{1/2}} \quad \text{(A9)}$$

and

$$D' = \tau\, D^* \quad \text{(A10)}$$

v (L/T) is the groundwater velocity in the fracture, b (L) is the half-aperture of the fracture, D' (L^2/T) is the effective diffusion coefficient, ε (-) is the matrix porosity, τ (-) is the tortuosity of the matrix pores, and D^* (L^2/T) is the molecular diffusion coefficient in water.

As shown in Figure A.3.2.3, the model validation at this step is sufficient. The differences decrease with increasing advective travel time. On the yearly stages, the difference up to 10 % appears.

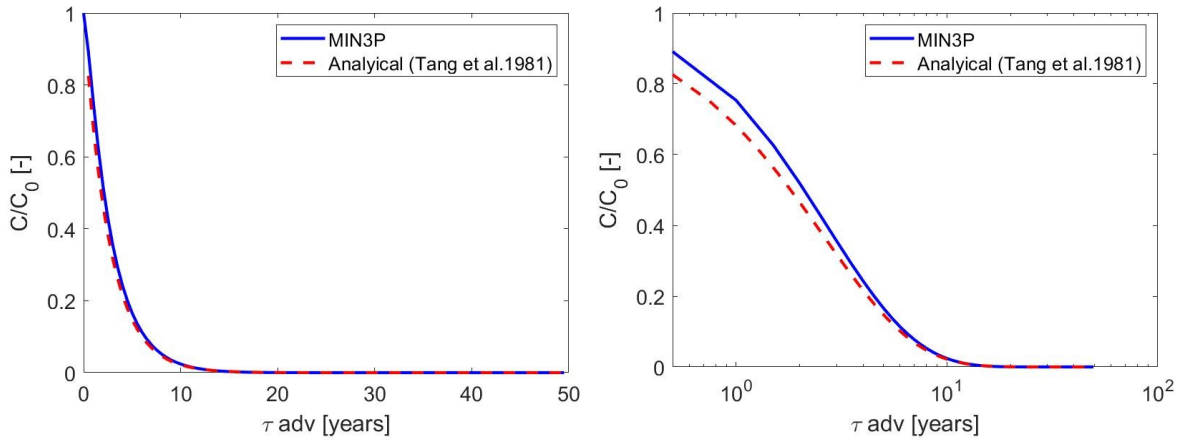

Figure A.3.2.3. Verification of the MIN3P model with the analytical solution of the ^{3}H radioactive decay (same data, plot with different scale on abscissa)

Table A.3.2.1. Conceptual model scenarios of tritium and helium transport in the fracture

Case	Advective flow	Matrix diffusion	Species-specific diffusion coefficients	Transient tritium input	Colour code
1	+				**Black**
2	+	+			**Red**
3	+	+	+		**Green**
4	+	+	+	+	**Blue**

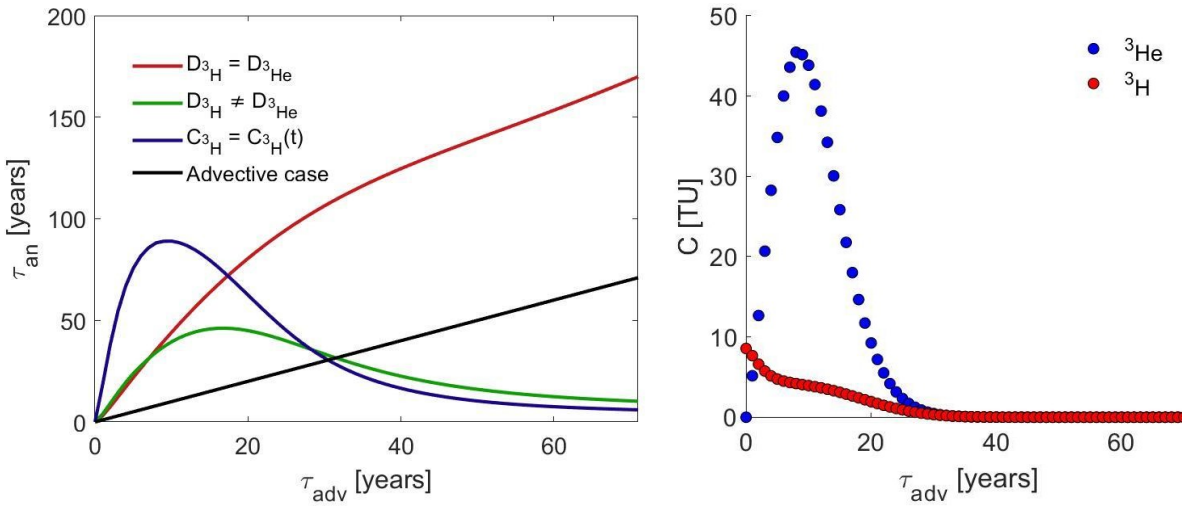

Figure A.3.2.4. Left: comparison of the advective travel times in the fracture with analytical estimates for different models; right: reactive curves of tritium and helium in (a = 0.2 mm, ε = 1 %, D_{3H} = 2.2e^{-9} m^2/s, D_{He} = 8.2e^{-9} m^2/s, and the real input function of ^{3}H).

If different diffusion coefficients for tritium and helium are implemented (green line) then the analytically derived groundwater age is not unique. Later on, the difference in the diffusion coefficients (D_{He}/D_{3H} = 3.7) leads to a decrease in the estimated travel time. When introducing the transient tritium input (blue line), the effect of the latter is coupled with the input concentration variations leading to decreasing analytical travel time with age as reported before by Neumann et al. (2008). These results highlight the necessity to apply direct modelling with matching ^{3}H and He to the measured values instead of using the analytical solution.

APPENDIX 3. DATASET OF THE ISOTOPE MEASUREMENTS IN DIFFERENT LOCATIONS ACROSS THE AMMER CATCHMENT USED FOR THE MODELLING

Site	Longitude	Latitude	year	^{3}H	σ ^{3}H	^{3}He	σ ^{3}He	^{4}He	σ ^{4}He
ArtA	3492682.03	5380614.78	2017	4.9	0.3	22.8	2.4	3.9E-08	6.0E-09
ArtA	3492682.03	5380614.78	2004	9.8	1.8				
TBEnt1	3497370.36	5378062.64	2011	6.0	0.9	6.6	1.9	1.1E-08	4.5E-09
TBEnt1	3497370.36	5378062.64	2004	10.2	1.5				
TBEnt1	3497370.36	5378062.64	2014	6.0	0.3				
TBEnt2	3497336.58	5378005.83	2011	7.2	1.1	8.6	1.8	1.5E-08	4.5E-09
TBEnt2	3497336.58	5378005.83	2004	11.6	2.0				
TBEnt2	3497336.58	5378005.83	2018	4.7	0.3	7.2	2.0	1.0E-08	4.5E-09
TBPol1	3496810.90	5377126.07	2011	9.1	1.4	9.8	1.8	3.0E-09	4.0E-09
TBPol1	3496810.90	5377126.07	2004	16.5	2.7				
TBPol1	3496810.90	5377126.07	2006	14.1	1.5				
TBPol1	3496810.90	5377126.07	2007	11.9	1.5				
TBPol1	3496810.90	5377126.07	2018	5.5	0.3				
TBPol2	3496925.00	5377080.00	2018	5.2	0.3	8.5	1.8	7.0E-09	4.5E-09
TBPol2	3496925.00	5377080.00	2004	14.4	2.1				
TBPol2	3496925.00	5377080.00	2006	13.8	1.5				
TBPol2	3496925.00	5377080.00	2007	10.6	1.5				
TBPol2	3496925.00	5377080.00	2011	8.4	1.3	11.4	2.0	8.0E-09	4.5E-09
TBAlt3	3493648.85	5379699.97	2004	13.4	2.1				
TBAlt3	3493648.85	5379699.97	2011	6.9	1.1	18.8	3.0	2.5E-08	9.0E-09
TBAlt3	3493648.85	5379699.97	2018	4.8	0.3	14.8	3.2	2.1E-08	9.0E-09
TBBrhz	3496407.00	5380889.00	2004	5.6	1.7				
TBBrhz	3496407.00	5380889.00	2012	3.7	0.7	23.0	4.1	1.7E-08	1.1E-08
TBBrhz	3496407.00	5380889.00	2018	2.8	0.2	23.0	3.8	2.0E-08	1.1E-08
Bon3	3484967.90	5376426.76	2018	2.8	0.2	12.9	2.9	8.0E-09	9.0E-09
AMQ	3489251.00	5382948.00	2007	9.3	1.1				
AMQ	3489251.00	5382948.00	2012	7.2	1.2	1.9	1.2	1.3E-08	3.0E-09
Sul4	3484912.40	5387175.60	2014	6.1	0.3	0.9	3.0	1.0E-09	7.5E-09
Sul4	3484912.40	5387175.60	2018	5.8	0.3	0.0	2.6	1.0E-09	9.0E-09
TBAlt2	3493648.27	5379447.88	2018	5.1	0.3				
PWHrbg	3489809.00	5383047.00	2012	7.6	1.4	2.9	1.4		
PWGül	3490730.01	5381558.55	2018	5.8	0.3	1.5	3.3		
PWReu			2006	11.2	0.8				
Sul1	3485385.60	5387180.00	2014	6.1	0.3	2.3	2.5		
Sul1	3485385.60	5387180.00	2018	5.5	0.3	1.5	4.8		
Sul2a	3485717.00	5386562.00	2018	4.5	0.8				
Sul3	3484978.60	5386458.50	2014	5.9	0.3	0.2	1.7		
Sul3	3484978.60	5386458.50	2018	6.0	0.3				

Sul5	3485158.00	5386184.20	2018	5.5	0.3				
Sul7	3484504.00	5387507.00	2014	5.7	0.3				
Sul8	3485154.00	5386572.00	2018	5.8	0.3	0.7	3.0		
Has1	3487922.00	5383608.00	2014	5.4	0.4	3.2	1.8		
Has1	3487922.00	5383608.00	2018	4.2	0.4				
Has2	3488400.00	5383702.00	2014	5.0	0.4	1.7	1.8		
Has3a	3488499.50	5383250.40	2018	4.3	0.3	14.1	4.1	7.0E-09	1.4E-08
Has4	3488539.50	5383429.60	2014	4.7	0.3	16.6	3.3	6.0E-09	9.0E-09
Has4	3488539.50	5383429.60	2018	4.5	0.4	7.6	2.9		
Has5	3488067.40	5383612.30	2014	6.1	0.4	5.8	1.8		
Has5	3488067.40	5383612.30	2018	5.0	0.4	6.0	3.0		
Has6	3488002.70	5383430.70	2014	5.2	0.4	4.7	2.6		
Möz1	3482492.47	5378234.70	2018	6.2	0.4	0.4	2.7		
Möz2	3482352.60	5378841.30	2018	5.4	0.8				
Möz3	3482941.10	5378765.30	2018	5.1	0.3	16.0	2.3	9.0E-09	6.0E-09
Möz4	3482935.90	5378006.90	2018	4.8	0.3	5.6	2.1	3.0E-09	6.0E-09

.

4. LEGACY POLLUTANTS IN FRACTURED AQUIFERS: ANALYTICAL APPROXIMATIONS FOR BACK DIFFUSION TO PREDICT ATRAZINE CONCENTRATIONS UNDER UNCERTAINTY

Abstract

We present novel analytical approximations for the estimation of travel distance and relative height of solute concentration peaks within a single fracture system for pollutants that have been temporarily applied at a constant rate in the past. These approximations are used to investigate the spatiotemporal evolution of the concentration of atrazine, as an example for many other so-called legacy compounds that are still found in the groundwater of fractured rock aquifers even decades after their application has stopped. This is done in a stochastic framework to account for the uncertainty in relevant parameters, focusing on probabilities of exceeding the given legal concentration limit and the expected length of the recovery period. We specifically consider the properties of the Muschelkalk limestone aquifer in the Ammer river catchment in SW Germany, and the three major types of carbonate rock facies: Shoal, Tempestite, and Basinal limestones. Atrazine sorption parameters have been determined in laboratory experiments. The simulations confirm that diffusion-limited sorption and desorption may cause considerable atrazine levels long after application stop. For the properties of the considered rock facies types, and corresponding parameter ranges, atrazine concentration above the legal limit is supposed to be limited to locations referring to only a few years of travel time. If the concentration exceeds the legal limit by the year 2022, it will take decades to centuries until recovery.

* Reproduced from: Petrova, E., Meierdierks, J., Finkel, M., Grathwohl, P. (2023) Legacy pollutants in fractured aquifers: analytical approximations for back diffusion to predict atrazine concentrations under uncertainty, *Journal of Contaminant Hydrology*, doi.org: 10.1016/j.jconhyd.2023.104161

4.1. INTRODUCTION

Groundwater is a major source of public drinking water supplies and plays a key role in sustaining human life in many regions of the world. The quality of groundwater is at risk due to human activities and possible inputs of environmentally hazardous compounds. Today, a large variety of anthropogenic compounds is being found in groundwater. Among these compounds, there is a range of so-called legacy contaminants, including pesticides, e.g., herbicides such as atrazine, which are often detected in groundwater samples even decades after application stop (Farlin et al. 2022; Gutierrez and Baran, 2009; Lapworth et al. 2015; Loos et al. 2010; McKnight and Finkel, 2013; Stuart et al. 2012). Often these compounds show no or negligible degradation or transformation in groundwater but may undergo significant sorption during transport (e.g., Ammann et al. 2019; Beegum et al. 2020; Bertuzzo et al. 2013; Reberski et al. 2022). Sorption leads to the storage of pollutants in the subsurface long after the application has stopped (Pietrzak et al. 2020; Roulier et al. 2006), and limits their bioavailability. In fractured aquifers, concentrations of sorptive pollutants in groundwater depend on the duration of mass transfer between fractures and the rock matrix.

Slow diffusion may contribute to the lasting presence of pollutants long after input was stopped (Chapman and Parker, 2005; Farlin et al. 2022; Parker et al. 2008). Solute transport in fractured systems is typically modelled by coupling fracture flow and diffusion in the adjacent rock matrix (Rahman et al. 2004; Sidborn and Neretnieks, 2007; Sudicky and Frind, 1984; Tang et al. 1981). Propagation of a plume within a single fracture model is, e.g., described by Grisak and Pickens (1981). The adequate parameterization of a model in a deterministic manner is feasible in well controlled systems typically at a small scale with sufficient data allowing unique and stable inversion (e.g., Carrera, 1993; Carrera et al. 2005; Zhou et al. 2014). Contaminant transport in real-world fractured systems typically comes with high parameter uncertainty and a lack of data (Lindahl et al. 2005). As a consequence of this, Poeter and Townsend (1994) concluded that “The era of drawing conclusions on the basis of deterministic flow and transport models has come to a close.”

Stochastic methods comprise well-established mathematical tools for probabilistic predictions (Cirpka and Valocchi, 2016; Fiori et al. 2016; Tartakovsky et al. 2009).

Being developed in multiple branches of hydrogeology (e.g., Cromwell et al. 2021; Erdal and Cirpka, 2019; Hsueh et al. 2022; Jeong et al. 2020; Ramgraber et al. 2021; Riva et al. 2006; Sánchez-León et al. 2020), stochastic modeling has gained a great interest among modeling practitioners, because it acknowledges parametric or structural uncertainty, assesses the sensitivity of the model, improves the model quality, and enhances predictive capability. Typically implemented stochastic methods include Monte Carlo, Kriging (Kitanidis, 1991), Gaussian random fields (Hammond et al. 2005), hydro facies models (dell'Arciprete et al. 2012), multi-point statistics and training images.

Resulting ensembles of model outcomes are used for stochastic prediction with the uncertainty of parameters being acknowledged. One way of stochastic prediction is conditioning the model outcomes into a series of yes-no answers based on some hypothesis and classifying the model outcomes accordingly (Enemark et al. 2019). The model outcome that confirms the hypothesis reads as 1 and 0 otherwise.

In this study, stochastic simulations of solute transport within fractured sedimentary rocks are used for risk assessment with respect to legal limit concentrations of a target compound. We test the hypothesis that groundwater contamination by pesticides observed in fractured aquifers (Baran et al. 2008; Burri et al. 2019; Mali et al. 2021; McManus et al. 2017) is caused by matrix diffusion and sorption in the rock matrix. In this work, an analytical model accounting for sorption and diffusive solute exchange with the rock matrix was employed to elucidate the transport characteristics of atrazine in a fractured limestone aquifer. The sensitivity of atrazine transport on matrix properties (effective diffusion, sorption), fracture apertures, and application time periods is analysed based on simple analytical approximations for the relative maximum concentration ("peak") and corresponding location of the peak along the streamline. This allows breaking down the complexity of the sorptive compound transport and the knowledge about peak location and concentration to address the following questions for any given location in the aquifer in a stochastic way:

1. Will the concentration exceed the legal limit?
2. Will contaminant concentrations further increase or decline?
3. How long will it take to achieve the legal limit?

We consider atrazine as an example of sorptive pollutants in groundwater still being detected long after stop of application (input). Atrazine is one of the pesticides still contaminating groundwater with a trackable history of application. Soon after its discovery in 1958 (Müller, 2008), atrazine (6-Chloro-N-ethyl-N'-(1-methylethyl)-1,3,5-triazine-2,4-diamine) was among the most widely applied pesticides in agricultural use. Atrazine was used extensively as a non-selective herbicide, as a weed control component for the cultivation of maize, sorghum, and sugar cane in concentrations of ~1 kg ha^{-1}, and as a total herbicide in concentrations of up to 9 kg ha^{-1} (Tappe et al. 2002). Wide agricultural application of atrazine led to groundwater pollution exceeding the legal limit values in many countries worldwide (Nasseri et al. 2009; Silva et al. 2012; Tappe et al. 2002). In Europe, atrazine was used until the early 1990s, when it was banned or severely restricted in most European countries due to its potentially harmful properties. In Germany, atrazine has been banned since 1991. The European Water Framework Directive (WFD e 2000/60/EC, OJEC, 2000) established objectives to achieve a good qualitative and chemical status of groundwater. Nevertheless, atrazine is continuously found in groundwater decades after official ban on its application (Vonberg et al. 2014). The legal limit for all pesticides in source waters was set to 0.1 µg l^{-1} for single substances and 0.5 µg l^{-1} for the sum of pesticides incl. relevant metabolites (European Drinking Water Directive, 98/83/EEC).

Atrazine degrades in soil primarily microbially; reported half-lifes range from 13 to 261 days (Schwab et al. 2006). Atrazine undergoes slow hydrolysis; it has a moderate to low water solubility of 70 mg l^{-1} and accumulates in lipids or fat tissues (Harper et al. 2020; Pathak and Dikshit, 2012; Ross et al. 2009) and soil organic matter (Chavez Rodriguez et al. 2021; Rojas et al. 2022; Silva et al. 2012).

In this study, Atrazine sorption isotherms were measured for the four major facies types in fractured Triassic limestone aquifer (Muschelkalk, Southern Germany, Tübingen); field observations and recent work on the characterization of rock facies (Osenbrück et al. 2021) provided the model with realistic ranges of transport relevant parameters (e.g. fracture apertures and porosities).

4.2. PHYSICO-CHEMICAL PARAMETERS FOR ATRAZINE TRANSPORT IN THE UPPER MUSCHELKALK AQUIFER IN SW GERMANY

4.2.1. GEOLOGY AND ROCK PROPERTIES

The fractured limestone (Muschelkalk) aquifer is located in the river Ammer catchment in the south-west of Germany (D'Affonseca et al. 2020) and comprises an important drinking water reservoir (Osenbrück et al. 2021). The geological setting is well described in the literature (Koehrer et al. 2010; Palermo et al. 2010; Schauer and Aigner, 1997; Warnecke and Aigner, 2019) and briefly outlined here. Three major types of carbonate rock facies may be distinguished within the aquifer: Shoal, Tempestite, and Basinal limestones (Palermo et al. 2010; Schauer et al. 1997). These facies types are the result of different sedimentary and diagenetic conditions leading to different rock properties (Fig. 1). The up to 5 m thick Shoal facies contains light grey, calcareous grain- to packstone with bioclastic debris, shell fragments and intraclasts, as well as open pore spaces within shell debris partially filled with iron-stained calcite. The Shoal facies has the highest porosity in the range of 10 - 30%. The Tempestite facies (8 - 15 m thick) comprises medium to light gray 10 - 15 cm thick layers of limestones, mostly calcareous bioclastic pack- to wakestones composed of skeletal debris and lithoclasts (mm - cm sized) with porosities of 0.5 - 10%. The Basinal facies comprises dark gray marlstones and micritic limestones with weak or absent wavy bedding and bioturbation, low porosity (0.5 - 5%), and considerably small pore sizes. The field-scale hydraulic conductivity of the Upper Muschelkalk aquifer varies from 2.6×10^{-6} to 1×10^{-4} m s^{-1} (D'Affonseca et al. 2020), which indicates representative fracture aperture ranges of 0.1 - 1 mm (Osenbrück et al. 2021; Petrova et al. 2022).

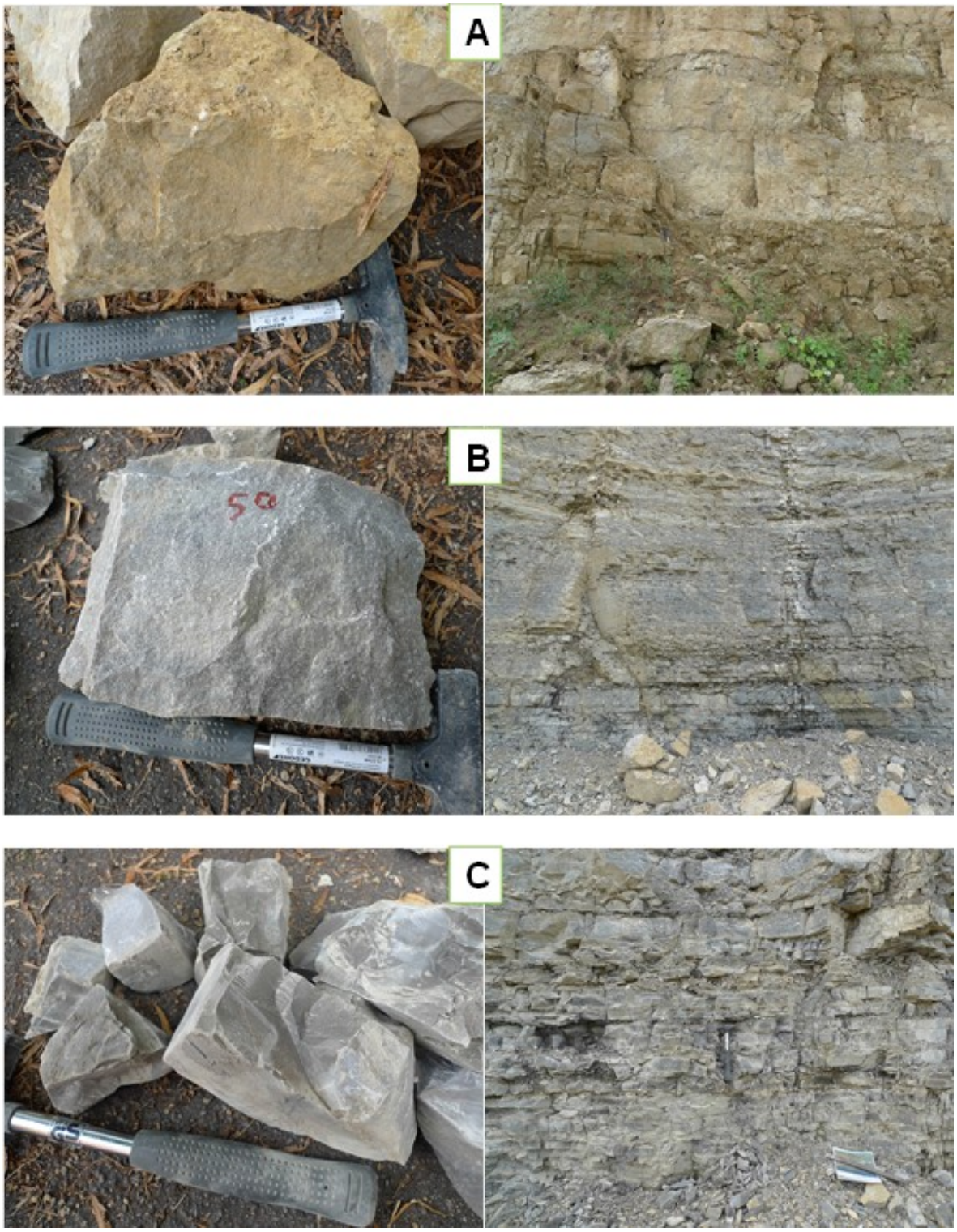

Figure 4.1. Rock and outcrops from main facies types of the Muschelkalk in the Ammer catchment (SW Germany): A – Shoal, B – Tempestite, C – Basinal facies.

4.2.2. ATRAZINE TRANSPORT PARAMETERS

To investigate the sorption properties of the rock facies of the Upper Muschelkalk, samples were collected from a quarry in Mötzingen (Fig. 4.1). Sampling locations were carefully selected according to the geological, sedimentological, and tectonic conditions of the study area (Osenbrück et al. 2021). To quantify the distribution coefficient K_d needed in the reactive transport equation (eq. 4.7) atrazine sorption isotherms were determined for the 3 major facies types (Fig. 4.1). For each sample 10 grams of pulverized rock (typical particle size around 50 µm) were mixed with 30 ml of water spiked with atrazine in 50 ml glass vials with teflon-lined caps. Tests were performed in triplicates with initial aqueous concentrations of atrazine of 0.1, 4, 22, 175, 770, 2930, 3140, and 11400 µg l^{-1}. The vials were kept in a horizontal shaker (150 rpm) for 10 days in the dark and at 20°C. To separate soil solids from water, the vials were kept standing for 3 days until fine particles settled. A test with filtering the supernatant aqueous phase proved sufficient removal of particles by pure sedimentation. Around 20 ml of the supernatant water was transferred into clean 50 ml glass vials using glass pipettes; attention was paid to transfer as much water as possible without resuspending the sediment. As an internal standard we added 20 ng of atrazine-D5 into the aqueous sample before further processing. For quality control, we used blanks with pure water (procedure blank), blanks with water and rock samples, and water spiked with atrazine (control for loss to the system) – all in triplicates.

We observed neither atrazine within the blanks nor significant losses from the system. For chemical analysis, low concentration samples (< 0.2 µg l^{-1}) were enriched via solid phase extraction (Waters OASIS HLB, MA, 1 cc). Samples with concentrations between 0.2 and 10 µg l^{-1} were filtered through 0.25 µm PTFE syringe filters and 2% (Vol.) of acetonitrile was added. Samples with concentrations above 10 µg l^{-1} were diluted with a MilliQ water: acetronitrile mixture (98:2). Atrazine was quantified by liquid-chromatography tandem mass spectrometry (Agilent 1290 Infinity HPLC and 6490 triple-quadrupole mass spectrometry) with a Poroshell 120 EC-C18 (2.7 µm, 2.1 x 100 mm) reversed-phase column. We measured 10 external standards with a range of 0.001 µg l^{-1} – 20 µg l^{-1} at the beginning and the end of the analysis to determine the calibration curve for the calculation of sample concentrations. One

standard (2.5 µg l^{-1}) was measured repeatedly in every 20th run as quality control concerning potential instrument shifts. Both, the external and the internal standard showed the same drift with increasing peak areas over time. Thus, we used both calibration curves simultaneously for the quantification and accepted the remaining uncertainty as insignificant. Additionally, the internal standard showed no dependency on the type of sample (blank, control, or rock sample), nor the corresponding processing of the sample (SPE, filtration, dilution), confirming no significant losses or matrix effects on the measurement with an acceptable coefficient of variation of 10 %.

Figure 4.2 shows almost linear sorption isotherms with distribution coefficients (K_d = Freundlich coefficients at 1 µg l^{-1}) of 6.4 l kg^{-1} for Shoal, 8.5 l kg^{-1} for Tempestite and 34.3 l kg^{-1} for the Basinal facies (Fig. 2). Therefore, retardation factors in the rock matrix $R_{im} = 1 + K_d \frac{\rho_b}{\varepsilon}$, ρ_b and ε denote limestone density and rock matrix porosity, correspondingly, range from 52 ($\varepsilon = 0.3$) to 188 ($\varepsilon = 0.1$) for Shoal, 207 ($\varepsilon = 0.1$) to 5005 ($\varepsilon = 0.005$) for Tempestite and 1668 ($\varepsilon = 0.005$) to 20375 ($\varepsilon = 0.05$) for Basinal facies (mineral density 2.7 kg l^{-1}).

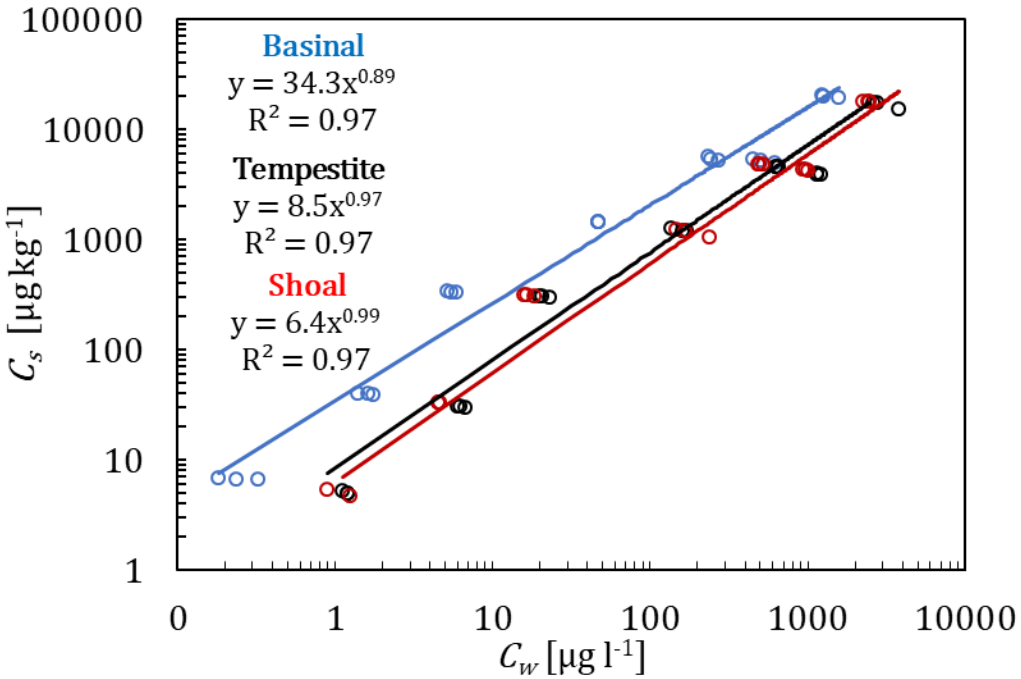

Figure 4.2. Experimentally measured sorption isotherms for the three main facies types of the aquifer, colour refers to the rock facies type: Shoal (red), Tempestite (black), Basinal (blue).

An aqueous diffusion coefficient of atrazine (D_{aq}) of 6.6 × 10^{-10} m^2s^{-1} was reported for 23 °C (Scott and Pnillips, 1973). At an aquifer temperature of 10 °C D_{aq} of 4.8 × 10^{-10} m^2s^{-1} is expected. The apparent diffusion coefficient in the rock matrix may be defined as:

$$D_a = \frac{D_{aq}\ \varepsilon^m}{\varepsilon + K_d\ \rho_{im}} = \frac{D_{aq}\varepsilon^{m-1}}{R_{im}} \tag{4.1}$$

where m is an empirical exponent (Archie's law), which for sedimentary rocks is about 2.2 (Boving and Grathwohl, 2001); ε^{m-1} denotes the tortuosity, $D_{aq}\ \varepsilon^{m-1}$ is known as pore diffusion coefficient.

We assume a time period of 33 years from the start of atrazine application until its ban (1958-1991). This neglects delayed leaching of atrazine stored in the upper soil layer, which however would be very low because of the biodegradation of atrazine in agricultural soils (Chavez Rodriguez et al. 2021).

Atrazine persistence in groundwater was assumed to be related to its arguably absent degradation in the aquifer. Reported atrazine degradation pathways under saturated conditions include physicochemical or biochemical processes into metabolites (Schocken and Speedie 1984; Radosevich et al. 1989). Low porosities and small pore sizes a in the Muschelkalk (Osenbrück et al, 2021) as well as mostly anoxic conditions in the aquifer (Petrova et al, 2022) limit growth of the microorganisms which degrade atrazine metabolically (Barbash and Resek, 1996).

Concentrations of atrazine in groundwater recharge depend on the application and properties of the soil and the unsaturated soil zone. Literature data on atrazine leaching vary widely (Hafner, 1995; Gutierrez and Baran, 2009; Roulier et al. 2006; Tappe et al. 2002; Vonberg et al. 2014) and may reach 5 µg l-1 in fractured aquifers (Gutierrez and Baran, 2009; Selg et al. 2005;), which we used for C0. The ultimate catchment-specific parameter ranges including porosity and distribution coefficients for each facies type were summarized in Table 1.

4.3. TRANSPORT MODELING

4.3.1. ANALYTICAL SOLUTION AND APPROXIMATIONS

We consider advective solute transport of a compound along a single fracture that is retarded by the interaction with the adjacent rock matrix (Fig. 4.3).

Assuming an entirely void fracture with negligible solute retardation in the fracture, the governing equation for the mass transport along the fracture being subject to exchange with the rock matrix is:

$$\frac{\partial C_m}{\partial t} + v\frac{\partial C_m}{\partial x} = -\frac{\partial m_{im}}{\partial t} \tag{4.2}$$

where C_m and m_{im} denote solute concentration (M L^{-3}) in the fracture (mobile region) and total mass of solute in the rock matrix (immobile region) per unit volume (M L^{-3}) of the fracture;; *v*, *x* and *t* denote flow velocity, the spatial coordinate (L T^{-1}) in flow direction along the fracture (L) and time (T).

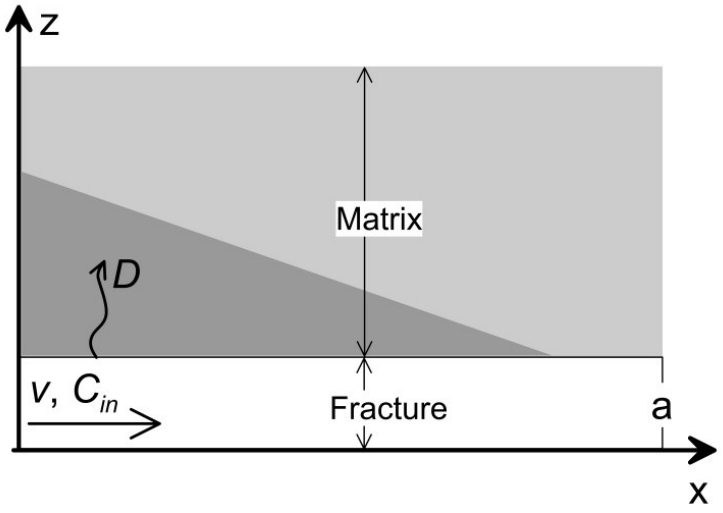

Figure 4.3. Conceptual model of solute transport in a fracture controlled by diffusion into the rock matrix; dark grey area indicates the diffusive front of the solute within the rock matrix; light grey area represents pristine matrix area.

In case of linear sorption the mass of solute per unit volume in the rock matrix is given by:

$$m_{im} = \frac{1}{a}\int_{a}^{+\infty}\left(\varepsilon + K_{d,im}\,\rho_{im}\right)C_{im}\,dz \tag{4.3}$$

where $1/a$ denotes the surface-to-volume ratio (L^{-1}), with *a* being the half fracture aperture of the fracture (L), *z* is the spatial coordinate perpendicular to the flow direction (i.e. depth in the rock matrix), and C_{im} denotes the solute concentration (M L^{-3}) in pore water of the rock matrix; ε, $K_{d,im}$ and ρ_{im} denote porosity of the rock matrix (dimensionless), the distribution coefficient (L^3 M^{-1}), and the dry bulk density of the matrix region (M L^{-3}), respectively. Combining eq. 2 and eq. 3 yields:

$$\frac{\partial C_m}{\partial t} + v\frac{\partial C_m}{\partial x} = -\frac{1}{a}\left(\varepsilon + K_{d,im}\,\rho_{im}\right)\int_{a}^{+\infty}\frac{\partial C_{im}}{\partial t}\,dz \tag{4.4}$$

To describe the transport of a solute that has been applied only over a certain finite time period (input), t_0, and assuming a constant input concentration, C_0, eq. 4 is to be solved for the following initial and boundary conditions:

$$C_m(x,0) = 0$$

$$C_m(0,t) = C_0,\ 0 < t \le t_0$$

$$C_m(0,t) = 0\ t > t_0$$

$$C_m(\infty,t) = 0$$

The differential equation describing the diffusive transport of solute in the rock matrix region in the direction perpendicular to the fracture is:

$$\frac{\partial C_{im}}{\partial t} = D_a\frac{\partial^2 C_{im}}{\partial z^2} \tag{4.5}$$

where D_a (L^2 T^{-1}) denotes the apparent diffusion (or retarded pore diffusion) coefficient. Initial and boundary conditions are:

$$C_{im}(x,z,0) = 0$$

$$C_{im}(x,+\infty,t) = 0$$

$$C_{im}(x,a,t) = C_m(x,t)$$

Inserting eq. 4.5 into eq. 4.4 gives

$$\frac{\partial C_m}{\partial t} + v\frac{\partial C_m}{\partial x} = \frac{1}{a}(\varepsilon + K_{d,im}\,\rho_{im})\,D_a\frac{\partial C_{im}}{\partial z}(x, a, t) \tag{4.6}$$

Following Rahman et al. (2004) who derived an analytical solution for the equivalent case of a macropore column by superposition of the solution developed by Grisak and Pickens (1981) for continuous solute input, the solute concentration in the fracture is given by:

$$C_m(x,t) = C_o\left[\operatorname{erfc}\left(\frac{(\varepsilon + K_{d,im}\,\rho_{im})\frac{x}{v}\sqrt{D_a}}{2a\sqrt{t-\frac{x}{v}}}\right) - \operatorname{erfc}\left(\frac{(\varepsilon + K_{d,im}\,\rho_{im})\,\frac{x}{v}\sqrt{D_a}}{2a\sqrt{t-\frac{x}{v}-t_0}}\right)\right] \tag{4.7}$$

Expressing the spatial coordinate along the fracture in terms of travel time of water $\tau = \frac{x}{v}$, the relative concentration is given by:

$$\frac{C_m}{C_o} = \operatorname{erfc}\left(\frac{(\varepsilon + K_{d,im}\,\rho_{im})\,\tau\sqrt{D_a}}{2a\sqrt{t-\tau}}\right) - \operatorname{erfc}\left(\frac{(\varepsilon + K_{d,im}\,\rho_{im})\,\tau\sqrt{D_a}}{2a\sqrt{t-\tau-t_0}}\right) \tag{4.8}$$

Transport of any sorptive compound in the considered case (eq. 4.8) follows a unimodal function with a concentration maximum propagating through the system (Fig. 4.4). Figure 4.4 depicts the concentration profile in the fracture (Fig. 4.4-left) and a breakthrough curve at a given location (Fig. 4.4-right). The conservative tracer which does not sorb in the solid phase has a sharp front and higher maximum concentration. Sorption of the solute in the rock matrix causes retardation and concentration tailing even decades after the application stopped.

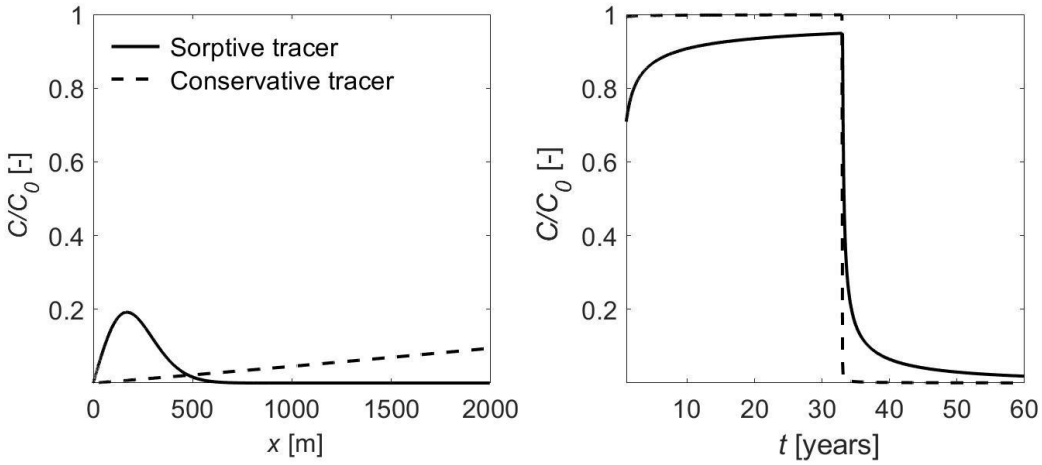

Figure 4.4. Propagation of atrazine compared to a conservative tracer: concentration profiles in the fracture after t = 64 years (left) and concentration breakthrough curve at distance x = 10 m (right). The assumed input period is from 1958 to 1991 (t_0 = 33 years), *t=0* corresponds to the first application in 1958, *t=60* corresponds to year 2018, accordingly (eq. 8 with a = 0.1 mm, ε = 1 %, hydraulic gradient = 0.001, K_d = 7 l kg^{-1}, D_{aq} = 4 $\times$ 10^{-10} m^2 s^{-1}).

Thanks to unimodality of the plume, concentrations along the fracture are linearly increasing until a maximum is reached followed by a monotonically decrease (Fig 4.5, top-left). The breakthrough curve at any location is also unimodal: concentrations first increase until the peak is reached and then decrease with $t^{-3/2}$ typical for back diffusion (Fig. 4.5 top-right). To highlight the effect of both application time t and distance x, a response surface was constructed (Fig. 4.5, bottom) in order to illustrate the concentration of atrazine in the fracture as a function of time and distance.

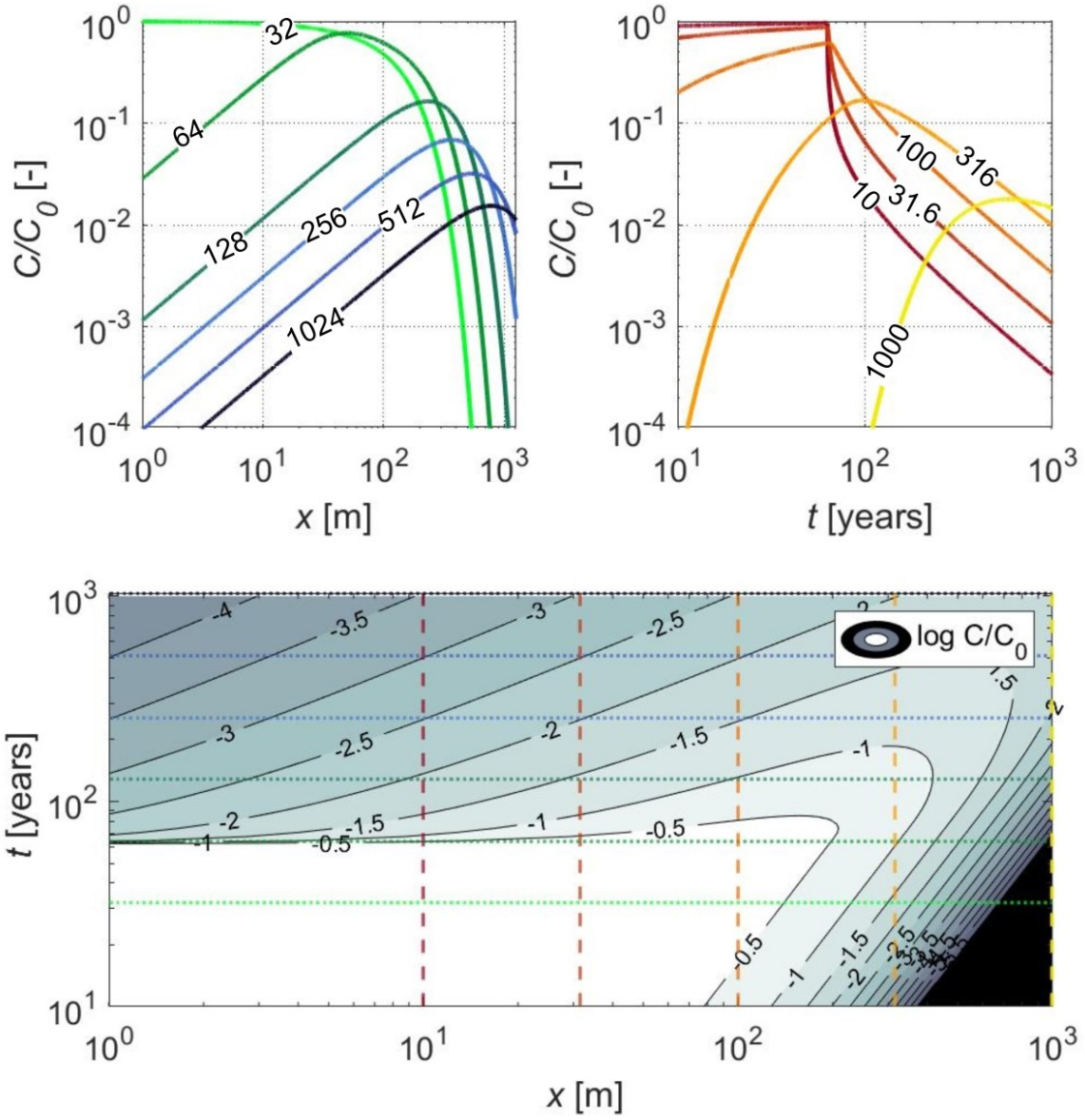

Figure 4.5. Atrazine concentrations in the fracture in time and space; top-left: concentration profiles along the fracture for real times t_0 from 32 to 1024 years (light green to black), concentration is linearly increasing until the peak is reached; top-right: concentration breakthrough curves at different locations in the fracture (in terms of distance from the inlet, x = 10 - 1000 m (red to yellow)), in the tailing part concentrations drop with $t^{-1.5}$; bottom: relative atrazine concentrations in the fracture as a function of real time and travel distance along the fracture, isolines denote logarithmic relative concentrations (a = 0.1 mm, ε = 1 %, t_0 = 33 years, $I = 3 \cdot 10^{-3}$, K_d = 7 l kg^{-1}, $D_{aq} = 4 \times 10^{-10}$ m^2 s^{-1}); dashed lines refer to locations (i.e. travel distances)

considered in the top-right panel, dotted lines correspond to the real time values considered in the top-left panel.

The contour plots of the peak travel time shown in Fig. 4.5, however, allow arriving at simple solutions for the distance travelled by the peak and how the maximum concentration declines. Following a heuristic approach and a detailed analysis of the results obtained by the analytical model (eq. 4.7 and 4.8, Fig. 4.5), simple analytical approximations for the relative maximum concentration and location of the concentration maximum along the fracture were derived (eq. 4.9 and 4.10). These approximations follow from the investigation of the model behaviour in the parameter space (Fig. 4.5). First, obtained expressions (eq. 4.9 and 4.10) were verified through the local sensitivity of parameters following one-at-time approach and aiming to represent the direct effect of parameter variation (Fig. 4.6-4.7). To confirm the combined effect of parameter variation, equations 4.9 and 4.10 were verified through the global parameter variation with corresponding solution (eq. 4.8) (Fig. 4.8).

The relative peak concentration, C_{max} /C_0 was found to depend mainly on the application time t_0 and total time t, like the solute mass in ordinary back diffusion (e.g., diffusion into and out of a low permeability layer, Grathwohl, 1998a):

$$\frac{C_{max}}{C_0} = \frac{t_0}{4\,t} \tag{4.9}$$

Since diffusion into the rock matrix depends on the same physical parameters as of diffusion out of the rock matrix, sorption and diffusion parameters cancel out.

The location of the peak concentration X_{Cmax} (L) may be approximated by the following equation, which involves all transport parameters of the analytical solution (eq. 4.7):

$$X_{Cmax} = \frac{\sqrt{2}\,a\,v\,(t - t_0/\pi)}{\sqrt{(\varepsilon + K_d\,\rho)\,D_{aq}\,\varepsilon^{2.2}\,t}} \approx \frac{\sqrt{2}\,a\,v\,t}{\sqrt{K_d\,\rho\,D_{aq}\,\varepsilon^{2.2}\,t}} \tag{4.10}$$

$D_{aq}\,\varepsilon^{2.2}$ represents the effective diffusion coefficient (Boving and Grathwohl, 2001) and the denominator in the long term approximation ($t >> t_0$) is a retardation factor. The velocity (v), according to the cubic law ($v = \frac{I\rho g(2a)^2}{12\mu}$) depends on the hydraulic gradient I and a^2 (g, μ, ρ denoting acceleration of gravity, dynamic groundwater viscosity and density, resp.). The peak location depends on various parameters with

different sensitivities, of which the most significant is the aperture a, X_{Cmax} then increases with a^3).

To confirm the correct reflection of the local sensitivity, one-factor-at-a-time method also known as monothetic analysis was implemented to the newly derived approximations. The base model parameter set and corresponding parameter ranges typical for fractured aquifers are: a = 0.2 (from 0.1 to 10) mm, ε = 1 (from 1 to 20) %, t_0 = 33 (from 10 to 100) years, t = 200 (from t_0 to 1000) years, $i = 3 \times 10^{-3}$, K_d = 10 (from 1 to 100) L kg^{-1}, $D_{aq} = 4 \times 10^{-10}$ (from 1×10^{-10} to 1×10^{-9}) m^2 s^{-1}. To test the approximations fit to the solution (eq. 4.8), each of the model parameters was varied within the reasonable ranges 500 times, while other parameters kept constant. Figures 4.6-4.7 illustrate the local sensitivity and compare both, analytical solution (eq. 4.8) and approximations (eqs. 4.9 and 4.10). Both analytical solution and approximation reflect that C_{max}/C_0 is not very sensitive to ε, K_d, D_{aq} and a. Aperture is by far the most sensitive parameter for X_{Cmax} showing a positive correlation, while ε, K_d, D_{aq} showing a negative correlation. Approximated and analytical estimates of X_{Cmax} and C_{max}/C_0 for 500 values of each parameter closely mimic the true model behavior with respect to changes of individual parameters. In case of $C_{max}/C_0 < 0.1$ and $t > t_0$ the approximation of X_{Cmax} represents the analytical solution reasonably well.

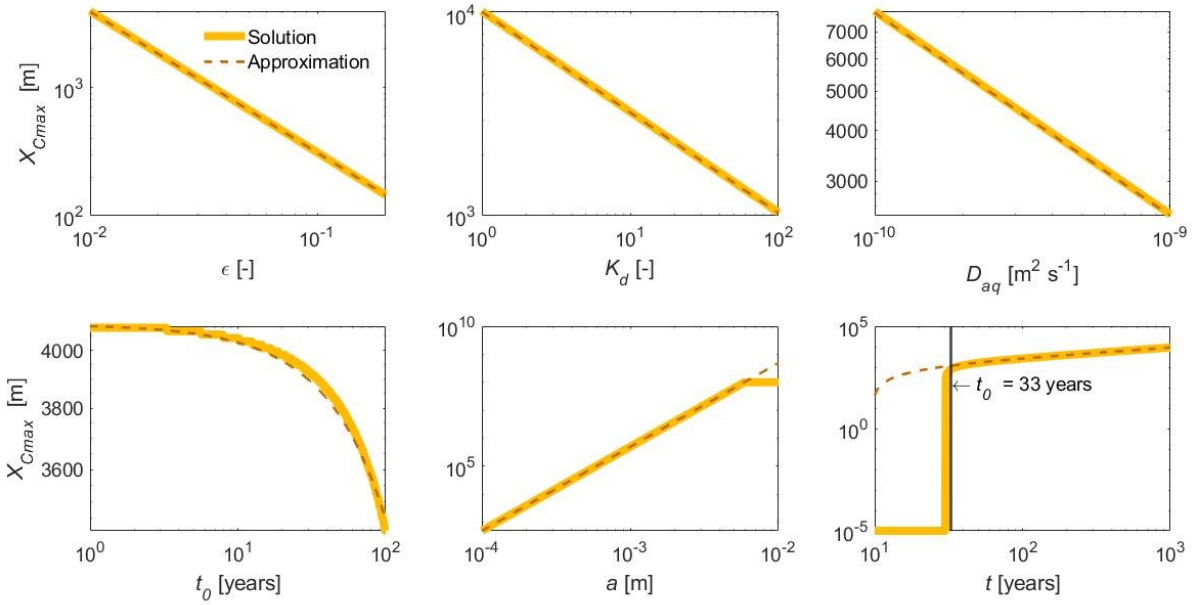

Figure. 4.6. Verification of analytical approximations (dashed lines, eqs. 4.10) for X_{Cmax} with analytical solution (eq. 4.8, solid lines) for with respect to one-at-time variation of every parameter.

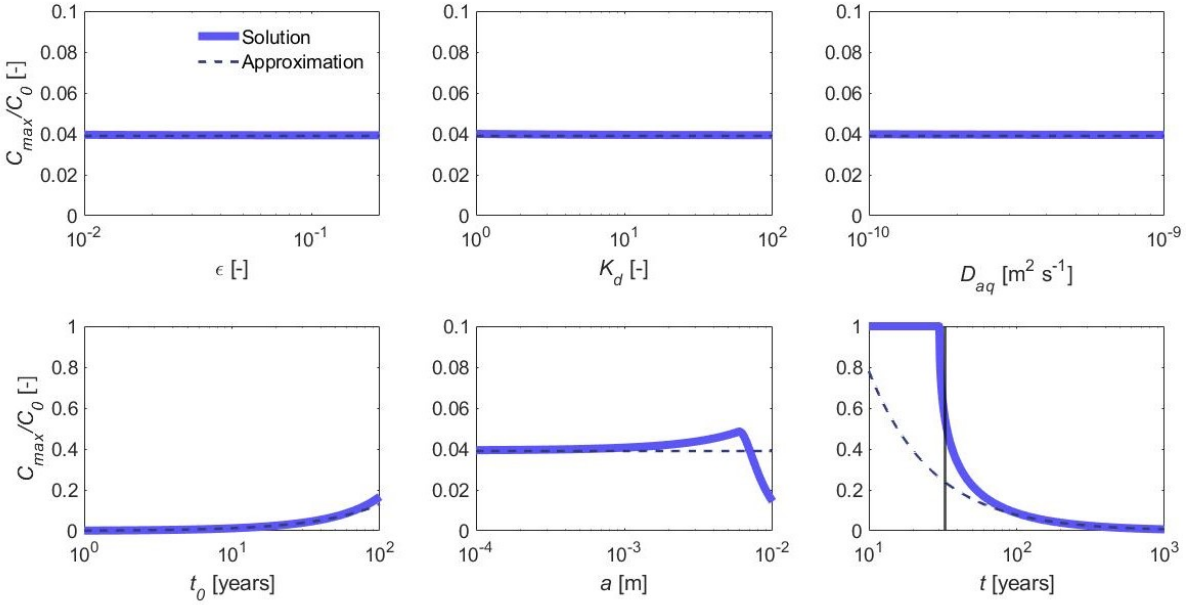

Figure. 4.7. Verification of analytical approximations (dashed lines, eq. 4.9) for C_{max}/C_0 with analytical solution (eq. 4.8, solid lines) for with respect to one-at-time variation of every parameter.

Comparison for parameter settings from simultaneous random sampling within given parameter ranges confirms the good agreement of approximations and analytical solution for C_{max}/C_0 and X_{Cmax} (see Fig. 4.8). The quality of analytical approximations was evaluated by computing the coefficient of determination R^2:

$$R^2 = \frac{\sum_{k=1}^{n}(y_k - \widehat{y_k})^2}{\sum_{k=1}^{n}(y_k - \underline{y})^2} \tag{4.11}$$

where y_k, $\widehat{y_k}$ and $\underline{y}$ denote the true values, calculated values, and mean of the true values accordingly. Computed values for an ensemble of 500 random parameter combinations resulted in R^2 of 0.99 and 1.0 for C_{max}/C_0 and X_{Cmax} accordingly. Large Deviations are very low except for high concentrations – a situation which occurs either close to the inlet of the fracture or if the solute breakthrough is fast due to slow matrix diffusion and low sorption. These deviations are not relevant to practical applications that typically aim at long-term predictions of sorptive compounds.

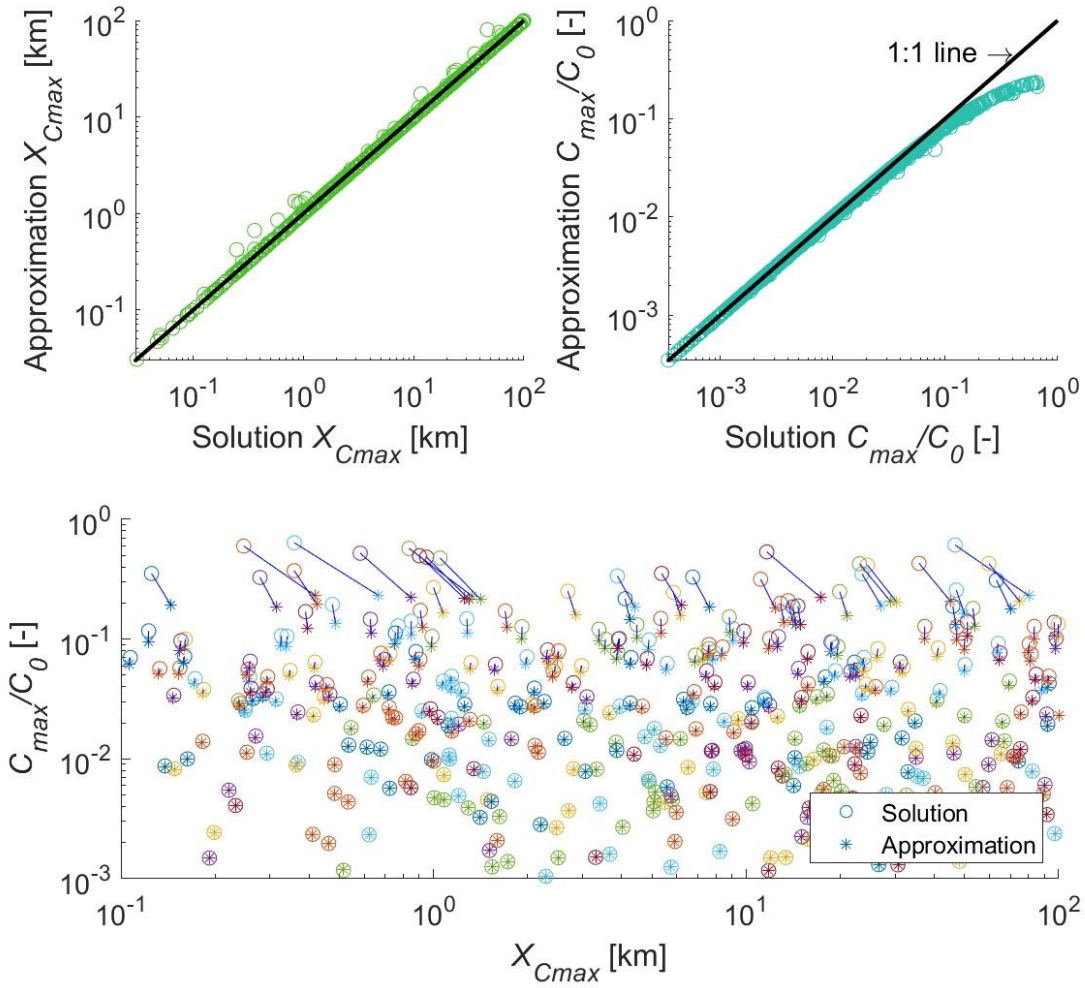

Figure 4.8. Match of approximations of relative peak concentrations (eq. 4.8) in the fracture and travel distance of the peak (eq. 4.9) with the analytical solution (eq. 4.7) for 500 random parameter combinations of aperture, porosity, total time, plume duration, aqueous diffusion coefficient, and distribution coefficient. Top: scatter plot of analytical solutions against approximations; bottom: relative concentration vs. the distance along the fracture of the peak derived analytically (circles) and approximated (stars); symbols are connected via a blue line to clarify corresponding results.

4.3.2. MODEL PREDICTIONS UNDER UNCERTAINTY

From a practical point of view, the critical characteristics of the sorptive compound's breakthrough curve are peak concentration and the time after the concentration finally drops below the groundwater legal limit (= threshold concentration C_{th}) (Farlin et al. 2022). While the peak concentration only depends on the duration of the input

and time (eq. 4.9), the peak location depends on retardation (eq. 4.10, i.e. sorption, effective diffusion , velocity and aperture). As all relevant parameters can be estimated only with more or less uncertainty in the field, stochastic model predictions are required. Assuming sorption coefficients determined in the lab can be quantified sufficiently well, we consider solute input concentration, fracture half-aperture, and porosity as the most uncertain parameters (Table 4.1).

Table 4.1. Transport parameter and ranges for stochastic estimates

Parameter		Value	Unit
Deterministic parameters			
Aqueous diffusion coefficient	D_{aq}	4.8×10^{-10}	$m^2\ s^{-1}$
Input duration	t_0	33	years
Distribution coefficient, Shoal	K_d	6.4	$l\ kg^{-1}$
Distribution coefficient, Tempestite	K_d	8.5	$l\ kg^{-1}$
Distribution coefficient, Basinal	K_d	34	$l\ kg^{-1}$
Probablistic parameters			
Fracture half-aperture	a	5×10^{-5} to 5×10^{-4}	m
Input concentration	C_{in}	>0.1 to 10	$\mu g\ l^{-1}$
Porosity, Shoal	ε	0.1 to 0.3	-
Porosity, Tempestite	ε	0.01 to 0.1	-
Porosity, Basinal	ε	0.01 to 0.05	-

With given ranges of uncertain parameters (a, C_{in}, ε) normalized to the range [0, 1], a 3-dimensional Halton sequence with the targeted ensemble size of 10000 elements was generated. Each ensemble member included solute concentration $C(\tau, t)$ where travel time τ is a proxy of distance reducing the influence of the aperture (please see eq. 10 for the parameter dependencies), and t>64 refers to the time from the atrazine application in 1958 until 2022 (please see Fig. 4.9 and Appendix for illustration). Results were analysed with respect to three questions listed below.

Q_1) Will the concentration exceed the legal limit (binary answer)?

Model runs are first evaluated with respect to the question of whether concentrations at a certain location/travel time will exceed the legal limit value (for Atrazine in Germany: C_{th} = 0.1 µg l^{-1}) in the future or not. Evaluation is binary, if concentration $C(\tau^*, t > t_P)$ for a certain travel time τ^* will exceed the limit, the evaluation results in answer $A_1(\tau^*) = 1$, otherwise in $A_1(\tau^*) = 0$.

Q_2) Will the concentration decline (binary answer)?

Thanks to the unimodality of the concentration breakthrough curve, concentrations monotonically decrease after the peak passed by (Fig. 4.8). Answers to question Q_2 are easily determined with the help of the travel time of the concentration peak at present time $\tau_{peak}(t_P)$: $A_2(\tau^*) = 0 \; \forall \; \tau^* > \tau_{peak}(t_P)$ and $A_2(\tau^*) = 1 \; \forall \; \tau^* \leq \tau_{peak}(t_P)$.

Q_3). If the concentration in the fracture now (2022) exceeds the legal limit C_{th}, how long will it take to drop below it ($C < C_{th}$)?

For the range of travel time where the concentration exceeds the legal limit, the expected time Δt_d until the concentration will drop below C_{th} is calculated.

The ensemble of answers A_1 and A_2 is expressed in terms of facies-specific probabilities $P(A_1(\tau)=1)$ and $P(A_2(\tau)=1)$, evaluations of recovery period Δt_d are given as distributions.

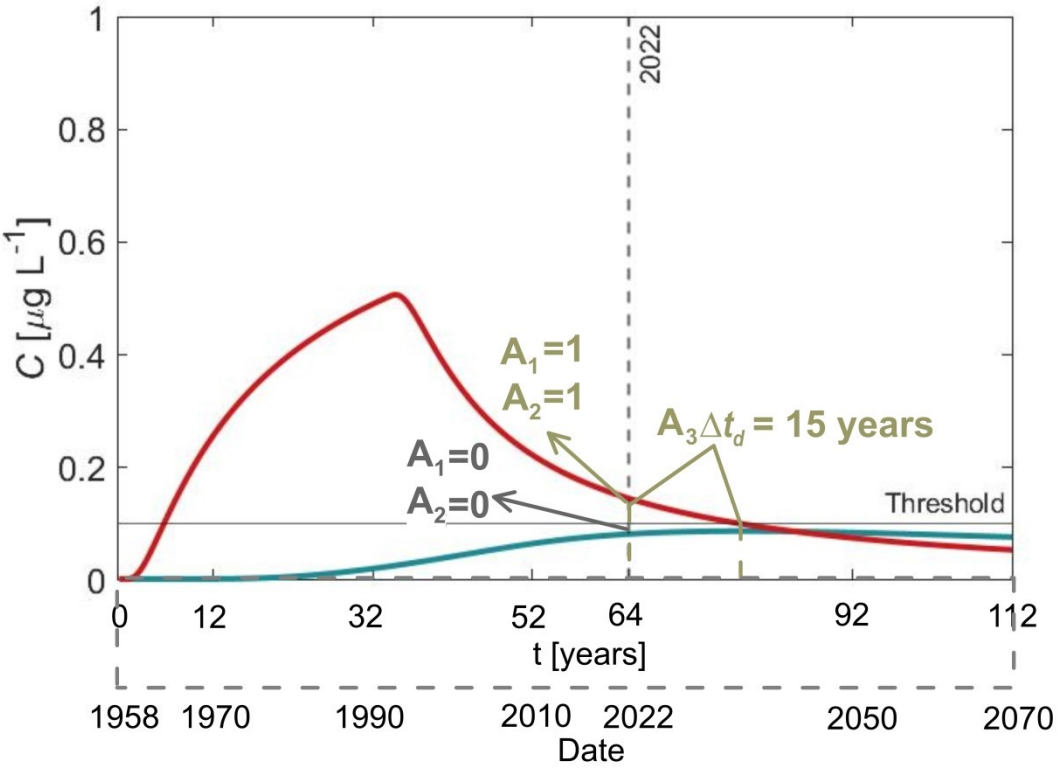

Figure 4.8. Illustration of the breakthrough curve analysis by means of two exemplary breakthrough curves: red - concentration in 2022 is still exceeding the legal limit (A_1 = 1), the peak concentration has already passed (A_2 = 1) and it will take Δt_d = 13 years (2035) until the legal limit is reached (parameter set: a = 1 mm, ε = 0.5 %, t_0 = 33 years, t = 64 years, x = *3 m*, K_d = 6 L kg^{-1}, D_{aq} =4.8 × 10^{-10} m^2 s^{-1}).blue: concentration in 2022 is below the legal limit (A_1 = 0), but the peak concentration is still to come (A_2 = 0), although it will not exceed the limit (parameter set: a = 0.05 mm, ε = 1 %, t_0 = 33 years, t = 64 years, x = *3 m*, K_d = 6 L kg^{-1}, D_{aq} =4.8 × 10^{-10} m^2 s^{-1}).

4.4. RESULTS AND DISCUSSION

4.4.1. STOCHASTIC ANALYSIS

Answers A_1 and A_2, and recovery period Δt_d were computed for an ensemble of 10000 relevant model parameter settings for every rock facies type. Travel time was split in the interval $0.01 \leq \tau \leq 3$ years into 20 steps, logarithmically increasing from 0.01 years to a maximum step size of 1 year for $\tau \geq 3$ years. Probabilities $P(A_1(\tau)=1)$ and $P(A_2(\tau)=1)$ are depicted in Fig. 4.10.

In all facies types, the highest probability to exceed the legal limit after 2022 refers to the "young" water. The groundwater with longer travel times will stay below the legal limit. Although this generally holds for all rock facies, it is most distinct for the Shoal facies. In Shoal, high matrix porosity leads to high atrazine attenuation in the rock matrix. As a result, already close to the fracture inlet the concentration will stay below C_{th} for travel times longer than 0.6 years (Fig. 4.10, left graph, solid line). For travel times larger than 0.2 years the peak concentration may still come in the future (Fig. 4.10, left graph, dashed line) but will most likely not exceed C_{th} (as $P(A_1)$ is reasonably low for $\tau > 1$).

In Tempestite, the concentration peak passed already for $\tau < 2$ years (Fig. 4.10, middle graph) and is to come for larger travel times. At the same time, the probability of reaching C_{th} for travel time between 2 and 6 years stays low (Fig. 4.10, middle graph). Similar relationships with lower solute attenuation are expected for the Basinal facies (Fig. 4.10, right graph). Thus, for travel times of up to 2 years the legal limit may be exceeded. Differences between Basinal and Tempestite are mainly due to the K_d value, which is almost four times higher in Basinal than in Tempestite facies types (Table 4.1). A comparison of results in Shoal and Tempestite reveals the significant control of the matrix porosity on solute transport. Though having similar K_d values, facies types show significant differences in the values of probability to exceed the legal limit.

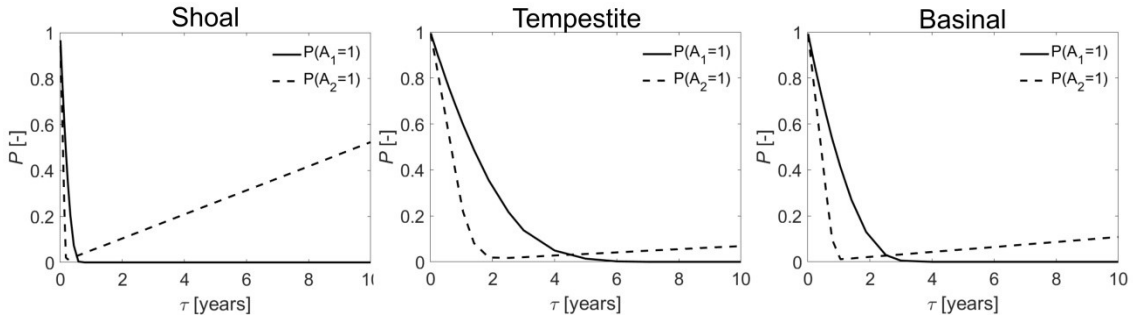

Figure 4.10. Facies type-dependent probabilities of exceeding the legal limit concentration for atrazine in 2022 in groundwater (C_{th} = 0.1 µg l^{-1}, solid line and of declining concentrations (dashed line) as a function of travel time for Shoal (left), Tempestite (middle) and Basinal (right) rock facies types.

While the probability to exceed the legal limit reflects the risk of atrazine contamination at a certain travel time, the recovery period Δt_d reveals the severity of

the contamination. If exceeding the atrazine concentration is highly likely (based on probabilities, see Fig.4.10), then the recovery period refers to the intensity of contamination and duration of corresponding recovery time. Therefore, the duration of the recovery is depicted against the probability of atrazine exceedance in the groundwater for Shoal, Tempestite and Basinal facies types (Fig. 4.11, left to right).

In all facies types, recovery durations have a tendency to the same value at $P(A_1)$ = 0. The recovery duration varies only slightly in the range of hundreds of years for the probability less than 70%. For probabilities larger than 70 %, the recovery duration is inversely proportional to the probability. The minimum recovery duration corresponding to the probability of 90%, is 30-60 years. The width of possible recovery durations at a given probability value is verying between facies types.

The largest variability of the recovery period relates to the Tempestite facies type (Fig.4.11, right) due to the highest porosity variability (and therefore, highest uncertainty). If atrazine in groundwater likely exceed the legal limit, i.e. if $P(A_1=1)$ is close to 100% (which corresponds to travel times of only a few months, see. Fig. 4.10), the expected length of the recovery period, Δt_d, ranges between 20 years (Tempestite and Basinal) and 50 years (Shoal).

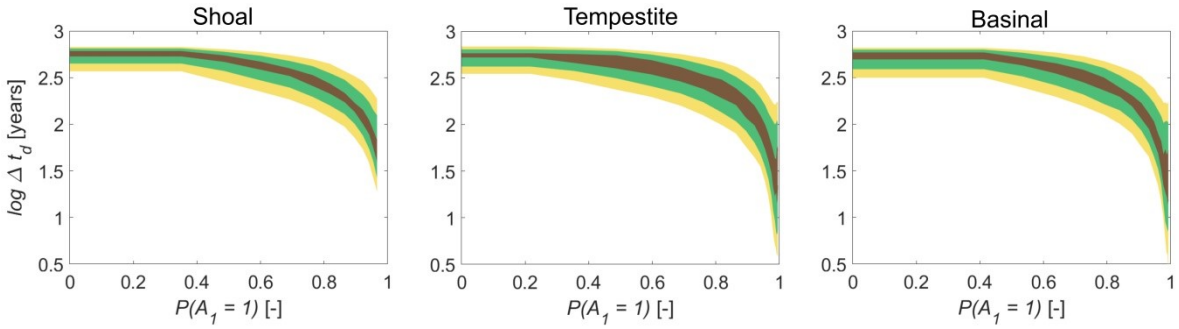

Figure 4.11. Aquifer recovery period in terms of facies type-specific probability of time Δt_d until atrazine concentration will drop as a function of probabilities of exceeding the legal limit concentration for atrazine in groundwater for Shoal (left, K_d = 6.4 l kg^{-1}, $\varepsilon \in [10\,\%; 30\,\%]$), Tempestite (middle, K_d = 8.5 l kg^{-1}, $\varepsilon \in [1\,\%; 10\,\%]$) and Basinal (right K_d = 34 l kg^{-1}, $\varepsilon \in [1\,\%; 5\,\%]$) facies types. Deep brown, green and yellow lines denote the confidence levels of 50%, 70% and 90% accordingly.

4.4.2. LIMITATIONS IN APPLICABILITY TO REAL CATCHMENTS

The description of solute transport of a sorptive compound in a fractured aquifer using a travel time-based analytical solution for transport in a single fracture shows to be a computationally very efficient tool to develop a more specific picture of the behaviour of legacy compounds like atrazine in fractured rock. Using a simplified single fracture model, the focus is set to the reactive part of the problem and the sensitivity to corresponding parameters. The fate and behaviour of legacy compounds in real fractured rock aquifers, however, is also governed by the particular groundwater flow conditions resulting from the heterogeneity of aquifer properties and given hydraulic boundary conditions and forcing. Water quality predictions for real locations such as water supply wells are only possible if this hydraulics can be described in the model.

In a travel time-based model framework, this is done by means of a probability density function (pdf) of travel time (e.g., Cirpka and Kitanidis, 2000; Petrova et al. 2022), which quantifies the mixing of water in the well that has travelled along different streamtubes. Given such pdf of travel time for the location of interest, the risk (probability) of unacceptable atrazine contamination can be simulated by convolution of this *PDF* with the probability profile of exceeding the legal limit concentration for atrazine in groundwater (Fig. 10).

The problem is that – at best – only mean or average travel time can be derived in terms of apparent groundwater age from isotopic data (Suckow, 2014). However, the mixing of water cannot be measured or reliably quantified in any other way (note that even tracer tests wouldn't reflect the real situation of solutes being applied on large areas in agriculture). This lack of information may be partly overcome by using parametric pdf such as gamma distributions (Petrova et al. 2022). This is why, despite the difficulties described above, we see a potential for using the herein derived probability curves (Fig. 10) for atrazine transport assessment.

The presented model is accounting for aquifers where no relevant microbial degradation of atrazine occurs in the saturated zone. However, any microbial degradation that take place in the unsaturated zone (including dechlorination, dealkylation, hydroxylation and ring cleavage (Shuwen et al, 2021)) and may effectively attenuate atrazine concentration (Beegum et al., 2020) is considered in

the definition of the model's boundary condition, namely the definition of the atrazine input concentration in the recharge entering the saturated zone. A detailed knowledge of the atrazine degradation pathways in the subsurface would reduce the uncertainty of the current model by defining narrower range of the boundary condition (input concentration, Tab. 1). .

Any spatial variability of this concentration, however, cannot be taken into account. Such variability may result from spatial heterogeneity of soil characteristics, variablity in land surface characteristics, and spatially differentiated application of atrazine, as well as from spatially variable hydraulics in the vadose zone. As we believe that it is vitally impossible to reliably estimate atrazine concentration in recharge to groundwater in a spatially differentiated way on the catchment scale, we address atrazine input concentration as uncertain model input parameter with a rather broad range of possible values (Table 1).

Noticeably, if atrazine degradation in the saturated zone of the aquifer cannot be considered negligible, another solution instead of eq. 8-10 must be considered. Due to the large time scale, even small degradation rates (i.e. half-life in the order of years) may remarkably decrease atrazine concentration (e.g., Sidborn, 2007). This would lower the risk of exceeding the legal limit concentration for atrazine. Probability profiles shown in Fig. 10 will be shifted to the left.

4.5. CONCLUSIONS

The stochastic analysis of pesticide transport in a fractured Muschelkalk aquifer is summarized in the following conclusions:

- Sorption of the atrazine in the Muschelkalk aquifer is almost linear and fairly similar in all facies (K_d values in the range 6.4 - 34.3 l kg^{-1}). Larger differences are observed for matrix porosities (ε = 0.1 - 0.3 for the Tempestite and ε = 0.01 - 0.05 for the Basinal facies), which strongly influence the effective diffusivity in rock matrix ($D_e = \varepsilon^{2.2}$).
- Newly derived approximations for maximum concentration and corresponding travel distance of the peak reflect and clarify parametric dependencies of pesticide transport in fractured systems.

- The approximations could be applied to any other legacy compound as well. Higher risks can be anticipated for compounds that have been applied over a longer application period than atrazine and/or at a higher input concentration in relation to the legal limit (e.g., chlorinated hydrocarbons).
- Maximum pesticide concentration in the fracture depends only on the ratio of input time to total time, whereas the retardation of the peak increases with the square root of time and is inverse proportional to the aperture.
- Fracture aperture and porosity are the most sensitive transport parameters followed by sorption and aqueous diffusion coefficients. Fractures with small apertures lead to slow transport and high attenuation of the peak concentration.
- Although the atrazine application stopped in 1991, increasing concentrations have to be expected in fractures with groundwater travel times of less than 0.6 - 2 years due to slow mass exchange and storage within the rock matrix.
- All Muschelkalk facies types will likely exhibit atrazine concentrations below legal limit of 0.1 µg l^{-1} if groundwater travel time exceeds 2 years. In the view of the mean travel times estimated for the wells in the Ammer catchment which are in the order decades (Petrova et al. 2022), that implies very low probability to exceed the legal limit. On the other side, locations with the mean travel times up to 2 years deserve an increased attention in terms of the atrazine concentration increase.
- If the legal limit of the concentration is exceeded at a given location, it will take most likely centuries for recovery.
- The curves of the probability of both legal limit exceedance and concentration decline (Fig. 4.10) may be used as a reaction curve in catchment-scale travel time-based modeling (see, e.g., Petrova et al. 2022).

Acknowledgments

Financial support for this research was provided by the DFG (German Research Foundation) through the Research Training Group ‘Integrated Hydrosystem Modelling’ (GRK 1829/2) and through the Collaborative Research Center CAMPOS (SFB 1253/1).

APPENDIX. STOCHASTIC ANALYSIS OF ATRAZINE BREAKTHROUGH CURVES

Monte-Carlo sampling of parameter settings according to the given parameter ranges (Table 4.1) was done using a quasirandom Halton sequence (Halton, 1960) as provided by the *haltonset* function in MATLAB according to Kocis and Whiten (1997). Figures A.1a-A.1e show results for facies type Tempestite for a selection of distinct values of travel time. Please note that – to obtain a clear representation – only 200 model runs are considered here (results displayed in the main part are based on 10000 runs). With regard to answers to question Q_1 (see section 4.3.2), obviously, most of the breakthrough curves exceed the legal limit value at small travel time, whereas barely any does so at the larger travel times. At the same time, at the early travel times most of the breakthrough curves is on the declining part, and this is changing for the travel time from τ = 2 years onwards. The result of the conversion to the probabilities of obtaining a positive answer to questions 1 and 2 is shown in Fig. A.4.1f curve ensembles for several representative travel time distances (Fig.A.4.1.).

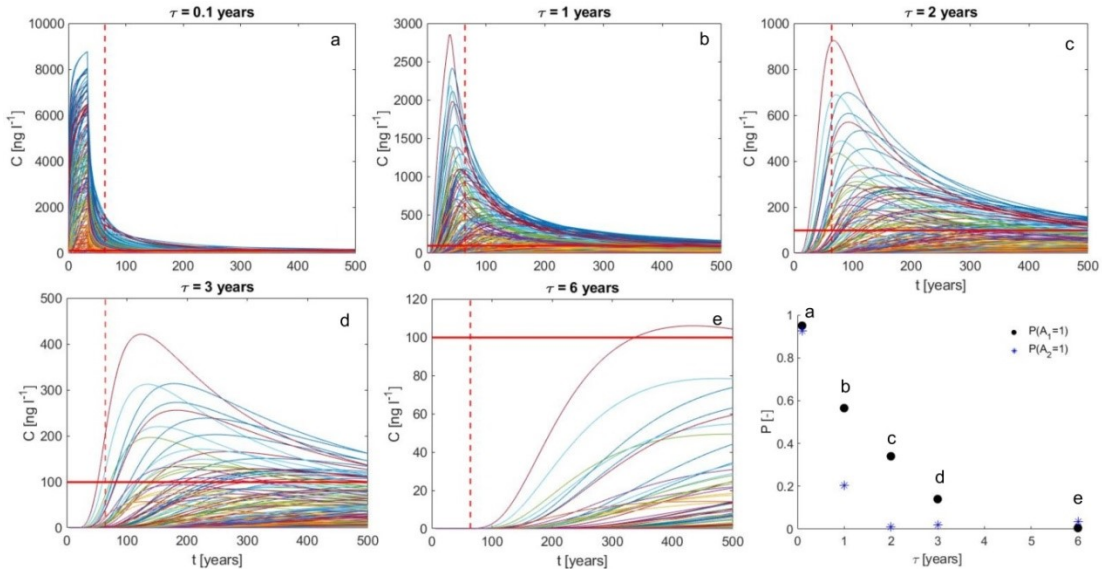

Figure A.4.1. a-e: an ensemble of random 200 atrazine breakthrough curves increasing travel times from 0.1 to 6 years; the red horizontal line denotes to the drinking water legal limit C_{th}; the dashed vertical lines represent 64 years (year 2022); bottom-right – corresponding probabilities of exceeding the legal limit concentration for atrazine in 2022 in groundwater (circles) and of declining concentrations (stars) as a function of travel time.

References

Ammann, L., Fenicia, F. and Reichert, P. (2019) A likelihood framework for deterministic hydrological models and the importance of non-stationary, autocorrelation, *Hydrology and Earth System Sciences, 23*(4), pp. 2147–2172. doi: 10.5194/hess-23-2147-2019.

Baran, N., Lepiller, M. and Mouvet, C. (2008) Agricultural diffuse pollution in a chalk aquifer (Trois Fontaines, France): Influence of pesticide properties and hydrodynamic constraints, *Journal of Hydrology*, 358(1–2), pp. 56–69. doi: 10.1016/j.jhydrol.2008.05.031.

Beegum, S., Vanderborght, J., Šimůnek, J., Herbst, M., Sudheer, K. P. and Nambi, I. M. (2020) Investigating atrazine concentrations in the Zwischenscholle aquifer using MODFLOW with the HYDRUS-1D package and MT3DMS, *Water (Switzerland)*, 12(4), pp. 1–24. doi: 10.3390/W12041019.

Bertuzzo, E., Thomet, M., Botter, G. and Rinaldo, a. (2013) Catchment-scale herbicides transport: Theory and application, *Advances in Water Resources*, 52, pp. 232–242. doi: 10.1016/j.advwatres.2012.11.007.

Boving, T. B. and Grathwohl, P. (2001) Tracer diffusion coefficients in sedimentary rocks: correlation to porosity and hydraulic conductivity, *Journal of Contaminant Hydrology*, 53, pp. 85–100. doi: 10.1016/s0169-7722(01)00138-3.

Burri, N. M., Weatherl, R., Moeck, C. and Schirmer, M. (2019) A review of threats to groundwater quality in the Anthropocene, *Science of the Total Environment*, 684, pp. 136–154. doi: 10.1016/j.scitotenv.2019.05.236.

Carrera, J. (1993) An overview of uncertainties in modelling groundwater solute transport, *Journal of Contaminant Hydrology*, 13(1–4), pp. 23–48. doi: 10.1016/0169-7722(93)90049-X.

Carrera, J., Alcolea, A., Medina, A., Hidalgo, J. and Slooten, L. J. (2005) Inverse problem in hydrogeology, *Hydrogeology Journal*, 13(1), pp. 206–222. doi: 10.1007/s10040-004-0404-7.

Chapman, S. W. and Parker, B. L. (2005) Plume persistence due to aquitard back diffusion following dense nonaqueous phase liquid source removal or isolation, *Water Resources Research*, 41(12), pp. 1–16. doi: 10.1029/2005WR004224.

Chavez Rodriguez, L., Ingalls, B., Meierdierks, J., Kundu, K., Streck, T. and Pagel, H. (2021) Modeling bioavailability limitations of atrazine degradation in soils, *Frontiers in Environmental Science*, 9(September), pp. 1–13. doi: 10.3389/fenvs.2021.706457.

Cirpka, O. A. and Kitanidis, P. K. (2000) An advective-dispersive stream tube approach for the transfer of conservative-tracer data to reactive transport,

Water Resources Research, 36(5), pp. 1209–1220. doi: 10.1029/1999WR900355.

Cirpka, O. A. and Valocchi, A. J. (2016) Debates— Stochastic subsurface hydrology from theory topractice: Does stochastic subsurface hydrology help solving practical problems of contaminant hydrogeology? *Journal of the American Water Resources Association*, 5(3), pp. 2–2. doi: 10.1111/j.1752-1688.1969.tb04897.x.

Cromwell, E., Shuai, P., Jiang, P., Coon, E. T., Painter, S. L., Moulton, J. D., Lin, Y. and Chen, X. (2021) Estimating watershed subsurface permeability from stream discharge data using deep neural networks, *Frontiers in Earth Science*, 9(February), pp. 1–13. doi: 10.3389/feart.2021.613011.

D Affonseca, F. M., Finkel, M. and Cirpka, O. A. (2020) Combining implicit geological modeling, field surveys, and hydrogeological modeling to describe groundwater flow in a karst aquifer, *Hydrogeology Journal*. doi: 10.1007/s10040-020-02220-z.

Dell Arciprete, D., Bersezio, R., Felletti, F., Giudici, M., Comunian, A. and Renard, P. (2012) Comparison of three geostatistical methods for hydrofacies simulation: a test on alluvial sediments, *Hydrogeology Journal*, 20(2), pp. 299–311. doi: 10.1007/s10040-011-0808-0.

Enemark, T., Peeters, L. J. M., Mallants, D., Batelaan, O., Valentine, A. P. and Sambridge, M. (2019) Hydrogeological Bayesian hypothesis testing through trans-dimensional sampling of a stochastic water balance model, *Water (Switzerland)*, 11(7). doi: 10.3390/w11071463.

Erdal, D. and Cirpka, O. A. (2019) Global sensitivity analysis and adaptive stochastic sampling of a subsurface-flow model using active subspaces, *Hydrology and Earth System Sciences*, 23(9), pp. 3787–3805. doi: 10.5194/hess-23-3787-2019.

Farlin, J., Gallé, T., Bayerle, M., Pittois, D., Braun, C., El Khabbaz, H., Elsner, M. and Maloszewski, P. (2013) Predicting pesticide attenuation in a fractured aquifer using lumped-parameter models, *GroundWater*, 51(2), pp. 276–285. doi: 10.1111/j.1745-6584.2012.00964.x.

Farlin, J., Gallé, T., Bayerle, M. and Pittois, D. (2022) On using lumped-parameter models in groundwater protection zones to predict aquifer response to reduced agrochemical input, *Journal of Hydrology*, 613(October 2021). doi: 10.1016/j.jhydrol.2022.128306.

Fiori, A., Cvetkovic, V., Dagan, G., Attinger, S., Bellin, A., Dietrich, P., Zech, A. and Teutsch, G. (2016) Debates—stochastic subsurface hydrology from theory to practice: The relevance of stochastic subsurface hydrology to practical problems of contaminant transport and remediation. What is characterization and stochastic theory good for?, *Water Resources Research*, 52(12), pp. 9228–9234. doi: 10.1002/2015WR017525.

Grisak, G. E. and Pickens, J. F. (1981) An analytical solution for solute transport through fractured media with matrix diffusion, *Journal of Hydrology*, 52(1–2), pp. 47–57. doi: 10.1016/0022-1694(81)90095-0.

Gutierrez, A. and Baran, N. (2009) Long-term transfer of diffuse pollution at catchment scale: Respective roles of soil, and the unsaturated and saturated zones (Brevilles, France), *Journal of Hydrology*, 369(3–4), pp. 381–391. doi: 10.1016/j.jhydrol.2009.02.050.

Häfner, H. (1995). Atrazin- und Desethylatrazin-Gehalte nehmen im Grund- und Trinkwasser ab. In Heft 6 (Vol. 47, Issue 6, pp. 144–148).

Halton, J.H. (1960) On the efficiency of certain quasi-random sequences of points in evaluating multi-dimensional integrals, *Numer. Math.*, 2, pp. 84–90. doi: 10.1007/BF01386213

Hammond, G. E., Valocchi, A. J. and Lichtner, P. C. (2005) Application of Jacobian-free Newton-Krylov with physics-based preconditioning to biogeochemical transport, *Advances in Water Resources*, 28(4), pp. 359–376. doi: 10.1016/j.advwatres.2004.12.001.

Harper, A. P., Finger, B. J. and Green, M. P. (2020) Chronic atrazine exposure beginning prenatally impacts liver function and sperm concentration With Multi-Generational Consequences in Mice, *Frontiers in Endocrinology*, 11, pp. 1–13. doi: 10.3389/fendo.2020.580124.

Hsueh, H., Guthke, A., Wöhling, T. and Nowak, W. (2022) Diagnosis of model errors with a sliding time-window Bayesian analysis, *Water Resources Research*, 58(2). doi: 10.1029/2021wr030590.

Jeong, H., Sun, A. Y., Jeon, J., Min, B. and Jeong, D. (2020) Efficient ensemble-based stochastic gradient methods for optimization under geological uncertainty, *Frontiers in Earth Science*, 8(May), pp. 1–14. doi: 10.3389/feart.2020.00108.

Kitanidis, P. K. (1991) Orthonormal residuals in geostatistics: model criticism and parameter estimation, *Mathematical Geology*, 23(5), pp. 741–758. doi: 10.1007/BF02082534.

Kocis, L., and Whiten, W. J. (1997) Computational Investigations of Low-Discrepancy Sequences, *ACM Transactions on Mathematical Software*, Vol. 23, No. 2, pp. 266-294. doi: 10.1145/264029.264064

Koehrer, B. S., Heymann, C., Prousa, F. and Aigner, T. (2010) Multiple-scale facies and reservoir quality variations within a dolomite body - outcrop analog study from the Middle Triassic, SW German Basin, *Marine and Petroleum Geology*, 27(2), pp. 386–411. doi: 10.1016/j.marpetgeo.2009.09.009.

Lapworth, D. J., Baran, N., Stuart, M. E., Manamsa, K. and Talbot, J. (2015) Persistent and emerging micro-organic contaminants in Chalk groundwater of England and France, *Environmental Pollution*, 203, pp. 214–225. doi: 10.1016/j.envpol.2015.02.030.

Lindahl, A. M. L., Kreuger, J., Stenström, J., Gärdenäs, A. I., Alavi, G., Roulier, S. and Jarvis, N. J. (2005) Stochastic modeling of diffuse pesticide losses from a small agricultural catchment, *Journal of Environmental Quality*, 34(4), pp. 1174–1185. doi: 10.2134/jeq2004.0044.

Loos, R., Locoro, G., Comero, S., Contini, S., Schwesig, D., Werres, F., Balsaa, P., Gans, O., Weiss, S., Blaha, L., Bolchi, M. and Gawlik, B. M. (2010) Pan-European survey on the occurrence of selected polar organic persistent pollutants in ground water, *Water Research*, 44(14), pp. 4115–4126. doi: 10.1016/j.watres.2010.05.032.

Loschko, M., Wöhling, T., Rudolph, D. L. and Cirpka, O. A. (2016) Cumulative relative reactivity: a concept for modeling aquifer-scale reactive transport, *Water Resources Research*, 52(10), pp. 8117–8137. doi: 10.1002/2016WR019080.

Mali, N., Korosa, A. and Urbanc, J. (2021) Prevalence of pesticides in Krško-Brežice polje aquifer, *Geologija*, 64(2), pp. 267–288. doi: 10.5474/geologija.2021.015.

McKnight, U. S. and Finkel, M. (2013) A system dynamics model for the screening-level long-term assessment of human health risks at contaminated sites, *Environmental Modelling and Software*, 40, pp. 35–50. doi: 10.1016/j.envsoft.2012.07.007.

McManus, S. L., Coxon, C. E., Mellander, P. E., Danaher, M. and Richards, K. G. (2017) Hydrogeological characteristics influencing the occurrence of pesticides and pesticide metabolites in groundwater across the Republic of Ireland, *Science of the Total Environment*, 601–602, pp. 594–602. doi: 10.1016/j.scitotenv.2017.05.082.

Müller, G. (2008) History of the Discovery and Development of Triazine Herbicides, pp. 13–29. doi: 10.1016/B978-044451167-6.50005-2.

Nasseri, S., Dehghani, M., Amin, S., Naddafi, K. and Zamanian, Z. (2009) Fate of atrazine in the agricultural soil of corn fields in Fars province of Iran, *Journal of Environmental Health Science and Engineering*, 6(4), pp. 223–232.

Osenbrück, K., Blendinger, E., Leven, C., Rügner, H., Finkel, M., Jakus, N., Schulz, H. and Grathwohl, P. (2021) Nitrate reduction potential of a fractured Middle Triassic carbonate aquifer in southwest Germany, *Hydrogeology*, doi:10.1007/s10040-021-02418-9

Palermo, D., Aigner, T., Nardon, S. and Blendinger, W. (2010) Three-dimensional facies modeling of carbonate sand bodies: Outcrop analog study in an epicontinental basin (Triassic, southwest Germany), *AAPG Bulletin*, 94(4), pp. 475–512. doi: 10.1306/08180908168.

Parker, B. L., Chapman, S. W. and Guilbeault, M. A. (2008) Plume persistence caused by back diffusion from thin clay layers in a sand aquifer following TCE source-zone hydraulic isolation, *Journal of Contaminant Hydrology*, 102(1–2), pp. 86–104. doi: 10.1016/j.jconhyd.2008.07.003.

Pathak, R. K. and Dikshit, A. K. (2012) Atrazine and Human health, *International Journal of Ecosystem*, 1(1), pp. 14–23. doi: 10.5923/j.ije.20110101.03.

Petrova, E., Kortunov, E., Mayer, K. U., Grathwohl, P. and Finkel, M. (2022) Travel time-based modelling of nitrate reduction in a fractured limestone aquifer by pyrite and iron carbonates under pore size limitation, *Journal of Contaminant Hydrology*, 248. doi: 10.1016/j.jconhyd.2022.103983.

Pietrzak, D., Kania, J., Kmiecik, E., Malina, G. and Wątor, K. (2020) Fate of selected neonicotinoid insecticides in soil–water systems: current state of the art and knowledge gaps, *Chemosphere*, 255. doi: 10.1016/j.chemosphere.2020.126981.

Poeter, E. and Townsend, P. (1994) Assessment of critical flow path for improved remediation management, *Groundwater*. doi: 10.1111/j.1745-6584.1994.tb00661.x.

Rahman, M. M., Liedl, R. and Grathwohl, P. (2004) Sorption kinetics during macropore transport of organic contaminants in soils: laboratory experiments and analytical modeling, *Water Resources Research*, 40(1), p. n/a--n/a. doi: 10.1029/2002WR001946.

Ramgraber, M., Weatherl, R., Blumensaat, F. and Schirmer, M. (2021) Non-Gaussian parameter inference for hydrogeological models using Stein variational gradient descent, *Water Resources Research*, 57(4). doi: 10.1029/2020WR029339.

Reberski, L. J., Terzić, J., Maurice, L. D. and Lapworth, D. J. (2022) Emerging organic contaminants in karst groundwater: a global level assessment, *Journal of Hydrology*, 604. doi: 10.1016/j.jhydrol.2021.127242.

Riva, M., Guadagnini, L., Guadagnini, a., Ptak, T. and Martac, E. (2006) Probabilistic study of well capture zones distribution at the Lauswiesen field site, *Journal of Contaminant Hydrology*, 88(1–2), pp. 92–118. doi: 10.1016/j.jconhyd.2006.06.005.

Rojas, R., Repetto, G., Morillo, J. and Usero, J. (2022) Sorption/Desorption and kinetics of atrazine, chlorfenvinphos, endosulfan sulfate and trifluralin on agro-industrial and composted organic wastes, *Toxics*, 10(2), p. 85. doi: 10.3390/toxics10020085.

Ross, M. K., Jones, T. L. and Filipov, N. M. (2009) Disposition of the herbicide 2-chloro-4-(ethylamino)-6- (isopropylamino)-s-triazine (Atrazine) and its major metabolites in mice: a liquid chromatography/mass spectrometry analysis of urine, plasma, and tissue levels, *Drug Metabolism and Disposition*, 37(4), pp. 776–786. doi: 10.1124/dmd.108.024927.

Roulier, S., Baran, N., Mouvet, C., Stenemo, F., Morvan, X., Albrechtsen, H. J., Clausen, L. and Jarvis, N. (2006) Controls on atrazine leaching through a soil-unsaturated fractured limestone sequence at Brévilles, France, *Journal of Contaminant Hydrology*, 84(1–2), pp. 81–105. doi: 10.1016/j.jconhyd.2005.12.004.

Sánchez-León, E., Leven, C., Erdal, D. and Cirpka, O. A. (2020) Comparison of two ensemble-kalman filter based methods for estimating aquifer parameters from real 3-d hydraulic and tracer tomographic tests, *Geosciences (Switzerland)*, 10(11), pp. 1–30. doi: 10.3390/geosciences10110462.

Schauer, M. and Aigner, T. (1997) Cycle stacking pattern, diagenesis and reservoir geology of peritidal dolostones, Trigonodus-Dolomite, Upper Muschelkalk (Middle Triassic, SW-Germany), *Facies*, 37(1), pp. 99–113. doi: 10.1007/BF02537373.

Schwab, A. P., Splichal, P. A. and Banks, M. K. (2006) Persistence of atrazine and alachlor in ground water aquifers and soil, *Water, Air, and Soil Pollution*, 171(1–4), pp. 203–235. doi: 10.1007/s11270-005-9037-2.

Scott, H. D. and Pnillips, R. E. (1973) Self-diffusion coefficients of selected herbicides in water and estimates of their transmission factors in soil, *Soil Science Society of America Journal*, 37(i), pp. 965–967. doi: /10.2136/sssaj1973.03615995003700060046x

Selg, M., Mair, C. and Bauer, M. (2005) Die Altersstruktur des Kluft- und Karstgrundwassers im Oberjura der Schwäbischen Alb und deren Bedeutung für den anhaltenden Atrazinaustrag, *Berichte der naturforschenden Gesellschaft zu Freiburg im Breisgau*, 95.

Shuwen L., Zhen Z., Xiaoping Z., Lei R., Weijian W., Weijian Z., Yijie C., Dayi Z., Zhiguang S., Zhong L., Yan-Qiu L. (2021) Accelerated atrazine degradation and altered metabolic pathways in goat manure assisted soil bioremediation, *Ecotoxicology and Environmental Safety*, 221, doi: 10.1016/j.ecoenv.2021.112432

Sidborn, M. and Neretnieks, I. (2007) Long term redox evolution in granitic rocks: modelling the redox front propagation in the rock matrix, *Applied Geochemistry*, 22(11), pp. 2381–2396. doi: 10.1016/j.apgeochem.2007.05.007.

Silva, E., Mendes, M. P., Ribeiro, L. and Cerejeira, M. J. (2012) Exposure assessment of pesticides in a shallow groundwater of the Tagus vulnerable zone (Portugal): a multivariate statistical approach (JCA), *Environmental Science and Pollution Research*, 19(7), pp. 2667–2680. doi: 10.1007/s11356-012-0761-z.

Soler, J. M., Meng, S., Moreno, L., Neretnieks, I., Liu, L., Kekäläinen, P., Hokr, M., Říha, J., Vetešník, A., Reimitz, D., Višňák, J., Vopálka, D., Kröhn, K. P., Tachi, Y., Ito, T., Svensson, U., Iraola, A., Trinchero, P., Voutilainen, M., Deissmann, G., Bosbach, D., Park, D. K., Ji, S. H., Gvoždík, L., Milický, M., Polák, M., Gylling, B. and William Lanyon, G. (2022) Modelling of the LTDE-SD radionuclide diffusion experiment in crystalline rock at the Äspö Hard Rock Laboratory (Sweden), Geologica Acta, 20(7), pp. 1–32. doi: 10.1344/GeologicaActa2022.20.7.

Stuart, M., Lapworth, D., Crane, E. and Hart, A. (2012) Review of risk from potential emerging contaminants in UK groundwater, *Science of the Total Environment*, 416, pp. 1–21. doi: 10.1016/j.scitotenv.2011.11.072.

Suckow, A. (2014) The age of groundwater - definitions, models and why we do not need this term, *Applied Geochemistry*. 50, 222–230, doi: 10.1016/j.apgeochem.2014.04.016.

Sudicky, E. A. and Frind, E. O. (1984) Contaminant transport in fractured porous media: analytical solution for a two-member decay chain in a single fracture, *Water Resources Research*, 20(7), pp. 1021–1029. doi: 10.1029/WR020i007p01021.

Tang, D. H., Frind, E. O. and Sudicky, E. A. (1981) Contaminant transport in fractured porous media: analytical solution for a single fracture, *Water Resources Research*, 17(3), pp. 555–564. doi: 10.1029/WR017i003p00555.

Tappe, W., Groeneweg, J. and Jantsch, B. (2002) Diffuse atrazine pollution in German aquifers, *Biodegradation*, 13(1), pp. 3–10. doi: 10.1023/A:1016325527709.

Tartakovsky, A. M., Tartakovsky, G. D. and Scheibe, T. D. (2009) Effects of incomplete mixing on multicomponent reactive transport, *Advances in Water Resources*, 32(11), pp. 1674–1679. doi: 10.1016/j.advwatres.2009.08.012.

Vonberg, D., Vanderborght, J., Cremer, N., Pütz, T., Herbst, M. and Vereecken, H. (2014) 20 years of long-term atrazine monitoring in a shallow aquifer in western Germany, *Water Research*, 50. doi: 10.1016/j.watres.2013.10.032.

Warnecke, M. and Aigner, T. (2019) Asymmetry of an epicontinental basin-facies, cycles, tectonics and hydrodynamics: the Triassic Upper Muschelkalk, South Germanic Basin, *The Depositional Record*, (January). doi: 10.1002/dep2.59.

Zhou, H., Gómez-Hernández, J. J. and Li, L. (2014) Inverse methods in hydrogeology: Evolution and recent trends, *Advances in Water Resources*, 63, pp. 22–37. doi: 10.1016/J.ADVWATRES.2013.10.014.

OVERALL CONCLUSIONS AND OUTLOOK

All parts of this thesis aimed to study the reactive transport of solutes and reduce parametric uncertainty in a fractured aquifer. By performing numerical modeling, we present a detailed investigation to provide a better understanding of the redox and reactive processes in two-dimensional fractured media. Verified with field observations and measurements of nitrate, atrazine, groundwater age isotopes, and sorption coefficients of different facies of the aquifer, numerical models were employed to provide insights into pore size-limited denitrification, groundwater age distributions, and atrazine transport in a fractured limestone aquifer (Muschelkalk). Based on the conceptual model of fully coupled travel time-based reactive transport simulations, this work tries to link explicitly geochemical processes in the fractured system to the assessment of parameter uncertainty. Stochastic simulation of reactive transport facilitated by a spatially implicit approach of the travel time was a helpful combination for obtaining new knowledge about the Muschelkalk fractured aquifer system. At the same time, the work highlights that sophisticated mechanistic modeling is necessary for the correct reflection of the multicomponent diffusion and redox reactions in fractured aquifers. Addressing uncertainty was done by accounting for multiple components within a stochastic framework for age tracers considering different scenarios developed for nitrate and a probabilistic network for trend prediction of atrazine.

In more details, the main outcomes of this work can be summarized as follows:

- **Age tracers - isotopes.** The necessity of using reactive transport models of isotopes instead of the commonly used analytical equation to estimate groundwater age was confirmed by comparing advective and estimated groundwater age in the fracture. Surrogate modeling, specifically, Gaussian Processes Emulation was employed for pre-selection of isotope model parameters Multiobjective stochastic optimization of groundwater isotopes resulted in estimates of groundwater ages of the Muschelkalk to vary from 1 to 62 years. The majority of locations indicate groundwater captured from the micritic limestone facies with porosity of less than 5 % and large fractures. Although both, repeated measurements of the same component

and single measurements of different components can assist in uncertainty reduction, using multiple components provided narrower posterior distributions for the isotope study. Considering a second and a third tracer helps to reduce the uncertainty in the mean travel time by a factor of 2 - 5 and to get rid of the bimodality in posterior distributions. Worth mentioning that using several components of different reactive behavior and origins helps to reduce a possible conceptual bias compared to using just one component. This holds, of course, only when no additional uncertainty was introduced by the parameterization of the new component. The study confirmed that surrogate modeling is a helpful tool for pre-evaluating of the parameter combinations and finally leads to successful model outcomes. Besides travel time distributions, a good guess about possible porosity and fracture apertures can be deduced from the simulation results for each location. Within the Muschelkalk aquifer, however, it seems that there is not a single effective porosity and aperture value that can be used to describe reactive transport within the Ammer river catchment.

- **Nitrate.** This work for the first time confirmed the hypothesis of sufficient denitrification even if limited solely to the fracture with a supply of electron donors by diffusion out of the rock matrix. Careful parameterization of the geochemistry and reaction system, as well as facies-specific porosity and amounts/distribution of iron-bearing minerals and fracture apertures, are essential for the correct quantification of denitrification. It is also important to distinguish between concentrations of different iron-bearing minerals, for example, pyrite and siderite (and saddle dolomites). Model calibration should be then performed by applying the posterior parameter distributions of the travel time, mixing, aperture and porosities, and can be coupled as a reactive curve for the spatially explicit simulation results. A further remarkable research destination could comprise grain-scale simulations of the rock matrix evolution under denitrification and pyrite oxidation conditions, and the use of secondary minerals such as different iron hydroxides as fingerprints of the rock corrosion. Some uncertainty of the mineral distributions in the rock matrix, armoring of the mineral surface, additional minerals inhabiting the fracture, and being freely available for bacteria, need to be explored.

Legacy compounds – atrazine. Analytical approximations of the travel distance and value of the maximum concentration developed in this work reflect the sensitivity of the sorptive compound transport to physical and chemical parameters.

Stochastic simulations based on the analytical solution of the transport equation and parameter ranges of the Muschelkalk aquifer allowed us to work out the most sensitive parameters for the atrazine transport. The aperture value is one of the most influential yet most uncertain in time-space variability parameters. However, based on the available analytical solutions and the time window of interest (10-1000 years), relevant aperture values are likely to vary within a quite narrow range (0.1-0.5 mm). On the other side, a combination of the cubic law and the available fracture aperture range within the catchment results in a rather young possible advective travel time which is generally confirmed by the isotope groundwater age estimates. Interestingly, the value of the maximum relative concentration of a sorptive compound depends only on the duration of the plume and the model time. Measured atrazine isotherms in all three facies types of the Muschelkalk aquifer in the Ammer catchment reflect almost linear sorption. Stochastic simulations of the Muschelkalk aquifer resulted in a series of ensemble-based model predictions. Due to the mass exchange with the rock matrix, only very young groundwater with travel times less than 5 years is likely to exceed threshold values of atrazine in all facies types. Although sorption coefficients and porosity are varying within three described rock facies types, in all of them, if the measured concentration in 2022 exceeds the legal limit (which could happen with relatively young groundwater and with sufficiently high input concentration), it will take centuries until the concentration is decreased under the limit. This conclusion might serve as an alarm for careful consideration when applying and/or allowing leachate of the pesticides and other sorptive contaminants in the groundwater. For example, in the case of DNAPL contamination where input concentration is a factor 1000 above the legal limit, increases in natural remediation time are $250t_0$.

Considering achievements and challenges of this work, further suggestions on the advance of the research in this area include:

- **Conceptual model selection.** As noticed above, a detailed and unique parameterization of the geochemical model on a catchment scale seems to be close to impossible. At the same time, proper groundwater management demands concrete knowledge about the hydrosystem functioning on the catchment scale. Generally saying, the golden cut between model complexity and uncertainty needs to be established for any type of modeling task (compound, reactions to being considered,

input scenarios, and rhythms). Scenario testing of the nitrate model has particularly highlighted the importance of careful conceptual model selection.

- **Model upscaling/multiscaling.** The current challenge of the model upscaling is a global issue for any natural system. We am deeply convinced that current IT-inspired techniques (AI, ML, GPE, data assimilation) along with the empowerment of computational technologies will make a step forward in the next years. This still comes with a price: the correctness of the AI technology, just like with the modeling, depends massively on the modeler's profile: discipline-fitting education, experience, and background. Besides computational costs, a deeper view of the scale-relevant physical processes is required along with keeping the eye on the mass balance conservation.

- **Technological development.** As confirmed in this work, physics-based modelling accounting for relevant reactive transport processes is decisive for model predictions. Although comprehensive characterization of fractured aquifers on the catchment scale is an expensive goal and is likely unreachable, computational technology was advancing considerably in the last decades, creating new methods involving machine learning and big data analysis. Conventional time-space explicit modelling seems to be even more demanding than different reality analogues like replacing the coordinate with the travel time, applying surrogates for pre-evaluation or sensitivity analysis, or cellular automata-based modelling based on the mass balance computation. At the moment, however, this task is only feasible within high computational capacity (e.g. supercomputing) and is not available for the wide auditory of practitioners and scientists.

- **Advances in common data management.** Possible development of the data management and availability, and establishment of free access to information (open source software, free access to the research data management and scientific papers) within a uniformly organized data framework would significantly improve the modeling quality by creating data abundance. If more data in common formatting is available, the modern tools could be used to improve the performance of the models and bridge the interdisciplinary gap for creating integrated hydro system models.

- **Openness, acceptance and encouragement to interdisciplinary research.** Whereas creating a global database network and developing

computational tools seems to be a predictable continuation of the (geo)science development, the integrative part requires fruitful communication between different scientific fields, to improve the quality of a single modeler and the modeling community. I am deeply convinced that the scientific community will profit from being more integrated and collaborative, and it is hard to say which factor – a collaborative community of interdisciplinary researchers or advances in computational technologies, is more important. The first factor prioritizes cross-scientific interaction, data sharing, and connection of different scientific directions over the technological progress, and tends to overtake it.

The attempt to connect detailed hydrogeochemical modelling with catchment-scale travel time models with a detour to the universe of stochastic modelling was our small contribution.

SUPPLEMENTARY MATERIALS

SUPPLEMENTARY MATERIAL 1. COMPOUNDS AND MINERALS CONCENTRATION DISTRIBUTION IN THE MODEL DOMAIN AT THE START (SIMULATION TIME T = 10000 YEARS) AND THE END (T = 10100 YEARS) OF NITRATE INPUT FOR THE REFERENCE MODEL SCENARIO.

TRAVEL TIME-BASED MODELLING OF NITRATE REDUCTION IN A FRACTURED LIMESTONE AQUIFER BY PYRITE AND IRON CARBONATES UNDER PORE SIZE LIMITATION

Compounds and minerals concentration distribution in the model domain at the start (simulation time t = 10000 years) and the end (t = 10100 years) of nitrate input for the reference model scenario.

1 Conditions at the start of the nitrate input (after 10 000 years of oxygen ingress)

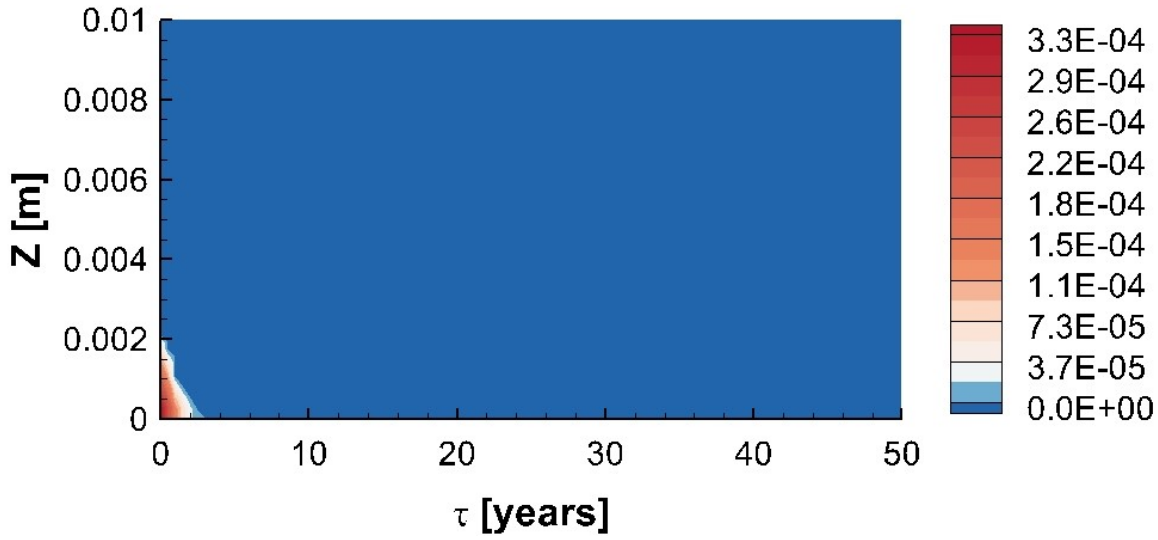

Fig. S.M.1 .1.1 Simulation results for the reference scenario after 10000 years O_2 input (t = 10000 years): concentration distribution of O_2 [mol/l] in the model domain close to the fracture (0 m ≤ z ≤ 0.1 m)

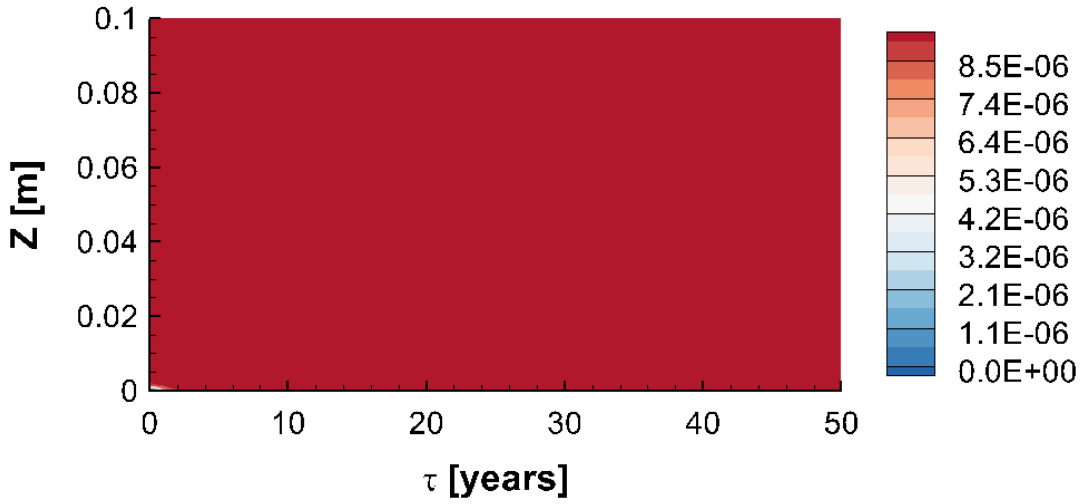

Fig. S.M.1 .1.2 Simulation results for the reference scenario after 10000 years O_2 input (t = 10000 years): concentration distribution of Fe^{2+} [mol/l] in the model domain close to the fracture (0 m ≤ z ≤ 0.1 m)

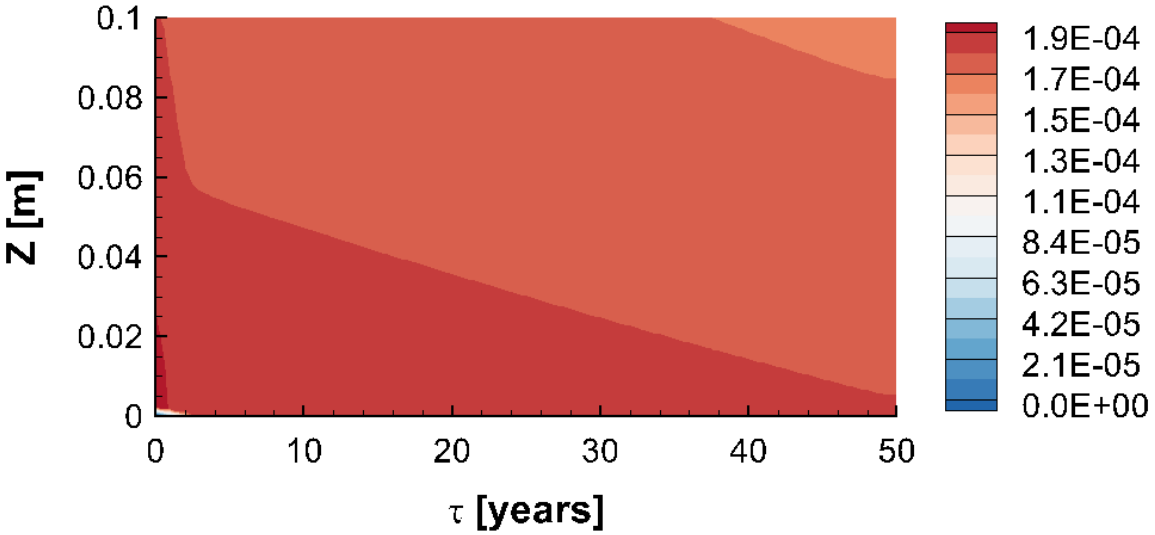

Fig. S.M.1 .1.3 Simulation results for the reference scenario after 10000 years O_2 input (t = 10000 years): concentration distribution of SO_4^{2-} [mol/l] in the model domain close to the fracture (0 m ≤ z ≤ 0.1 m)

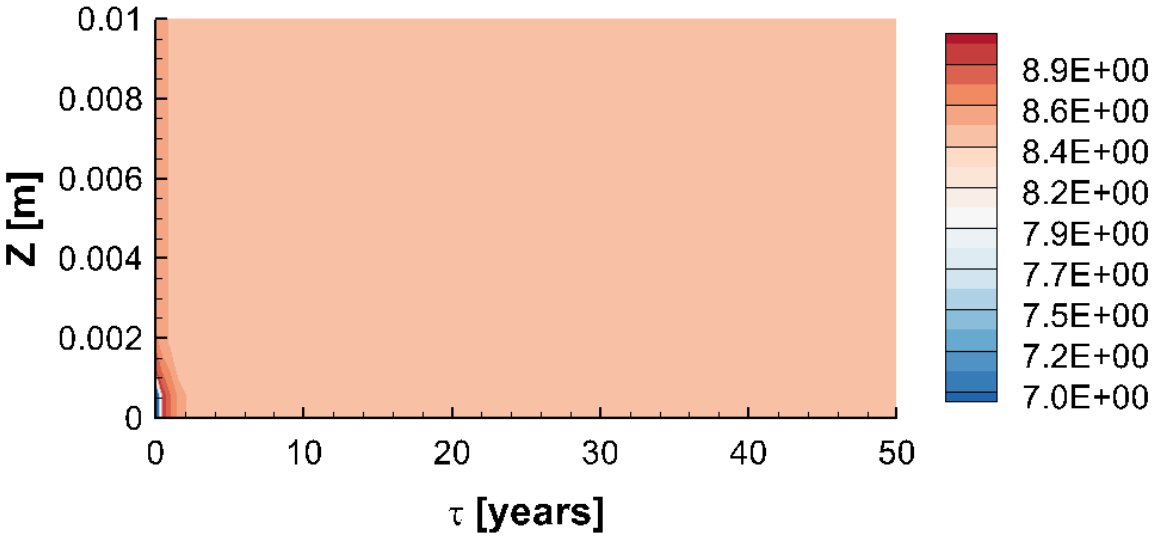

Fig. S.M.1 .1.4 Simulation results for the reference scenario after 10000 years O_2 input (t = 10000 years): concentration distribution of pH in the model domain close to the fracture (0 m ≤ z ≤ 0.1 m)

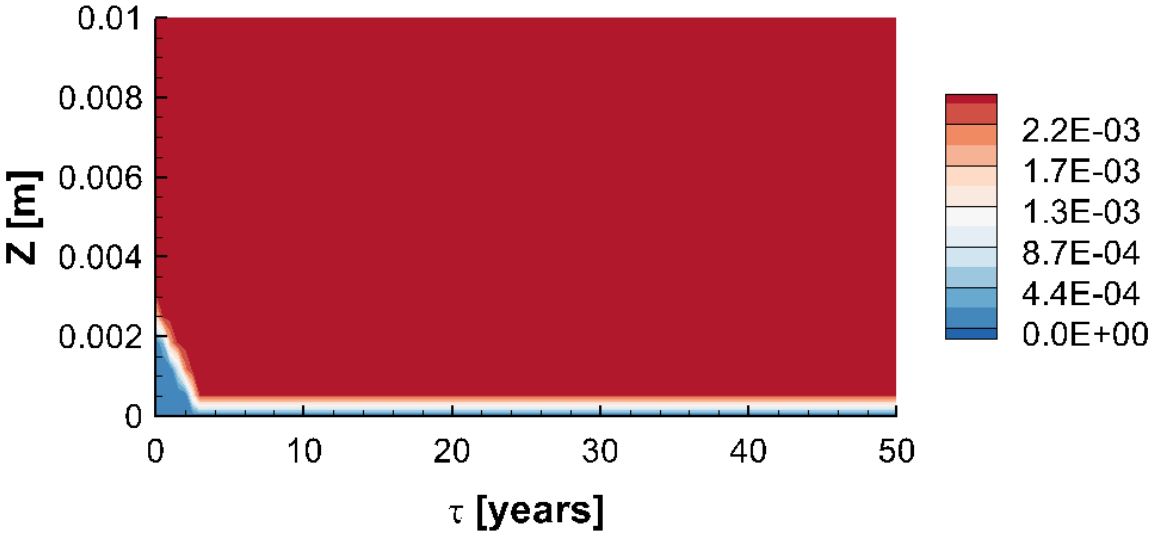

Fig. S.M.1 .1.5 Simulation results for the reference scenario after 10000 years O_2 input (t = 10000 years): distribution of pyrite in the model domain close to the fracture (0 m ≤ z ≤ 0.1 m)

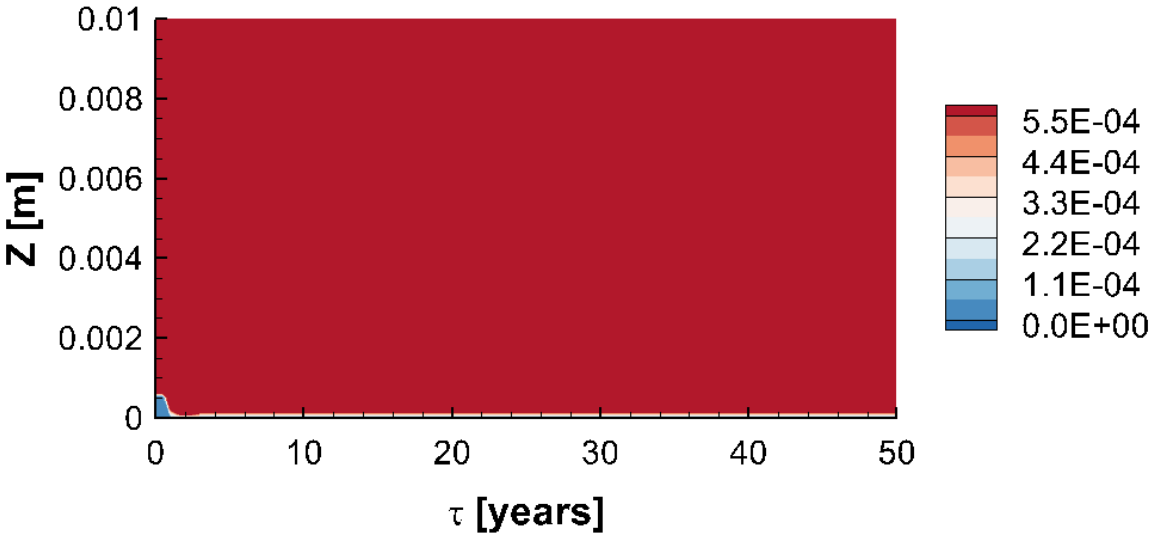

Fig. S.M.1 .1.6 Simulation results for the reference scenario after 10000 years O_2 input (t = 10000 years):: distribution of siderite [Vol.%] in the model domain close to the fracture (0 m ≤ z ≤ 0.1 m)

.2 Concentration in the rock matrix after 100 years of NO_3^- input

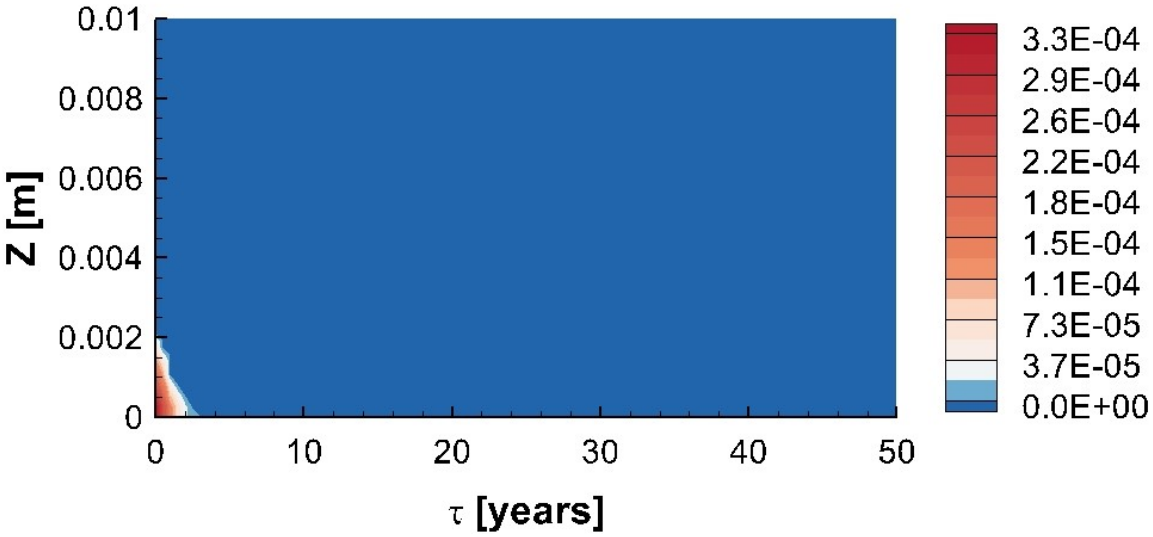

Fig. S.M.1 .2.1 Simulation results for the reference scenario after 100 years NO_3^- input (t = 10100 years): concentration distribution of O_2 [mol/l] in the model domain close to the fracture (0 m ≤ z ≤ 0.1 m)

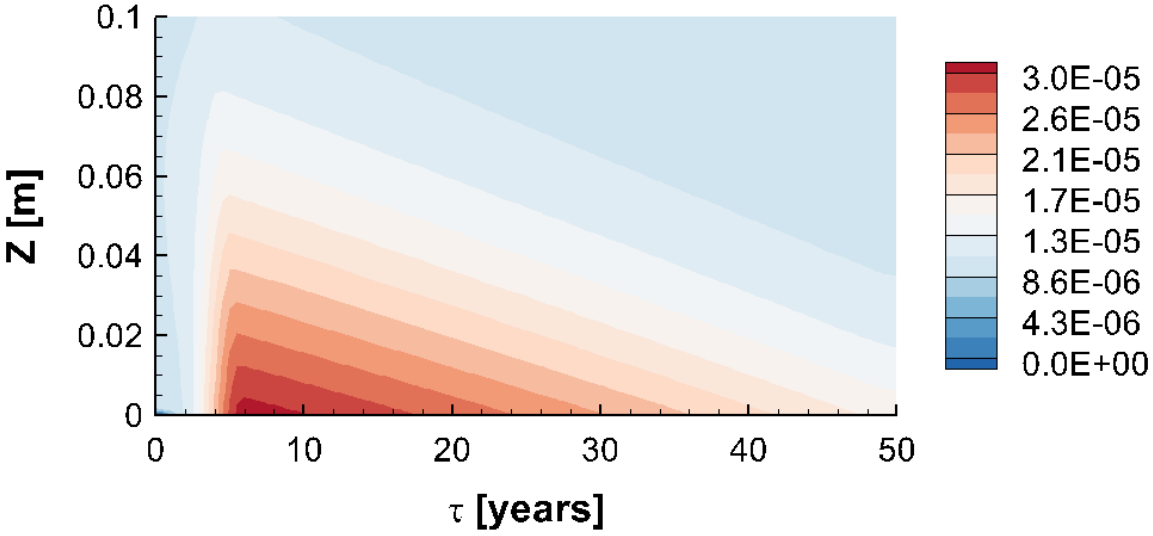

Fig. S.M.1 .2.2 Simulation results for the reference scenario after 100 years NO_3^- input (t = 10100 years): concentration distribution of Fe^{2+} [mol/l] in the model domain close to the fracture (0 m ≤ z ≤ 0.1 m)

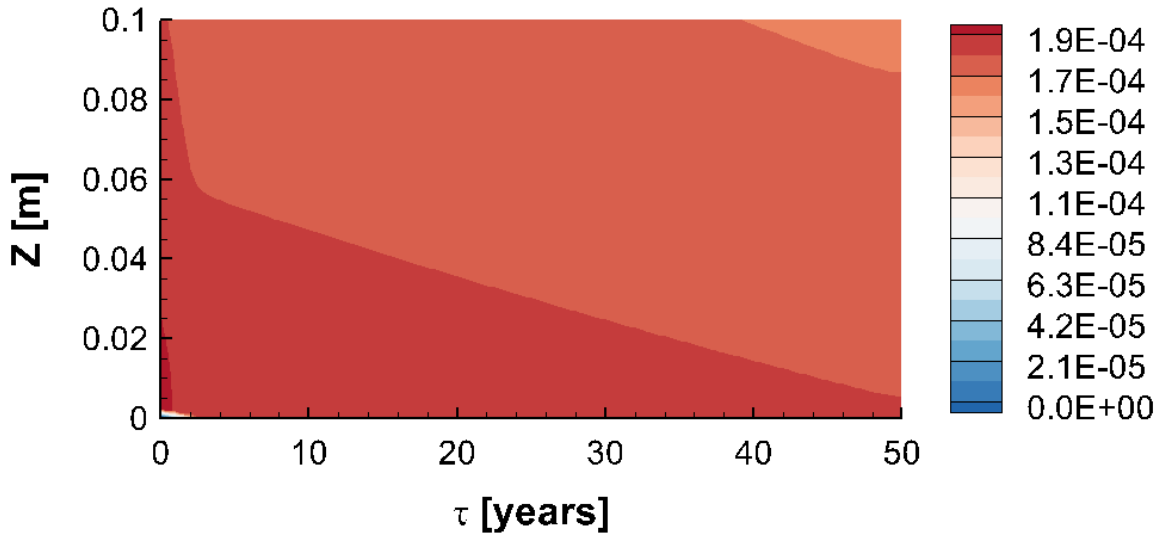

Fig. S.M.1 .2.3 Simulation results for the reference scenario after 100 years NO_3^- input (t = 10100 years): concentration distribution of SO_4^{2-} [mol/l] in the model domain close to the fracture (0 m ≤ z ≤ 0.1 m)

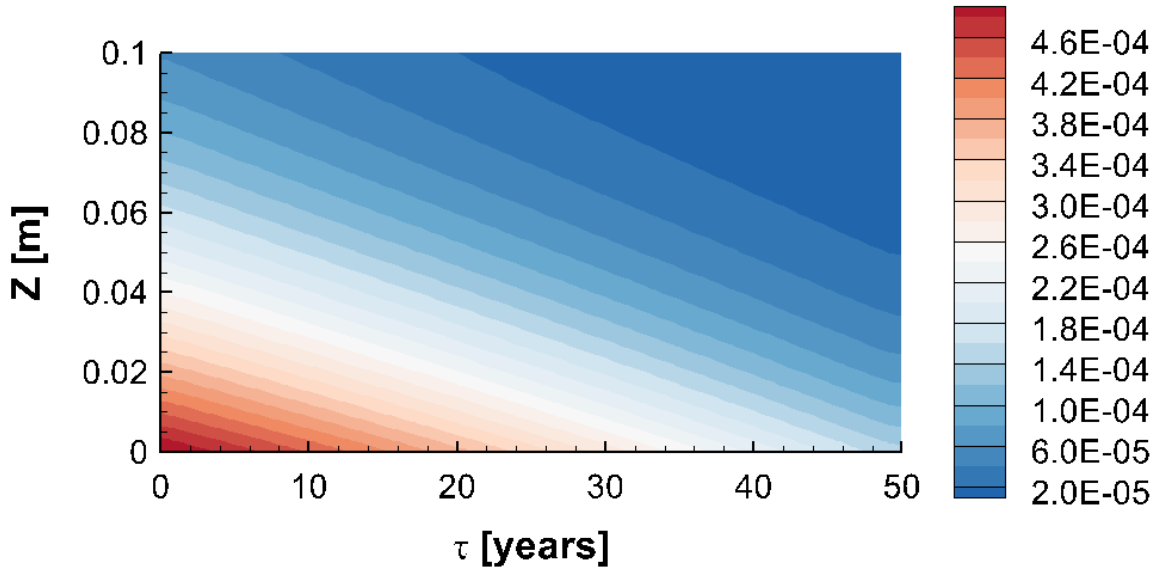

Fig. S.M.1 .2.4 Simulation results for the reference scenario after 100 years NO_3^- input (t = 10100 years): concentration distribution of Conservative tracer [mol/l] in the model domain close to the fracture (0 m ≤ z ≤ 0.1 m)

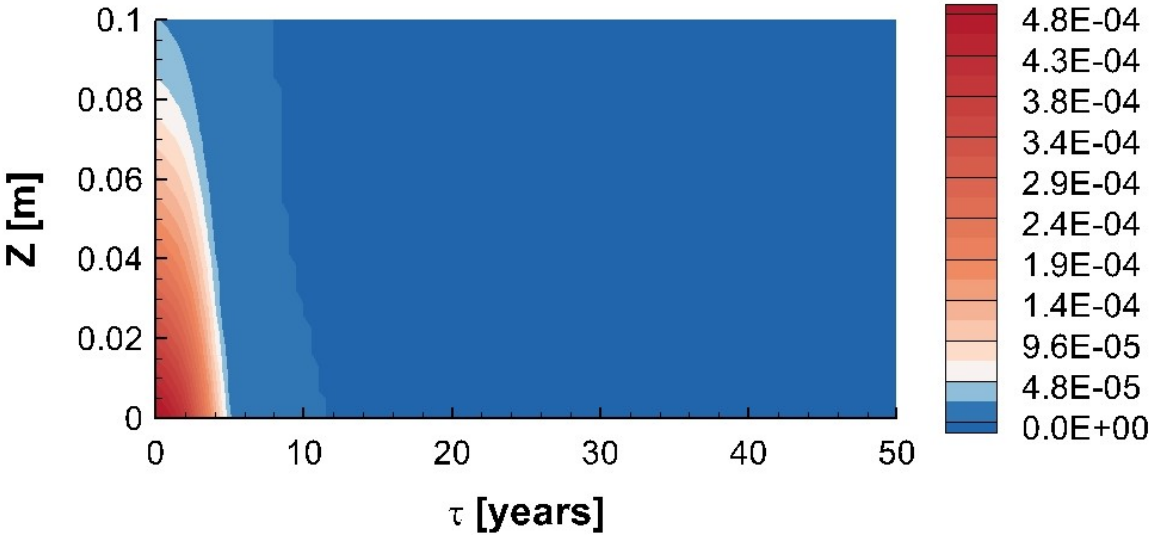

Fig. S.M.1 .2.5 Simulation results for the reference scenario after 100 years NO_3^- input (t = 10100 years): concentration distribution of NO_3^- [mol/l] in the model domain close to the fracture (0 m ≤ z ≤ 0.1 m)

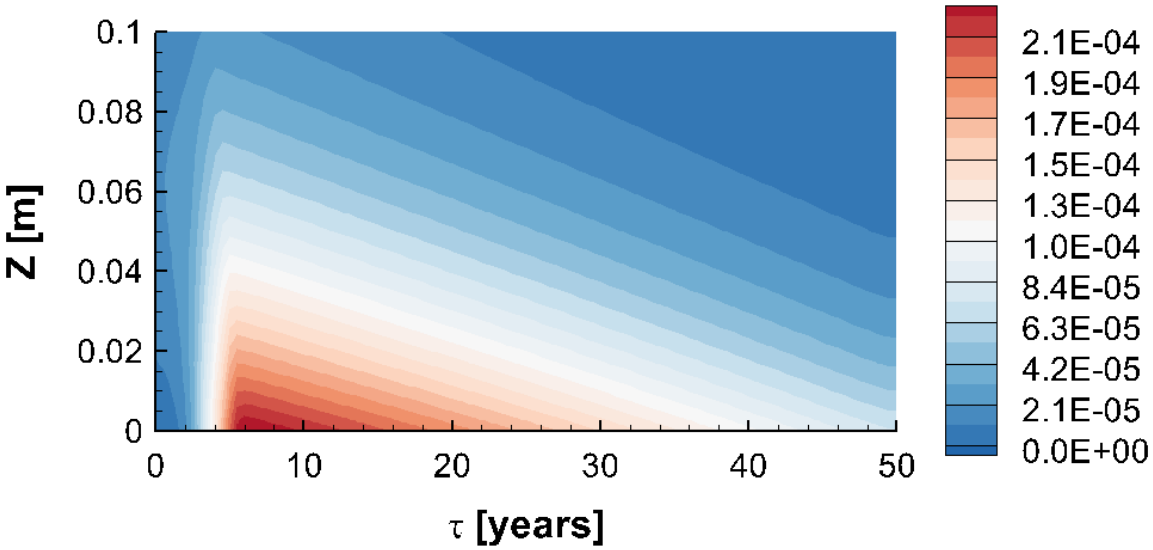

Fig. S.M.1 .2.6 Simulation results for the reference scenario after 100 years NO_3^- input (t = 10100 years): concentration distribution of N_2 [mol/l] in the model domain close to the fracture (0 m ≤ z ≤ 0.1 m)

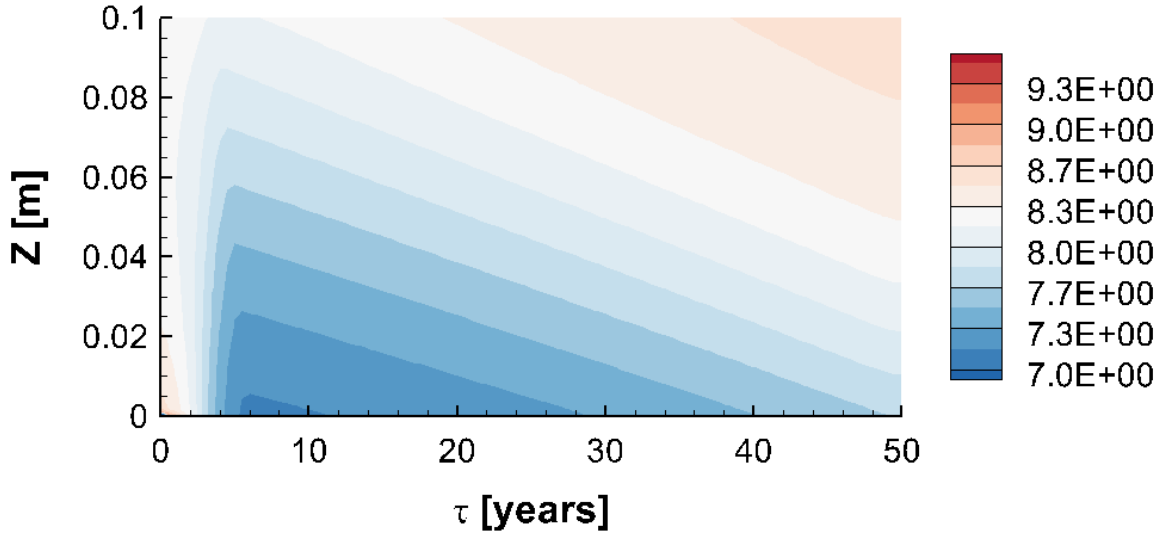

Fig. S.M.1 .2.7 Simulation results for the reference scenario after 100 years NO_3^- input (t = 10100 years): concentration distribution of pH in the model domain close to the fracture (0 m ≤ z ≤ 0.1 m)

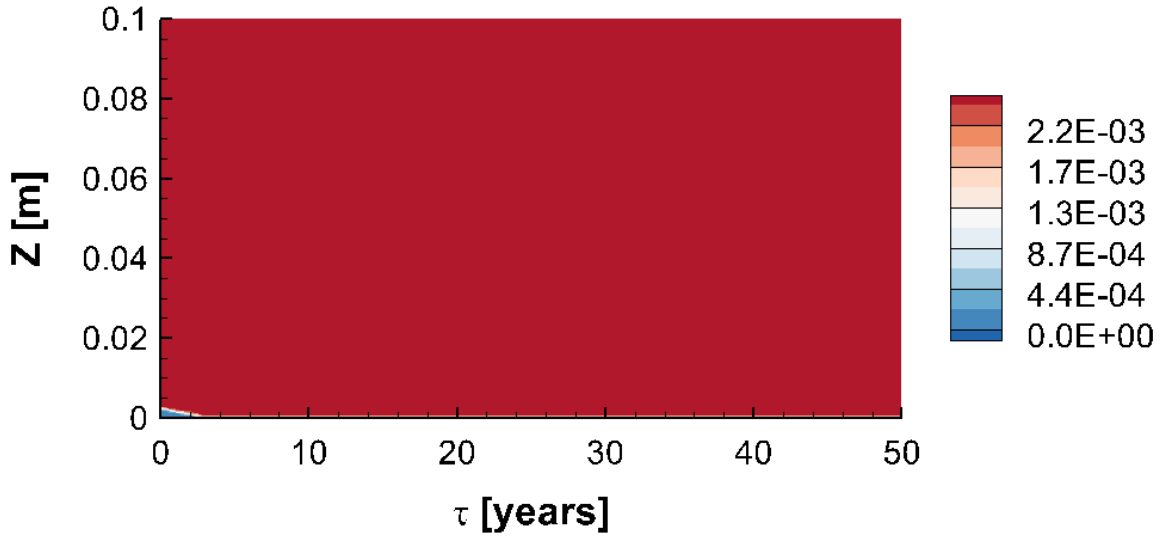

Fig. S.M.1 .2.8 Simulation results for the reference scenario after 100 years NO_3^- input (t = 10100 years): distribution of pyrite in the model domain close to the fracture (0 m ≤ z ≤ 0.1 m)

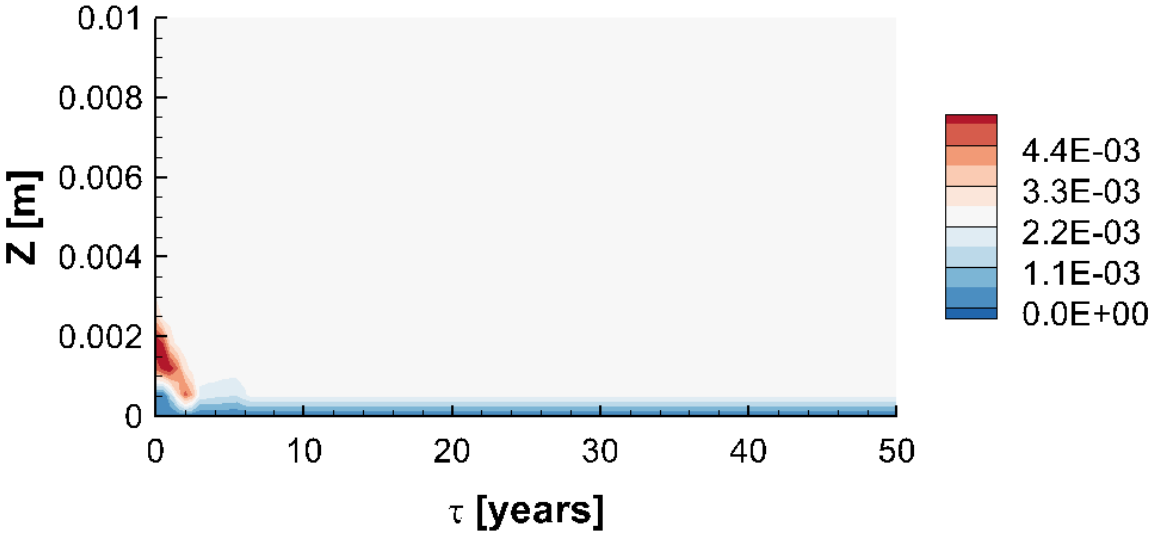

Fig. S.M.1 .2.9 Simulation results for the reference scenario after 100 years NO_3^- input (t = 10100 years): distribution of siderite in the model domain close to the fracture (0 m ≤ z ≤ 0.1 m)

SUPPLEMENTARY MATERIAL 2. COMPOUNDS AND MINERALS CONCENTRATION DISTRIBUTION IN THE MODEL DOMAIN AT THE START (SIMULATION TIME T = 10000 YEARS) AND THE END (T = 10100 YEARS) OF NITRATE INPUT FOR THE 'SINGLE-MINERAL' MODEL SCENARIO CONSIDERING PYRITE AS ELECTRON DONOR.

TRAVEL TIME-BASED MODELLING OF NITRATE REDUCTION IN A FRACTURED LIMESTONE AQUIFER BY PYRITE AND IRON CARBONATES UNDER PORE SIZE LIMITATION

Scenario tests whether non-biotic oxidation of pyrite alone provides enough Fe^{2+} to the fracture to attenuate nitrate. Pyrite is the only source of the electron donor in the system. Pyrite oxidation results in the consumption of oxygen already at the inlet and oxygen penetrates only a few cm into the rock matrix even after preconditioning for 10000 a as in the base scenario. In the fracture oxygen is depleted already after 5 years of travel time (Fig. A.1, S.M. 10). Fe^{2+} diffuses from the matrix to the fracture and potentially reacts with NO_3^- (Fig. A.1). However, the flux of Fe^{2+} into the fracture in this scenario is far too low and does not lead to a significant nitrate reduction. Thus NO_3^- behaves almost like an conservative tracer being only slighty retarded by diffusion into the matrix. Ferrihydrite coatings are produced as a result of pyrite oxidation, but the volume is quite low and amouts to less than 0.1% of the aperture width (after 10000 a in the first 5 a of residence time). Goethite precipitation as further product of the reaction of Fe with nitrate is even lower.

.1 Conditions at the start of the nitrate input (after 10 000 years of oxygen ingress)

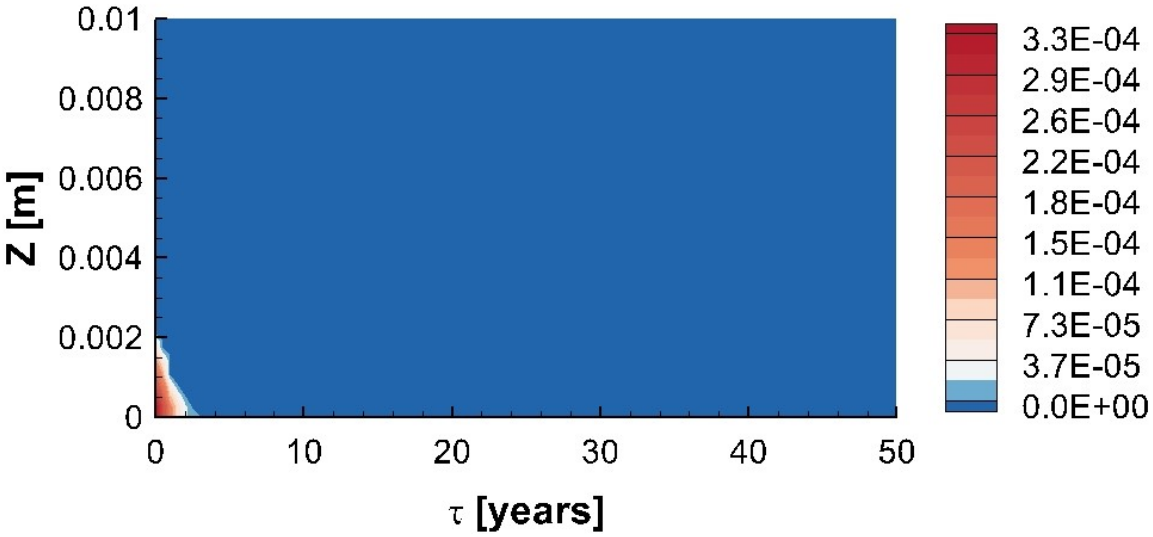

Fig. S.M.2 .1.1 Simulation results for scenario 'only-pyrite' after 10000 years O_2 input (t = 10000 years): concentration distribution of O_2 [mol/l] in the model domain close to the fracture (0 m ≤ z ≤ 0.1 m)

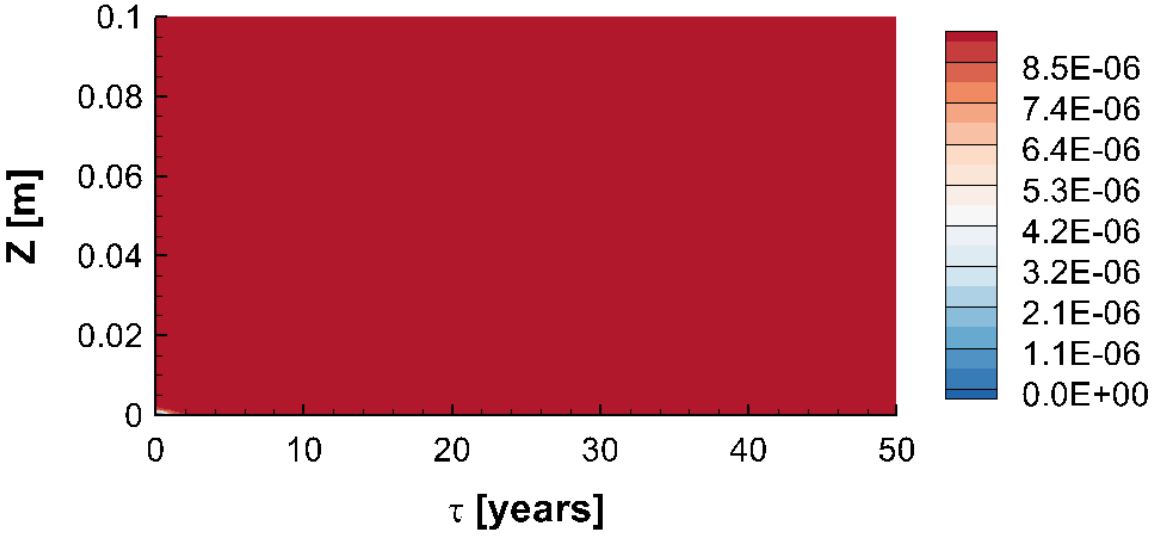

Fig. S.M.2 .1.2 Simulation results for scenario 'only-pyrite' after 10000 years O_2 input (t = 10000 years): concentration distribution of Fe^{2+} [mol/l] in the model domain close to the fracture (0 m ≤ z ≤ 0.1 m)

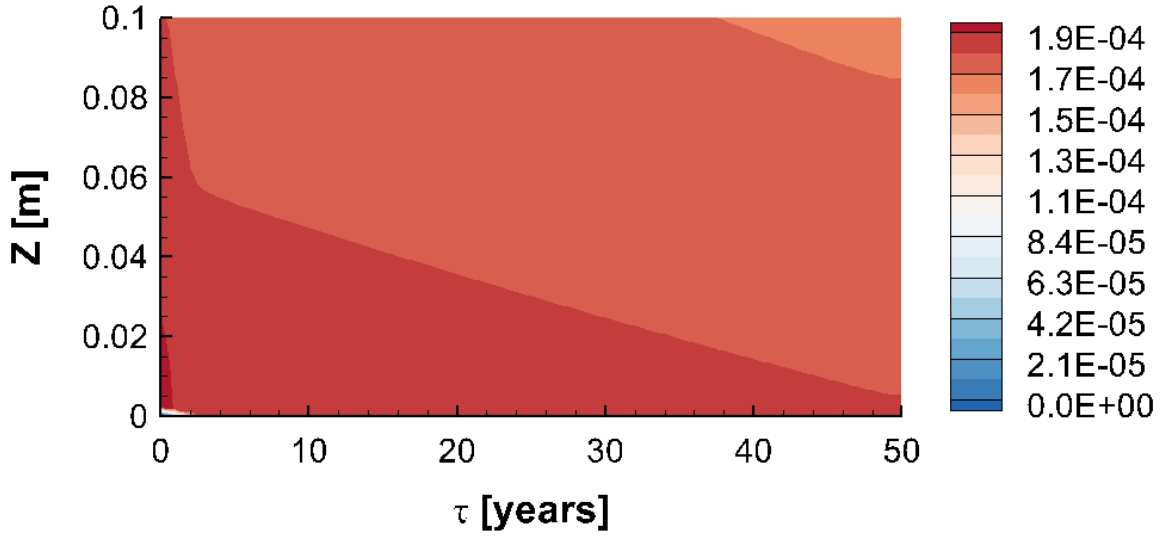

Fig. S.M.2 .1.3 Simulation results for scenario 'only-pyrite' after 10000 years O_2 input (t = 10000 years): concentration distribution of SO_4^{2-} [mol/l] in the model domain close to the fracture (0 m ≤ z ≤ 0.1 m)

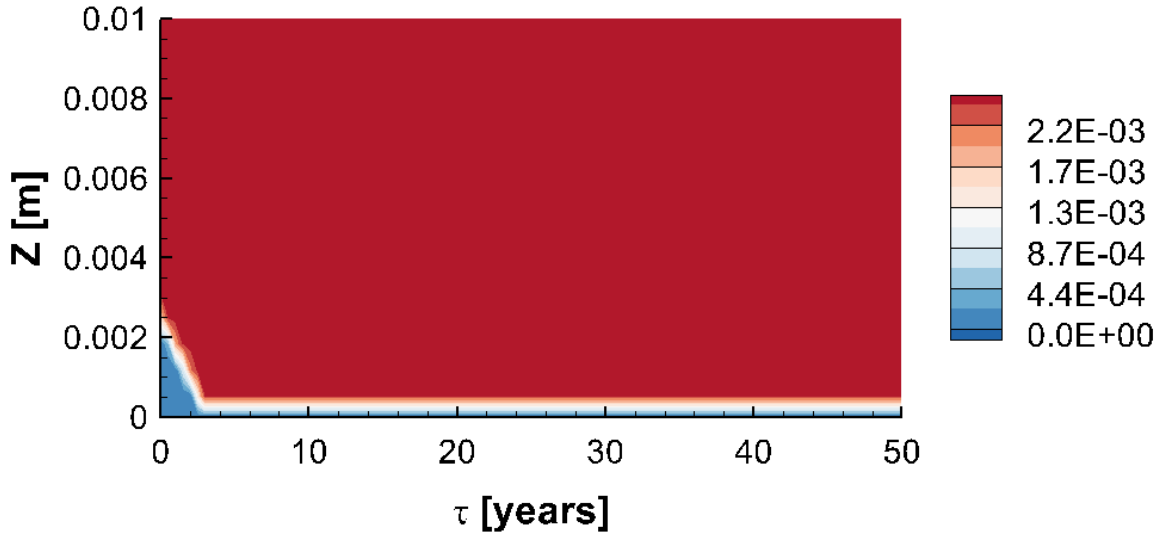

Fig. S.M.2 .1.4 Simulation results for scenario 'only-pyrite' after 10000 years O_2 input (t = 10000 years): concentration distribution of pyrite [Vol.%] in the model domain close to the fracture (0 m ≤ z ≤ 0.1 m)

.2 Conditions after 100 years of NO_3^- input

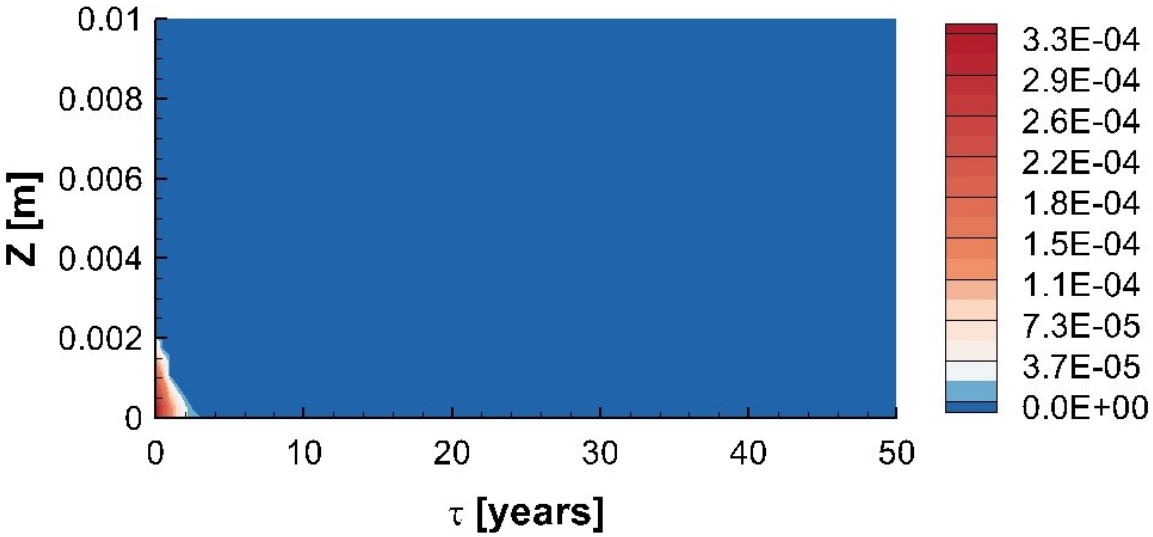

Fig. S.M.2 .2.1 Simulation results for scenario 'only-pyrite' after 100 years NO_3^- input (t = 10100 years): concentration distribution of O_2 [mol/l] in the model domain close to the fracture (0 m ≤ z ≤ 0.1 m)

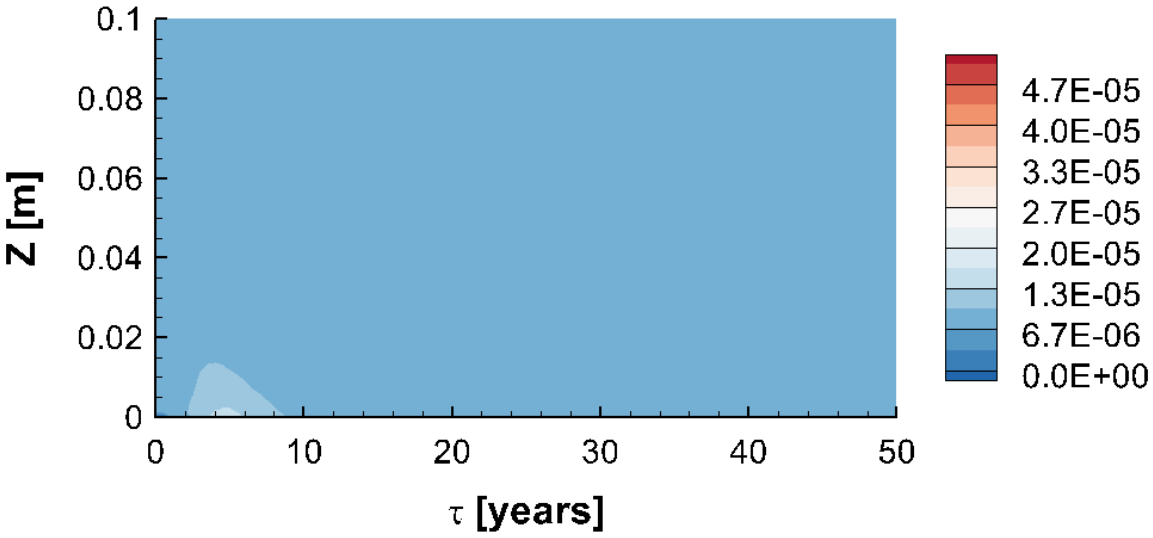

Fig. S.M.2 .2.2 Simulation results for scenario 'only-pyrite' after 100 years NO_3^- input (t = 10100 years): concentration distribution of Fe^{2+} [mol/l] in the model domain close to the fracture (0 m ≤ z ≤ 0.1 m)

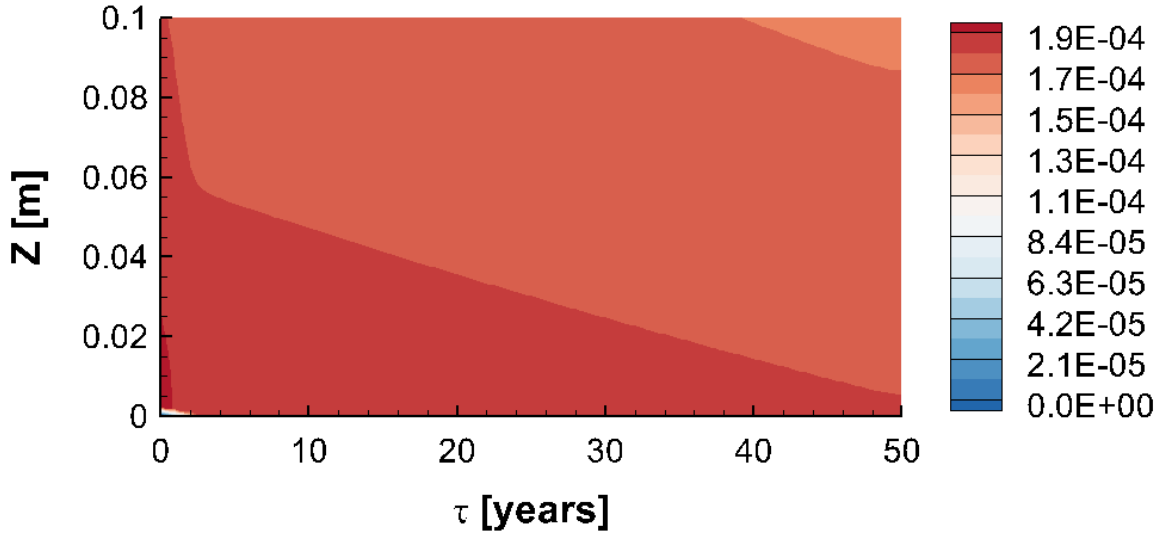

Fig. S.M.2 .2.3 Simulation results for scenario 'only-pyrite' after 100 years NO_3^- input (t = 10100 years): concentration distribution of SO_4^{2-} [mol/l] in the model domain close to the fracture (0 m ≤ z ≤ 0.1 m)

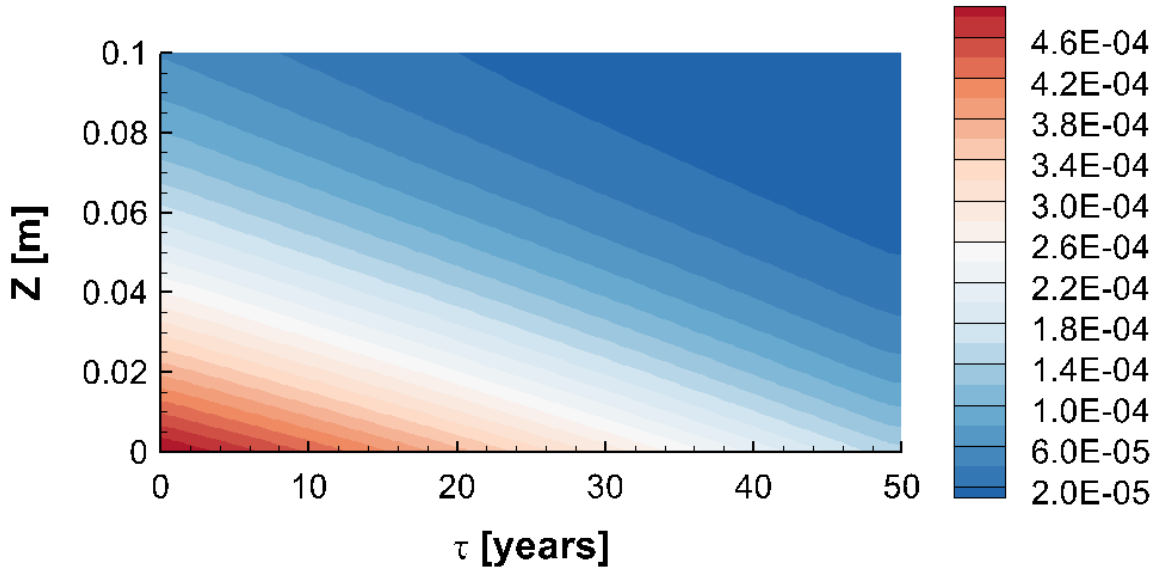

Fig. S.M.2 .2.4 Simulation results for scenario 'only-pyrite' after 100 years NO_3^- input (t = 10100 years): concentration distribution of Conservative tracer [mol/l] in the model domain close to the fracture (0 m ≤ z ≤ 0.1 m)

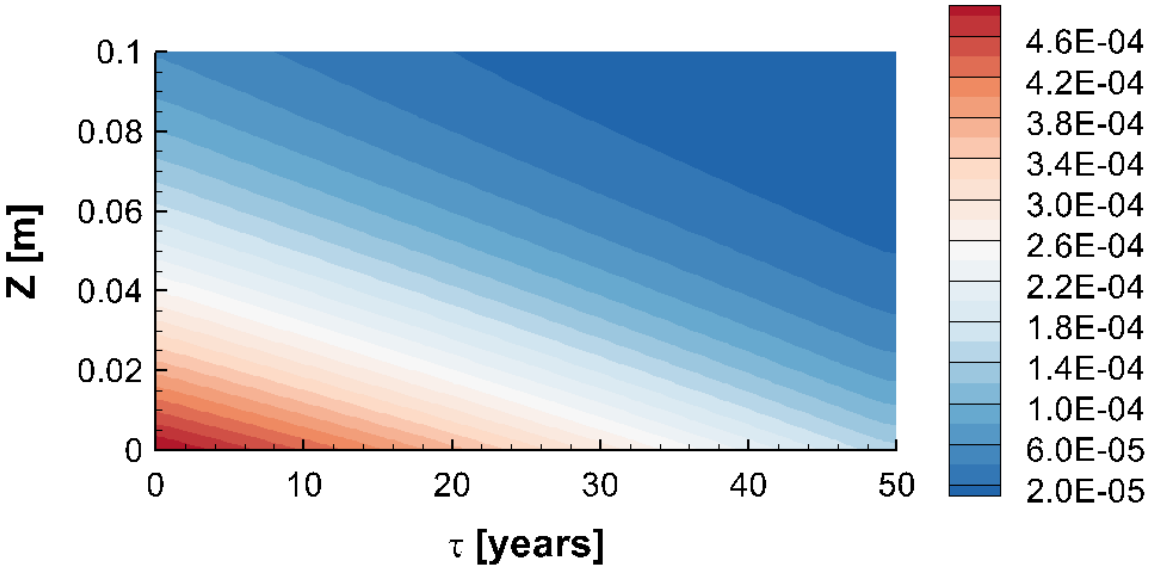

Fig. S.M.2 .2.5 Simulation results for scenario 'only-pyrite' after 100 years NO_3^- input (t = 10100 years): concentration distribution of NO_3^- [mol/l] in the model domain close to the fracture (0 m ≤ z ≤ 0.1 m)

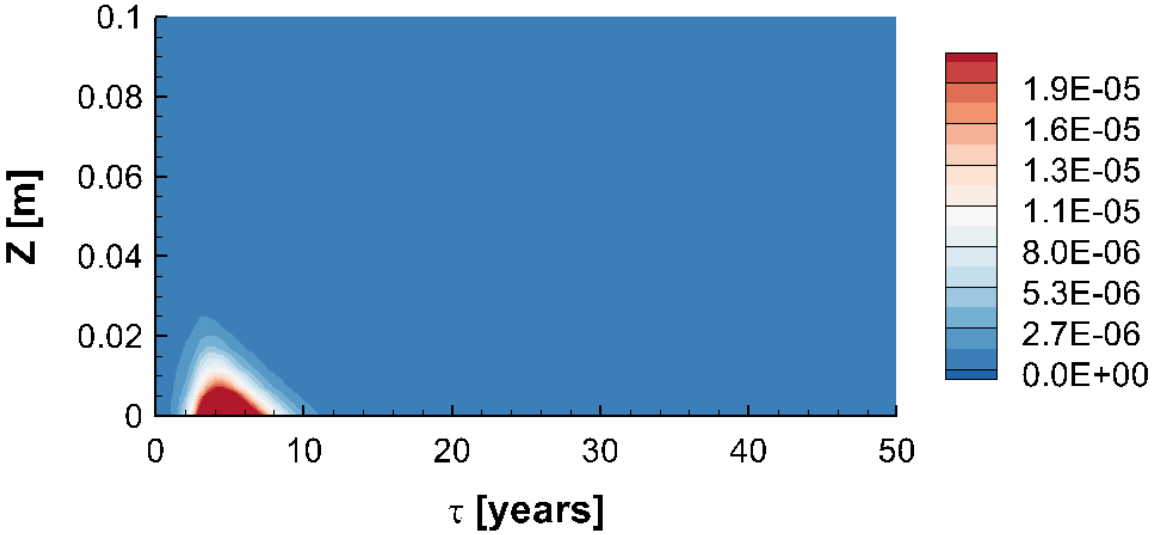

Fig. S.M.2 .2.6 Simulation results for scenario 'only-pyrite' after 100 years NO_3^- input (t = 10100 years): concentration distribution of N_2 [mol/l] in the model domain close to the fracture (0 m ≤ z ≤ 0.1 m)

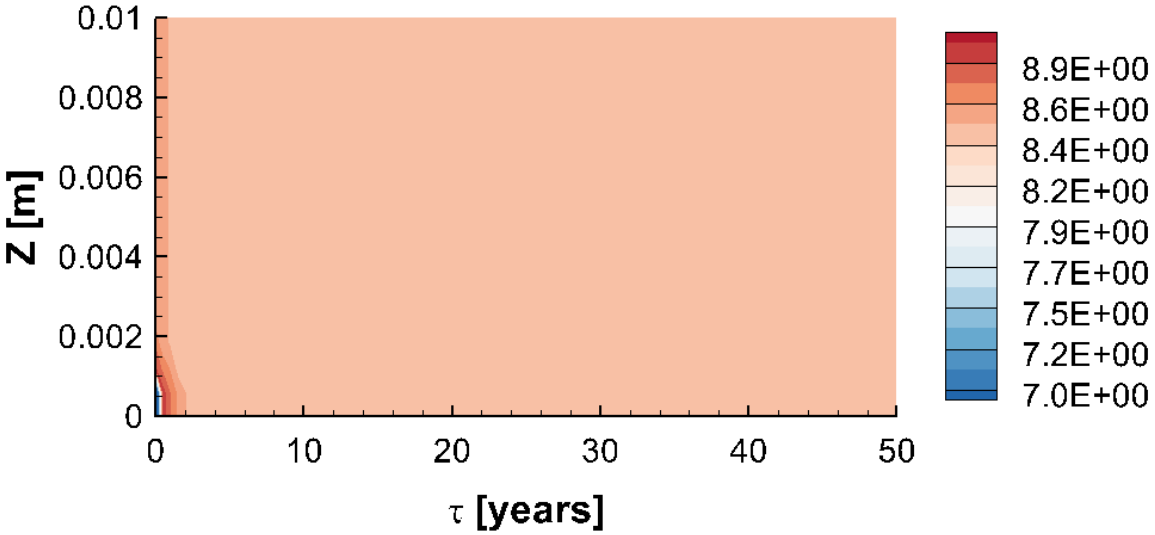

Fig. S.M.2 .2.7 Simulation results for scenario ‘only-pyrite’ after 100 years NO_3^- input (t = 10100 years): concentration distribution of pH in the model domain close to the fracture (0 m ≤ z ≤ 0.1 m)

SUPPLEMENTARY MATERIAL 3. COMPOUNDS AND MINERALS CONCENTRATION DISTRIBUTION IN THE MODEL DOMAIN AT THE START (SIMULATION TIME T = 10000 YEARS) AND THE END (T = 10100 YEARS) OF NITRATE INPUT FOR THE 'SINGLE-MINERAL' MODEL SCENARIO CONSIDERING SIDERITE AS ELECTRON DONOR.

TRAVEL TIME-BASED MODELLING OF NITRATE REDUCTION IN A FRACTURED LIMESTONE AQUIFER BY PYRITE AND IRON CARBONATES UNDER PORE SIZE LIMITATION

Siderite is the only iron-bearing mineral. Dissolution of siderite is not stimulated by pyrite oxidation and produced Fe^{2+} does not lead to significant consumption of oxygen in the rock matrix and after the preconditioning time oxygen concentrations are high throughout the rock matrix. Oxidation of Fe^{2+} leads to some ferrihydrite precipitation in the fracture and releases H^{+}. In this scenario, the oxygen concentration at the beginning of nitrate input is considerably high in the entire model domain and thus denitrification is suppressed and nitrate behaves again as a conservative tracer.

.1 Conditions at the start of the nitrate input (after 10 000 years of oxygen ingress)

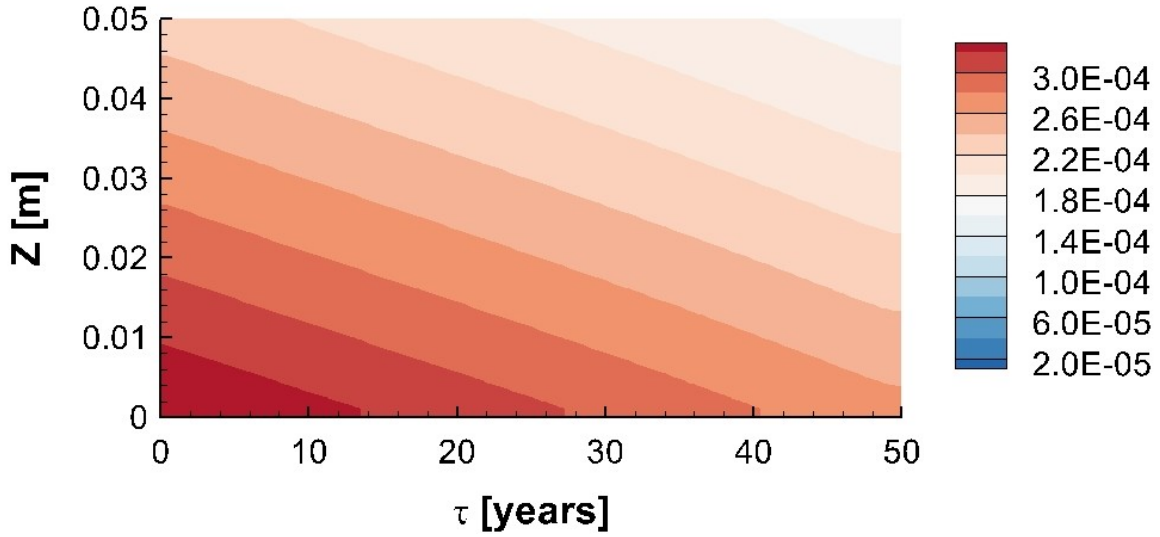

Fig. S.M.3 .1.1 Simulation results for scenario 'only-siderite' after 10000 years O_2 input (t = 10000 years): concentration distribution of O_2 [mol/l] in the model domain close to the fracture (0 m ≤ z ≤ 0.1 m)

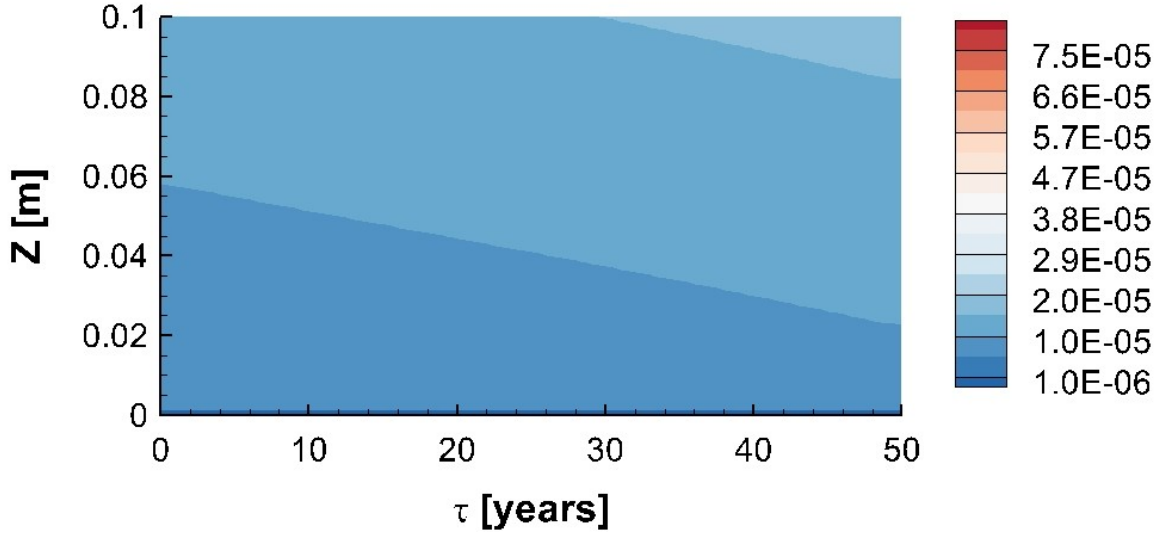

Fig. S.M.3 .1.2 Simulation results for scenario 'only-siderite' after 10000 years O_2 input (t = 10000 years): concentration distribution of Fe^{2+} [mol/l] in the model domain close to the fracture (0 m ≤ z ≤ 0.1 m)

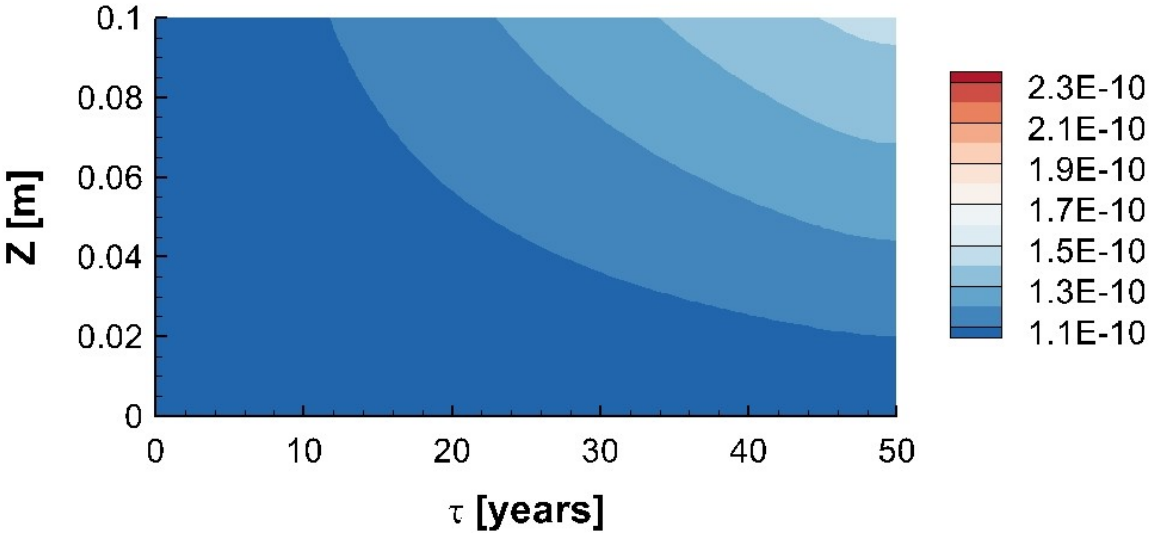

Fig. S.M.3 .1.3 Simulation results for scenario 'only-siderite' after 10000 years O_2 input (t = 10000 years): concentration distribution of SO_4^{2-} [mol/l] in the model domain close to the fracture (0 m ≤ z ≤ 0.1 m)

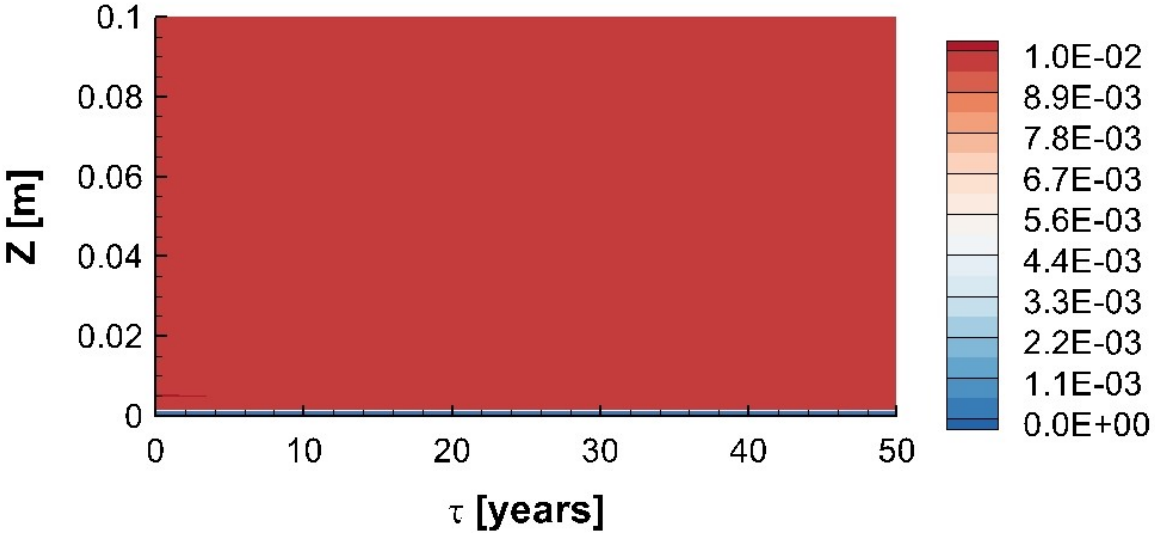

Fig. S.M.3 .1.4 Simulation results for scenario 'only-siderite' after 100 years NO_3^- input (t = 10100 years): distribution of siderite [Vol.] in the model domain close to the fracture (0 m ≤ z ≤ 0.1 m)

.2 Conditions after 100 years of NO_3^- input

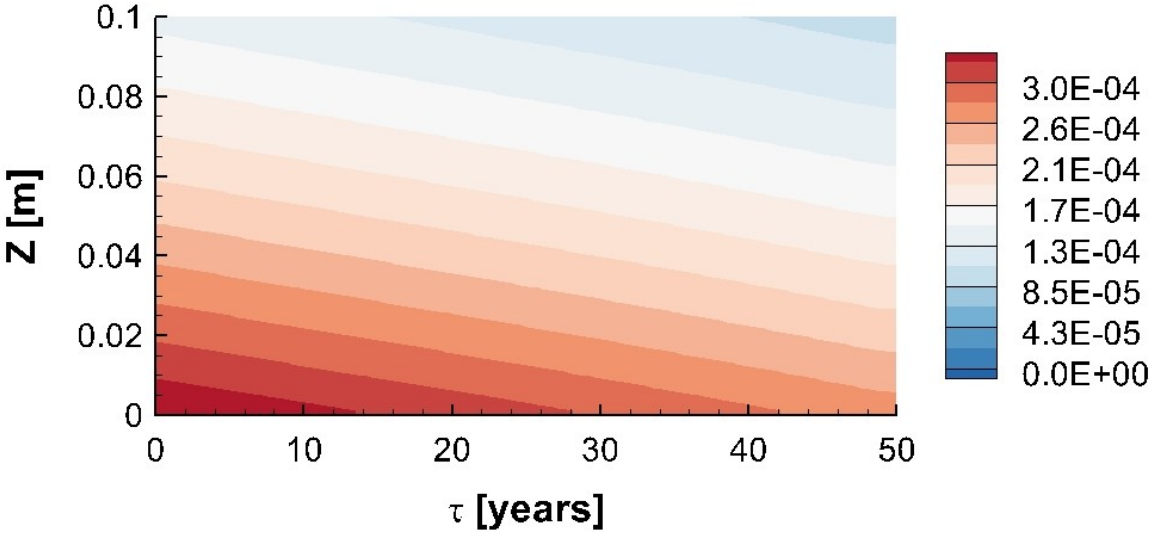

Fig. S.M.3 .2.1 Simulation results for scenario 'only-siderite' after 100 years NO_3^- input (t = 10100 years): concentration distribution of O_2 [mol/l] in the model domain close to the fracture (0 m ≤ z ≤ 0.1 m)

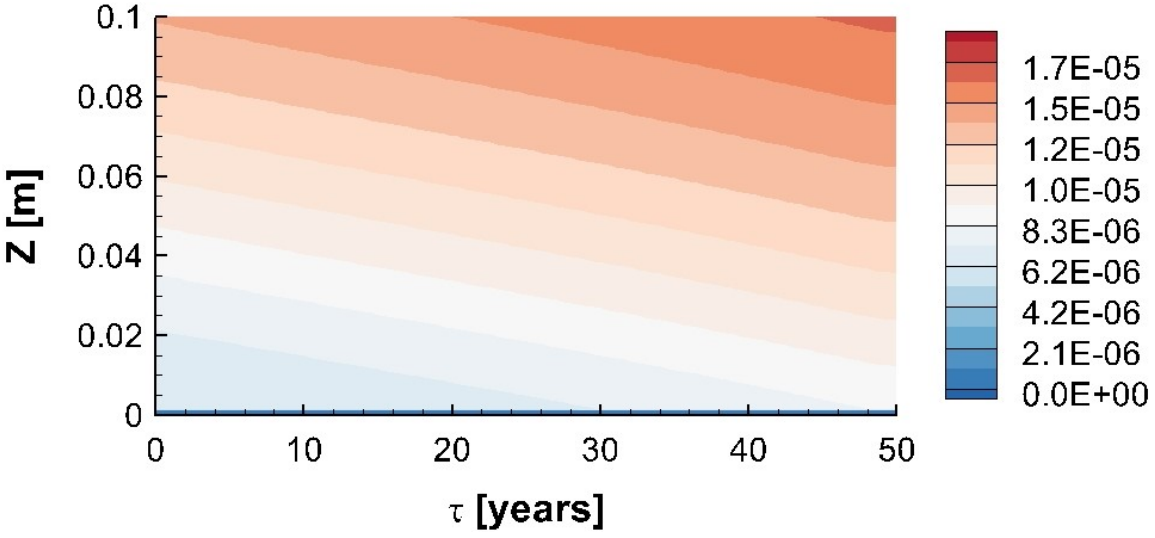

Fig. S.M.3 .2.2 Simulation results for scenario 'only-siderite' after 100 years NO_3^- input (t = 10100 years): concentration distribution of Fe^{2+} [mol/l] in the model domain close to the fracture (0 m ≤ z ≤ 0.1 m)

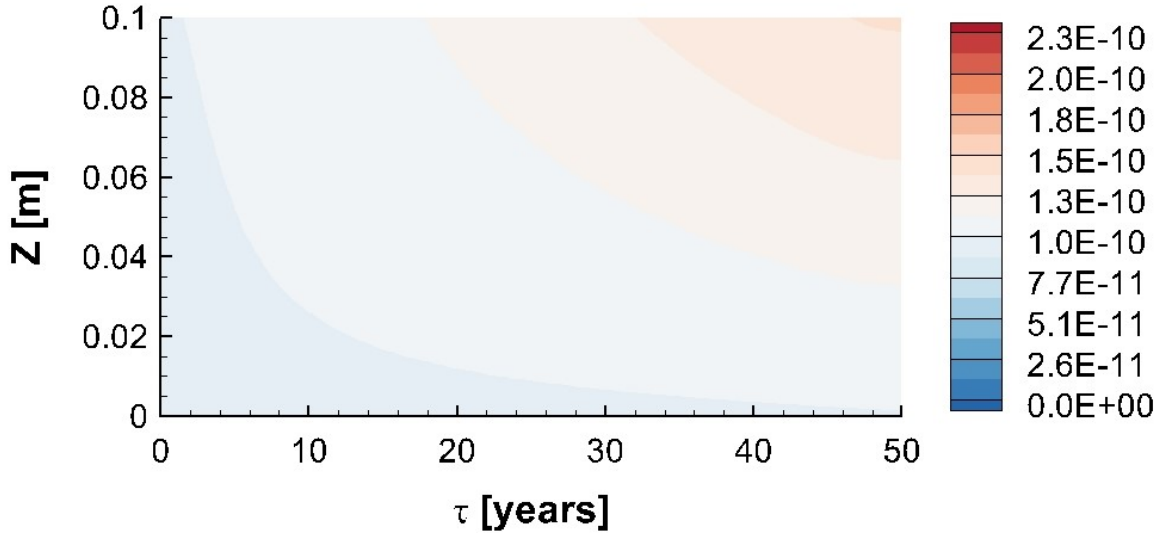

Fig. S.M.3 .2.3 Simulation results for scenario 'only-siderite' after 100 years NO_3^- input (t = 10100 years): concentration distribution of SO_4^{2-} [mol/l] in the model domain close to the fracture (0 m ≤ z ≤ 0.1 m)

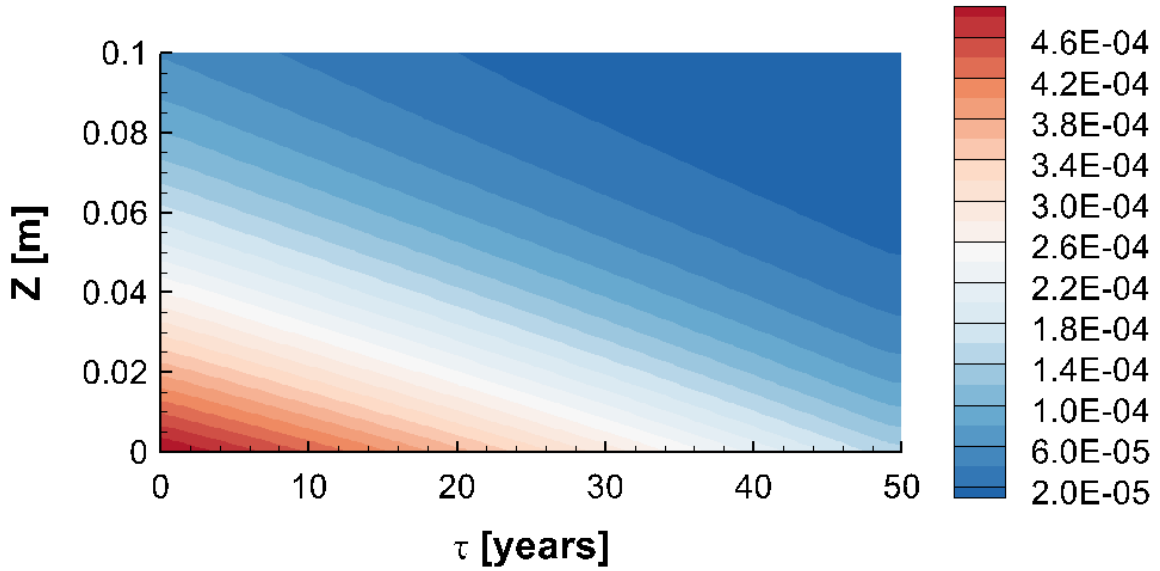

Fig. S.M.3 .2.4 Simulation results for scenario 'only-siderite' after 100 years NO_3^- input (t = 10100 years): concentration distribution of Conservative tracer [mol/l] in the model domain close to the fracture (0 m ≤ z ≤ 0.1 m)

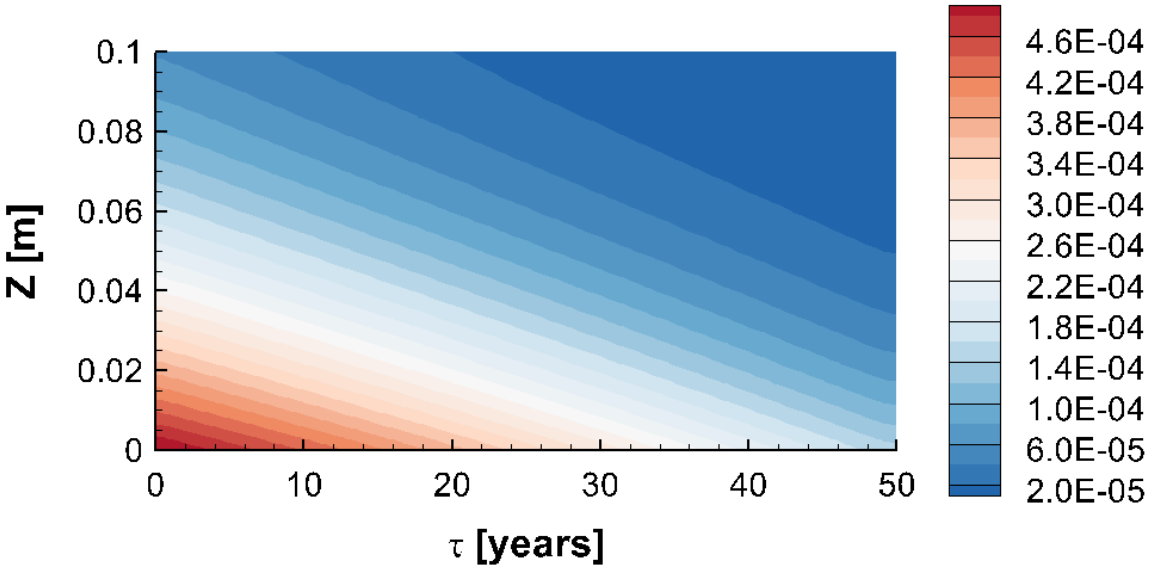

Fig. S.M.3 .2.5 Simulation results for scenario 'only-siderite' after 100 years NO_3^- input (t = 10100 years): concentration distribution of NO_3^- [mol/l] in the model domain close to the fracture (0 m ≤ z ≤ 0.1 m)

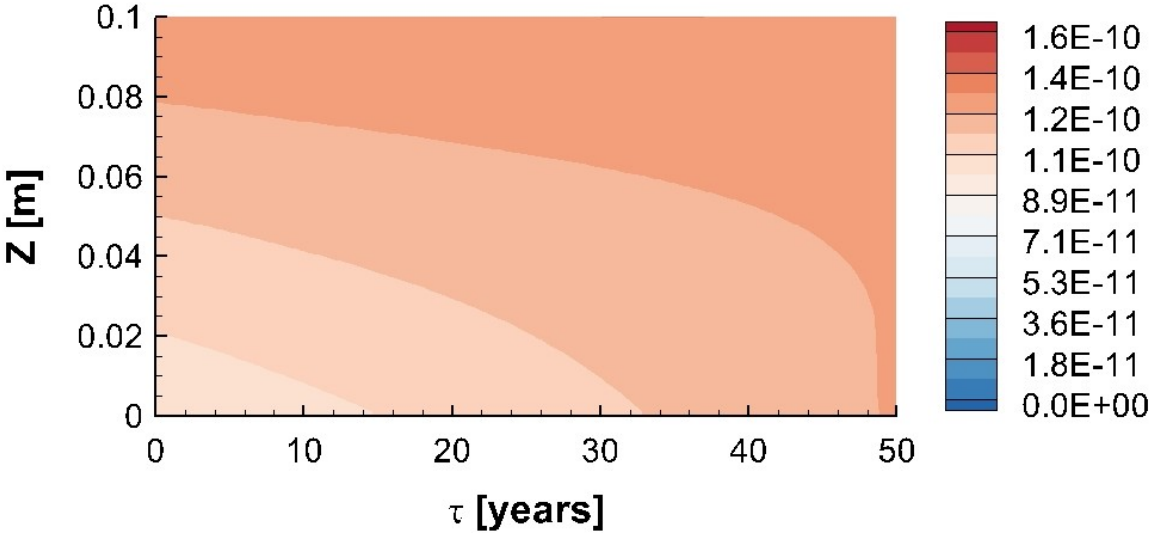

Fig. S.M.3 .2.6 Simulation results for scenario 'only-siderite' after 100 years NO_3^- input (t = 10100 years): concentration distribution of N_2 [mol/l] in the model domain close to the fracture (0 m ≤ z ≤ 0.1 m)

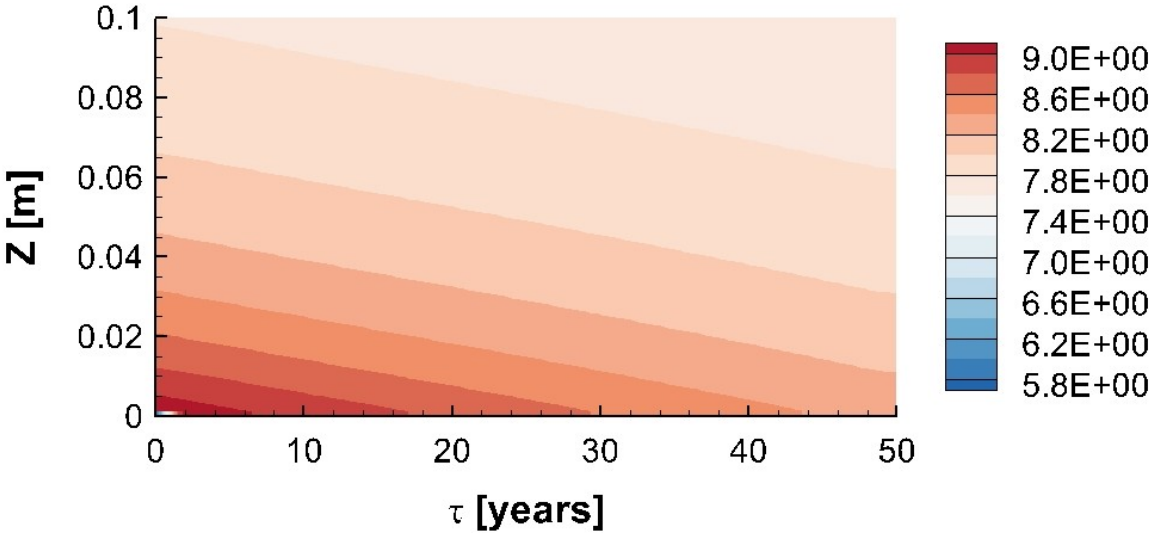

Fig. S.M.3 .2.7 Simulation results for scenario 'only-siderite' after 100 years NO_3^- input (t = 10100 years): concentration distribution of pH in the model domain close to the fracture (0 m ≤ z ≤ 0.1 m)

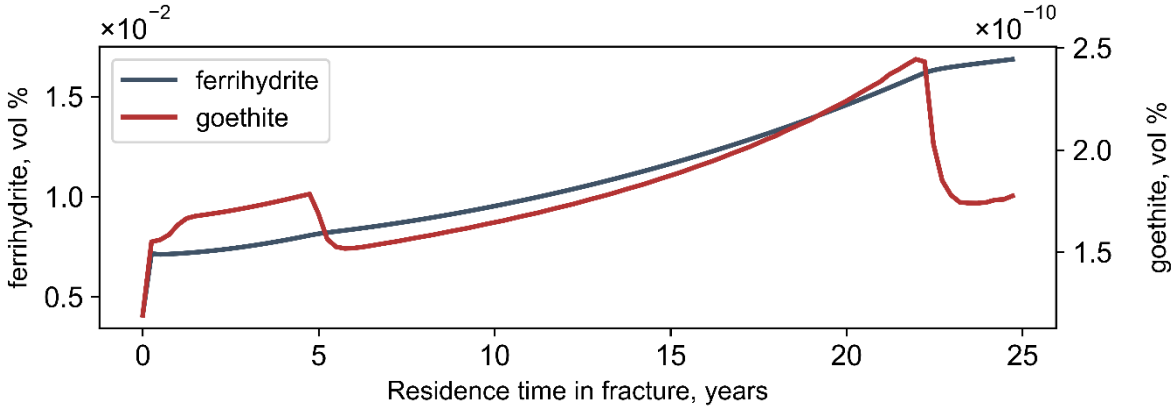

Fig. S.M.3 .2.8 Simulation results for scenario 'only-siderite' after 100 years NO_3^- input (t = 10100 years): Secondary minerals volumetric content (ferrihydrite and goethite representing reactions with oxygen and nitrate, respectively) in the fracture

SUPPLEMENTARY MATERIAL 4 POSTERIOR DISTRIBUTION OF MODEL PARAMETERS FOR STOCHASTIC MONO- AND MULTI ISOTOPE MODELLING ESTIMATED IN EACH LOCATION

ENHANCING RELIABILITY OF ESTIMATED TRAVEL TIME DISTRIBUTIONS USING MULTI-ISOTOPE MODEL OPTIMISATION

Posterior distribution of model parameters for stochastic mono- and multi isotope modelling estimated in each location. Compilation of figures.

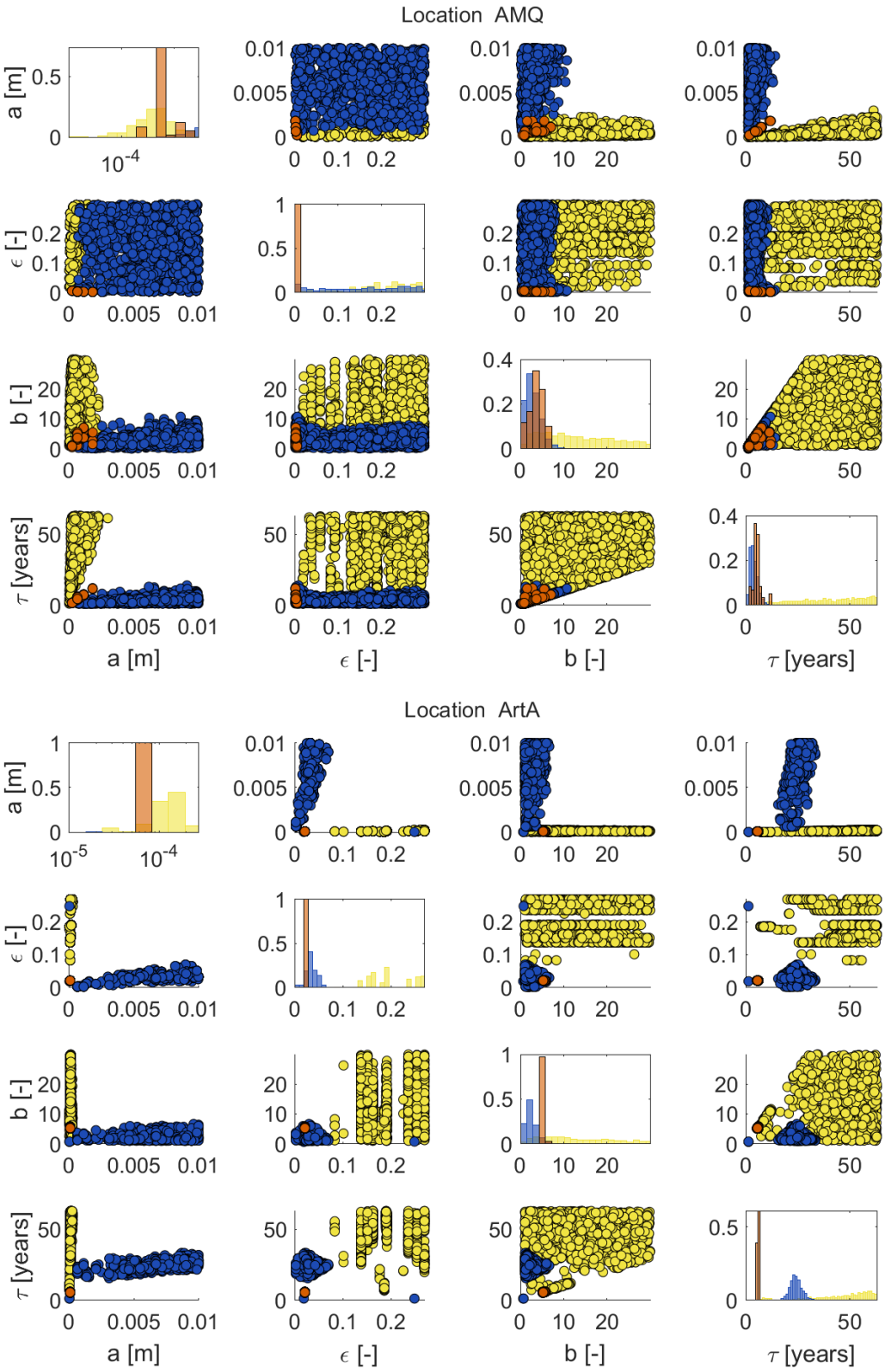
Location AMQ
a [m]
ϵ [-]
b [-]
τ [years]
Location ArtA
a [m]
ϵ [-]
b [-]
τ [years]

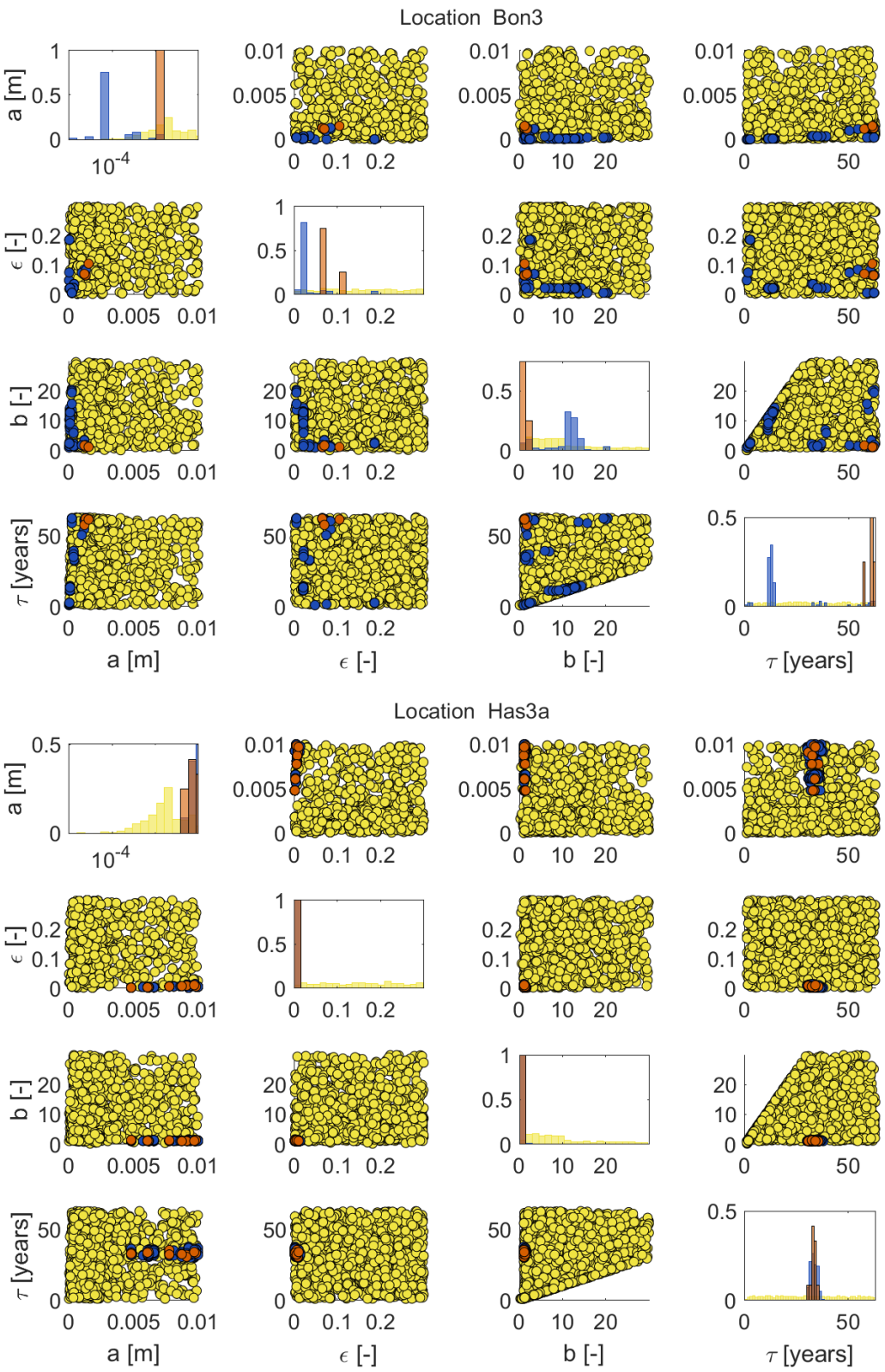
Location Bon3
a [m]
ϵ [-]
b [-]
τ [years]
10^{-4}
Location Has3a

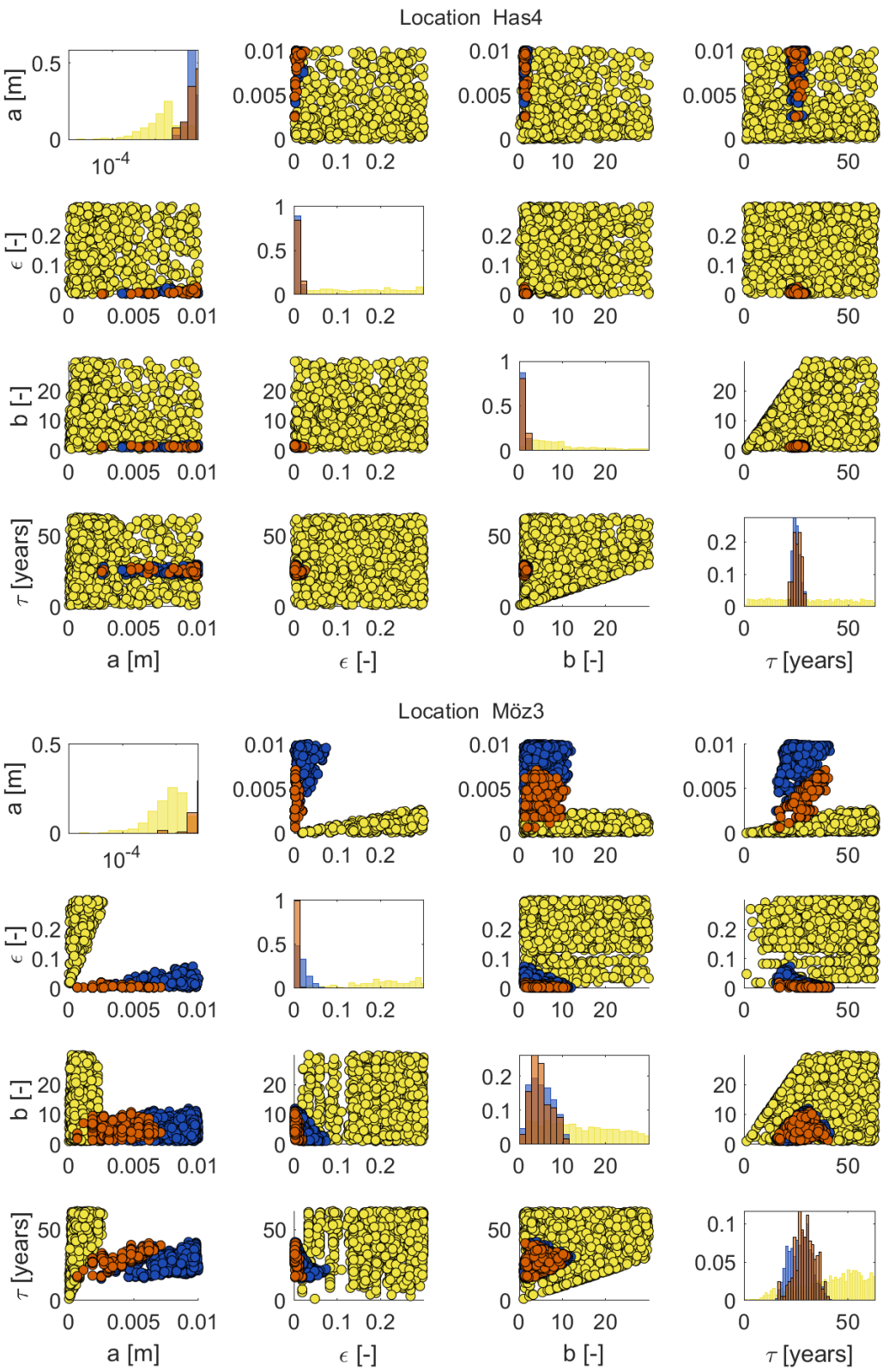
Location Has4
a [m]
ϵ [-]
b [-]
τ [years]
10^{-4}
a [m]
ϵ [-]
b [-]
τ [years]
Location Möz3
a [m]
ϵ [-]
b [-]
τ [years]
10^{-4}
a [m]
ϵ [-]
b [-]
τ [years]

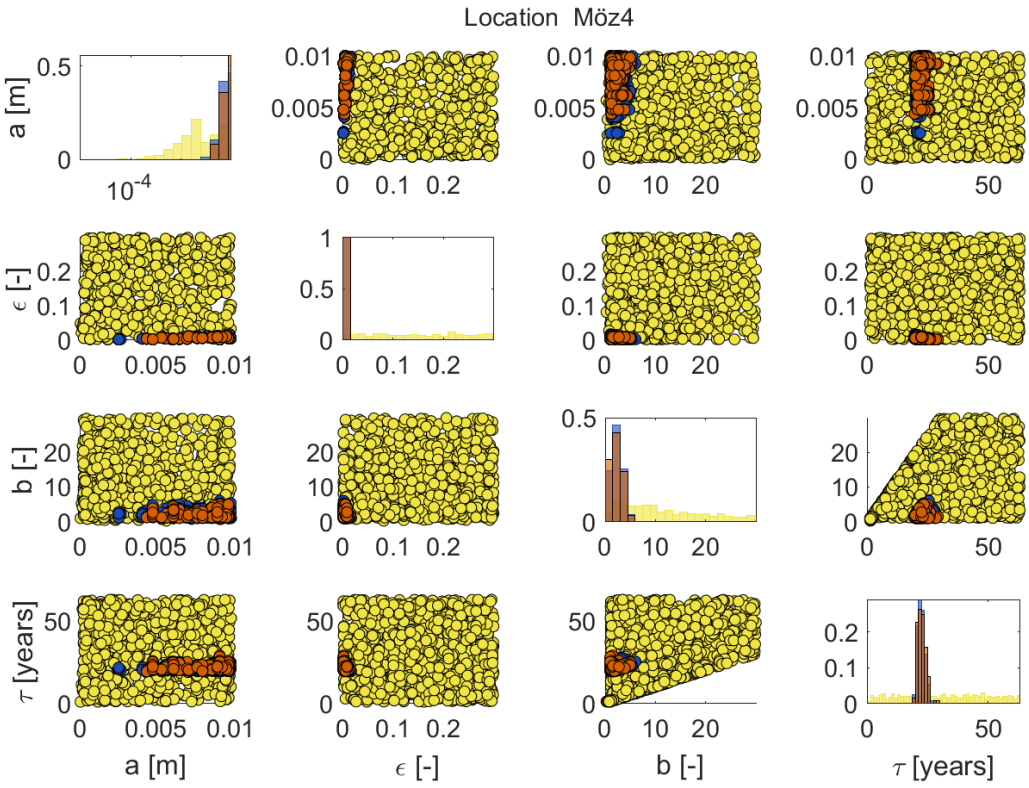
Location Möz4
a [m]
ϵ [-]
b [-]
τ [years]
10^{-4}
a [m]
ϵ [-]
b [-]
τ [years]

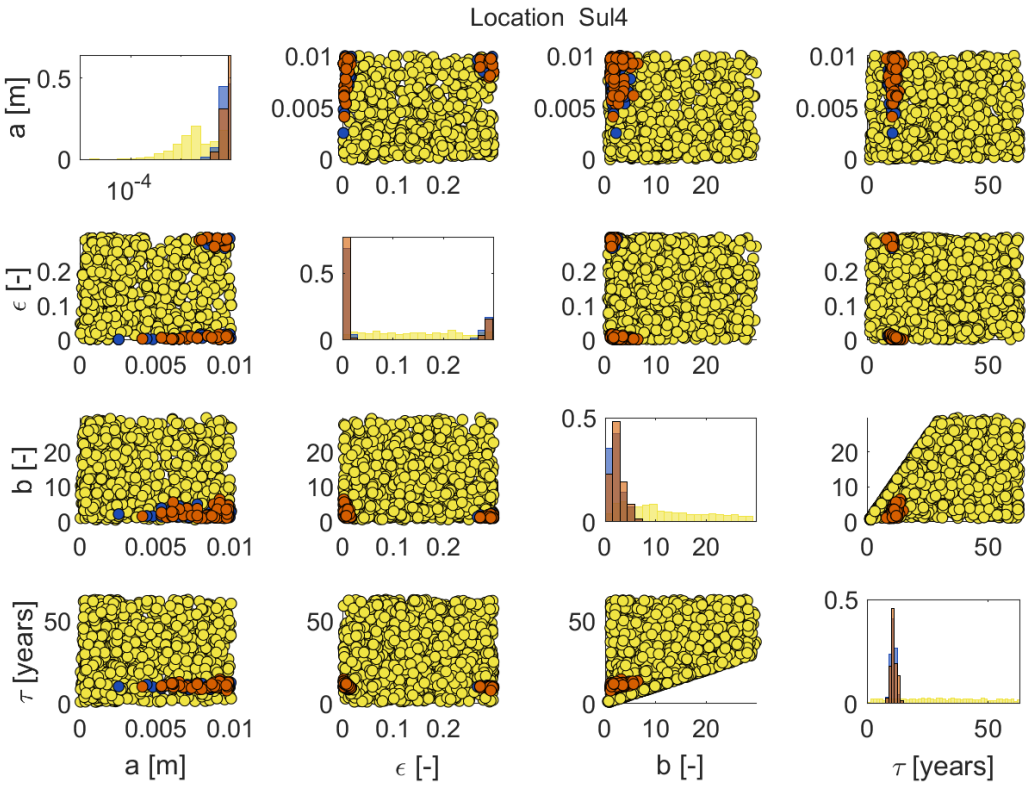
Location Sul4
a [m]
ϵ [-]
b [-]
τ [years]
10^{-4}
a [m]
ϵ [-]
b [-]
τ [years]

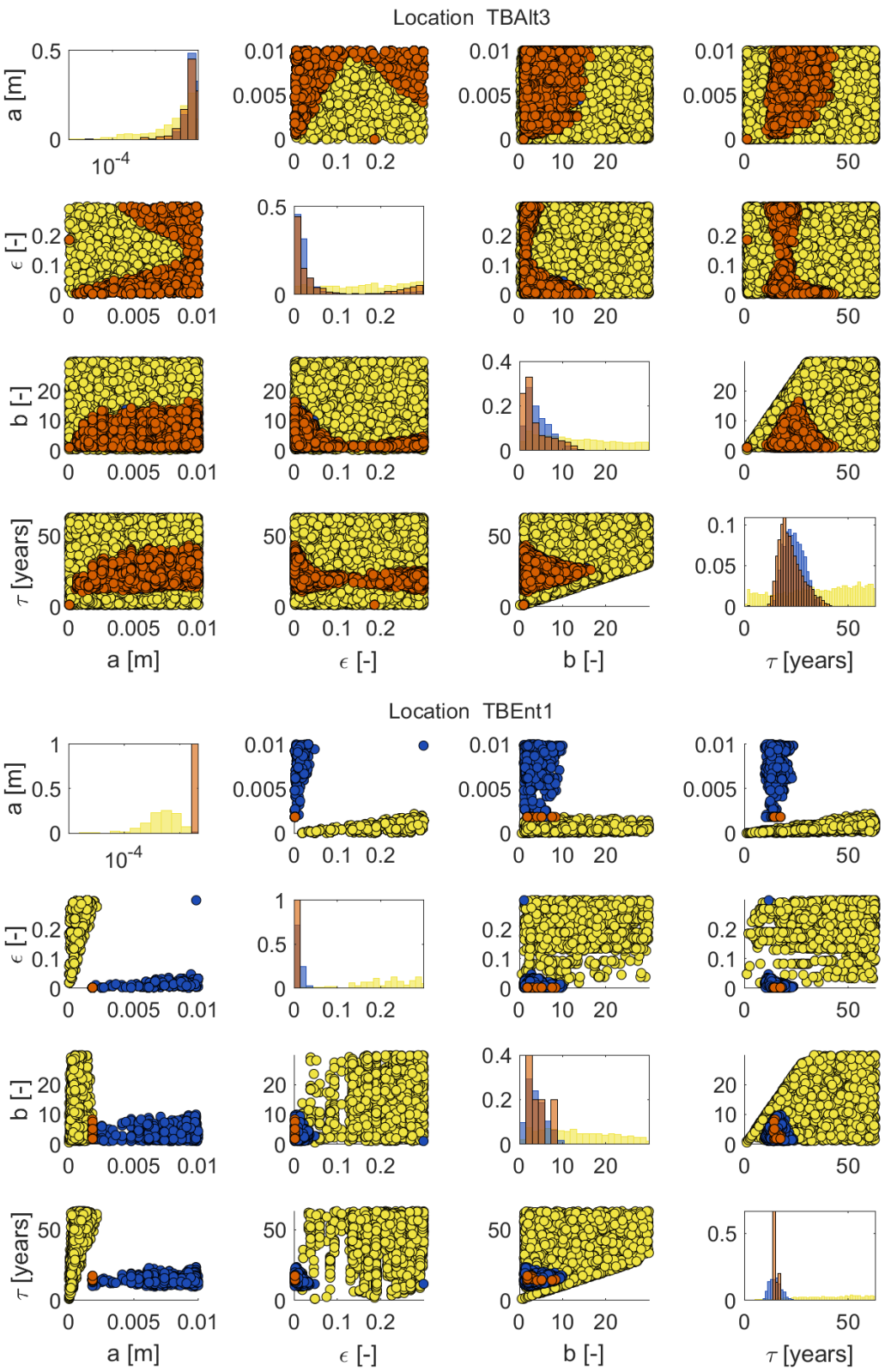
Location TBAlt3
a [m]
ϵ [-]
b [-]
τ [years]
10^{-4}
Location TBEnt1
a [m]
ϵ [-]
b [-]
τ [years]

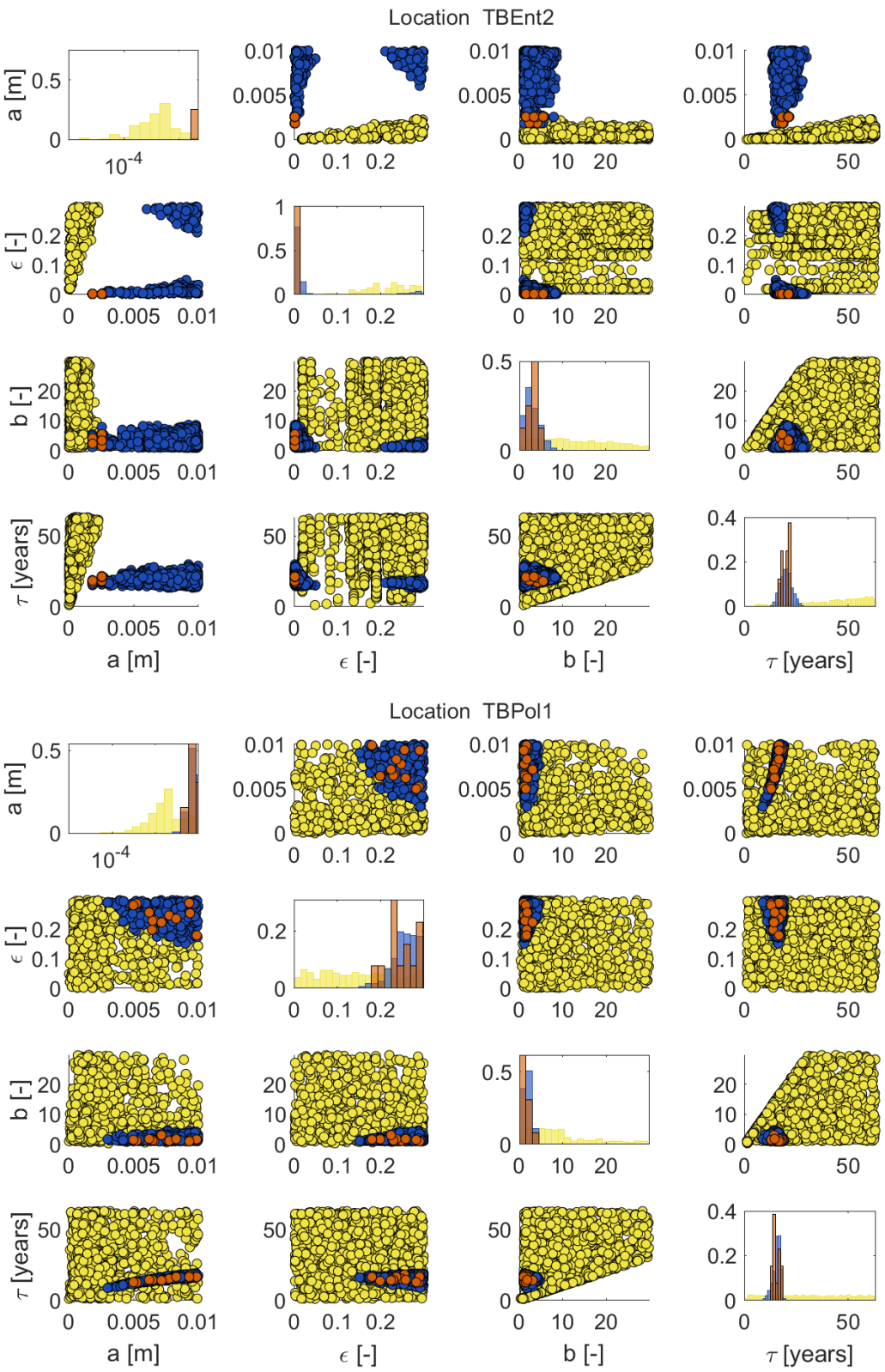
Location TBEnt2
a [m]
ϵ [-]
b [-]
τ [years]
10^{-4}
Location TBPol1

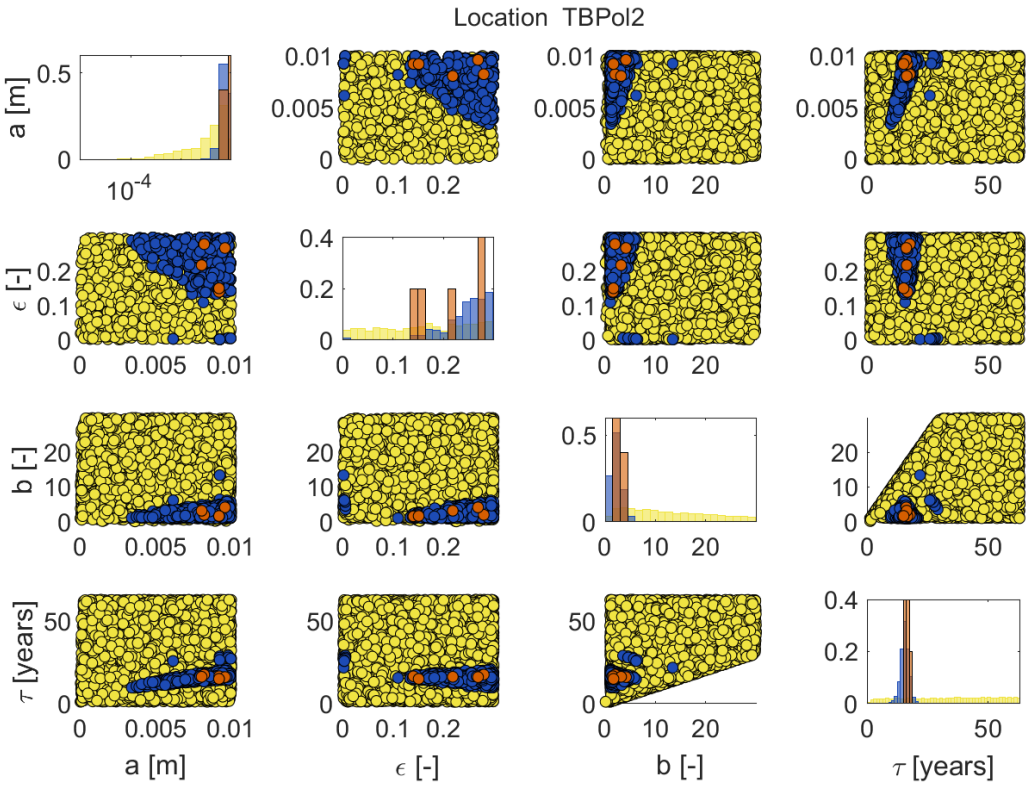
Location TBPol2
a [m]
ϵ [-]
b [-]
τ [years]
10^{-4}
a [m]
ϵ [-]
b [-]
τ [years]

SUPPLEMENTARY MATERIAL 5. POSTERIOR DISTRIBUTIONS OF THE MEAN TRAVEL TIME FOR STOCHASTIC MONO- AND MULTI-ISOTOPE MODELLING ESTIMATED IN EACH LOCATION

ENHANCING RELIABILITY OF ESTIMATED TRAVEL TIME DISTRIBUTIONS USING MULTI-ISOTOPE MODEL OPTIMISATION

Posterior distributions of the mean travel time for stochastic mono- and multi- isotope modelling estimated in each location. Compilation of figures.

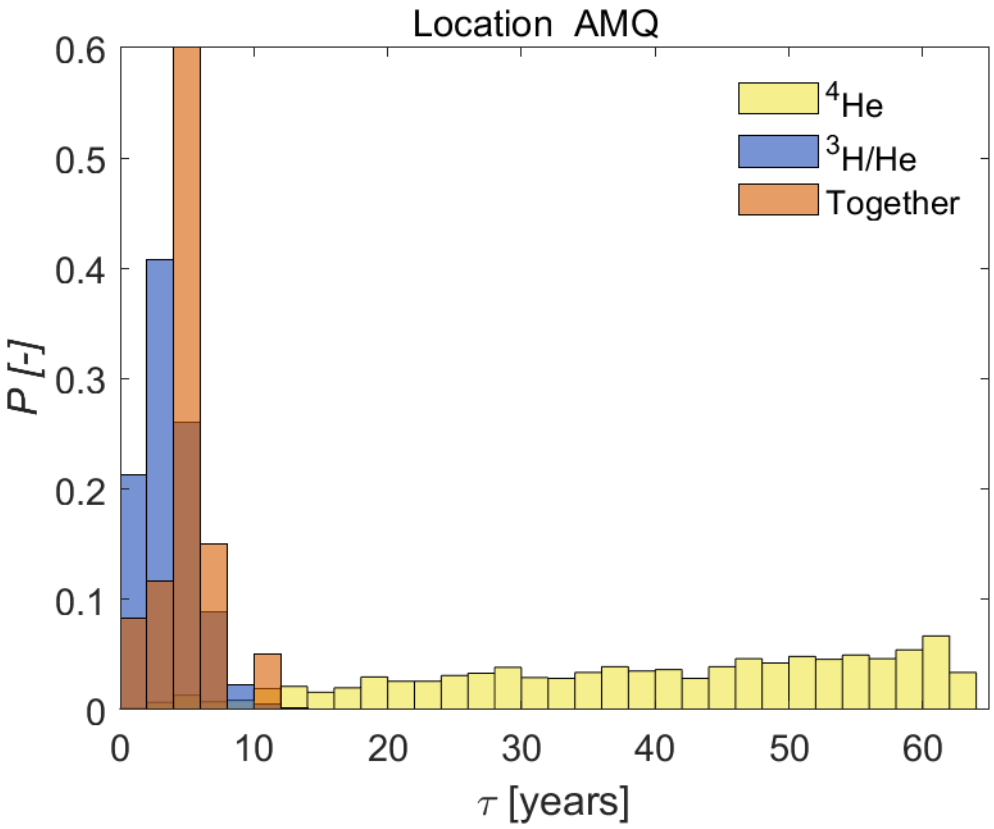
Location AMQ
P [-]
τ [years]
4He
3H/He
Together
0
0.1
0.2
0.3
0.4
0.5
0.6
0
10
20
30
40
50
60

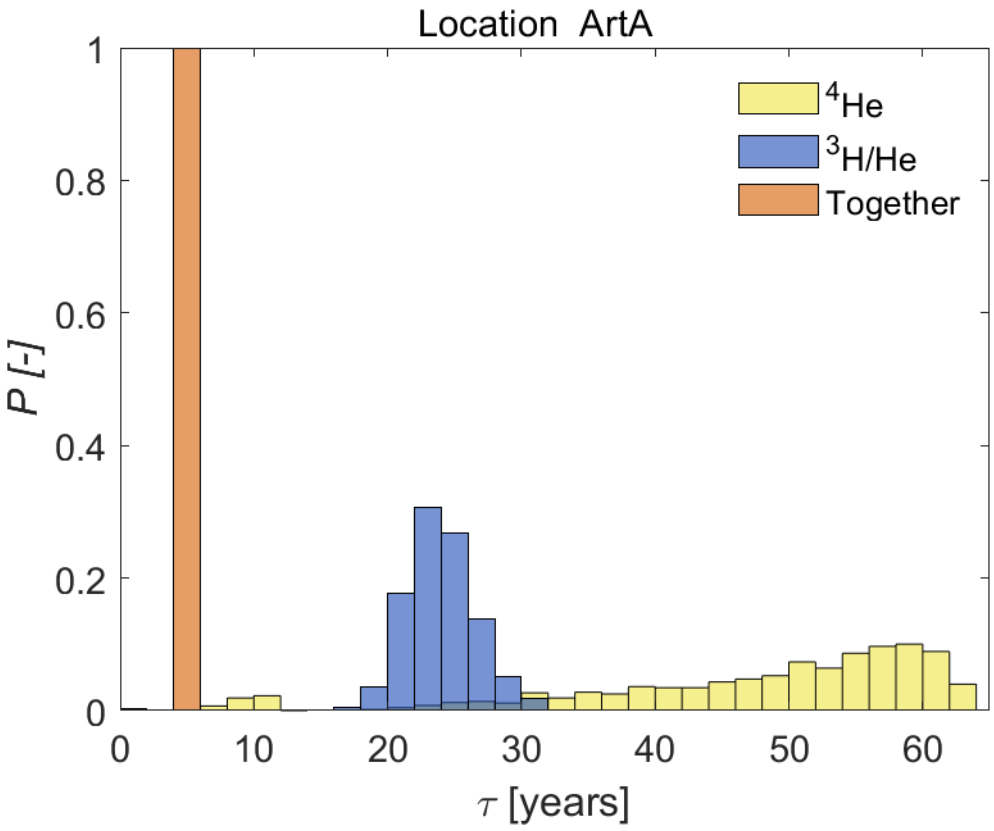
Location ArtA
P [-]
τ [years]
4He
3H/He
Together
0
0.2
0.4
0.6
0.8
1
0
10
20
30
40
50
60

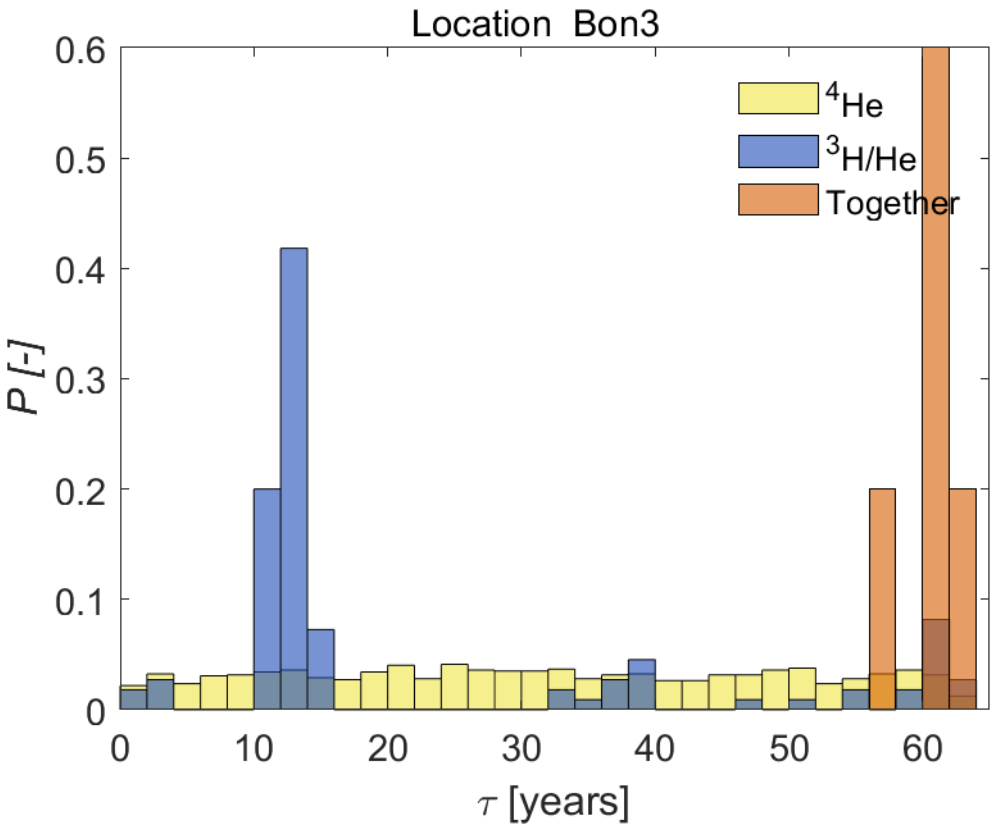
Location Bon3
0.6
0.5
0.4
0.3
0.2
0.1
0
P [-]
0
10
20
30
40
50
60
τ [years]
4He
3H/He
Together

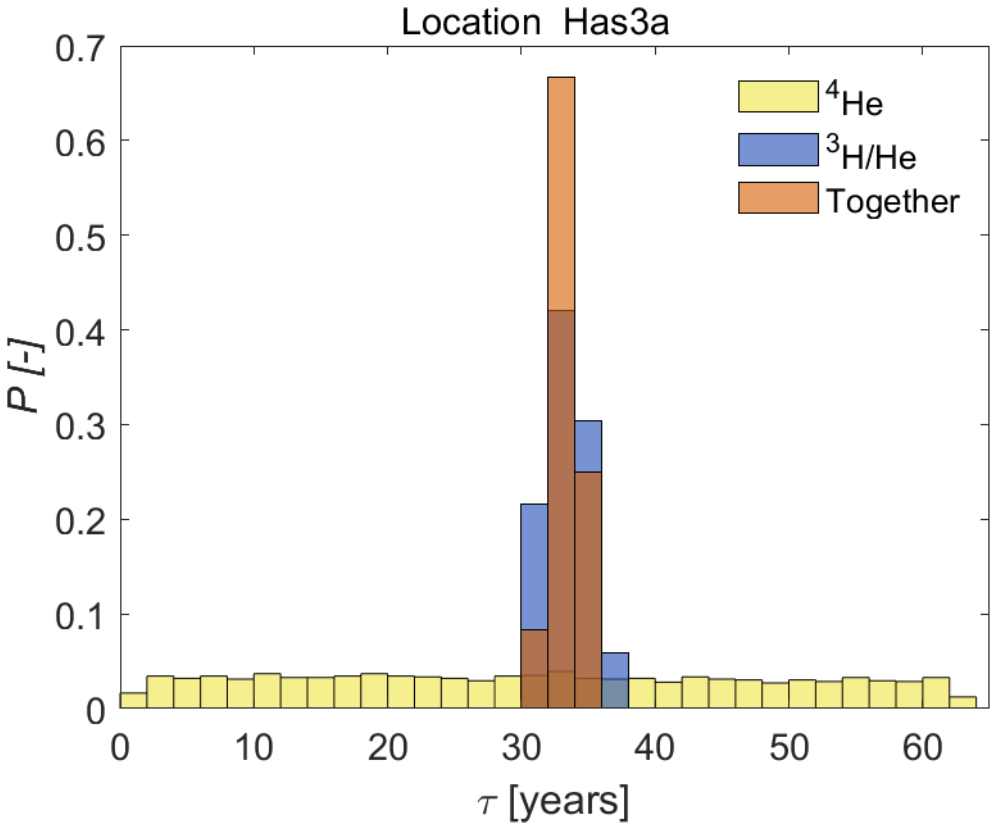
Location Has3a
0.7
0.6
0.5
0.4
0.3
0.2
0.1
0
P [-]
0
10
20
30
40
50
60
τ [years]
4He
3H/He
Together

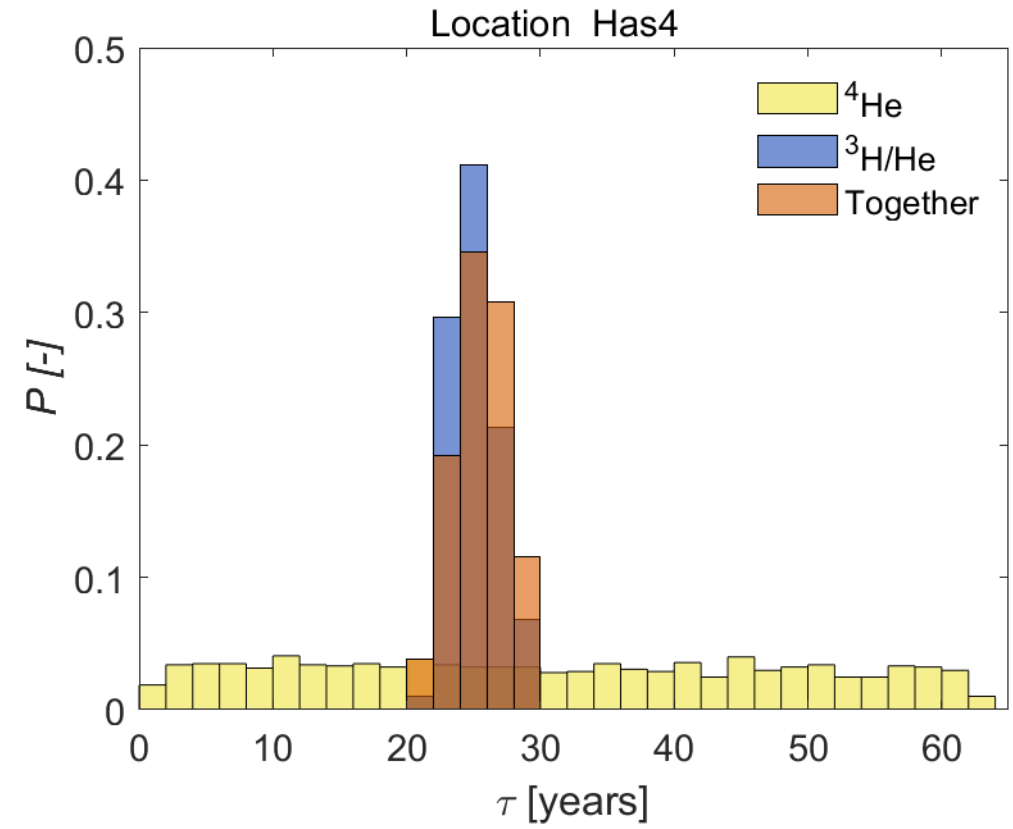
Location Has4
0.5
0.4
0.3
0.2
0.1
0
P [-]
0
10
20
30
40
50
60
τ [years]
4He
3H/He
Together

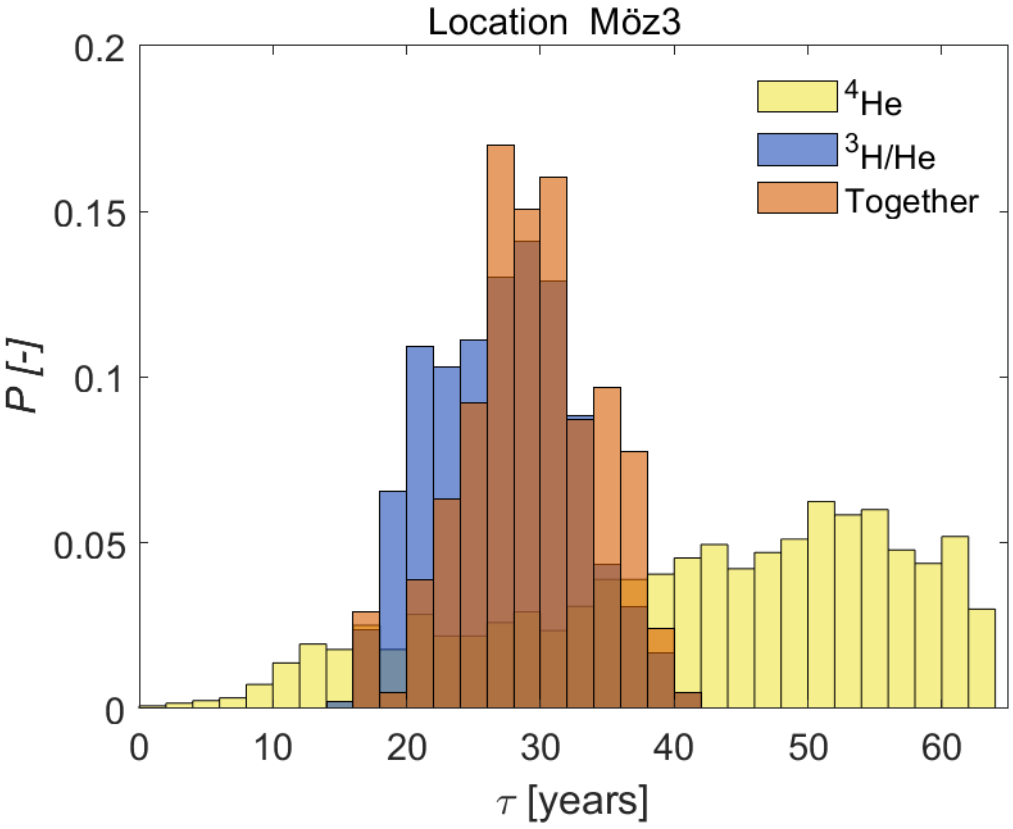
Location Möz3
0.2
0.15
0.1
0.05
0
P [-]
0
10
20
30
40
50
60
τ [years]
4He
3H/He
Together

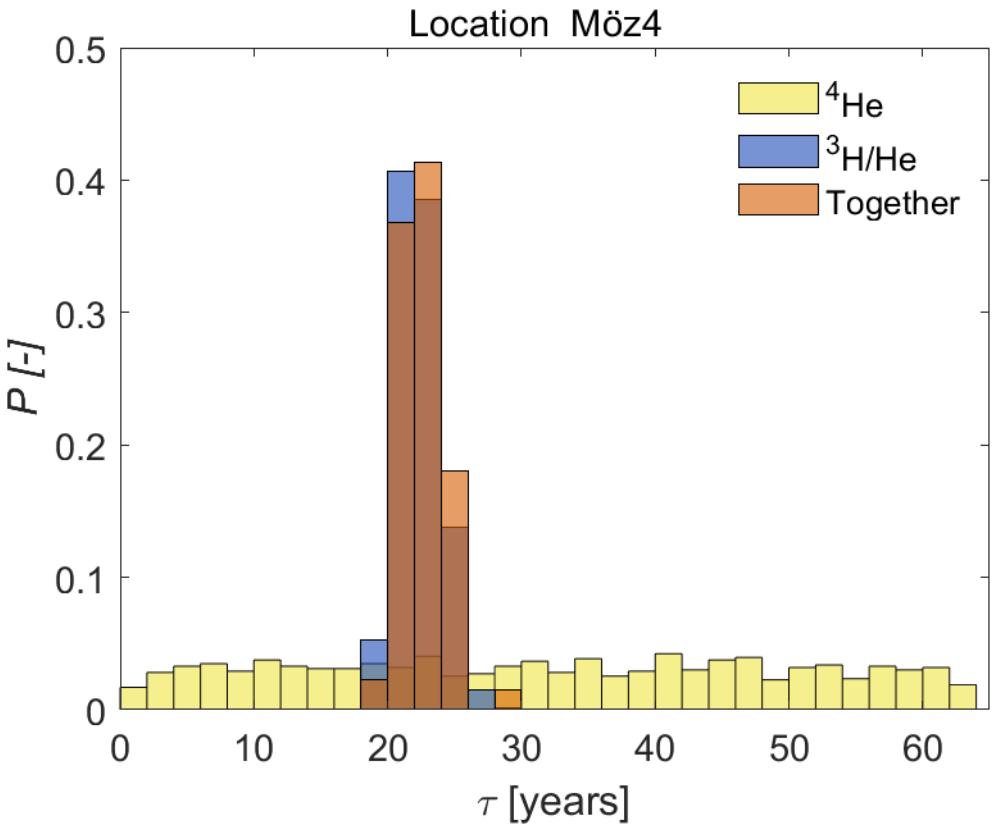
Location Möz4
0.5
0.4
0.3
0.2
0.1
0
P [-]
0
10
20
30
40
50
60
τ [years]
4He
3H/He
Together

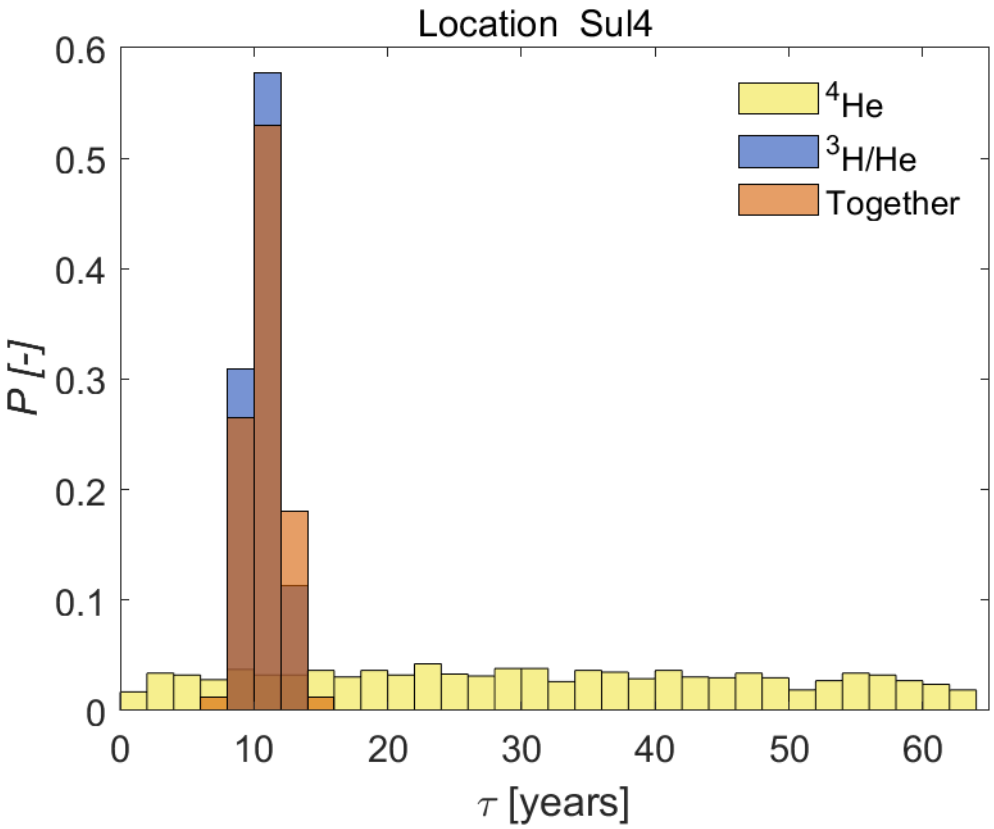
Location Sul4
0.6
0.5
0.4
0.3
0.2
0.1
0
P [-]
0
10
20
30
40
50
60
τ [years]
4He
3H/He
Together

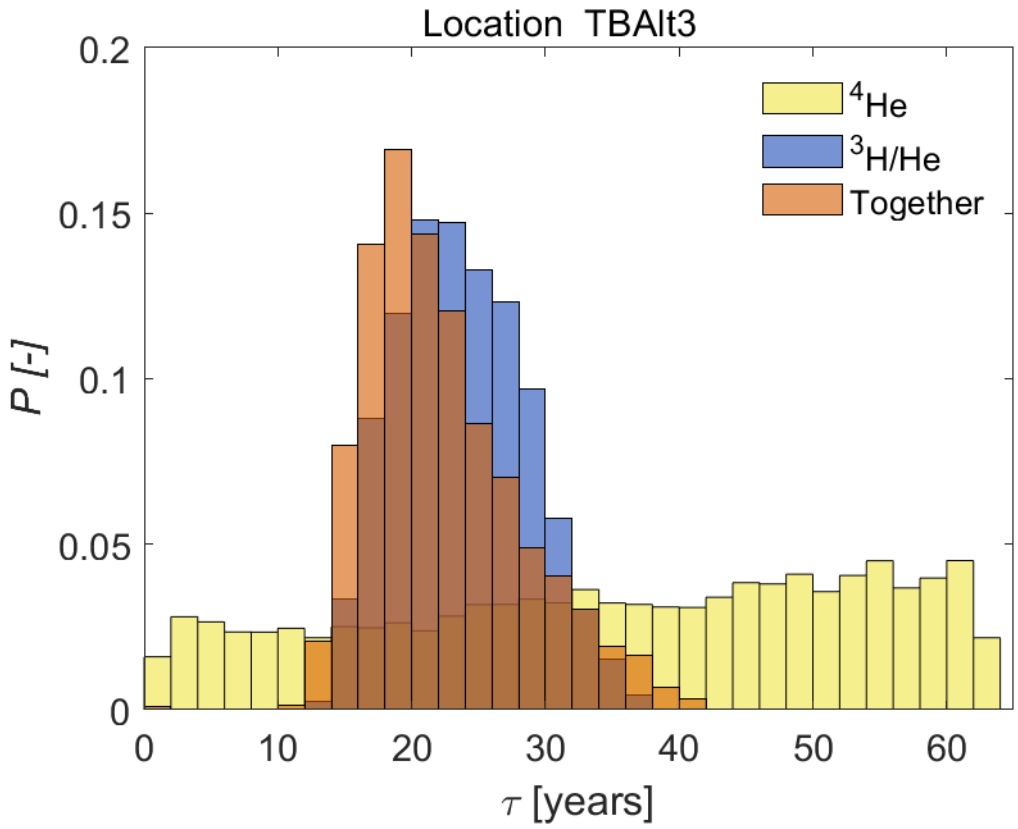
Location TBAlt3
0.2
0.15
0.1
0.05
0
P [-]
0
10
20
30
40
50
60
τ [years]
4He
3H/He
Together

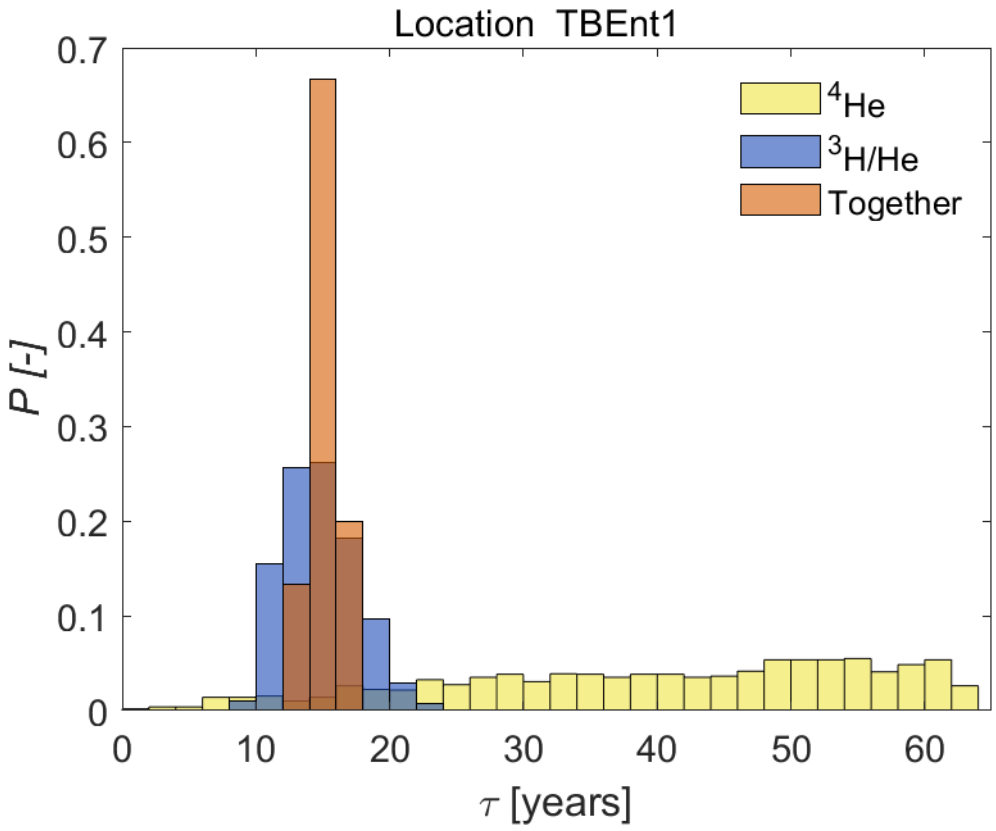
Location TBEnt1
0.7
0.6
0.5
0.4
0.3
0.2
0.1
0
P [-]
0
10
20
30
40
50
60
τ [years]
4He
3H/He
Together

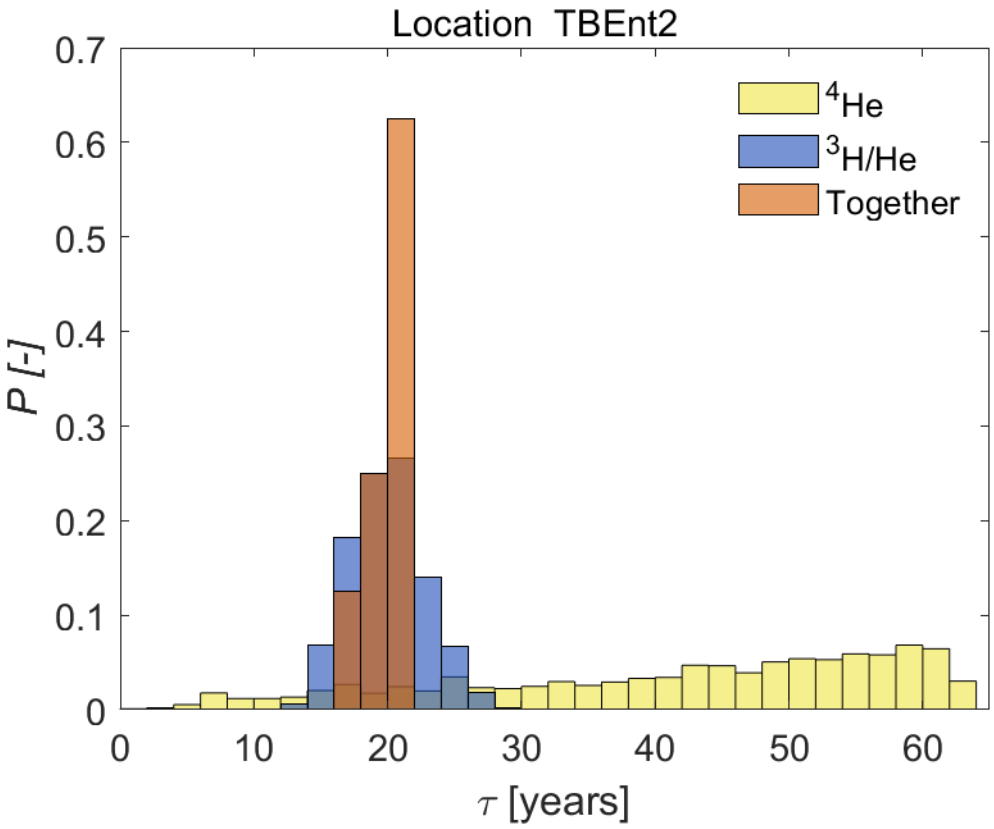
Location TBEnt2
0.7
0.6
0.5
0.4
0.3
0.2
0.1
0
P [-]
0
10
20
30
40
50
60
τ [years]
4He
3H/He
Together

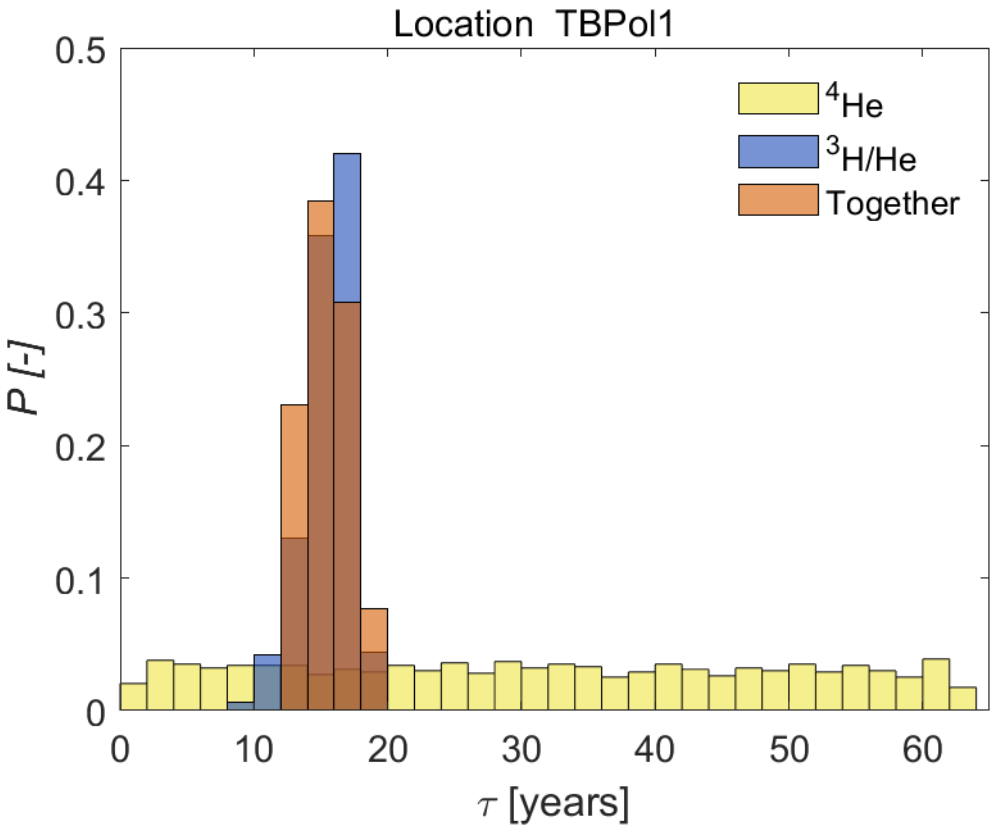
Location TBPol1
0.5
0.4
0.3
0.2
0.1
0
P [-]
0
10
20
30
40
50
60
τ [years]
4He
3H/He
Together

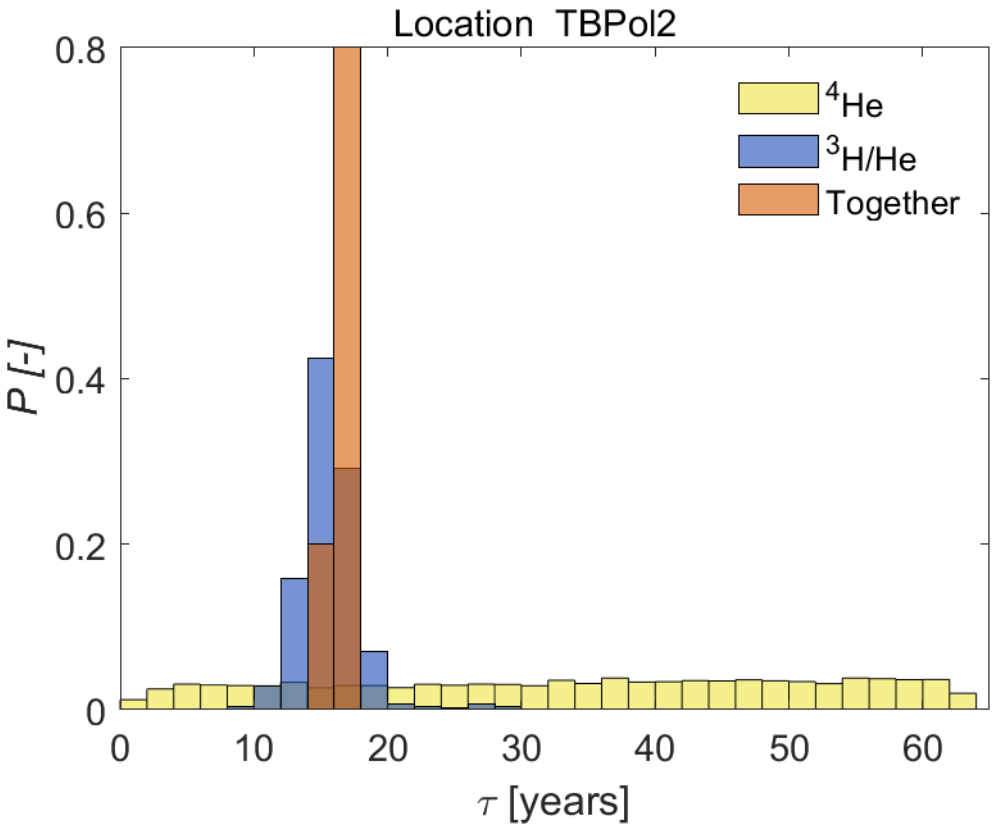
Location TBPol2
0.8
0.6
0.4
0.2
0
P [-]
0
10
20
30
40
50
60
τ [years]
4He
3H/He
Together

SUPPLEMENTARY MATERIAL 6. POSTERIOR DISTRIBUTION OF APERTURE AND POROSITY FOR STOCHASTIC MONO- AND MULTI ISOTOPE MODELLING ESTIMATED IN EACH LOCATION

ENHANCING RELIABILITY OF ESTIMATED TRAVEL TIME DISTRIBUTIONS USING MULTI-ISOTOPE MODEL OPTIMISATION

Posterior distribution of aperture and porosity for stochastic mono- and multi isotope modelling estimated in each location. Compilation of figures.

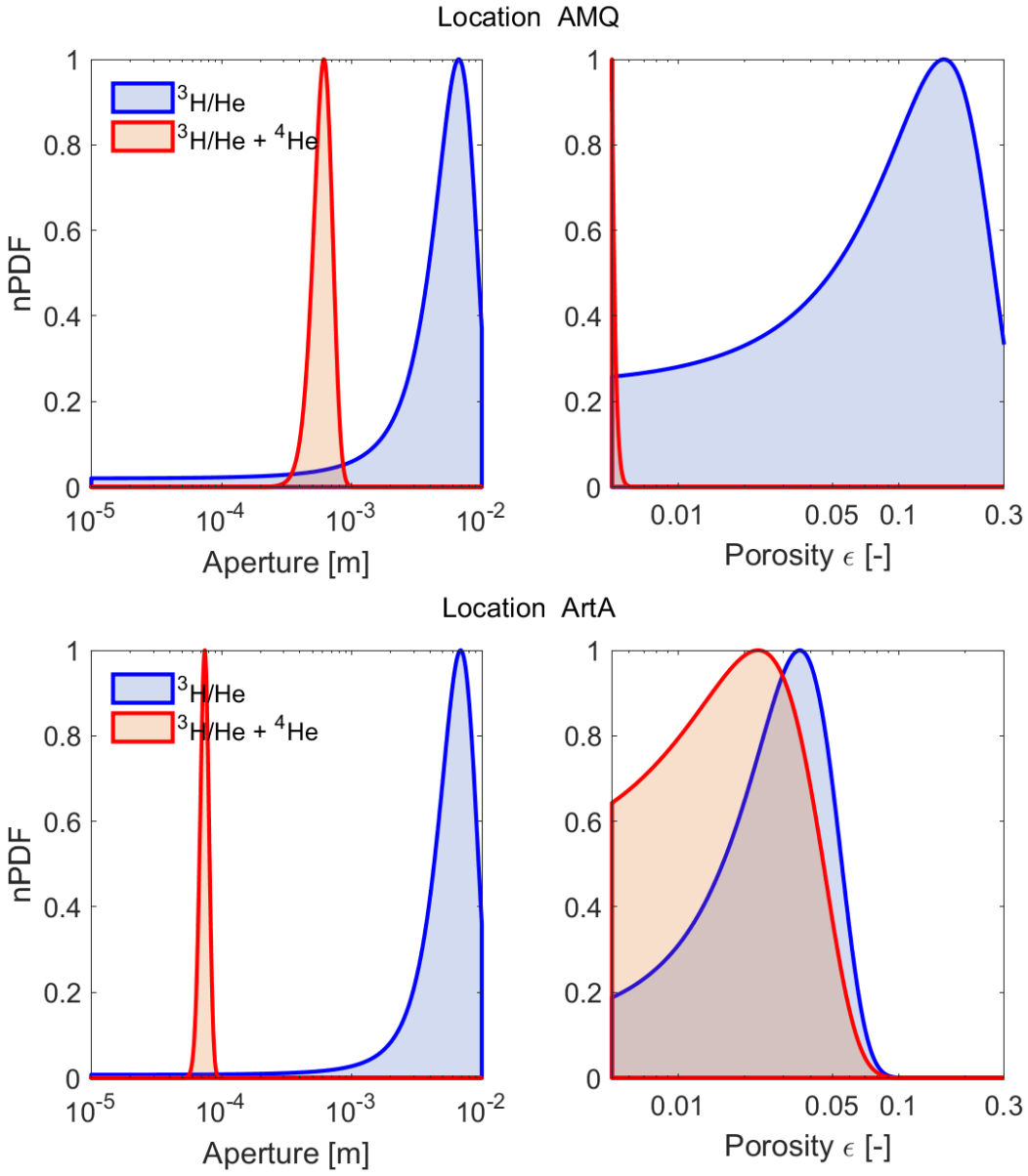
Location AMQ
nPDF
^{3}H/He
^{3}H/He + ^{4}He
Aperture [m]
Porosity ϵ [-]
Location ArtA
nPDF
^{3}H/He
^{3}H/He + ^{4}He
Aperture [m]
Porosity ϵ [-]

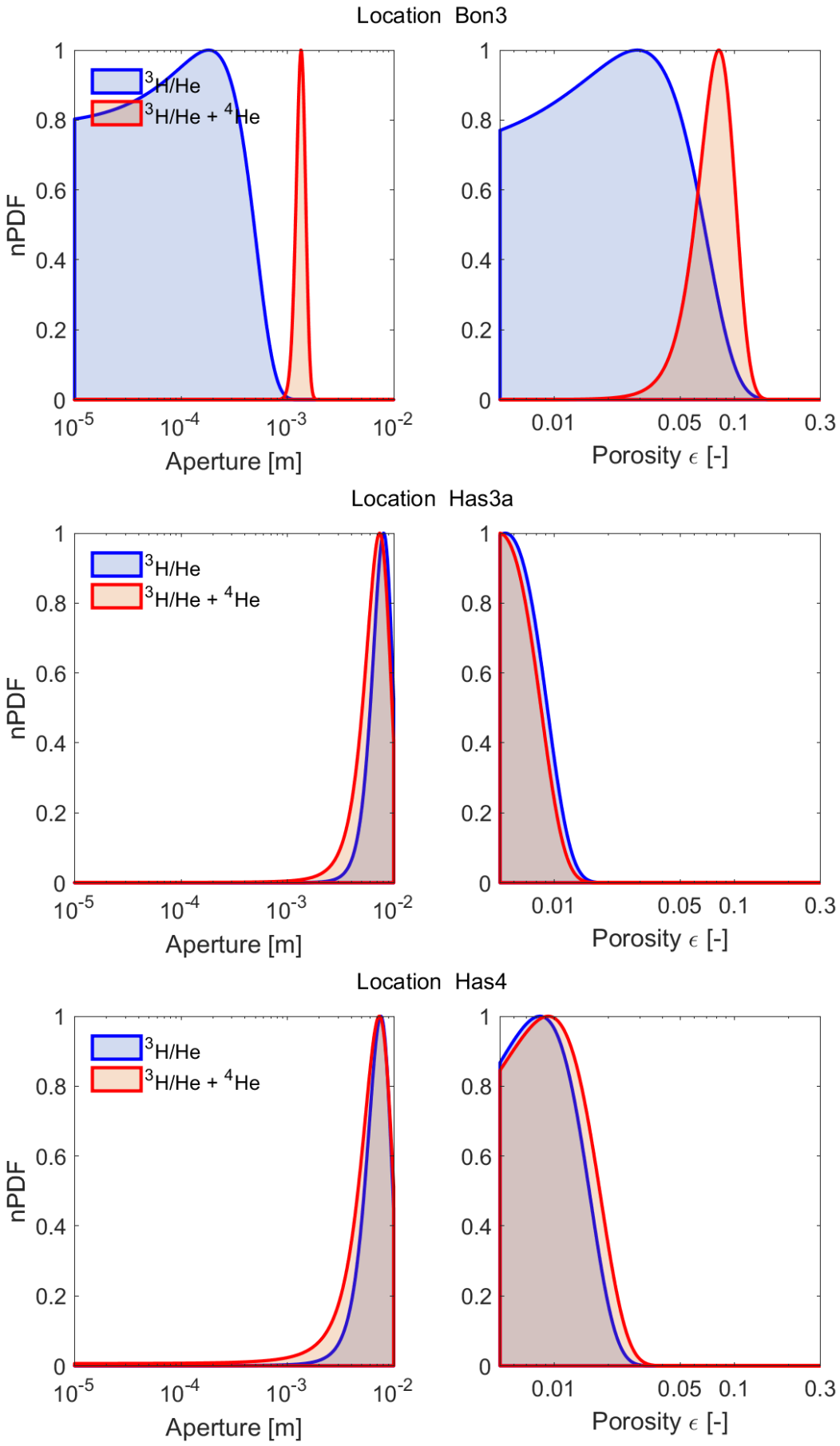
Location Bon3
nPDF
^{3}H/He
^{3}H/He + ^{4}He
Aperture [m]
Porosity ϵ [-]
Location Has3a
nPDF
^{3}H/He
^{3}H/He + ^{4}He
Aperture [m]
Porosity ϵ [-]
Location Has4
nPDF
^{3}H/He
^{3}H/He + ^{4}He
Aperture [m]
Porosity ϵ [-]

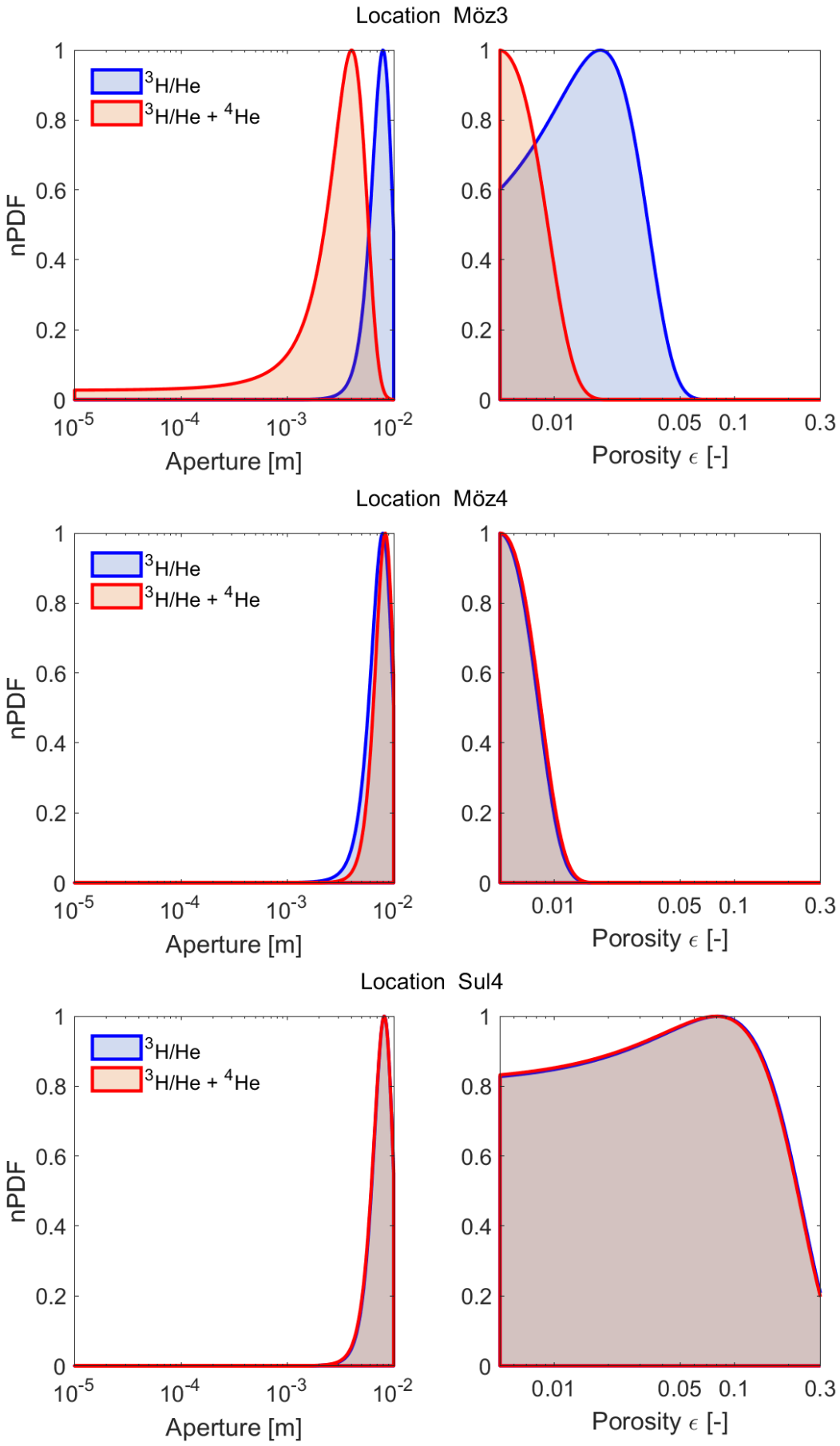
Location Möz3
nPDF
^{3}H/He
^{3}H/He + ^{4}He
Aperture [m]
Porosity ϵ [-]
Location Möz4
nPDF
^{3}H/He
^{3}H/He + ^{4}He
Aperture [m]
Porosity ϵ [-]
Location Sul4
nPDF
^{3}H/He
^{3}H/He + ^{4}He
Aperture [m]
Porosity ϵ [-]

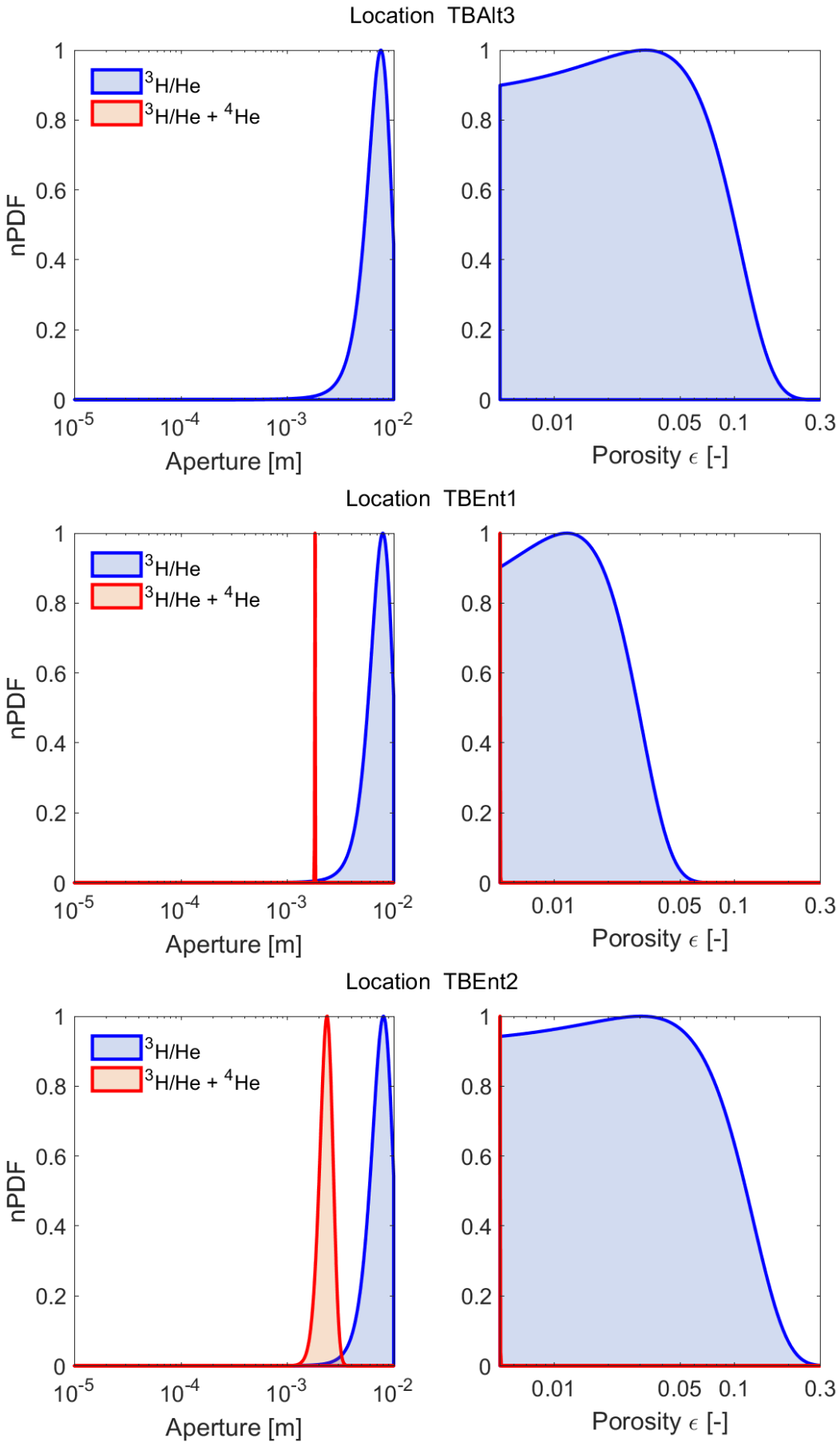
Location TBAlt3
nPDF
^{3}H/He
^{3}H/He + ^{4}He
Aperture [m]
Porosity ϵ [-]
Location TBEnt1
nPDF
^{3}H/He
^{3}H/He + ^{4}He
Aperture [m]
Porosity ϵ [-]
Location TBEnt2
nPDF
^{3}H/He
^{3}H/He + ^{4}He
Aperture [m]
Porosity ϵ [-]

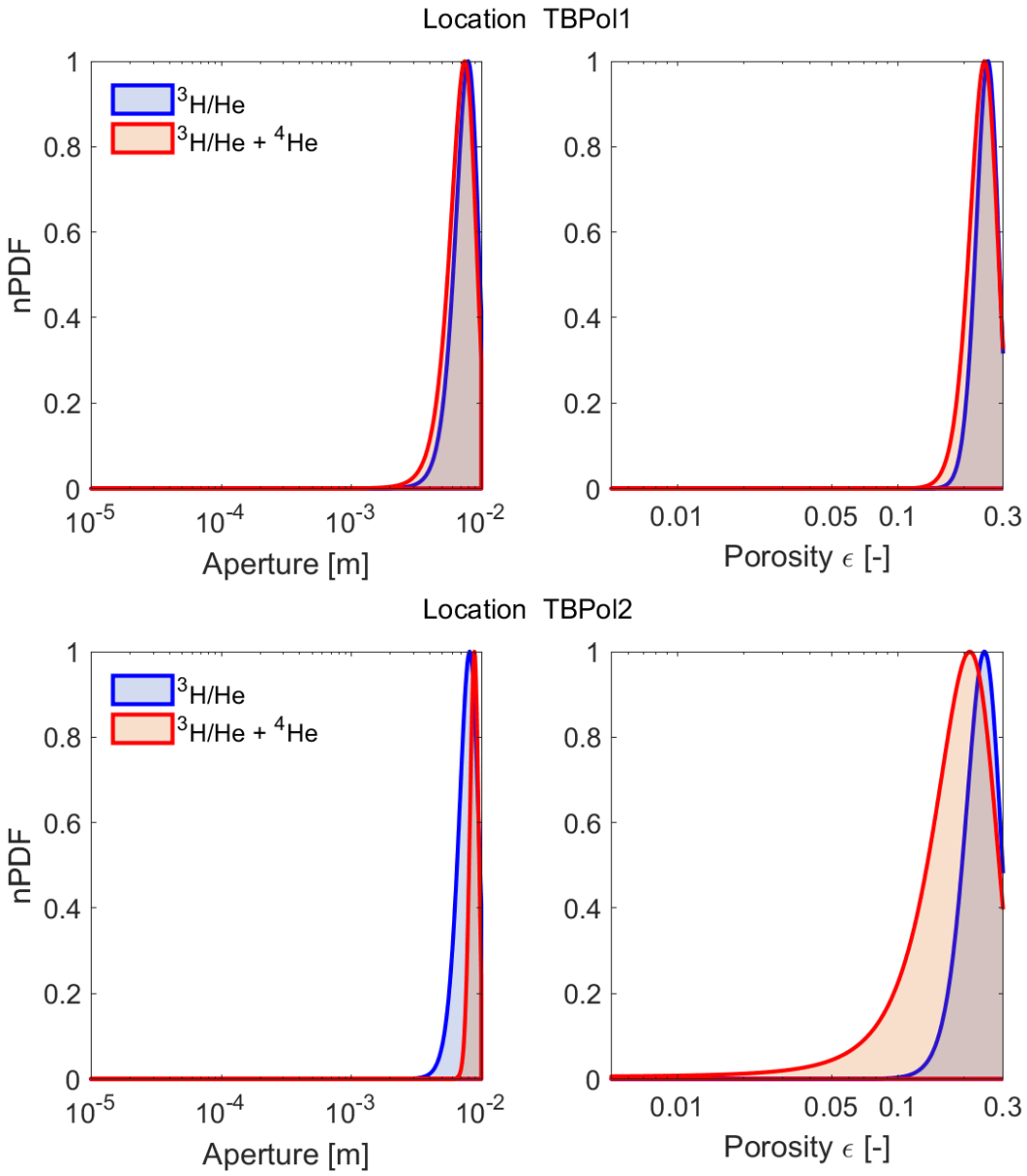
Location TBPol1
nPDF
^{3}H/He
^{3}H/He + ^{4}He
Aperture [m]
Porosity ϵ [-]
Location TBPol2
nPDF
^{3}H/He
^{3}H/He + ^{4}He
Aperture [m]
Porosity ϵ [-]